

City Research Online

City St George's, University of London

Citation: Swain, R. C. (1993). The application of pulsed laser Electronic Speckle Pattern Interferometry to the measurement of in-plane strain on high speed rotating components. (Unpublished Doctoral thesis, City, University of London)

This is the accepted version of the paper.

This version of the publication may differ from the final published version. To cite this item please consult the publisher's version.

Permanent repository link: https://openaccess.city.ac.uk/id/eprint/29609/

Copyright and Reuse: Copyright and Moral Rights remain with the author(s) and/or copyright holders. Copies of full items can be used for personal research or study, educational, or not-for-profit purposes without prior permission or charge, unless otherwise indicated, provided that the authors, title and full bibliographic details are credited, a hyperlink and/or URL is given for the original metadata page and the content is not changed in any way. For full details of reuse please refer to City Research Online policy.

City Research Online: http://openaccess.city.ac.uk/ publications@citystgeorges.ac.uk

The Application of Pulsed Laser Electronic Speckle Pattern Interferometry to the Measurement of In-Plane Strain on High Speed Rotating Components.

Thesis submitted for the Degree of Doctor of Philosophy

by

Robin Carlton Swain

Department of Mechanical Engineering and Aeronautics

Thermo-fluids Engineering Research Centre

CITY University

MAY 1993

Abstract

Increasingly sophisticated rotating system designs demand a need for more advanced experimental measurement systems, providing highly accurate data over a large number of measurement points. Described within is an interferometric measurement system based upon a speckle correlation technique, referred to in the literature as Electronic Speckle Pattern Interferometry (ESPI), TV holography or Digital Speckle Pattern Interferometry (DSPI). The interferometer is configured to measure radial in-plane displacement. A pulsed laser, necessary because of the rotary motion of the specimen, provides the illumination source. The output from the ESPI system is a fringe pattern, which must be further processed to yield useful data. The work is a continuation of an existing project, and focuses on three main aspects:

- To increase the operable speed range and reliability of the system.
- To extract quantitative engineering data from the fringe patterns.
- To develop the existing design into a 'user-friendly' system, capable of transfer into an industrial environment.

A set of two-dimensional Fourier transform programs, running on an 80486 computer, enable accurate phase data to be extracted from the fringes, delivering quantitative measurements of radial strain to subfringe accuracy.

Major advancements include the construction of a new electronic system to control the pulsed laser, enabling interferograms to be obtained at rotational speeds up to 23,842rpm, with a tip speed increase of 2.75 times any previous result (from 132m s^{-1} to 364m s^{-1}). The new control unit, unlike its predecessor, is designed to be immune to the electromagnetic interference generated by the laser, and allows speckle patterns to be obtained at any rotational speed, up to 24,000rpm, which is the maximum speed of the drive motor. An innovative shaft encoder was also incorporated into the system, producing highly reliable timing data from the rotating specimen. Efforts to increase the reliability of the measurements concentrated on the vibration and windage generated by the disc. A significant increase in the repeatability at all speeds up to approximately 14,000rpm is reported. Above this speed, the vibrations are too severe to enable repeatable results to be obtained. However, high contrast fringes are still obtained, establishing that speckle correlation occurs, and is likely to at even higher speeds.

Results from static specimens indicate that the computer software functions effectively, showing close correlation with measured strains. When used with rotating specimens, the system yields results which are generally higher than the established theory. Investigation into this phenomenon suggests that windage heating of the disc surface induces additional stresses in the specimen, as shown in a series of windage tests. Tests conducted under conditions which minimise the windage heating have good agreement with the analytical theory.

Acknowledgements

I would like to extend my appreciation to my research supervisor Dr Richard Preater from the Mechanical and Aeronautical Engineering Department of City University. It is the efforts of Dr Preater both technically and administratively which ensured the smooth running of this research project.

I would also like to thank Rick Parker (who moved to the Composites and Ceramics Group of Rolls-Royce during this project) and John Brownell from the Company Applied Science Laboratory of Rolls-Royce, Derby for invaluable assistance and patience. The considerable effort to provide additional facilities and secure supplementary funding is most certainly appreciated. An additional thank you is due to John for providing finite element data about rotating discs together with a printout of his flood unwrapping software, which was useful in the design of my program.

I wish to express my thanks to Dr Roger Green from King's College, London for explaining the implementation of the Fourier transform method of fringe analysis. Interesting discussions with Clive Buckberry from the Optics Laboratory of Rover Group and Dr Johnathon Huntley from the University of Cambridge have helped to sort out one or two difficulties. Thanks to Dr Ad Maas from Fokker Aircraft, Netherlands, for some interesting suggestions about flood unwrapping techniques. Some imaginative suggestions from Professor Malgorzata Kujawińska from Warsaw University of Technology, Poland, with regard to wrapped phasemap generation without using the Fourier transform are acknowledged. Thanks to Kenneth Perry Jr from the University of Strathclyde for providing me with a couple of code fragments to generate optimum Fourier filters. I received some useful advice on the drive of high speed rotating discs from Dr Keith Pullen from Imperial College of Science, Technology and Medicine. Appreciation is given to Chris Pugmire of the Industrial Research Institute, Christchurch, New Zealand for permission to use his three dimensional graph plotting software.

The technical support offered by Garry Peterson, Alan Cox, Steve King and Eric Skinner was excellent, and I wish to express my thanks for all the help they extended. Also, thanks to Dave Jackson of the Electrical Engineering Department and Jim Grant from the Department of Music for interesting and useful exchanges on the hardware and software.

The City University School of Engineering, Department of Mechanical and Aeronautical Engineering, Thermo-fluids research centre is acknowledged for providing space and facilities.

The combined funding of Rolls-Royce Aerospace, the Science and Engineering Research Council, the Defence Research Agency, and the City University is gratefully acknowledged.

Finally, I would like to extend my thanks to Miss Sarah O'Brien for patiently correcting the typographical errors in this document.

Declaration

"I grant powers of discretion to the University Librarian to allow this thesis to be copied in whole or in part without further reference to me. This permission covers only single copies made for study purposes, subject to normal conditions of acknowledgement."

Signed .....

Date 15 September 1995

Contents

Abstract i

Acknowledgements ii

Declaration iv

Contents v

List of figures ix

List of tables xii

List of graphs xiii

List of images xiv

Nomenclature xviii

1.0 Introduction 1
- 1.1 Overview of this thesis 3
- 1.2 Interferometric techniques 4
  - 1.2.1 Holographic Interferometry 7
  - 1.2.2 Moiré Interferometry 10
  - 1.2.3 Speckle Photography 11
  - 1.2.4 Speckle Interferometry 13
  - 1.2.5 Electronic Speckle Pattern Interferometry 14
    - 1.2.5.1 Enhancements to the basic technique 15
    - 1.2.5.2 Fringe quality in ESPI 16
    - 1.2.5.3 ESPI at elevated temperatures 17
    - 1.2.5.4 ESPI used to measure vibration 17
    - 1.2.5.5 ESPI used to measure shape 18
    - 1.2.5.6 ESPI used to measure strain 18
- 1.3 Research of direct significance 18
  - 1.3.1 Application of ESPI to rotating systems 18

2.0 Theory 27
- 2.1 Speckle formation 27
  - 2.1.1 Speckle correlation fringe formation 30
  - 2.1.2 In-plane displacement measurement 31
    - 2.1.2.1 Radially sensitive in-plane interferometer 33
  - 2.1.3 Decorrelation of speckle patterns 34
    - 2.1.3.1 Out-of-plane translation 34
    - 2.1.3.2 In-plane translation 35
    - 2.1.3.3 In-plane rotation 35
  - 2.1.4 Tilt fringes 36
- 2.2 Strain measurement 36
- 2.3 Strain in rotating discs 39
  - 2.3.1 General equations in polar coordinates 39
  - 2.3.2 Thin rotating disc 41

3.0 Experimental methods 44
3.1 Prototype system 44
3.1.1 Electronic subsystem 44
3.1.1.1 Specification of the laser firing problem 45
3.1.1.2 Electronic Control Unit (ECU) 46
3.1.1.3 Shaft encoder and timing considerations 49
3.1.1.4 Camera blanking 50
3.1.1.5 Frame capture and subtraction 51
3.1.1.6 Electromagnetic Interference 51
3.1.2 Mechanical subsystem 53
3.1.3 Optical subsystem 55
3.1.3.1 Alignment of the pulsed laser 55
3.1.3.2 Addition of carrier fringes 56
3.2 Modified system 58
3.2.1 Electronic subsystem 58
3.2.1.1 Electronic Control Unit (ECU) 58
3.2.1.1.1 Theory of operation 59
3.2.1.1.2 Laser pulse transmission 60
3.2.1.1.3 Computer control 61
3.2.1.2 Shaft encoder 64
3.2.1.3 Camera blanking 65
3.2.1.4 Frame capture system 66
3.2.1.5 Data storage 68
3.2.2 Mechanical subsystem 68
3.2.2.1 Reduction of windage effects 68
3.2.2.2 Increased rigidity of optical mounts 69
3.2.3 Optical subsystem 70
3.2.3.1 Alignment with the pulsed laser 71
3.2.3.2 Correct addition of carrier fringes 73

4.0 Fringe analysis 75
4.1 Overview of fringe analysis techniques 75
4.1.1 Intensity based analysis 76
4.1.2 Phase measurement 77
4.1.2.1 Temporal phase measurement 77
4.1.2.2 Spatial phase measurement 79
4.2 Fourier transform fringe analysis 83
4.2.1 The sampling process and the DFT 86
4.2.1.1 One-dimensional DFT 87
4.2.1.2 Two-dimensional DFT 88
4.2.1.3 Sequence reordering 89
4.2.1.4 Windowing in the spatial domain 90
4.2.1.5 Filtering in the Fourier transform domain 92
4.2.1.6 Spectral leakage 94
4.2.1.7 Noise and the DFT 94
4.2.2 Fourier transform analysis with a linear carrier 95
4.2.2.1 Tilt removal in the spatial frequency domain 101
4.2.2.2 Tilt removal in the spatial domain 102
4.2.3 Fourier transform analysis with a sectored concentric carrier . . 103
4.2.4 Incomplete fringe fields 105
4.2.4.1 Domain detection 109
4.2.5 Subpixel manipulations 109
4.3 Phase Extraction 110
4.3.1 Wrapped phase 110
4.3.2 Phase unwrapping 111
4.3.2.1 Flood unwrapping algorithm 113

4.4 Displacement data extraction 115
4.5 Computer software 116
4.5.1 Computation of forward 2D DFT 117
4.5.2 Filtering in the Fourier domain 120
4.5.3 Computation of inverse 2D DFT 122
4.5.4 Phase unwrapping 123
4.5.5 Speckle image quality determination 123
4.5.6 Disc centre coordinates 124
4.5.7 Camera calibration 124

5.0 Results 126
5.1 Results from static specimens 127
5.1.1 Experimental apparatus 127
5.1.2 Experimental procedure 129
5.1.3 Tensile tests 131
5.1.3.1 Flat plate tensile specimen without hole 131
5.1.3.2 Flat plate tensile specimen with hole 138
5.2 Results from rotating specimens 146
5.2.1 Experimental apparatus 146
5.2.2 Speed variation tests 148
5.2.2.1 Experimental procedure 148
5.2.2.2 Results (low speed) 150
5.2.2.3 Results (medium speed) 158
5.2.2.4 Results (high speed) 165
5.2.2.5 Results (very high speed) 168
5.2.3 Windage tests 170
5.2.3.1 Experimental procedure 170
5.2.3.2 Results 171
5.2.3.3 Computed windage expansion 181

6.0 Sources of error 182
6.1 Sensitivity vector error 182
6.1.1 Contribution due to optical system abberations 182
6.1.2 Contribution due to divergence of the laser beam 184
6.1.3 Contribution due to area determination 188
6.1.4 Contribution due to centre coordinate calculation 189
6.1.5 Contribution due to incidence angle measurement 190
6.1.6 Fringe field angular skew 191
6.2 Data acquisition and processing 192
6.2.1 Camera noise 192
6.2.2 Quantization 193
6.2.3 Speckle noise 194
6.2.4 Post processing (after acquisition and storage) 196
6.3 Phase extraction errors 196
6.4 Errors resulting from the mechanical system 199
6.4.1 Vibrations 199
6.4.2 Atmospheric perturbations 201
6.4.3 Surface preparation 203
6.4.4 Timing errors 204
6.5 Errors due to the specimen 205
6.5.1 Constriction under load 205
6.5.2 In-plane vibrations 206
6.5.3 Out-of-plane vibrations 206

Discussion and Conclusion 208
Discussion of results 208
Conclusion 213

Further work 214
Interferometer 214
Laser illumination source 216
Fringe analysis 217
Data processing 217
Experimentation 219
Errors 221

References 222

Appendix A: PC Fundamentals 241
A.1 Intel 80x86 processor family 241
A.2 MS-DOS operating system (Version 5.0) 242
A.3 Extended Memory Specification 242
A.4 Minimum hardware requirements 243

Appendix B: Software fragments 244
B.1 One dimensional FFT algorithm 244
B.2 Fourier transform calling program 246
B.3 Modified snap instruction of VS100 246

Appendix C: Numerical results 248

Appendix D: Electronic diagrams 257

List of figures

Figure 1: Two beam interferometry 5
Figure 2: Typical holographic setup 8
Figure 3: Simple moiré fringe pattern 11
Figure 4: Speckle photography 11
Figure 5: Speckle interferometry 14
Figure 6: Out-of-plane ESPI system 15
Figure 7: Original optics [Preater, 1980a] 19
Figure 8: Original electronic setup [Preater, 1980a] 20
Figure 9: Updated electronics [Preater, 1985] 21
Figure 10: Plane mirror decorrelation 22
Figure 11: Updated optics [Preater, 1985b] 23
Figure 12: Speckle generation 27
Figure 13: Drunkard's walk 28
Figure 14: Image plane speckle formation 29
Figure 15: In-plane sensitive interferometer 32
Figure 16: In-plane rotation sensitivity 32
Figure 17: Radially sensitive interferometer (as Figure 11) 33
Figure 18: In-plane translation 34
Figure 19: Element coordinate system 40
Figure 20: Electronic system 45
Figure 21: Block diagram of prototype ECU 47
Figure 22: ECU counter operation 47
Figure 23: ECU operation flowchart 48
Figure 24: Timing example 49
Figure 25: Timing pulse improvement 49
Figure 26: JK 2000 firing sequence 51
Figure 27: Interference, Correct operation (left), Incorrect operation (right) 52
Figure 28: Mechanical support 54
Figure 29: Periscope mirrors 55
Figure 30: Original optical delivery 56
Figure 31: Alignment of the pulsed laser 56
Figure 32: Cylindrical misalignment 58
Figure 33: Modified electronic system 59
Figure 34: Diagram of modified ECU 60
Figure 35: ECU counter profiles 60
Figure 36: Modified ECU flowchart 61
Figure 37: Enable pulse timing diagram 61
Figure 38: Laser pulse delivery 62
Figure 39: Computer interface 63
Figure 40: Image capture flowchart 64
Figure 41: Modified shaft encoder 66
Figure 42: Modified encoder 66
Figure 43: Rig with air baffle 70
Figure 44: Air baffle 70
Figure 45: New optical delivery 72
Figure 46: Pulsed laser alignment 74
Figure 47: Tilt mirror mounting 74
Figure 48: Fringe analysis techniques 76
Figure 49: Heterodyne method 77
Figure 50: Temporal phase shift method 78
Figure 51: Spatial phase shift method 80
Figure 52: Periodic nature of 2D DFT 92
Figure 53: Ideal filters 92

Figure 54: 2D FFT of Image 19 100
Figure 55: Filtered spectrum 100
Figure 56: Tilt removal in the Fourier domain 101
Figure 57: Three methods of tilt removal in the spatial domain 102
Figure 58: Radial carrier 104
Figure 59: Fringes and their 2D DFT's 105
Figure 60: Gerchberg Saxton algorithm 108
Figure 61: FFT of Image 33 110
Figure 62: FFT of Image 34 110
Figure 63: Wrapped phase 111
Figure 64: Flood unwrapping algorithm 114
Figure 65: Flood unwrapping algorithm flowchart 114
Figure 66: 3D Plot 115
Figure 67: Forward Fourier transform program flowchart 117
Figure 68: Extended Memory structure 118
Figure 69: Typical Fourier window 120
Figure 70: 2D FFT of Image 36 121
Figure 71: Tight filter (1) 121
Figure 72: Loose filter (2) 121
Figure 73: Inverse Fourier transform program flowchart 122
Figure 74: Optical measurement system 127
Figure 75: Specimen without hole 128
Figure 76: Specimen with central hole 128
Figure 77: Strain gauge configuration 128
Figure 78: Strain gauge configurations: Bending (left), strain (right) 129
Figure 79: Unwrapped phase A 133
Figure 80: Unwrapped phase B 133
Figure 81: Unwrapped phase C 133
Figure 82: Unwrapped phase D 134
Figure 83: Phase B - Phase A 134
Figure 84: Phase C - Phase A 134
Figure 85: Phase D - Phase A 134
Figure 86: Gauge array locations 135
Figure 87: Unwrapped phase E 140
Figure 88: Unwrapped phase F 141
Figure 89: Unwrapped phase G 141
Figure 90: Unwrapped phase H 141
Figure 91: Unwrapped phase I 141
Figure 92: Phase F - Phase E 141
Figure 93: Phase G - Phase E 142
Figure 94: Phase H - Phase E 142
Figure 95: Phase I - Phase E 142
Figure 96: Gauge array locations 143
Figure 97: Test specimen 146
Figure 98: Region of interest 147
Figure 99: Flowchart of image acquisition procedure 149
Figure 100: Diagrammatic representation of test schedule 150
Figure 101: Unwrapped phase A 152
Figure 102: Unwrapped phase B 152
Figure 103: Unwrapped phase C 152
Figure 104: Unwrapped phase D 152
Figure 105: Optical gauge locations 153
Figure 106: Unwrapped phase E 155
Figure 107: Unwrapped phase F 155
Figure 108: Unwrapped phase G 157
Figure 109: Diagrammatic representation of test schedule 158

Figure 110: Unwrapped phase H 160
Figure 111: Unwrapped phase I 160
Figure 112: Unwrapped phase J 160
Figure 113: Unwrapped phase K 160
Figure 114: Diagrammatic representation of test schedule 161
Figure 115: Unwrapped phase L 163
Figure 116: Unwrapped phase M 163
Figure 117: Unwrapped phase N 163
Figure 118: Unwrapped phase O 164
Figure 119: Diagrammatic representation of test schedule 165
Figure 120: Unwrapped phase P 167
Figure 121: Unwrapped phase Q 167
Figure 122: Unwrapped phase R 167
Figure 123: Unwrapped phase S 167
Figure 124: Windage test schedule 170
Figure 125: Spherical reflector 182
Figure 126: Zoom of Figure 125 182
Figure 127: Paraboloidal reflector 183
Figure 128: Zoom of Figure 127 183
Figure 129: Off axis ray 184
Figure 130: Additional ray 184
Figure 131: Another ray 184
Figure 132: In-plane divergence error 185
Figure 133: Geometrical representation (*xz* plane) 185
Figure 134: Plane mirror divergence (*xy* plane) 187
Figure 135: Error in measuring disc centre coordinates 189
Figure 136: Method of incidence angle determination 190
Figure 137: Acquisition system 192
Figure 138: Rounding of signal samples 193
Figure 139: Speckle noise mathematical model 195
Figure 140: Constriction of the disc under load 206
Figure 141: Out-of-plane flap of the specimen 206
Figure 142: 2D speckle correlation for measuring in-plane strain 215
Figure 143: PC memory 242
Figure 144: Optical gauge locations 248
Figure 145: Primary electronic counter 259
Figure 146: Secondary electronic counter 260

List of tables

Table 1: ECU programming table 62
Table 2: Tilt motor programming table 72
Table 3: Comparison of fringe pattern analysis methods (Kujawińska [1992a]) 82
Table 4: Fourier transform symmetries 84
Table 5: Computational advantage of using the FFT 89
Table 6: Strain measurements for 57μstrain load increase 135
Table 7: Strain measurements for 110μstrain load increase 136
Table 8: Strain measurements for 156μstrain load increase 136
Table 9: Strain measurements for 54μstrain load increase 144
Table 10: Strain measurements for 102μstrain load increase 144
Table 11: Strain measurements for 153μstrain load increase 145
Table 12: Capture times of the reference and load speckle patterns (A to D) 150
Table 13: Capture times of the reference and load speckle patterns (H to K) 158
Table 14: Error for plane system (45° nominal, 0.1m field of view and scan line) . . . 188
Table 15: Refractive index dependency on temperature and pressure 203
Table 16: Optical strain gauge readings for fringe pattern A (3mm gauge length) . . . 248
Table 17: Optical strain gauge readings for fringe pattern B (3mm gauge length) . . . 249
Table 18: Optical strain gauge readings for fringe pattern C (3mm gauge length) . . . 249
Table 19: Optical strain gauge readings for fringe pattern D (3mm gauge length) . . . 250
Table 20: Optical strain gauge readings for fringe pattern E (3mm gauge length) 250
Table 21: Optical strain gauge readings for fringe pattern F (3mm gauge length) 251
Table 22: Optical strain gauge readings for fringe pattern G (3mm gauge length) . . . 251
Table 23: Optical strain gauge readings for fringe pattern H (3mm gauge length) . . . 252
Table 24: Optical strain gauge readings for fringe pattern I (3mm gauge length) 252
Table 25: Optical strain gauge readings for fringe pattern J (3mm gauge length) 253
Table 26: Optical strain gauge readings for fringe pattern K (3mm gauge length) . . . 253
Table 27: Optical strain gauge readings for fringe pattern L (3mm gauge length) 254
Table 28: Optical strain gauge readings for fringe pattern M (3mm gauge length) . . . 254
Table 29: Optical strain gauge readings for fringe pattern N (3mm gauge length) . . . 255
Table 30: Optical strain gauge readings for fringe pattern O (3mm gauge length) . . . 255
Table 31: Optical strain gauge readings for fringe pattern P (3mm gauge length) . . . 256
Table 32: Optical strain gauge readings for fringe pattern Q (3mm gauge length) . . . 256
Table 33: Optical strain gauge readings for fringe pattern R (3mm gauge length) . . . 257
Table 34: Optical strain gauge readings for fringe pattern S (3mm gauge length) . . . 257

List of graphs

Graph 1: Normalized probability density 29
Graph 2: Radial and hoop stress distributions 43
Graph 3: Reordering a sequence (before) 90
Graph 4: Reordering a sequence (after) 90
Graph 5: One dimensional data weighting functions 91
Graph 6: DFT of Equation [90] with $n = 8$ 95
Graph 7: DFT of Equation [90] with $n = 5$ 95
Graph 8: Ripples from a discontinuity 106
Graph 9: Comparison of measured and theoretical radial strains 154
Graph 10: Radial strain for high acceleration rate (Fringe pattern E) 156
Graph 11: Radial strain for high acceleration rate (Fringe pattern F) 156
Graph 12: Comparison of measured and theoretical radial strains 157
Graph 13: Comparison of measured and theoretical radial strains 161
Graph 14: Comparison of measured and theoretical radial strains 163
Graph 15: Comparison of measured and theoretical radial strains 165
Graph 16: Comparison of measured and theoretical radial strains 168
Graph 17: Measured temperature change at 60mm and 120mm 171
Graph 18: Average expansion of disc with speed and time 180
Graph 19: Average expansion of disc with acceleration and time 180
Graph 20: Average expansion of disc with acceleration and time 180

List of images

Image 1: HI fringes 9
Image 2: Fringes from a static tension test 20
Image 3: Early correlation fringes at 250rpm 21
Image 4: Tension specimen at 400rpm 22
Image 5: Fringes on a perspex disc 24
Image 6: Fringe area reduction 24
Image 7: Propeller blade fringes 25
Image 8: Concentric fringes on a brake disc 26
Image 9: Example speckle pattern 28
Image 10: Radial fringes 35
Image 11: Tilt fringes 36
Image 12: Plan view of original rig 53
Image 13: Front view of test specimen 54
Image 14: View of laboratory 57
Image 15: Incorrect carrier fringes 57
Image 16: Correct carrier fringes 57
Image 17: Plan view of updated rig 69
Image 18: Front view of test specimen 71
Image 19: Example fringe pattern 100
Image 20: Wrapped phasemap 100
Image 21: Unwrapping mask 100
Image 22: Bad data removal 100
Image 23: Simulated cos fringes 106
Image 24: FFT of Image 23 (x4) 106
Image 25: Large discontinuity 107
Image 26: FFT of Image 25 (x4) 107
Image 27: Medium discontinuity 107
Image 28: FFT of Image 27 (x4) 107
Image 29: Small discontinuity 107
Image 30: FFT of Image 29 (x4) 107
Image 31: Image 25 + 1 iteration 108
Image 32: Image 25 + 3 iterations 108
Image 33: Uncorrelated image 110
Image 34: Correlated image 110
Image 35: Unwrapped phase 115
Image 36: Example fringes 121
Image 37: Unwrapped phase (1) 121
Image 38: Unwrapped phase (2) 121
Image 39: Static loading rig 129
Image 40: Imaging region 132
Image 41: Carrier fringes (A) 132
Image 42: Carrier + 57μstrain (B) 132
Image 43: Carrier + 110μstrain (C) 132
Image 44: Carrier + 156μstrain (D) 132
Image 45: Wrapped phase A 132
Image 46: Wrapped phase B 133
Image 47: Wrapped phase C 133
Image 48: Wrapped phase D 133
Image 49: Phase B - Phase A 134
Image 50: Phase C - Phase A 134
Image 51: Phase D - Phase A 135
Image 52: Imaging region 139

Image 53: Carrier fringes (E) 139
Image 54: Carrier + 50μstrain (F) 139
Image 55: Carrier + 100μstrain (G) 139
Image 56: Carrier + 150μstrain (H) 139
Image 57: Carrier + 200μstrain (I) 139
Image 58: Wrapped phase E 140
Image 59: Wrapped phase F 140
Image 60: Wrapped phase G 140
Image 61: Wrapped phase H 140
Image 62: Wrapped phase I 140
Image 63: Phase F - Phase E 141
Image 64: Phase G - Phase E 142
Image 65: Phase H - Phase E 142
Image 66: Phase I - Phase E 142
Image 67: Discontinuity 143
Image 68: FFT of discontinuity 143
Image 69: Fringe pattern A 151
Image 70: Fringe pattern B 151
Image 71: Fringe pattern C 151
Image 72: Fringe pattern D 151
Image 73: Wrapped phase A 151
Image 74: Wrapped phase B 151
Image 75: Wrapped phase C 152
Image 76: Wrapped phase D 152
Image 77: Fringe pattern E 155
Image 78: Fringe pattern F 155
Image 79: Wrapped phase E 155
Image 80: Wrapped phase F 155
Image 81: Fringe pattern G 157
Image 82: Wrapped phase G 157
Image 83: Fringe pattern H 159
Image 84: Fringe pattern I 159
Image 85: Fringe pattern J 159
Image 86: Fringe pattern K 159
Image 87: Wrapped phase H 159
Image 88: Wrapped phase I 159
Image 89: Wrapped phase J 160
Image 90: Wrapped phase K 160
Image 91: Fringe pattern L 162
Image 92: Fringe pattern M 162
Image 93: Fringe pattern N 162
Image 94: Wrapped phase L 162
Image 95: Wrapped phase M 162
Image 96: Wrapped phase N 162
Image 97: Fringe pattern O 164
Image 98: Wrapped phase O 164
Image 99: Fringe pattern P 166
Image 100: Fringe pattern Q 166
Image 101: Fringe pattern R 166
Image 102: Fringe pattern S 166
Image 103: Wrapped phase P 166
Image 104: Wrapped phase Q 166
Image 105: Wrapped phase R 167
Image 106: Wrapped phase S 167
Image 107: Fringe pattern T 169
Image 108: Fringe pattern U 169

Image 109: Fringe pattern V 169
Image 110: Fringe pattern W 169
Image 111: Fringe pattern X 169
Image 112: Fringe pattern Y 169
Image 113: Corr(0,1) - 10s (Windage test 1) 173
Image 114: Corr(0,2) - 31s (Windage test 1) 173
Image 115: Corr(0,3) - 41s (Windage test 1) 173
Image 116: Corr(0,4) - 51s (Windage test 1) 173
Image 117: Corr(0,8) - 95s (Windage test 1) 173
Image 118: Corr(0,13) - 150s (Windage test 1) 173
Image 119: Corr(0,2) - 19s (Windage test 2) 174
Image 120: Corr(0,3) - 29s (Windage test 2) 174
Image 121: Corr(0,4) - 38s (Windage test 2) 174
Image 122: Corr(0,5) - 48s (Windage test 2) 174
Image 123: Corr(2,3) - 19s, 29s (Windage test 2) 174
Image 124: Corr(2,5) - 19s, 37s (Windage test 2) 174
Image 125: Corr(0,1) - 10s (Windage test 3) 175
Image 126: Corr(0,2) - 20s (Windage test 3) 175
Image 127: Corr(0,4) - 39s (Windage test 3) 175
Image 128: Corr(1,3) - 10s, 29s (Windage test 3) 175
Image 129: Corr(1,4) - 10s, 39s (Windage test 3) 175
Image 130: Corr(0,1) - 10s (Windage test 4) 176
Image 131: Corr(0,2) - 19s (Windage test 4) 176
Image 132: Corr(0,3) - 29s (Windage test 4) 176
Image 133: Corr(1,2) - 10s, 19s (Windage test 4) 176
Image 134: Corr(1,3) - 10s, 29s (Windage test 4) 176
Image 135: Corr(2,3) - 19s, 29s (Windage test 4) 176
Image 136: Corr(0,1) - 10s (Windage test 5) 177
Image 137: Corr(0,2) - 20s (Windage test 5) 177
Image 138: Corr(1,2) - 10s, 20s (Windage test 5) 177
Image 139: Corr(1,3) - 10s, 29s (Windage test 5) 177
Image 140: Corr(1,4) - 10s, 39s (Windage test 5) 177
Image 141: Corr(3,5) - 29s, 49s (Windage test 5) 177
Image 142: Corr(0,2) - 9s (Windage test 6) 178
Image 143: Corr(0,3) - 28s (Windage test 6) 178
Image 144: Corr(0,4) - 38s (Windage test 6) 178
Image 145: Corr(1,4) - 9s, 38s (Windage test 6) 178
Image 146: Corr(1,5) - 9s, 48s (Windage test 6) 178
Image 147: Corr(3,4) - 28s, 38s (Windage test 6) 178
Image 148: Corr(0,1) - 9s (Windage test 7) 179
Image 149: Corr(1,2) - 9s, 18s (Windage test 7) 179
Image 150: Corr(1,3) - 9s, 31s (Windage test 7) 179
Image 151: Corr(2,4) - 18s, 41s (Windage test 7) 179
Image 152: Corr(2,5) - 18s, 50s (Windage test 7) 179
Image 153: Obstruction at 1mm 202
Image 154: Obstruction at 0.2mm 202
Image 155: Paint-free fringes 203

Nomenclature

0x	Indicates a Hexadecimal number (base 16, rather than 10)
AM	Amplitude Modulation
ANSI	American National Standards Institute
BCD	Binary Coded Decimal
BIOS	Basic Input Output System (on Intel based computers)
CCIR	European (Australian) television standard
CPU	Central Processing Unit
C	C programming language (usually Microsoft C, in this thesis)
C++	C++ programming language (usually Microsoft C++, in this thesis)
DC	Direct Current (or sometimes refers to zero frequency)
DFT	Discrete Fourier Transform
DOS	See MS-DOS
ECU	Electronic Control Unit
EI	Electromagnetic Interference
EM	Electromagnetic
ESPI	Electronic Speckle Pattern Interferometry
FFT	Fast Fourier Transform
FM	Frequency Modulation
FTP	File Transfer Protocol (used over the global Ethernet network)
FTS	File Tracking System
GIF	Graphical Image File
HCT	High speed CMOS with TTL compatibility
HeNe	Helium Neon (laser)
HI	Holographic Interferometry
HOE	Holographic Optical Element
I/O	Input/Output
IR	Infra-Red
ITEX™	Imaging Technology image processing link library (Version 2.0)
KB	Kilobyte (1,024 bytes)
MB	Megabyte (1,024KB or 1,048,576 bytes)
MHz	Megahertz
MS-DOS™	Microsoft Disk Operating System (Version 5.0)
Nd:YAG	Neodymium YAG laser
PC	Intel 80x86 based AT compatible computer
PC36AT	Amplicon Liveline 24 line I/O controller card
PLL	Phase Locked Loop
PM	Phase Modulation
PZT	Piezoelectric translator
PWM	Pulse Width Modulation

r^2	A statistic ranging from 0.0 to 1.0. Indicates how much of the change in the dependant variable results from changing the indepenent variable. 1.0 is an exact correlation.
RAM	Random Access Memory
SCSI	Small Computer Serial Interface
SVGA	Super VGA (a higher graphical resolution than VGA)
TIFF	Tagged Image File Format
TTL	Transistor Transistor Logic
UNIX™	AT&T UNIX version 5.0 operating system or similar
VGA	Video Graphics Array
VS100 (768/2)	Imaging Technology variable scan frame store model 100
WINDOWS™	Microsoft WINDOWS 3.1 operating system
XMS	Extended Memory Specification
XRAM	Extended Memory (see Appendix A)

MS-DOS and WINDOWS are a registered trademarks of Microsoft Corporation.
ITEX is a registered trademark of Imaging Technology Incorporated.
UNIX is a registered trademark of AT&T Incorporated.

1 INTRODUCTION AND REVIEW

1.0 Introduction

Rotating components are essential elements in many modern machines, from hand drills and computer disk drives to turbo jet engines. As such, they receive considerable attention from scientists and engineers. The design engineer has a need to measure dependable engineering data from such systems under normal operating conditions. A typical requirement would involve obtaining measurements of strain at various locations on the surface of the specimen under different loading conditions. The normal means of measuring strains on rotating objects consists of attaching some form of sensor to the surface of the specimen. Typically, a strain gauge is bonded to the surface and the electrical output is fed via slip rings to the measuring device. This method gives a good indication of the conditions in the region of the gauge, but a single point measurement is not satisfactory for complex specimen geometries. In some cases, for example gas turbine engines, the specimen is driven at elevated temperatures which would often cause the loss of the sensor.

In the case of rotating component *expansion*, some of the methods devised to measure the overall expansion can be rather rudimentary. For example, the aerospace industry uses a video camera focused close to the perimeter of a rotating specimen. The specimen is rotated at a certain speed, and the resultant arc displayed on the screen of the video monitor is marked with a pen. The speed is altered and the new arc is marked on the screen. Calculation of the overall expansion, from the difference between the arcs, is simple but inaccurate. Also, only significant expansions (of the order of a millimetre or so), can be measured in this way. Proximity detectors can also be used to measure the overall expansion of a component as it rotates.

The vibration of rotating components has attracted considerable interest, as it has long been recognised that vibrations cause many in-service failures. Standard techniques to measure the vibration of a rotating component involve attaching accelerometers to the specimen surface, and the use of proximity sensors mounted on the stator. Again, the engineer is faced with data at only a limited number of points. Attaching a sensor to a rotating component can radically alter the experimental conditions, since the device itself can dramatically modify the vibration modes. In the case of jet engine fans, simply painting the surface of the component can be enough to affect the aerodynamic performance, due to increased surface roughness

and leading edge thickness. In this case, a non-contact measurement system is essential to understand correctly the phenomena under investigation. Many different forms of non-contact techniques exist, but in this thesis, the discussion will be limited to *optical* techniques, and in particular *interferometric* techniques.

Optical techniques, as the term suggests, use electro-magnetic radiation (usually light), as the information-bearing medium. The incident light (in many cases from a laser), may be used in one of two ways: in straightforward reflection or transmission, or interferometrically.

One established use of laser light in ordinary *reflection* is in the measurement of distance. For example, in civil engineering, the method of *triangulation* is frequently used to measure reasonably large distances (of the order of metres), where the angle between the incident and reflected beams gives a measure of the distance. *Laser ranging* is used over larger distances, where a 'burst' of light is emitted, and the time taken for it to return after reflection is used to determine the distance to the object[1].

Interferometric techniques represent quite a different approach to measurement. In basic terms, the light is split into two waves: the *object* and *reference* waves. The object wave, after returning from the specimen, is *compared* with the reference wave. The difference between the two waves gives an indication of the effect of the specimen on the wavefronts prior to incidence, and hence a measure of some quantity. By their nature, interferometric techniques are very accurate in contrast to more conventional measurement techniques.

The widespread availability of high quality optical components and powerful electronic acquisition and processing devices has enabled interferometry to expand into many diverse fields (the prohibitive cost restrictions that existed previously have all but disappeared). Hence, interferometric techniques have matured, and the general confidence of potential users has increased dramatically.

The aerospace industry in particular has been investigating the use of non-contact optical measurement techniques. Holographic interferometry (discussed in section 1.2.1) has been widely used by the industry to measure vibrations on rotating specimens. The method offers considerable benefits over conventional contact techniques, since it provides a full field view of the specimen with overlaid vibrational information. Holographic Interferometry is now used

---

[1]A very interesting example of laser ranging is described by Mulholland and Calame [1978]. In their work, a laser beam emitted from the McDonald Observatory at the University of Texas is reflected from a group of retroreflectors placed on the lunar surface by Apollo 16. The moon was determined to be actually 'wobbling' from the impact of an asteroid in 1178 (AD). The impact was witnessed and documented by a group of Canterbury Monks.

routinely to detect flaws in aircraft tyres, to examine the vibrational modes of new turbine blade designs, and many other applications. In addition, Speckle Photography (section 1.2.4) has been used successfully by the aerospace industry to measure in-plane strains on high speed rotating discs at the typical temperatures found in the hot section of jet engines.

It seems only right to mention some of the drawbacks of optical non-contact measurement systems. Generally, such systems are comprised of complex and fragile pieces of equipment, requiring skilled operators to perform the measurements, *and* to interpret the results. In the case of rotating components, a *pulsed laser* is required, which increases the cost significantly. Each result (in the form of an image or hologram), represents a snapshot of what was occurring at the instant the data was recorded (or the difference between two states). There is no way of obtaining continuous data output (the analogue equivalent of a discrete time signal). Several of the techniques require the use of photographic processing and darkened ambient conditions, which deviates from the current trend of real-time all digital processing.

In parallel with this experimental research, computer scientists together with engineers, have developed mathematical models of the mechanical phenomena associated with complex rotating systems. The models have evolved with time, and are still doing so. The verification of such models is vital, and hence the investigator must devise better methods of extracting data from experiments. The drive towards full field techniques is without doubt a step in the right direction, since additional data measurement points provide a more accurate estimate of the condition of the specimen. The combination of full field and non-contact techniques provide the closest estimate of the required measurement parameter.

1.1 Overview of this thesis

This chapter continues by introducing several of the common interferometric techniques in use today, and by describing some of the reasons why they have attained such high importance in the experimental world. A brief introduction to the *applications* of these techniques is also included. A review of the early work directly related to this thesis is then presented (section 1.3). Deeper consideration is given to the various applications of Electronic Speckle Pattern Interferometry (ESPI), for this reason.

The theoretical basis for speckle correlation fringe formation, together with its specific application to in-plane strain measurement, is discussed in Chapter two. The theory of the radially sensitive in-plane interferometer is then examined, and the strain of a simple thin disc in rotation is analyzed using established formulae.

Chapter three describes in depth the main work conducted by the author. Initially the system that existed prior to the start of the project is described, followed by the modifications and improvements to the system. Each subsystem is examined individually, including a before/after description.

A description of the computer software produced to store and analyze the interference fringe patterns of the modified experimental system is presented in the following chapter (Chapter four). Various fringe pattern analysis techniques are reviewed, providing an introduction to the two dimensional Fourier transform method of fringe analysis, which was implemented to extract phase information from the fringe patterns. The details of the implementation on a small computer are also discussed.

Chapter five presents a selection of the results obtained using the modified experimental system. Results from *static* specimens are presented initially, in order to assess the usefulness of the software. The results from rotating specimens are then given and compared with theoretical models.

In the final chapter, the sources of error are reviewed. Errors associated with the experimental rig are discussed, followed by those arising from the data processing. Wherever possible, numerical estimates of the errors are quoted.

1.2 Interferometric techniques

The idea that the wave nature of light might be used to make measurements of extremely high accuracy is attributed to Michelson [1902]. Since that time, measurement techniques using light waves have grown and followed many different paths, finding applications in almost all aspects of science. The patterns produced when light beams interfere are known as fringe patterns, and the technique by which these beams interfere is interferometry [Steel, 1967; Dyson, 1970].

Interferometry is a technique to compare the *shape* of a wavefront to that of a reference wavefront, and to show the difference in the form of bright and dark regions; interference fringes. Light waves are normally used for interferometric experiments, but any electromagnetic or indeed other wave could be employed equally well. The invention of the laser in the 1960's meant that a highly coherent source of illumination was readily available for making interferometric measurements, and greatly boosted the development of interferometric measurement systems. The same era produced reliable holograms as a direct result of this invention, although the theoretical possibility of holography was proposed much

earlier by Gabor [1948-1951][2]. Other technical advancements have also made a dramatic difference to the complexity and resolution of interferometry. The widespread use of high resolution detectors (such as field array CCDs), and advanced microprocessors, has increased the sophistication of the methods used. High speed processing, and the enormous increase in the memory capacity of small computers has enabled interferometry to become a routine laboratory tool, rather than an academic curiosity.

The principle of two beam interferometry is explained concisely by Schwider [1990], from which the following analysis is mostly taken. This principle is illustrated in Figure 1.

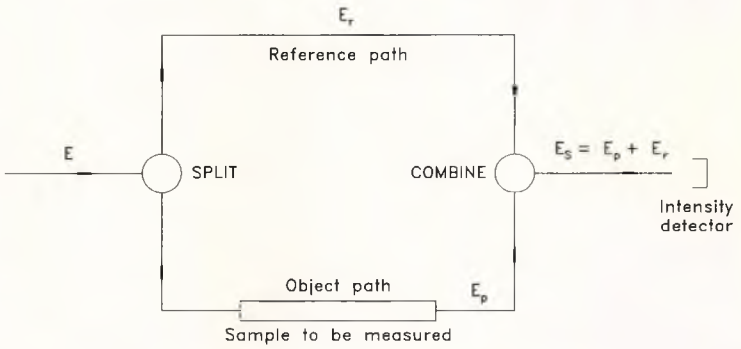


Figure 1: Two beam interferometry

An electromagnetic wave with a field strength of E is split coherently using a beamsplitter into the object wave E_p, and the reference wave E_r (other splitting devices exist, but the beamsplitter is most commonly used). The two coherent waves travel along different paths[3] and accumulate phase lags. The reference beam phase lags are effectively constant (they are also considered to be spatially invariant), whereas those of the object beam depend upon the sample to be measured. The two beams are then superimposed using a second beamsplitter. The resultant field strength is given by:

$$E_s = E_p + E_r \qquad [1]$$

In optics, only square law detectors exist, so the intensity, $I(x,y)$, is the quantity detected:

$$I(x,y) = E(x,y)\, E^*(x,y) \qquad [2]$$

where the field strength E is assumed to be a complex quantity, and E^* is the complex conjugate of E. In terms of the eikonal equation, the complex amplitude can be written in the form shown in Equation [3]:

---

[2]Dr Gabor was awarded the Nobel prize for physics for this work in 1971.

[3]Except in the case of holographic interferometry, which is explained later.

$$E(x,y) = A(x,y)\ e^{i\phi(x,y)} \qquad [3]$$

where A is the modulus of the field strength and ϕ is the phase term, bearing a direct relation to the optical path difference arising from refraction, reflection or propagation. The detected intensity can be written in the form:

$$I(x,y) = E_s(x,y)\ E_s^*(x,y) = (E_p+E_r)\ (E_p^*+E_r^*) \qquad [4]$$

which can be rewritten:

$$I(x,y) = A_p^2 + A_r^2 + 2A_pA_r\cos(\Phi_p - \Phi_r) \qquad [5]$$

The basic equation of two beam interferometry can then be written:

$$I(x,y) = I_o[\,1 + V(x,y)\cos(\Phi(x,y) - \phi)\,] \qquad [6]$$

where the 'background intensity' and 'fringe visibility' are given by:

$$I_o = A_p^2 + A_r^2 \qquad V(x,y) = \frac{2A_pA_r}{(A_p^2 + A_r^2)} \qquad [7]$$

The 'information of interest' is stored in the phase function $\Phi(x,y)$, where ϕ is the reference phase. Since the only measurable quantity is the intensity I, a means of extracting the phase $\Phi(x,y)$ is required. It should be noted that the phase is 'screened' by the two spatially dependent functions (background and visibility), which contribute to the intensity distribution. Also, two additional problems exist:

- The addition of $2\pi n$ (n is an integer) to the phase $\Phi(x,y)$, does not change the intensity pattern. Thus $\Phi(x,y)$ can only be determined mod 2π.
- Since the cosine function is even ($\cos\Phi = \cos -\Phi$), the sign of the phase $\Phi(x,y)$ cannot be determined from a single measurement without prior knowledge about the experiment.

Schwider [1990] continues the discussion by explaining some of the general features of a *real-time* interferometric system, which include:

- One or two dimensional photoelectric detection of the fringe patterns.
- Calculation of the phase, and extraction of the relevant function from the phase.
- Solution of the mod 2π and sign ambiguity problems.

In many cases, the photoelectric detector is either a line scan or field array CCD camera, coupled to a frame processor unit, which is often fitted to a computer. Fringe analysis

algorithms attempt to extract the phase (wrapped), and then use unwrapping algorithms to remove the 2π problem. The required quantity can then be derived from the phase. Beckers [1990] clarifies some important points which must be considered when utilising interferometry.

1.2.1 Holographic Interferometry

Holographic Interferometry was discovered quite by accident in 1964 by Powell and Stetson [1965], in an attempt to discover why some recorded holograms were of low quality. Many scientists agree that holographic interferometry is one of the most important applications to emerge from the field of holography, due to its ability to make interferometric measurements on both diffuse and opaque objects. In contrast to classical interferometers (Mach-Zehnder, Michelson ...), in which the interfering wavefronts travel simultaneously along *different* paths (Figure 1) before being mixed, the holographic interferometer allows the interfering wavefronts to travel the *same* path at different times. The common path has the advantage of compensating for the defects and misalignments of the optical components, since they have the same effect on both interfering wavefronts. A typical holographic setup is shown in Figure 2. The top diagram represents the configuration used to record the hologram. Once the hologram has been processed, it may be viewed by repositioning it and using the reference beam only as the reconstructing wave (lower diagram). This will generate an *exact copy* of the object wavefront, as if the object were still in position. If the hologram is viewed using the top arrangement, interference between the *recorded* and *real* object wavefronts will occur. It is the ability of holograms to store both the amplitude *and* phase information of a wavefront that enables this interference effect to occur. This is called *real time* holographic interferometry [Butters and Leendertz, 1971a; Pryputniewicz and Bowley, 1978; Vest, 1979; Spetzler, 1986]. If the object is loaded in some way, the resultant fringe pattern varies continuously with the load. In *double exposure* holographic interferometry [Vest, 1979; Parker and Jones, 1986], two records of the specimen wavefront are recorded, on the *same* hologram. Upon reconstruction (using the lower setup of Figure 2), these two wavefronts interfere with each other to produce an interference fringe pattern. This fringe pattern is 'frozen' into the hologram, and represents the physical change of the specimen at the two instants at which the wavefronts were recorded.

Until recently, vibration isolation and complete darkness were essential in order to make good quality holograms. This is because any slight movement of the holographic system during the exposure reduces the correlation between the two interfering wavefronts and therefore the quality of the interference fringe patterns. The enclosure must be darkened for obvious reasons. However, the development of 'thermoplastic holography', reviewed meticulously by

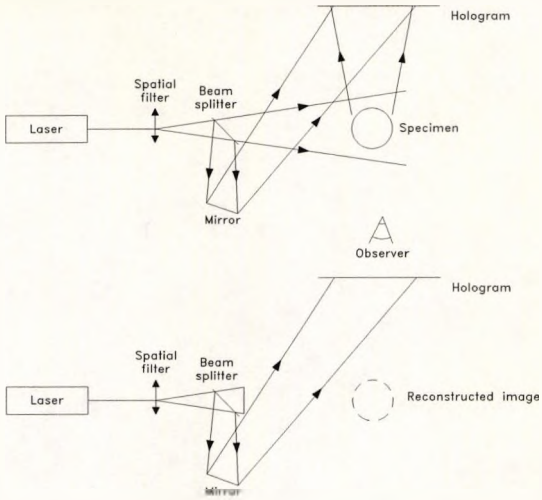


Figure 2: Typical holographic setup

Parker [1990], offers in-situ exposure and development of the hologram in seconds. An example of a holographic fringe pattern is shown in Image 1[4], which shows the vibrational mode of a hollow turbine blade being excited at 21.4kHz.

Holographic interferometry was applied to the measurement of in-plane surface strain by Ennos [1968]. This work, although possibly not the first attempt to perform this type of measurement, is interesting since it uses a technique of recording two double exposure holograms of the specimen simultaneously, but from different viewpoints. This elaborate system is necessary because holographic interferometry is unable to separate the in-plane and out-of-plane components of deformation. The method used by Ennos involved subtraction of the fringe contours, enabling the plane strain in one defined direction to be resolved. Another method to isolate the in-plane strain is described by Pirroda [1989]. Here, the object is illuminated normally with a plane wave and also symmetrically by two reference waves. One of the in-plane displacement components is mapped by the interference fringes in much the same way as in-plane speckle pattern interferometry (which is described later). The complete separation of all components of displacement, and assignment of absolute fringe order, which is one of the main problems associated with holographic interferometry, is described by Stetson [1990].

The measurement of out-of-plane deformation using holographic interferometry has been examined thoroughly. For example, Chang *et al.* [1985] describe the use of digital phase shifting holographic interferometry for high precision deformation measurement. The work is based on an earlier system described by Hariharan *et al.* [1983], but eliminates the

[4]Courtesy Robert K. Erf, United Technology Research Centre, East Hartford, Connecticut, USA.

requirement for PZT calibration. Creath [1989] examines both contour and deformation measurement, using a very high resolution detector array (1320x1035 pixels) to image the hologram. Creath reports excellent results, working with very high fringe densities, but requiring significant capture and computation times.

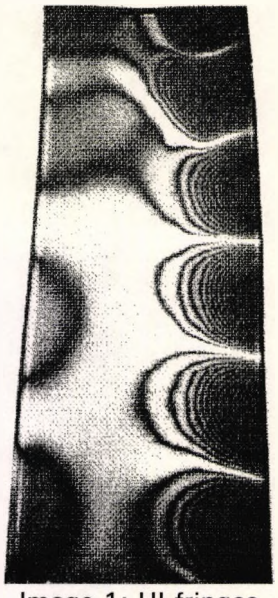


Image 1: HI fringes

A vibration analysis of a rotating propeller blade was performed by Sikora *et al.* [1974] using holographic interferometry. The hologram is fixed onto the axis of the rotating specimen, and a double exposure hologram is made of the blade at known resonances, using a pulsed laser. This follows work performed by Tsuruta and Itoh [1970], who established that it was possible to make a single exposure hologram of a rotating specimen, and subsequently correlate this with a second exposure of the stationary specimen. This idea was extended further by Vogt *et al.* [1985] who used an 'object related laser triggering method' to eliminate the rotary motion between exposures of the hologram. A similar technique to that used by Vogt *et al.* was reported earlier by Kawase *et al.* [1976]. In this paper, a hologram of the object is made at the desired rotary speed, and a shadow photograph (mounted on an arm rotating with the specimen) of a speckle pattern is made simultaneously. Accurate realignment of the speckle photograph ensures accurate realignment of the hologram with the stationary object. The idea is rather cumbersome, but appears to yield excellent results.

Holographic interferometry has been used extensively in conjunction with image derotation to study the out-of-plane behaviour of rotating components [Beeck, 1980; Stetson, 1975-1978; McBain *et al.*, 1979; Fagan *et al.*, 1981; Storey, 1984; Beeck, 1992]. Image derotation usually involves the use of a special prism mounted coaxially with the specimen. The prism is made to rotate at exactly half the speed of the specimen. If the specimen is viewed through the prism, it appears stationary. One of the major drawbacks of this technique is that the illumination and viewing directions are both on axis, restricting the range and type of measurements that can be made. A good summary paper explaining the various methods of recording holographic images of rotating specimens was published by Beeck [1988].

Another application of holographic interferometry, which is not directly related to the work in this thesis, but is becoming more widespread, is 'flow visualisation'. In flow visualisation, refractive index variations, resulting from density changes in flow fields, manifest themselves

as interference fringe orders in a double exposure hologram. Some excellent examples of these, taken in an industrial environment, are included in Parker and Jones [1986].

Two final references in this section are included for completeness. The first, is a comparison of the accuracies of holographic and speckle interferometry (discussed later) [Klimenko *et al.*, 1986]. Interestingly, it is found that the sensitivity of speckle interferometry can exceed that of holographic interferometry in some cases. Finally, the effect of speckle movement on the contrast of the fringes in holographic interferometry is examined by Shekher and Vaish [1983]. This work is rewarding, since it is important to know the approximate proportions over which a measurement system will reveal results prior to construction of the experimental system. A simple relationship between speckle movement and fringe visibility is derived.

1.2.2 Moiré Interferometry

The conventional moiré technique involves generating a moiré fringe pattern by the superposition of two gratings: a master and a model grating. The grating pattern is either projected or fixed onto the surface of the object under investigation, and is then modulated by either the surface shape or some deformation due to loading. When the modulated grating pattern is observed through the master grating of the same or a similar pitch, contours corresponding to the shape or deformation are seen. For example, consider the two superimposed gratings shown in Figure 3. The spatial frequency of the reference grating is increased by 5% in the upper example and 20% in the lower example. In the region of overlap between the reference and modulated gratings, bright and dark regions (fringes) are clearly seen. The resolution of a moiré system depends upon the pitch of the grating.

A good review paper on moiré techniques is Sciammarella [1982] and an excellent book on moiré applied to the analysis of strain is Theocaris [1969]. Luxmoore [1975] compares the use of laser speckle and moiré methods in strain analysis, and concludes that the moiré methods are in fact a special case of the laser speckle methods. Chiang [1979] discusses many of the same points, and arrives at a similar conclusion. The measurement of shape using moiré interferometry has been studied by several authors, for example Takasaki [1970] and Pirodda [1982]. Displacement measurement using moiré interferometry can be accomplished in several ways. Sciammarella *et al.* [1987] describe a computer based moiré technique which enables very small displacements to be measured.

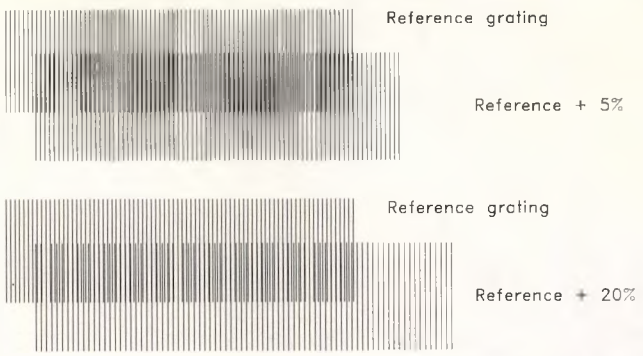


Figure 3: Simple moiré fringe pattern

An interesting paper by Morimoto *et al.* [1988] describes a shift technique in which the Fourier transform spectrum of the deformed grating is used to produce a 'complex moiré pattern'. The derivatives of the phase of the complex pattern produce the strain distribution.

Several research groups have used 'high resolution moiré', which was developed by Burch and Forno [1975, 1982][5]. In high resolution moiré, a slotted mask is positioned in the aperture plane of the imaging lens, through which the specimen grating is viewed. For example, Whitworth *et al.* [1991] use the technique for the measurement of a dynamic crack tip displacement field with great success.

1.2.3 Speckle Photography

The method of double exposure speckle pattern photography is a powerful way of determining both in-plane displacements and surface rotations [Ennos, 1975]. Basically, the specimen is illuminated with a divergent laser beam, and a double exposure photograph is taken of the surface, with the load altered between the two exposures[6]. The in-plane

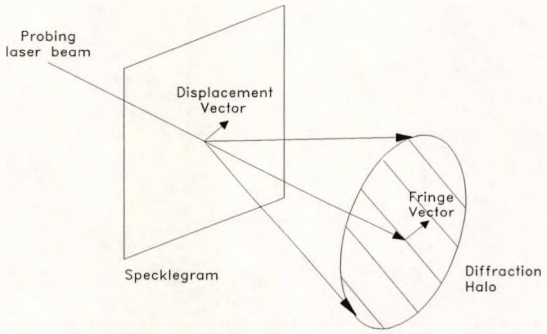


Figure 4: Speckle photography

[5]See also Forno [1988].

[6]The basis for this technique is attributed to Butters and Leendertz [1971b].

displacement vector at any point on the surface may be determined by measuring the separation of the two speckle patterns at the point of interest. This is often performed by probing the photograph with a fine laser beam and observing the Young's fringes in the far field, as shown in Figure 4 (see Archbold *et al.* [1970]; Ennos [1975]; Briers and Angus [1979]; Pryputniewicz [1985]). The fringe spacing is inversely proportional to the displacement of the speckle pattern, and the direction of the fringes is perpendicular to the displacement vector. Speckle photography is not limited to the measurement of surface phenomena, and has been used in flow visualisation, where it is referred to as 'speckle velocimetry' [Merzkirch, 1990].

Stetson [1975-1976b] explored the use of image derotation in the study of rotating specimens, and accumulated both holographic and speckle photographic results. The more interesting speckle photography results, presented in Stetson [1978], led eventually to a U.S. Air Force sponsored research programme commencing in 1983, to measure in-plane deformations on rotating discs at elevated temperatures [Dennis and Fulton, 1989]. In the report, a speckle photocomparator is described which measures both the radial and hoop stress of a rotating disc with reasonable accuracy, over a wide range of stress levels. The full field technique described is an excellent example of non-contact optical measurement in a very hostile environment.

A technique known as 'sandwich-speckle interferometry', which is similar to speckle photography, has also been applied to rotating components by Chien *et al.* [1982]. This technique requires two speckle patterns of the specimen to be recorded on two different negatives, which are later 'sandwiched' together to produce effectively a double exposure speckleogram. The results of this technique are in good agreement with theoretical predications for relatively 'slow' speeds (approximately 3,450rpm).

In speckle photography, it is essential to remember that the Young's fringe pattern resulting from the laser probe portrays the condition at the *probe point only*. Therefore, a very large number of *fringe patterns* have to be analysed in order to extract the global data for the experiment. According to Pickering and Halliwell [1986], 10,000 fringe patterns would be a typical requirement for a *single* flow visualisation experiment. Consequently, a large number of automated analysis techniques have been devised to measure the fringe spacing and orientation, some of which are discussed. Kaufmann [1981, 1982] digitally filters the data, using the one-dimensional Fourier transform, which eliminates the noise. This follows the work undertaken by Chambless and Broadway [1979], who devised the basic technique which is used by Kaufmann. The spacing and orientation of the fringes is easily derived from

the 'clean' data. Isacson and Kaufmann [1985a,b] extend the earlier work of Kaufmann [1981, 1982] into two dimensions, and consider both the noisy and noise-free cases of the influence of the diffraction halo on the fringes. Erbeck [1985] describes a high speed semi-automated processing system for speckle photography fringe patterns, based on economical hardware. The autocorrelation algorithm described by Erbeck is ingenious, and appears to be able to determine the spacing and direction of the Young's fringes extremely rapidly. Huntley [1986c] uses a global approach to the fringe evaluation problem, applying the two dimensional Walsh transform to the complete data set. The Walsh transform is found to be as accurate as the Fourier transform, and three times faster, for fringes of good visibility. For low quality images, the Fourier transform is preferred. Ansari and Ciurpita [1987] describe an automated peak detection method of fringe measurement for speckle photography fringes, which also has modest hardware requirements. A rather rudimentary but effective method of fringe measurement involves the use of a coordinate digitizer to determine the centres of the dark fringes, using operator assistance [Galkin *et al.*, 1988]. This is a good example of excellent work achieved without the use of powerful computers, but would be very tedious to use on a large number of fringe patterns. Deng and Yamaguchi [1990] report another automated method of analysis for Young's fringes. This method involves removal of the diffraction halo, followed by integration of the remaining data in various directions to determine the orientation of the fringe field. The data is then fitted to a sinusoidal function to determine fringe spacing. Results from this system appear very promising.

1.2.4 Speckle Interferometry

The introduction of the laser in the sixties extended the usefulness of interferometric techniques, but brought with it a side effect which was widely regarded as a nuisance. The speckle effect was not pronounced useful until it was realised that the individual speckles were able to interfere. It was later shown that two different speckle patterns could be made to interfere, and result in a third pattern with an intensity distribution related to the relative phases of the constituent patterns [Leendertz, 1970]. Leendertz superimposed two unique speckle patterns onto a photographic plate, which was processed and repositioned, acting as a shadow filter[7]. The construction was that of a Michelson type interferometer, but with both of the mirrors replaced with diffuse surfaces, and is shown in Figure 5. Viewing the object wavefront through the shadow filter, real-time correlation fringes from the specimen are observed. Almost immediately, the researchers at Loughborough University of Technology recognised the potential for this new technique, and replaced the photographic part of the experimental system with a video camera and subtraction unit [Butters and

[7]The brightest regions of the pattern irradiating the darkest regions of the plate.

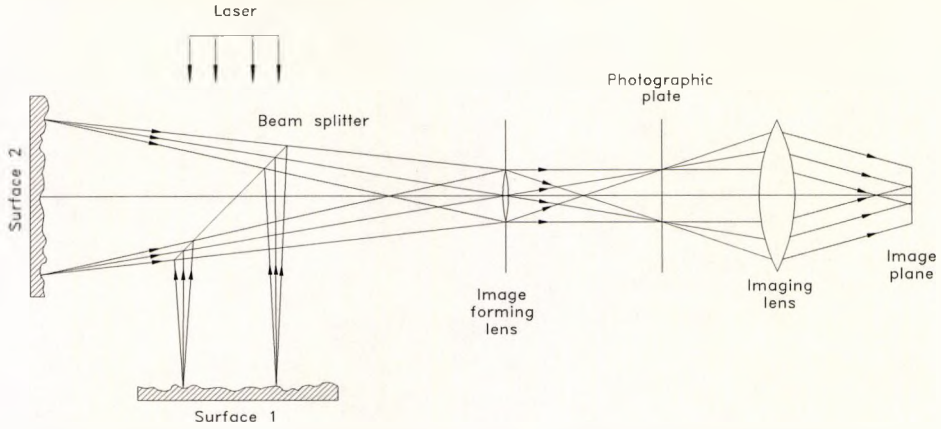


Figure 5: Speckle interferometry

Leendertz, 1971a], giving birth to Electronic Speckle Pattern Interferometry (ESPI). However, a certain amount of limited research involving speckle interferometry continued, which is reviewed extensively by Ennos [1975]. For example, Hung and Hovanesian [1972] used the technique to yield the displacements of arbitrarily curved surfaces. The authors explain that this technique is preferred to holographic interferometry, since the fringes localise on the object surface, and have a unique interpretation when related to displacements. Brdicko *et al.* [1979] study both in-plane and out-of-plane deformations, using a 'double aperture speckle camera' and a 'double aperture speckle shearing camera'. Huntley and Benckert [1992a,b] explain that in many high speed applications, ESPI is inappropriate, and photographic techniques must be used. They describe an example of such a situation, together with a very powerful way of removing the speckle noise from the images.

1.2.5 Electronic Speckle Pattern Interferometry

Although holographic interferometry produced a new class of measurement tools, it was not without problems. Quantitative measurements proved difficult because the separation of the in-plane and out-of-plane components was difficult. The processing of the holograms made the technique unattractive to industry in general, with only high technology industries showing any great commitment. It was soon realised that the speckle pattern obtained from a diffusely reflecting object could be used to make surface measurements, as explained in the previous section [Leendertz, 1970]. The introduction of a television camera in place of the photographic film and an image processing unit in place of the photographic mask led to the technique called 'Electronic Speckle Pattern Interferometry' (ESPI) or 'TV holography' [Butters and Leendertz, 1971a; Denby and Leendertz, 1974]. The schematic diagram of a commonly used ESPI setup is shown in Figure 6, which is an out-of-plane measurement system. The laser (often a HeNe) is divided by a beam splitter into an object and reference beam. Both

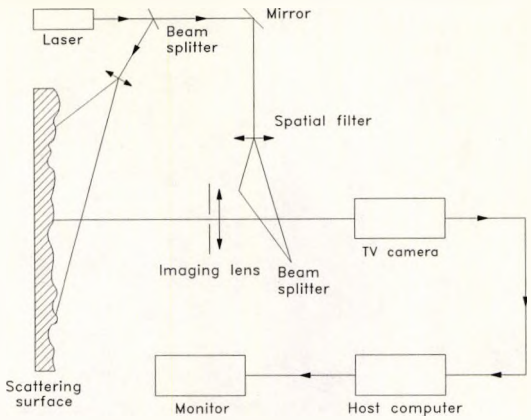


Figure 6: Out-of-plane ESPI system

beams are expanded and spatially filtered, the object beam illuminating the specimen under investigation at a certain angle of incidence. The reference beam is incident normally onto the photosensitive surface of the TV camera. The size of the speckle in the image plane of the photosensor is determined by adjusting the aperture of the imaging lens. For the case of resolved speckles, the mean speckle size is greater than or equal to the pixel size of the camera. The speckle patterns are stored either electronically on analogue circuits, or more commonly by digital electronics, in a framestore, which is often fitted to the host computer. The ESPI technique was very rapidly employed in diverse engineering fields. It was used to study vibrations, surface roughness, in-plane displacements, out-of-plane deformations and contouring. Butters [1975] and Butters *et al.* [1975, 1978] trace the history of the ESPI technique, indicating how far it had progressed within its first few years. Additionally, several general papers describing electronic speckle pattern interferometry and its applications have been published. The following are a selection found to be useful by the author: Butters [1977], Løkberg [1980], Jones [1982], Wykes [1982], Løkberg [1986], Tyrer [1986] and Sharp [1989]. No list of references to the general use of electronic speckle pattern interferometry would be complete without Jones and Wykes [1983].

1.2.5.1 Enhancements to the basic technique

Several authors have reported modifications to the basic ESPI technique, some of which are reviewed here. The use of a modulated reference wave for vibration studies was reported by Løkberg and Høhmoen [1976], which is similar to the modulation of the reference wave used in holographic interferometry. The reference wave is reflected at normal incidence from a mirror vibrating at the same frequency as the specimen under examination. The adjustment of the amplitude and/or phase of the reference mirror excitation enables the Bessel fringes to be shifted, yielding additional information about the specimen vibration. Slettemoen [1980] describes the use of a speckle reference beam which reduces the physical size of the ESPI

setup, and makes it less vulnerable to dust and scratches of the optical components. A comparison between conventional out-of-plane ESPI and the new technique shows that the use of a speckle reference beam does not reduce the quality of ESPI fringes. The use of a fibrescope to deliver the laser illumination and view the speckle pattern is reported by Løkberg and Krakhella [1981]. This paper describes the use of the fibrescope to view the vibration of a specimen under water. Fringes of reasonable quality are presented for the specimen in forced vibration. Moran *et al.* [1987,1989] report an optically phase locked electronic speckle pattern interferometer (OPL-ESPI). This new system appears to have overcome one of the major drawbacks of the ESPI technique, which is the need for rigorous vibration isolation. The system couples an optical phase locked loop (PLL) with an ESPI system to produce real time Doppler contours of moving objects from unstable platforms. Various ESPI experiments with different laser sources have been tried, for example Løkberg and Kwon [1984] use a carbon dioxide (CO_2) laser in an ESPI system. More interestingly, Wykes and Flanagan [1987] utilise a small Hitachi laser diode, which has a coherence length in excess of 1m, producing fringes with good contrast. Modulation of the diode injection current causes a deviation in the output wavelength, which was used by Tatam *et al.* [1990] to perform surface contouring with ESPI.

1.2.5.2 Fringe quality in ESPI

The poor signal-to-noise ratio and low resolution of ESPI systems has been one of the limiting factors to the widespread use of the technique. Therefore, optimization of electronic speckle pattern interferometers has been the subject of considerable attention. For example, two important papers on this issue are those of Slettemoen [1977,1979], which deal with the complete ESPI system theoretically as well as practically. A detailed study of the interferometer design, and fundamental factors affecting the performance of ESPI systems is also discussed by Jones and Wykes [1981]. Nakadate [1980] makes some negative points regarding the contrast of ESPI fringes, and indeed the ESPI technique itself. These are defended in a letter to the Editor of Applied Optics in 1981 [Wykes *et al.*, 1981].

A theoretical analysis of the optimization of an ESPI system in the presence of limited laser output power is discussed by Wykes [1987]. Wykes concludes that the optimum fringe clarity is obtained when the imaging system is set so that the speckles are not fully resolved, but this setting is dependant upon the scattering properties of the specimen surface, the sensitivity of the camera, and the resolution of the video system. The visibility of the fringes can be improved by computer techniques as well as system optimization. For example, in an article by Yonemura and Hagihara [1987], the object and reference intensities are recorded and used to normalize the two interference speckle patterns. Subtraction or addition of the normalized patterns produces increased visibility of the interference fringes. Joenathan [1990]

discusses the effect of TV camera non-linearity on ESPI systems. Normally the camera response is assumed to be linear to the incident light intensity, which is true for CCD cameras, but for vidicon or newvicon tube cameras, the transfer function is non-linear. Joenathan concludes that the non-linear effect of the TV camera transfer function is only prominent when the laser power is limited, in which case the signal-to-noise ratio of the system is low. In this case, the brightness of the object beam should be increased slightly. O'Donovan *et al.* [1992] explain a method of assessing the quality of a fringe field, by applying Fourier transform analysis techniques. The method appears to be robust for theoretical data, since it *compares* the Fourier coefficients of the actual data with those of a 'perfect waveform of the same type'. However, it is doubtful whether such an analysis would be of real use for practical engineering problems.

1.2.5.3 ESPI at elevated temperatures

Measurements using the ESPI technique have been made at elevated temperatures. The out-of-plane effects of the surface behaviour of steel, molybdenum and kanthal at temperatures approaching their melting points was studied by Løkberg *et al.* [1985]. In additional experiments involving molten tin, the behaviour was examined to study deformations, oxidation shell growth and melting zones. The results presented show interference fringe patterns at temperatures up to 1,700°C. Malmo *et al.* [1988] describe experiments to measure the surface vibrations and deformations at temperatures of up to 3,000°C using an out-of-plane sensitive time-averaged ESPI system.

1.2.5.4 ESPI used to measure vibration

Electronic speckle pattern interferometry has been used extensively to measure vibrations. The out-of-plane configuration shown in Figure 6 is the basis for the vibration measurement system, with a PZT mirror often included in order to phase shift the reference beam. An interesting early example is presented by Cookson *et al.* [1978] which shows a steel cabinet forced to vibrate by an electric motor. Another example in this paper is that of the transient behaviour of a loudspeaker. It is interesting to compare this paper with Tyrer [1988], which also examines the response of a loudspeaker. The use of a noise reduction scheme shows how excellent fringe patterns can be extracted from rather poor images. Davies and Buckberry [1989] publish details of a 'TV holography head', which is used to measure the vibration amplitude at various points on an automobile body. The instrument is a powerful tool for measuring vibrations 'in situ', since the laser source (which is launched in a mono-mode fibre optic cable) and electronic equipment can be remotely located. Santoyo *et al.* [1991] explain how the total in-plane vibration mode of a plate specimen can be extracted using a pulsed phase step technique.

1.2.5.5 ESPI used to measure shape

Winther and Slettemoen [1984] describe an ESPI contouring technique which is a variation of the holographic two beam illumination method. The object beam of an out-of-plane sensitive ESPI system is translated between the capture of the two speckle patterns. Maas [1991] uses a similar procedure, except the object beam source is fitted to a rotary illumination arm. Application of phase shifting allows the reconstructed contour data to be accurately determined.

1.2.5.6 ESPI used to measure strain

An early application of ESPI to the measurement of plane surface strain is that of Denby and Leendertz [1974]. This paper lays down the basic principles of in-plane strain measurement in a single resolved direction (see Figure 15 on Page 32) using electronic processing rather than photographic[8]. The results presented show excellent interference fringe patterns on various materials in several states of tension. Soon after the publication of this paper, Jones [1976] describes a system for total plane strain measurement using two orthogonal object illumination geometries. Preliminary results included show promise at this early stage. A later example of similar research, which incidently does not reference the work of Jones even though it comes from the same establishment, is Moore and Tyrer [1990]. In this paper, two in-plane interferograms of a centrally notched alloy specimen are simultaneously recorded. The use of phase-stepping (see section 4.1.2.1) allows accurate extraction of both components of displacement around a crack to be accomplished. Winther [1988] proposes a 3D strain measurement technique, which performs both deformation and contour measurements. The specimen to be examined is illuminated from three different directions by fibre optic cables. The capture and analysis of four images allows the complete determination of the strain tensor.

1.3 Research of direct significance

1.3.1 Application of ESPI to rotating systems

Before conducting rotating tests, Preater [1980a] performed some static in-plane tests, yielding fringe patterns like that of Image 2, which is a static test of a bar in tension. Following this work, Preater applied ESPI to the measurement in-plane displacements on rotating objects [Preater, 1980a]. This paper explains the principle of pulsed laser ESPI applied to rotating systems, and the hardware required to implement such a system. A diagram[9] of

---

[8]There are suggestions to this type of measurement in Butters and Leendertz [1971b].

[9]This diagram does not appear in the paper in this form, but is drawn in this way for added clarity. Also, the method of shaft encoding, which is not explained in the paper, was established after discussions with the author.

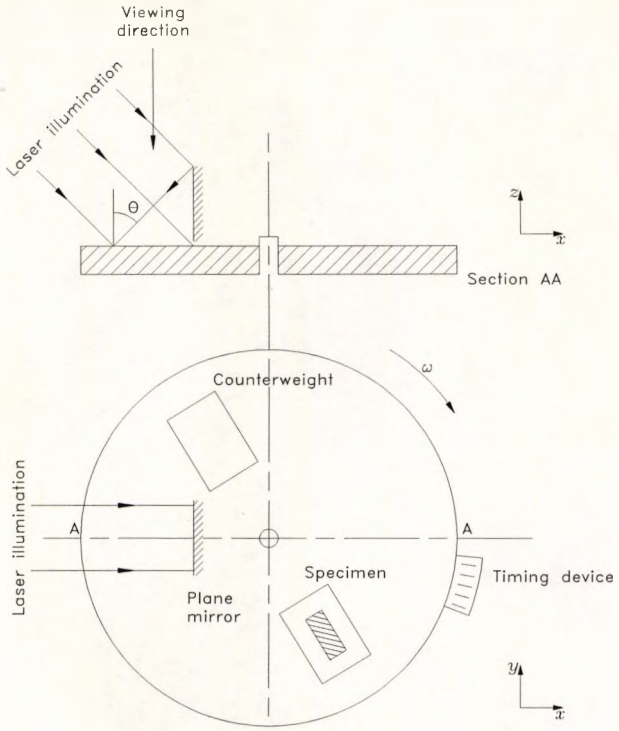


Figure 7: Original optics [Preater, 1980a]

the original optical system, used for rotating tests, is shown in Figure 7. Although it is not made clear in the paper, the specimen is fitted into a tensile loading device which is mounted on the surface of the disc, and therefore rotates simultaneously. The control system ensures that the specimen is in the camera's field of view when the laser illumination is generated. A block diagram of the hardware which accomplishes this is shown in Figure 8. The optical system constitutes a conventional in-plane sensitive electronic speckle pattern interferometer [Jones and Wykes, 1983], the theory of which is explained in section 2.1.2. The pulsed laser, triggered with sufficient accuracy, enables repeatable speckle patterns of the *same* region of the specimen to be captured and later correlated (section 2.1.1). Accurate triggering is accomplished by means of a purpose built electronic processor, coupled to a 'shaft encoder'. The details of the shaft encoder are not presented in the paper, but discussions with the author revealed that it consisted of about ten slots attached to the perimeter of the specimen, from which pulses were generated, as illustrated in Figure 7. A pulsed ruby laser (JK 2000), with a pulse width of 40-70ns, provided the illumination source, which was imaged with a low resolution TV camera. The speckle images were stored in a video disc, and also on video tape. The system demonstrated interference fringes from both static and rotating specimens. Initially, the rotating specimen (100rpm-250rpm), produced fringes from various mis-matched speckle images, which were produced by tilting one of the interferometer mirrors. An example of such fringes is shown in Image 3, taken from Preater [1980a]. Skewing of the fringes was

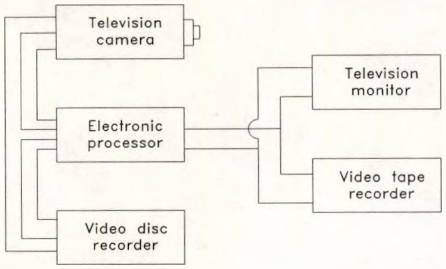


Figure 8: Original electronic setup [Preater, 1980a]

thought to be the result of a slight timing error, as explained in the paper[10]. In further tests, it was found that the correlation of the images was reduced substantially by applying a load to the specimen. The details of the loading were not published, but presumably one speckle image was captured and stored in the video disc. The rig was then stopped, and a load applied to the specimen. Subsequent re-spinning and frame capture produced the results, an example of which is shown in Image 4[11]. An interesting result, presented in the paper, was that correlation fringes were obtained at a tangential velocity of 2.5m s^{-1}, which was greater than a prediction of the upper limit suggested by Cookson *et al.* [1978]. Results at a tangential velocity of 3.4m s^{-1} soon followed, together with variable speed results, in which the two speckle images were recorded at different rotational speeds [Preater, 1980b]. In this early work, tangential velocity variations of 0.5m s^{-1} produced interference fringe patterns, but these patterns generally had little or no relationship with the quantity to be measured. This appeared to be due to the inaccuracy of the timing system. In order to eliminate this problem, an image derotator was used to view the rotating specimen [Preater, 1982]. Although this produced interference fringes, the quality was significantly lower than obtained by direct viewing. Therefore, a more advanced method of Q-switching the laser was

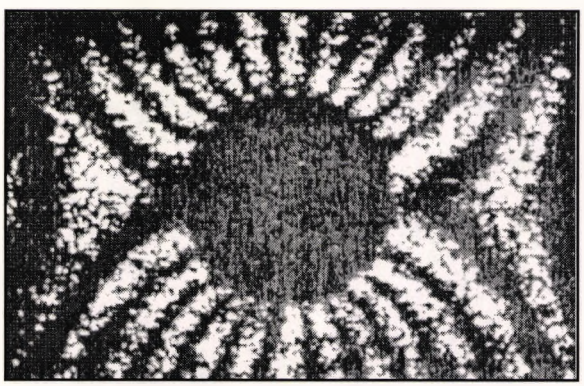


Image 2: Fringes from a static tension test

[10]After discussions with Preater, it was established that these fringes were obtained from a perspex disc, using a different inteferometric system than that shown in Figure 7.

[11]This fringe pattern was obtained from a different specimen than Image 2.

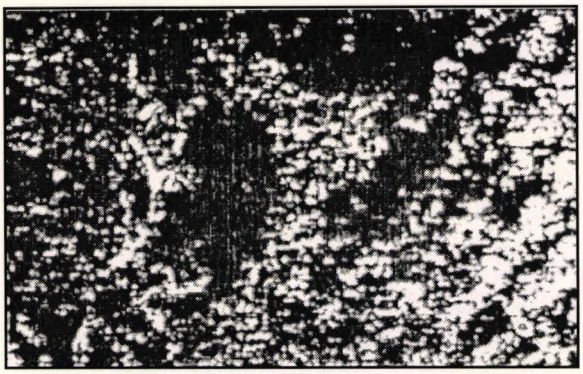


Image 3: Early correlation fringes at 250rpm

introduced, the preliminary results of which show fringes at 4.8m s^{-1}. Using a modified electronic triggering system, the basis of which is described in Preater [1982], some very interesting results (eg. Image 5) were obtained for a perspex flywheel with a steel segmented rim [Preater, 1983]. Although the details of the modified triggering system were not published, the implication was that direct Pockel's cell drive of the laser produced far greater Q-switch accuracy than the previous system. The incorporation of a high resolution speckle camera provided a significant boost to the research programme [Preater, 1984a][12]. Results taken from a component spinning with a tangential velocity of 14.5m s^{-1} were presented, which represented almost a three fold increase in tip speed. Preater [1984b] describes results obtained from an aluminium disc mounted in the chuck of a lathe, rotating with a tip speed of 30m s^{-1} (the reference is also ambiguous about the exact electronic subsystem, since the text describes the incorporation of a single frame digital subtraction unit, but the diagram represents the standard control system shown in Figure 8). The ambiguity was clarified in Preater [1985], which presented results representing an excellent advancement of the technology. The incorporation of the high resolution camera (Jackson speckle camera), the digital frame capture system (Vinten FS4), and the more advanced timing controller (Figure 9) paid tremendous dividends. In fact, the operable speed range increased to such an extent (up

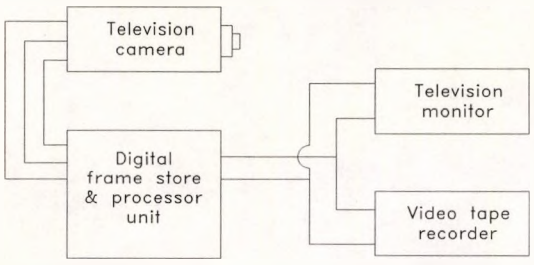


Figure 9: Updated electronics [Preater, 1985]

[12]It is unclear from this paper if the replacement was simply the camera, or the frame capture system also. However, after discussions with the author, it appears both items were replaced.

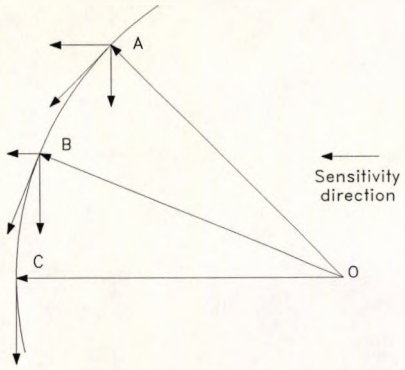


Figure 10: Plane mirror decorrelation

to 100m s^{-1}), that the *optical* system began to exhibit a limitation [Preater, 1985]. The region of available fringe information gradually *reduced* as the rotational speed *increased*, above approximately 5,000rpm, as shown in Image 6. This limitation was overcome by redesigning the interferometer to give radial sensitivity instead of the horizontal sensitivity produced by the plane mirror speckle pattern interferometer [Preater, 1985]. Although the *results* of the redesign were described in the previous reference, the *details* were not presented until

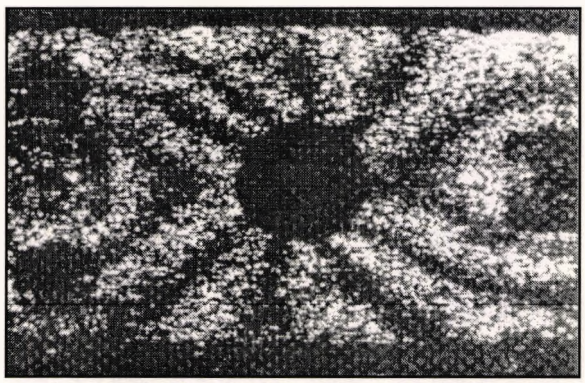


Image 4: Tension specimen at 400rpm

Nguyen [1986]. In this report, Nguyen explains that because a plane mirror interferometer gives horizontal sensitivity, only regions close to the horizontal through the axis of rotation produce fringes at the higher rotational speeds. This point is illustrated in Figure 10[13] which shows the cartesian components of the rotational velocity for a point on the disc, as it rotates. It is seen that as the point rotates from A to C, the component of the velocity *in the sensitivity direction* steadily reduces, until it reaches zero along the horizontal radius. Nguyen concluded: *"any point should not move more than a wavelength of laser light during surface illumination."* This argument at first appears flawed, since from the analysis presented in the report, Nguyen explains that the *height* of the fringe area is inversely proportional to the pulse

[13]This diagram is presented in a different format in the reference.

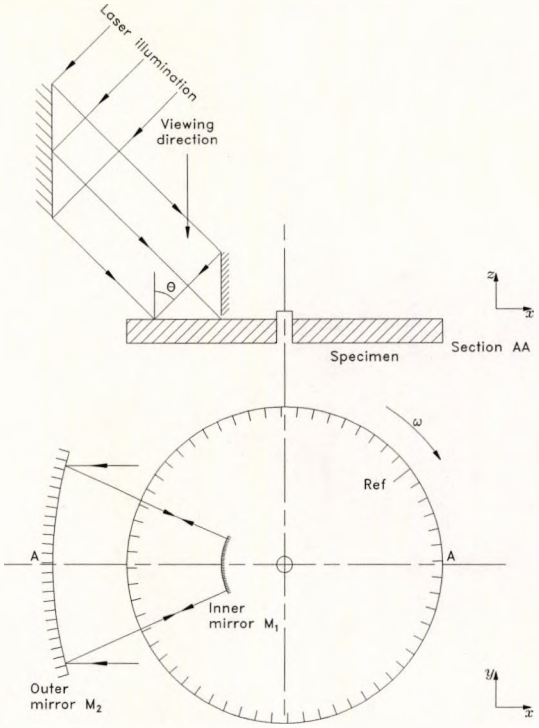


Figure 11: Updated optics [Preater, 1985b]

width of the laser, and yet he proceeds to demonstrate that, for a constant speed, a reduction in pulse width of half causes a four fold increase in fringe area[14]. A diagram of the modified interferometer, producing *radial* in-plane sensitivity, is shown in Figure 11. The shaft encoder pulses from the specimen were generated from slots cut into the perimeter of the specimen. Preater [1986a] presents further results obtained from the new optical system. The paper explains that the pulse width of the ruby laser was reduced by a factor of about two (to approximately 20ns) to give an extended fringe field. Preater [1986a][15] claims that whole field fringe data at tip speeds in the range 0 to 150m s^{-1} was available, however the results included demonstrate a maximum tip speed of 112m s^{-1}, which, although somewhat lower, is still quite a significant achievement. Another interesting point discussed in this paper is that the critical value of velocity *in the direction of sensitivity* was established, and found to be 5m s^{-1}. In order to apply the new optical technique to diverse applications, various specimens were tested. Preater [1986b] describes a simulated test on a rotating propeller blade[16], rotating with a tip speed of 27.5m s^{-1}, shown in Image 7. The carrier fringes show no

[14]This apparent error in reasoning was exonerated after discussion with Preater, who explained that no accurate means were available to determine the exact pulse width of the pulsed laser, and so when Nguyen quoted a reduction in pulse width by a factor of two, it was essentially an educated guess.

[15]Following discussions with the author, it appears that a single fringe pattern was obtained with a specimen rotating with a tip speed of 150ms^{-1}, but during the test, the drive motor failed, and the test was never repeated.

[16]First presented in Preater [1985].

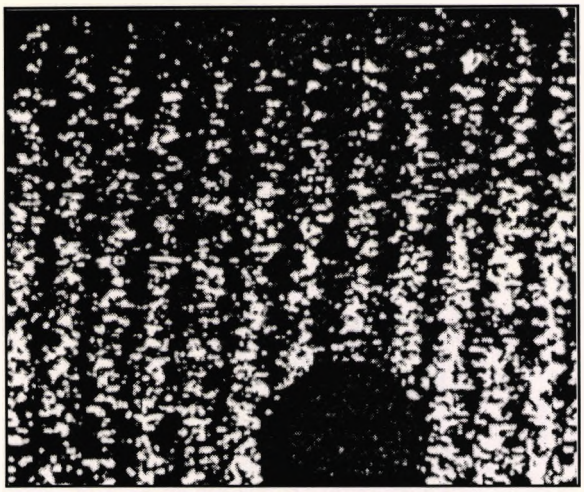


Image 5: Fringes on a perspex disc

discernible contrast reduction due to the curved surface of the specimen. A later set of results from this paper represent a major achievement in the chronicle of the project, since they were the first set of 'true' radial displacement results, an example of which is shown in Image 8. Unfortunately, no quantitative measurements were deduced from the images, so that the accuracy of the system at that time cannot be defined. All previous results from rotating components were simulated (carrier fringe patterns), or artificial (tension specimen mounted on a rotating disc). These results were taken from a high performance advanced brake disc design, and display pure contraction fringes due to the thermal cooling of the brake, which was held at a roughly constant rotational speed of 800rpm. For other results in the paper, optical mis-alignment appears to be a problem, since the anticipated concentric shape of the fringes does not remain constant.

It appears that the method of calculating the tip speed of the rotating component was redefined in Preater [1987b], although this is not stated explicitly. Consultations with the author revealed that previous calculations had been based on the *centre* of the image (with a smaller radius), but the definition was altered to the extremity of the image (a larger radius).

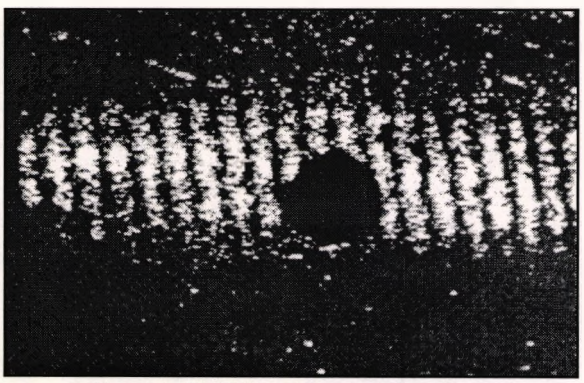


Image 6: Fringe area reduction

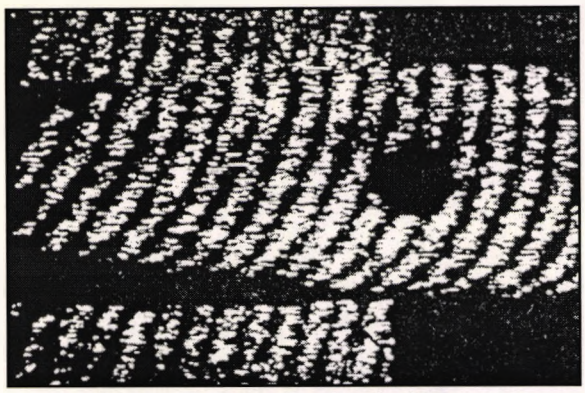


Image 7: Propeller blade fringes

The result was an increase of 20% in the defined tip speed, as illustrated in Preater [1987b], which contains many of the results from Preater [1986a], but quoted at significantly higher tip speeds[17]. Preater [1987d] reviews much of the work described in previous publications. However, the paper does indicate in which direction the research work was progressing, with a section on computerised fringe analysis. Apparently, interference fringe images had been successfully transferred from video tape into an IBM PC, which was fitted with a Data Translation PCVision framegrabber. No evidence of quantitative measurements was published, so it is concluded that the work was in its early stages at this time. An unusual set of results included with this paper were taken from an automobile tyre under stationary pressure loading. A plane mirror in-plane interferometer was used to produce fringes representing a pressure change for the tyre. Consultations with the author revealed that these were preliminary tests, conducted to establish whether the tyre material was suitable for rotating analysis. It was found that the tyre material was rather unstable, and inappropriate for interferometric analysis.

The use of fibre optics to provide the double beam illumination of the Leendertz interferometer is discussed in Preater [1988], having been presented initially in Preater [1987b]. It is interesting that the use of both continuous and stroboscopic illumination is presented, which forms the groundwork for a later idea: the use of a stroboscopic laser diode, strobing the specimen on every cycle, to allow *real time* fringes to be seen as the component load changes[18]. The later publications of Preater [1989,1990a-b], although published during the lifetime of this research project, are based upon earlier work, and do not introduce any new results or directions for the work.

---

[17]The justification appears to be that no degradation in the contrast of the fringes was evident at the outer edge of the interferogram, so it is valid to make the radius as large as possible. This is in fact true, as the higher figure is the more precise of the two, and as such, all previous measurements should be increased by 20%. Bearing this in mind, it is interesting to note that the redefinition did not occur earlier.

[18]This idea was not formally published.

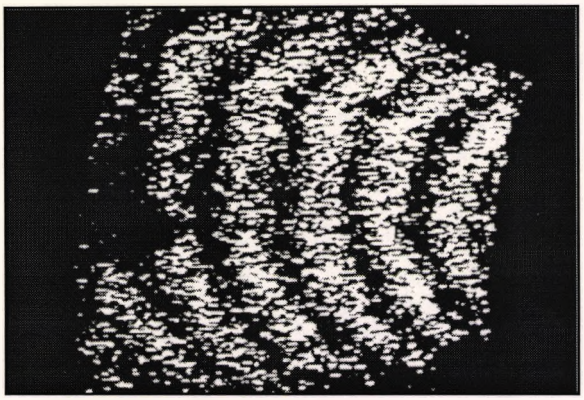


Image 8: Concentric fringes on a brake disc

In summary, to examine the situation at the start of 1989, a radially sensitive in-plane electronic speckle pattern interferometer was used to provide fringe patterns from rotating specimens over large speed ranges. The use of a JK 2000 illumination source with a pulse width of approximately 20ns, coupled to a modified electronic system enabled high contrast fringe images to be obtained and stored on video tape. Interestingly, almost all references since 1986 claim a maximum tip speed in excess of 150m s^{-1}, but none of the references contain any fringe patterns with a tip speed of greater than 135m s^{-1}, which was upgraded from 112m s^{-1} by a redefinition of tip speeds. Also, none of the papers published by Preater attempt to give any stress, strain or displacement values for various loading configurations. No comparison with mathematical models is provided, nor any undertaking to deduce valuable engineering measurements from the images. The latter point can be attributed for the most part to the inaccessibility of the interferometric data (stored as a single video image on a video tape recorder). Details of endeavours to access the image data are described in several of the papers published by Preater, but image processing technology, computers and cost were all acting against the construction of such a system at that time.

Electronic speckle pattern interferometry applied to rotating systems produced high contrast correlation fringes over a wide range of rotational speeds. The technique had provided no quantitative engineering data, but had shown sufficient promise to warrant further investigation. It was concluded that valuable data could be obtained from the system with several enhancements to the basic approach, a major improvement to the hardware, and the incorporation of a fringe analysis strategy.

2 THEORY

2.0 Theory

2.1 Speckle formation

When an optically rough surface[19] is illuminated by highly coherent light (a laser), as shown in Figure 12, a granular appearance is detected in the observation plane (objective speckle formation). The reflected light has random intensity variations, the individual *spots* being referred to as 'speckles', as illustrated in Image 9[20]. This is explained simply by the fact that the coherent illumination has the ability to interfere, so that at a point P, the resultant amplitude is the vectorial addition of the illumination from every point on the object surface. Each point will contribute light of a similar amplitude (assuming the laser beam has a good Gaussian profile and is adequately diverged), but random phase, due to the surface undulations. This is sometimes referred to as the 'drunkard's walk' in the complex plane[21] [Jones and Wykes, 1983]. Figure 13 depicts a true 'drunkard's walk'. An in-depth mathematical study of the formation of speckle holds little direct relevance to the ESPI systems under consideration and will therefore not be presented. However, several references describing in greater detail the theory of speckle formation help to provide an insight into the subject, which is substantial in itself. Goodman [1975] derives many of the basic equations associated with speckle formation. An interesting result is the *negative exponential probability*

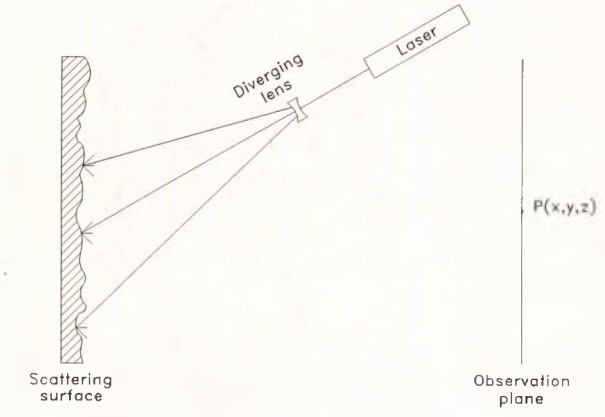


Figure 12: Speckle generation

[19]Defined as the surface height variations being greater than, or equal to the wavelength of the illumination light.

[20]This is actually an *image* of a speckle pattern (subjective speckle), but objective speckle looks very similar.

[21]Actually, a true 'drunkard's walk' has vectors of random magnitude as well as random phase.

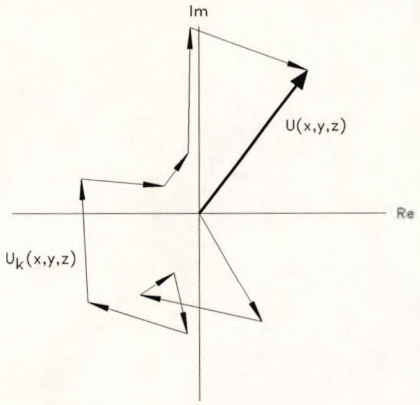


Figure 13: Drunkard's walk

of the speckle intensity. This is illustrated in Graph 1, showing the normalized probability density function, $<I>P_I(I)$, against the normalized intensity. It is clear that the probability of a speckle increases as the intensity decreases, hence dark speckles are more common than bright speckles. This point is discussed in section 4.5.5, where the software used to determine the quality of speckle images is described. Another publication by Goodman [1986] reviews some of the developments in the study of speckle, referencing several important articles. George [1985] reviews the primary physical description of speckle formation, the diffraction and statistical theory of speckle. The electromagnetic theory of speckle formation is presented by Rossi and Maystre [1985], and an experimental study of the speckle *phase* by Kadono *et al.* [1985].

Returning to the theory, when an *image* of the illuminated specimen is formed, as shown in Figure 14, the intensity distribution in the image plane is also speckled in appearance (subjective speckle formation). The spatial distribution of the speckle in the image plane obeys diffraction limited optical theory. The following analysis is taken from Jones and

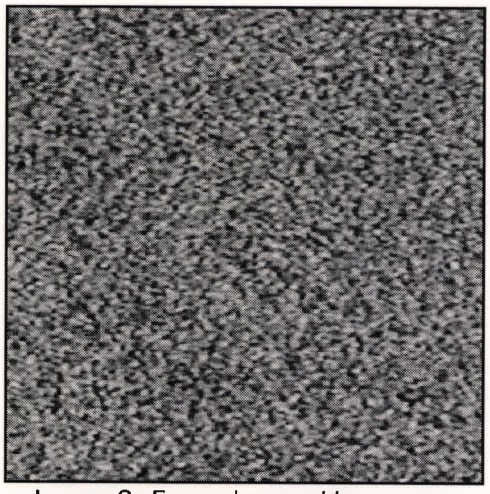
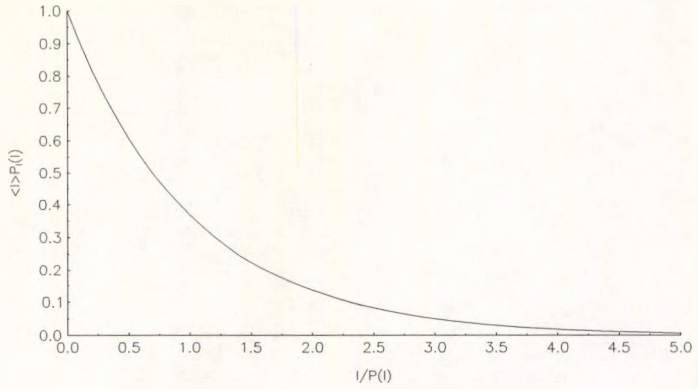


Image 9: Example speckle pattern



Graph 1: Normalized probability density

Wykes [1983]. Consider Figure 14, point P_1 forms a diffraction pattern centred on Q. The light from P_1 has a random phase due to the random surface height. The point Q is also illuminated by points surrounding P_1 since these points produce diffraction patterns which overlap Q. A point P_2, which is situated so that the first minimum of its diffraction pattern coincides with Q, does not contribute to the complex amplitude of the light at Q. Points which are further away also make negligible contributions to the light amplitude at Q. Therefore, the intensity of light at Q is the summation of the contributions from a circular area surrounding P_1, whose radius is the distance from P_1 to P_2. If the illumination wavelength is λ, v is the distance from the lens to the image plane and a is the aperture of the lens, then the distance QQ' and the diameter of the speckles ($d_{speckle}$) can be shown to be:

$$QQ' = \frac{1.22\lambda v}{a} \qquad d_{speckle} \approx \frac{2.4\lambda v}{a} \qquad [8]$$

Therefore, the size of the speckles in the image plane is inversely proportional to the aperture of the imaging system. In many cases, the lens to image plane distance and the illumination wavelength are constant, so the only adjustment available for speckle size is the aperture.

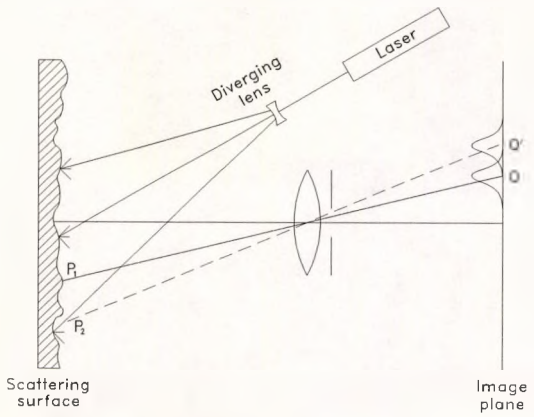


Figure 14: Image plane speckle formation

2.1.1 Speckle correlation fringe formation

The phase referenced speckle pattern formed in the image plane of an ESPI system is an interference pattern produced by the addition of two coherent wavefronts reflected from the scattering surface[22]. According to Jones and Wykes [1983], if $U_1 = u_1 \exp(i\psi_1)$ and $U_2 = u_2 \exp(i\psi_2)$ are the complex amplitudes of the two wavefronts, then the variables u_1, u_2 and ψ_1, ψ_2 are the randomly varying amplitude and phase of the individual image plane speckles. At any given point in the image plane, the intensity Δ_1 will be the addition of U_1 and U_2:

$$\Delta_1 = I_1 + I_2 + 2\sqrt{I_1 I_2}\cos\psi \qquad I_1 = U_1 U_1^* \qquad I_2 = U_2 U_2^* \qquad \psi = \psi_1 - \psi_2 \qquad [9]$$

If the surface under examination is shifted or loaded, a phase change to one or both wavefronts (depending upon the optical configuration), will result in an intensity change at the point of consideration:

$$\Delta_2 = I_1 + I_2 + 2\sqrt{I_1 I_2}\cos(\psi + \delta\psi) \qquad [10]$$

The correlation coefficient of Δ_1 and Δ_2 can be found in Goodman [1975]:

$$\rho(\delta\psi) = \frac{\langle \Delta_1 \Delta_2 \rangle - \langle \Delta_1 \rangle \langle \Delta_2 \rangle}{\sqrt{(\langle \Delta_1^2 \rangle - \langle \Delta_1 \rangle^2)\,(\langle \Delta_2^2 \rangle - \langle \Delta_2 \rangle^2)}} \qquad [11]$$

Jones and Wykes [1983] explain that this equation can be evaluated when one notes the following:

- I_1, I_2 and ψ are independent variables and can be averaged separately.
- $\langle \cos\psi \rangle = \langle \cos(\psi + \delta\psi) \rangle = 0$
- $\langle I^2 \rangle = 2 \langle I \rangle^2$
- Assume that $\langle I_1 \rangle = \langle I_2 \rangle = \langle I \rangle$

The correlation coefficient becomes:

$$\rho(\delta\psi) = \frac{1}{2}(1 + \cos\delta\psi) \qquad [12]$$

Thus the correlation is unity when $\delta\psi = 2n\pi$ (n is an integer) and zero when $\delta\psi = (2n+1)\pi$. If the terms I_1, I_2 and ψ vary, with the change giving rise to $\delta\psi$, then maximum correlation is not attained, and in extreme circumstances, the speckle patterns can become decorrelated. Correlation of the speckle patterns is often performed by simple subtraction on a point by point basis. Assuming the transfer function of the imaging system is linear, the subtraction of Δ_1 and Δ_2, results in the expression given in Equation [13]:

---

[22]This is only the case for in-plane ESPI. In out-of-plane ESPI, only *one* of the wavefronts is reflected from the scattering surface under examination.

$$\Delta_1 - \Delta_2 = 4\sqrt{I_1 I_2}\sin\left(\psi + \frac{\delta\psi}{2}\right)\sin\left(\frac{\delta\psi}{2}\right) \quad [13]$$

Equation [13] yields both positive and negative numbers. Invariably, ESPI systems *rectify* the video signal so that the resultant intensity distribution is proportional to:

$$|\Delta_1 - \Delta_2| = 4\left[I_1 I_2 \sin^2\left(\psi + \frac{\delta\psi}{2}\right)\sin^2\left(\frac{\delta\psi}{2}\right)\right]^{1/2} \quad [14]$$

Although this equation is strictly correct, the actual intensity distribution is not normally dependent upon the square root of the modulus. This is due to non-linearities in the system.

To summarise, it can be seen that the fringes follow a sine squared intensity distribution, with a dark zero order fringe and dark higher order fringes corresponding to lines of 2π, 4π,... phase change.

2.1.2 In-plane displacement measurement

In the classic paper of Leendertz [1970], a Michelson type interferometer with both mirrors replaced by scattering surfaces was constructed. An imaging system was used to record simultaneously the two superimposed speckle surfaces photographically. A photographic plate recorded the image, which, when developed and repositioned, resulted in the generation of speckle correlation fringes.

Speckle interferometers that measure the in-plane component of displacement all work on the principle that the specimen under loading acts as *both* of the scattering surfaces of a Michelson type interferometer. Leendertz [1970] originally showed that this was possible by illuminating the surface with two beams of coherent light incident at equal angles to the normal θ, as shown in Figure 15. Each illuminating beam produces its own speckle pattern which combines coherently with the speckle pattern of the other beam. If the surface is displaced in the z direction, the two illuminating beams suffer equal path length changes, resulting in the same speckle pattern in the image plane (only if the displacement is small). Similarly, movement in the y direction will result in no change to the speckle pattern (again assuming the movement is small). However, a differential displacement in the x direction of d_x will result in the path length of one of the beams being increased by $d_x\sin\theta$, and the other being reduced by the same amount. If the speckle pattern of the surface under differential displacement is correlated with the surface pattern prior to displacement, correlation will occur when:

$$2d_x\sin\theta = n\lambda \quad [15]$$

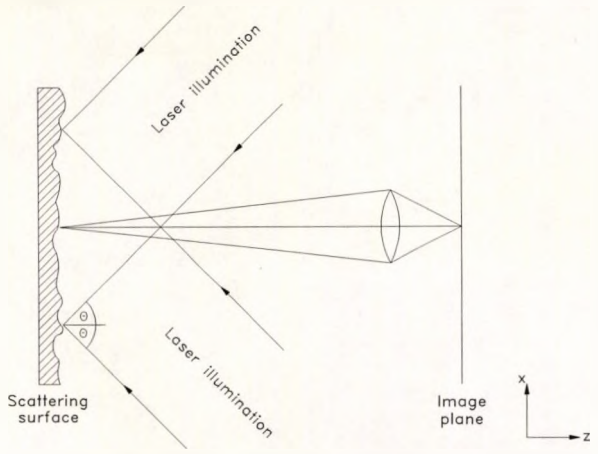


Figure 15: In-plane sensitive interferometer

Several correlation methods exist, but the most common is simply to subtract the two speckle patterns. Correlation will result in a fringe pattern relating to the component of the surface displacement resolved in the x direction. The spacing of the fringes corresponds to an incremental displacement of $\lambda/(2\sin\theta)$, the sensitivity of the interferometer being adjustable by altering θ. By plotting the positions of the fringes as a function of x, the linear strain $\delta d_x/\delta x$ can be computed over the entire region imaged by the interferometer. The conventional in-plane interferometer is insensitive to in-plane rigid body translations, but is affected by in-plane rotations. This is explained in Figure 16, which is exaggerated for clarity. Consider points P and Q on the surface of the specimen under examination. The points are at a vertical distance Y from the axis of rotation, O. A slight rotation α will move the points to positions P' and Q' respectively. The corresponding horizontal displacement for both points is d, which indicates that all the points at a vertical height Y from the axis will be subject to the same displacement in the sensitivity direction[23]. The displacement d is proportional to the height

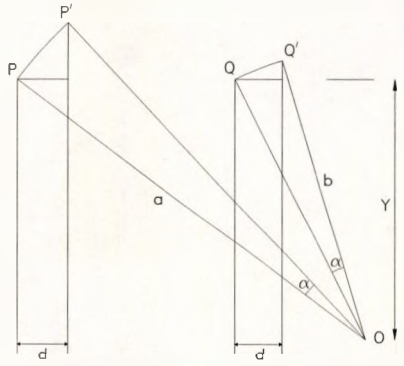


Figure 16: In-plane rotation sensitivity

[23]Both points do not move by *exactly* the same amount, but virtually the same, if the radius is large and the field of view is relatively small.

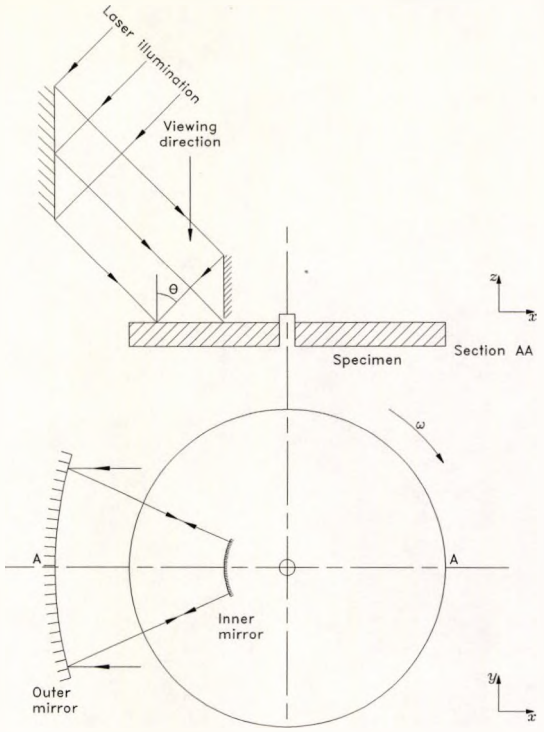


Figure 17: Radially sensitive interferometer (as Figure 11)

Y, hence, all points at height Y are subjected to the same *path length* change, and are thus contours of equal correlation. Therefore, for a small rotation, such that the interferometer does not become decorrelated, the horizontally sensitive in-plane interferometer will generate a field of *horizontal* fringes.

2.1.2.1 Radially sensitive in-plane interferometer

The conventional in-plane sensitive speckle pattern interferometer was found to be inadequate for use with high speed rotating specimens (see section 1.3.1 or Preater [1985]; Nguyen [1986]). A redesign of the optical delivery system resulted in the *radially* sensitive in-plane speckle pattern interferometer, shown in Figure 17 (see also Chapter 1, Figure 11). A slice along any radius would look exactly like Figure 15 (with x changed to r). Mathematically, for any radial displacement, the phase changes are identical to those of a conventional in-plane sensitive interferometer. The differences arise when one considers what happens when a rigid body movement occurs. The conventional in-plane interferometer of section 2.1.2 is insensitive to small movements in both the y and z directions. The radially sensitive in-plane interferometer is insensitive to small movements in the z direction and in-plane rotations, but is affected by rigid body movements in both the x and y directions. This can be explained with reference to Figure 18. Consider a point P with position vector r. A translation d is applied to the specimen, which moves from P to P', with position vector r'.

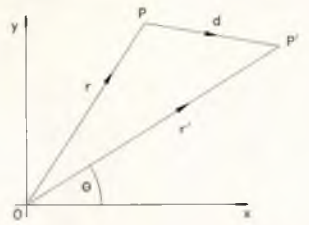


Figure 18: In-plane translation

The magnitudes of r and r' are unequal, since equality would represent an in-plane rotation. The vector d is small enough to prevent decorrelation of the speckle patterns. Suppose the in-plane translation is entirely in the positive x direction (ie. $d = x_d i$, where i is the unit vector along x). As r is rotated from $\theta=0$ to $\theta=\pi/2$, the *radial component* of the displacement reduces from x_d to 0. At any angle θ, all points suffer the same radial displacement. Hence, the radial component of displacement for a translation of the speckle patterns is proportional to the *angle* of the position vector only, the *distance* from the origin has no effect. The same approach can be used for an in-plane translation along any vector. All points on a radial line at any angle θ are subjected to the same *path length* change, and are thus contours of equal correlation. If the translation is small, such that the interferometer does not become decorrelated, the radially sensitive in-plane interferometer will generate a field of *radial* fringes. In Image 10, two speckle patterns were captured from a disc rotating at constant speed, and subtracted. In theory, the result should be a 'null field' since no change in the speckle pattern should have occurred. However, radial fringes are clearly visible in the image.

2.1.3 Decorrelation of speckle patterns

The following sections are taken for the most part from Jones and Wykes [1983]. Only the major results are stated, the derivations can be found in the previous reference.

2.1.3.1 Out-of-plane translation

When the specimen under examination is displaced along the viewing direction (the z axis), it can be shown that decorrelation will result when the specimen has moved:

$$\Delta z = \sqrt{2u\lambda} \qquad [16]$$

where u is the specimen-to-lens distance and λ is the wavelength of the illuminating beam. The decorrelation depends only on u, and a typical result for a ruby laser ($\lambda=694$nm) with the specimen-to-lens distance of 0.5m is approx. 830μm. The speckle pattern interferometer is therefore relatively insensitive to this form of displacement.



Image 10: Radial fringes

2.1.3.2 In-plane translation

When the specimen suffers a rigid body in-plane translation, the speckle pattern in the image plane moves in the opposite direction, in proportion to the magnification of the imaging system. The speckle pattern will be decorrelated if the translation is equal to, or greater than the resolution diameter of the imaging system, as expressed in Equation [17]:

$$\Delta x \leq \frac{A\lambda}{m} \qquad A = \frac{f}{a} \qquad [17]$$

where A is the numerical aperture of the imaging system (f is the focal length and a is the diameter of the lens aperture), λ is the wavelength of the light, and m is the magnification of the lens. Typically, for a ruby laser ($\lambda = 694$nm), with a magnification of 0.02 and numerical aperture of $f32$, the resolution diameter is approx. 1.1mm.

2.1.3.3 In-plane rotation

An in-plane rotation of the specimen causes a corresponding in-plane rotation of the speckle pattern in the image plane. A point at a distance R from the centre of rotation undergoes a shift along an arc of $R\alpha$, where α is the angle of rotation. To prevent speckle pattern decorrelation, the following equation must be adhered to:

$$\alpha \leq \frac{A\lambda}{Rm} \qquad A = \frac{f}{a} \qquad [18]$$

A typical result for a radius of 100mm, a ruby laser, $f32$ and a magnification of 0.02, would be decorrelation occurring when the specimen is rotated by 0.01rad (38min 11sec).

2.1.4 Tilt fringes

Tilt fringes, as the name implies, arise as a result of tilting one of the mirrors of the interferometer. They are sometimes referred to as *carrier fringes*, especially when used with Fourier transform fringe analysis, since they are used to 'carry' the phase information. Tilting one of the interferometer mirrors produces a *phase* change in one of the beams, which is proportional to the amount of tilt. With reference to Figure 15, tilting one (or both) of the beams in the *xz* plane has the effect of producing a set of equally spaced *vertical* fringes (fringes perpendicular to the sensitivity direction). Similarly, tilting the wavefront[24] of a *radially* sensitive in-plane interferometer has the effect of producing a set of sectored concentric fringes. Image 11 shows a set of such fringes. In this case, the wavefront was tilted by using a *plane* mirror prior to incidence on the cylindrical system (see Figure 45).

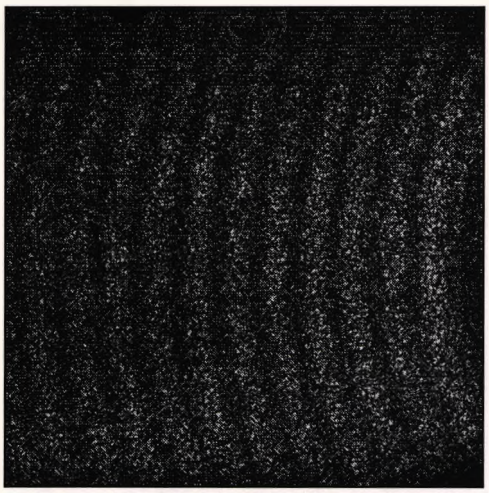


Image 11: Tilt fringes

2.2 Strain measurement

The effect of an external force on a body is to deform and/or shift the object. Expressed mathematically, strain is a tensor quantity which can be represented by the matrix shown in Equation [19]. The components of the displacement vector at point (x,y,z) are L_x, L_y and L_z [Winther, 1988]. The strain tensor contains six independent values because it has symmetry about the diagonal. According to Winther [1988], it is convenient to define a local coordinate system at each point on the surface. This system (x',y',z'), has the z' axis as the normal to the surface, and $x'y'$ as the tangential plane. The displacement vectors $L_{x'}$, $L_{y'}$ and $L_{z'}$ represent the displacements in the local coordinate system.

[24] In this case, it is essential that the wavefront is tilted *before* it reaches the twin cylindrical mirror optical system. Tilting one of the cylindrical mirrors causes severe misalignment of the interferometer, as explained in section 3.1.3.2.

$$S = \begin{bmatrix} \frac{\delta L_x}{\delta x} & \frac{1}{2}\left(\frac{\delta L_x}{\delta y}+\frac{\delta L_y}{\delta x}\right) & \frac{1}{2}\left(\frac{\delta L_x}{\delta z}+\frac{\delta L_z}{\delta x}\right) \\ \frac{1}{2}\left(\frac{\delta L_y}{\delta x}+\frac{\delta L_x}{\delta y}\right) & \frac{\delta L_y}{\delta y} & \frac{1}{2}\left(\frac{\delta L_y}{\delta z}+\frac{\delta L_z}{\delta y}\right) \\ \frac{1}{2}\left(\frac{\delta L_z}{\delta x}+\frac{\delta L_x}{\delta z}\right) & \frac{1}{2}\left(\frac{\delta L_z}{\delta y}+\frac{\delta L_y}{\delta z}\right) & \frac{\delta L_z}{\delta z} \end{bmatrix} \quad [19]$$

Since in-plane measurements are to be performed, this definition eliminates all terms in the strain tensor which contain either L_z or $\delta/\delta z$ and it becomes:

$$S' = \begin{bmatrix} \frac{\delta L_{x'}}{\delta x'} & \frac{1}{2}\left(\frac{\delta L_{x'}}{\delta y'}+\frac{\delta L_{y'}}{\delta x'}\right) \\ \frac{1}{2}\left(\frac{\delta L_{y'}}{\delta x'}+\frac{\delta L_{x'}}{\delta y'}\right) & \frac{\delta L_{y'}}{\delta y'} \end{bmatrix} \quad [20]$$

Computation of the tensor requires two independent orthogonal measurements[25].

Now, an in-plane speckle pattern interferometer measures changes in *phase*. For each point in the plane of the detector (x,y), the phase change is directly related to the displacement vector $\vec{d}(x,y)$ by Equation [21]:

$$\phi(x,y) = \vec{s}(x,y) \cdot \vec{d}(x,y) \quad [21]$$

where $\vec{s}(x,y)$ is the sensitivity vector of the interferometer. The sensitivity vector is a function of the spatial coordinates, since in many cases it varies with position [Pryputniewicz and Stetson, 1980]. However, in the cases under consideration in this thesis (in-plane systems), the *magnitude* of the sensitivity vector is fixed, and determined by the interferometer geometry. With reference to Figure 15 which shows a common in-plane sensitive system, the specimen lies in the xy plane and is illuminated by plane wavefronts at equal angles to the z axis. When a small element is displaced by a distance d_x (in the x direction), the relative phase change of the two beams is given by:

$$\Delta\phi = \frac{4\pi}{\lambda} d_x \sin\theta \quad [22]$$

which is Equation [15] rewritten with the phase equated to $2\pi n$ (n is the fringe order number). The x direction displacement can then be computed from the phase, as shown overleaf in Equation [23]:

[25]The complete tensor would require three independent measurements.

$$d_x = \Delta\phi \frac{\lambda}{4\pi \sin\theta} \quad [23]$$

In other words, the length of the sensitivity vector is constant at all pixel locations (x,y), and points in the x direction (the sign of the vector does not matter since the computation of the phase results in a sign ambiguity). Multiplication by the sensitivity is simply a scaling constant. The strain in the x direction is proportional to the first differential of the displacement with respect to x:

$$\epsilon_x = \frac{d}{dx} d_x \quad [24]$$

For a radially sensitive interferometer, the radial direction displacement, d_r, is computed from the equation:

$$d_r = \Delta\phi \frac{\lambda}{4\pi \sin\theta} \quad [25]$$

The radial strain is calculated from:

$$\epsilon_r = \frac{d}{dr} d_r \quad [26]$$

Once the unwrapped phase has been computed from the fringe pattern, the determination of strain is relatively straightforward. Initially, the gauge length over which the strain is to be determined must be selected. This requires a knowledge of the real-space *area* of the image, which can be determined in several ways:

- Select a feature in the image of known dimensions and compute the 'size' of each pixel using this. It is important to note that on some imaging systems, astigmatisms or other features may influence the measurement by different amounts in the horizontal and vertical directions. In this case, see below.
- Place a target in the object plane and store an image in the framestore. The horizontal and vertical mappings can be computed independently, as can the mapping in any arbitrary direction.
- Compute the mapping from known system parameters.

The last point is the least favoured since it requires accurate determination of the parameters of the lens and imaging system. For a reasonable quality lens, imaging onto a high resolution CCD camera, the first two options will almost always suffice. Typically, a steel rule can be placed in the object plane and imaged. Several measurements of the millimetre scale will often give a good estimate of the pixel-to-metre ratio (Equation [111] on Page 125), as explained in section 4.5.7. Once this is determined, the gauge length can be selected, in terms of the

number of pixels. An example of this is given on Page 132 (Image 40), where 1mm on the specimen corresponds to approximately 57 pixels in the VS100. It is often only possible to determine the distance to the nearest pixel.

2.3 Strain in rotating discs

2.3.1 General equations in polar coordinates

It is convenient to introduce a polar coordinate system to analyse the plane stress in a rotating disc (actually, the coordinate system should be cylindrical, but when considering plane stress problems, $\tau_{rz} = \tau_{\theta z} = 0$ and the other stress components are functions of r and θ only). The following analysis is taken largely from Wang [1963].

Consider the equilibrium of a small element $ABCD$ as shown in Figure 19. The arc AD is at a radius r, BC is a radius $r+\delta r$. The stresses J,K,L,M,P,Q,R and S are given by:

$$J=\sigma_r \qquad K=\sigma_\theta \qquad L=\sigma_r+\frac{\delta \sigma_r}{\delta r}dr \qquad M=\sigma_\theta+\frac{\delta \sigma_\theta}{\delta \theta}d\theta \qquad [27]$$

$$P=\tau_{r\theta} \qquad Q=\tau_{r\theta}+\frac{\delta \tau_{r\theta}}{\delta r}dr \qquad R=\tau_{r\theta}+\frac{\delta \tau_{r\theta}}{\delta \theta}d\theta \qquad S=\tau_{r\theta} \qquad [28]$$

where σ_r is the stress in the radial direction, σ_θ is the stress in the tangential direction and $\tau_{r\theta}$ is the shear stress. The radial component of the forces due to J and L is:

$$\left(\sigma_r+\frac{\delta \sigma_r}{\delta r}dr\right)(r+dr)d\theta - \sigma_r r d\theta \qquad [29]$$

The radial component of the forces due to M, K, R and P is:

$$-\left(\sigma_\theta+\frac{\delta \sigma_\theta}{\delta \theta}d\theta\right)dr\sin\left(\frac{d\theta}{2}\right)-\sigma_\theta dr\sin\left(\frac{d\theta}{2}\right)+\left(\tau_{r\theta}+\frac{\delta \tau_{r\theta}}{\delta \theta}d\theta\right)dr\cos\left(\frac{d\theta}{2}\right)-\tau_{r\theta}dr\cos\left(\frac{d\theta}{2}\right) \qquad [30]$$

Since $d\theta$ is small, this equation becomes:

$$-\left(\sigma_\theta+\frac{\delta \sigma_\theta}{\delta \theta}d\theta\right)dr\left(\frac{d\theta}{2}\right)-\sigma_\theta dr\left(\frac{d\theta}{2}\right)+\left(\tau_{r\theta}+\frac{\delta \tau_{r\theta}}{\delta \theta}d\theta\right)dr-\tau_{r\theta}dr \qquad [31]$$

Let F_r and F_θ be the components of the body force per unit volume in the radial and tangential directions respectively. Summing up the radial components of the forces (Equation [29] and Equation [31]), neglecting small quantities of higher order and dividing through by $rdrd\theta$, the equilibrium equation in the radial direction is given by Equation [32] overleaf:

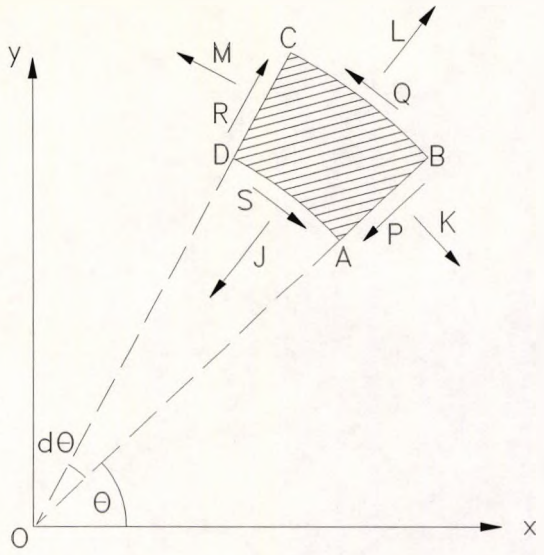


Figure 19: Element coordinate system

$$\frac{\delta \sigma_r}{\delta r} + \frac{1}{r}\frac{\delta \tau_{r\theta}}{\delta \theta} + \frac{\sigma_r - \sigma_\theta}{r} + F_r = 0 \qquad [32]$$

The equilibrium equation in the tangential direction can be obtained in a similar manner:

$$\frac{1}{r}\frac{\delta \sigma_\theta}{\delta \theta} + \frac{\delta \tau_{r\theta}}{\delta r} + \frac{2\tau_{r\theta}}{r} + F_\theta = 0 \qquad [33]$$

A solution to these partial differential equations is obtained by neglecting the body force and introducing the stress function ψ defined by Equation [34]:

$$\tau_{r\theta} = -\frac{\delta}{\delta r}\left(\frac{1}{r}\frac{\delta \psi}{\delta \theta}\right) \qquad \sigma_r = \frac{1}{r}\frac{\delta \psi}{\delta r} + \frac{1}{r^2}\frac{\delta^2 \psi}{\delta \theta^2} \qquad \sigma_\theta = \frac{\delta^2 \psi}{\delta r^2} \qquad [34]$$

Now, let $A'B'C'D'$ be the position of element $ABCD$ after strain, and let u,v be the displacements of the point A in the radial and tangential directions respectively. The displacements of B are $u + (\delta u/\delta r)dr$ and $v + (\delta v/\delta r)dr$, and $(A'B')^2$ is:

$$(A'B')^2 = \left(dr + \frac{\delta u}{\delta r}dr\right)^2 + \left(\frac{\delta v}{\delta r}dr\right)^2 \qquad [35]$$

By definition, $A'B'$ is equal to $(1 + \epsilon_r)dr$, where ϵ_r is the radial strain. Neglecting high order terms, the expansion of Equation [35] gives ϵ_r:

$$\epsilon_r = \frac{\delta u}{\delta r} \qquad [36]$$

A similar treatment for $A'D'$ yields:

$$(A'D')^2 = [(1+\epsilon_\theta)\,r d\theta]^2 = \left[(r+u)\,d\theta + \frac{\delta v}{r d\theta} r d\theta\right]^2 + \left(\frac{\delta u}{r d\theta} r d\theta\right)^2 \qquad [37]$$

Neglecting high order terms, the tangential strain is given by:

$$\epsilon_\theta = \frac{u}{r} + \frac{1}{r}\frac{\delta v}{\delta \theta} \qquad [38]$$

The shear strain can be found by computation of the change in angle DAB:

$$\gamma_{r\theta} = \frac{\delta u}{r\delta\theta} + \frac{\delta v}{\delta r} - \frac{v}{r} \qquad [39]$$

Elimination of u and v from ϵ_r, ϵ_θ and $\gamma_{r\theta}$ gives the compatibility equation:

$$\frac{\delta^2\epsilon_\theta}{\delta r^2} + \frac{\delta^2\epsilon_r}{r^2\delta\theta^2} + \frac{2}{r}\frac{\delta\epsilon_\theta}{\delta r} - \frac{1}{r}\frac{\delta\epsilon_r}{\delta r} = \frac{\delta^2\gamma_{r\theta}}{r\delta r\delta\theta} + \frac{1}{r^2}\frac{\delta\gamma_{r\theta}}{\delta\theta} \qquad [40]$$

For plane stress, the stress-strain relationships in polar coordinates are:

$$\epsilon_r = \frac{1}{E}(\sigma_r - \nu\sigma_\theta) \qquad \epsilon_\theta = \frac{1}{E}(\sigma_\theta - \nu\sigma_r) \qquad \gamma_{r\theta} = \frac{2(1+\nu)}{E}\tau_{r\theta} \qquad [41]$$

where E is the modulus of elasticity and ν is Poisson's ratio [Wang, 1963].

2.3.2 Thin rotating disc

Consider the case of a thin disc with constant thickness rotating at an angular velocity of ωrad s^{-1}. The disc has a central hole of radius a and the outer circumference is at radius b. The centrifugal body force acting is given by:

$$F_r = \rho\omega^2 r \qquad [42]$$

where ρ is the density of the material and r is the radius. Since the stress distribution in the disc must be symmetrical with respect to the axis of rotation, the equilibrium equation is:

$$\frac{d\sigma_r}{dr} + \frac{\sigma_r - \sigma_\theta}{r} + \rho\omega^2 r = 0 \qquad [43]$$

The introduction of a stress function ψ such that:

$$\sigma_r = \frac{\psi}{r} \qquad \sigma_\theta = \frac{d\psi}{dr} + \rho\omega^2 r^2 \qquad [44]$$

satisfies Equation [43].

In the case of rotational symmetry, u is a function of r only and $v=0$, so the tangential strain is given by $\epsilon_\theta = u/r$ and the compatibility equation reduces to:

$$\frac{d}{dr}(r\epsilon_\theta) - \epsilon_r = 0 \qquad [45]$$

The combination of Equations [41], [44] and [45] (the application of Hooke's law and the stress function ψ) transforms Equation [45]:

$$\frac{d^2\psi}{dr^2} + \frac{1}{r}\frac{d\psi}{dr} - \frac{\psi}{r^2} + (3+\nu)\rho\omega^2 r = 0 \qquad [46]$$

Integrating this equation with respect to r produces:

$$\psi = -\left(\frac{3+\nu}{8}\right)\rho\omega^2 r^3 + A\frac{r}{2} + B\frac{1}{r} \qquad [47]$$

where A and B are the constants of integration. Applying the boundary conditions that $\sigma_r=0$ when $r=a$ and $r=b$, and substitution of ψ into Equation [44] allows the constants to be computed, giving the radial and tangential stresses, Equations [48] and [49].

$$\sigma_r = \left(\frac{3+\nu}{8}\right)\rho\omega^2\left[b^2 + a^2 - \frac{a^2b^2}{r^2} - r^2\right] \qquad [48]$$

$$\sigma_\theta = \left(\frac{3+\nu}{8}\right)\rho\omega^2\left[b^2 + a^2 + \frac{a^2b^2}{r^2} - \left(\frac{1+3\nu}{3+\nu}\right)r^2\right] \qquad [49]$$

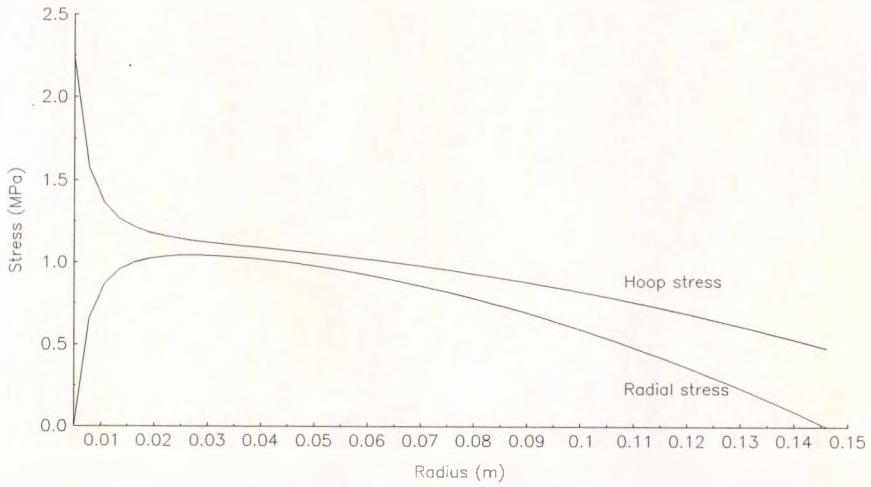
A plot of the above equations, shown in Graph 2, gives the typical shape of the radial and tangential stress distributions for a disc. This plot is for a disc with the following parameters:

- ω = 2000rad s^{-1} (approximately 19,100rpm)
- ρ = 7861Kg m^{-3}
- ν = 0.3
- a = 0.05m
- b = 0.15m

It is clear that the peak stress is the tangential stress around the central hole at radius a. Also, it is simple to show that the peak radial stress is at a radius of $\sqrt{ab}$.

Several investigators have examined the stresses in rotating specimens. Stern [1965] presents a quasi-static analysis of the effect of angular acceleration on the stresses in a rotating disc. The calculation reveals the existence of a shearing stress proportional to the acceleration, and the square of the outer radius, but independent of the angular velocity. This shearing stress varies both directly and inversely as the square of the distance from the disc axis, and the

normal stresses are unaffected by the acceleration. For a traction-free disc mounted on a shaft, the shearing stress was found to increase closer to the axis, reaching a peak value at the inner edge. Tang [1970] essentially confirms the findings of Stern. Philips and Schrock [1971] attempt to find an improved profile of disc in an effort to redistribute the shear. Using profiles of thickness which varied as a power of the radius, they find that inverse square and cube profiles minimise the variations of shear. Deresiewicz [1975] broadens this work by computing the shear stress distribution for arbitrary thickness profiles. Reddy *et al.* [1974] examine the stresses induced in an accelerating circular disc in which the fibres of a fibre reinforced material are aligned at a constant angle with respect to the radial direction. They conclude that fibre reinforced materials have induced stresses in the radial and tangential directions, in contrast to isotropic materials. Amada [1984] presents an analysis of the dynamic stresses in a solid rotating disc subject to an arbitrarily varying angular speed. Another publication by Amada [1985], examines the circumferential displacements and shear stresses for a hollow disc fixed to a rigid shaft undergoing variable rotations using the Laplace transform and Cauchy integral theorem. In addition, Amada [1986] presents similar work for a solid disc subjected to cyclically varying rotations.



Graph 2: Radial and hoop stress distributions

3 EXPERIMENTAL APPARATUS

3.0 Experimental methods

3.1 Prototype system

This section details the experimental system in existence at the commencement of this research programme. The prototype system was developed by Preater [1980-1990], but unfortunately the electronic control system lacked adequate documentation (the only available documentation was in the form of conference papers, which contained unsuitable diagrams, such as Figure 9 on Page 21). Therefore, a detailed description of the system operation is given here, in order to explain the design modifications which have taken place, to produce the system in operation today (which is discussed in section 3.2).

3.1.1 Electronic subsystem

The electronic subsystem lies at the heart of the entire experimental apparatus. The original control system, shown in Figure 9, was developed by Heaphy for the work of Preater [1980-1990], and enabled interference fringe patterns to be obtained on rotating components with a maximum documented tip speed of 135m s^{-1}, as explained in section 1.3.1[26]. However, the rapid development of modern electronics meant that the system lagged behind current technology, and was also unpredictable, not working at certain speeds, and unreliably at others. Furthermore, the output data was in a format incompatible with modern analysis systems. Figure 20 is more a detailed version of Figure 9, and shows a block diagram of the electronic system developed by Heaphy. The core of the system is an electronic control unit (ECU) which controls asynchronously the operation of the other components. The ECU was programmable via a bank of thumbwheel switches (keyboard), and enabled ESPI fringes of any section of the rotating component to be captured and stored on the video tape. The ECU had three basic inputs: the timing pulses from the shaft encoder, positional information from the keyboard, and video genlock[27]. A start signal was input to the system by the operator, to initiate a single fire operation. The ECU outputs were the fire and Q-switch pulses for the laser, a blanking pulse for the scanning electron beam of the camera, and relevant pulses to

[26]Preater actually obtained a single fringe pattern at a tip speed of 150ms^{-1}, but the drive motor failed during this test and it was neither documented nor repeated.

[27]It is noted that in addition to firing the laser, the ECU is required to perform supplementary functions; for example, the TV camera and framestore need to be synchronized so that correct image capture and registration can occur. These less important functions are not described in detail since many of them are superseded in the new control unit.

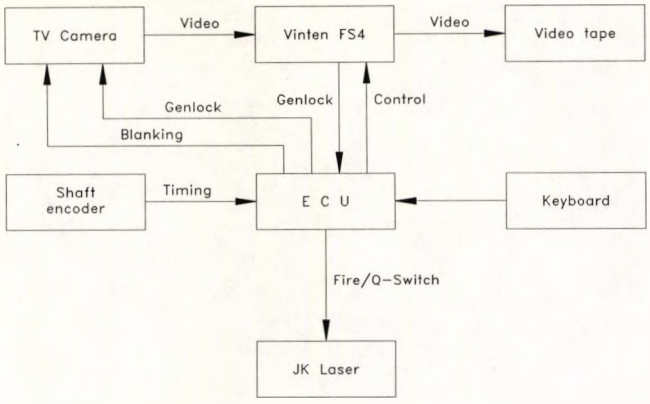


Figure 20: Electronic system

operate the Vinten frame capture system. A detailed description of the operation of the prototype ECU is given in section 3.1.1.2.

3.1.1.1 Specification of the laser firing problem

At first, it may appear relatively straightforward to pulse a laser at a specific point on the rotation cycle of a component. However, problems arise from the fact that the laser is Q-switched. Q-switching [Smith and Thompson, 1988] takes its name from electrical circuit theory, where the quality of a resonator is measured as a factor Q. In laser technology, the resonator is the optical cavity of the device. When the laser medium is excited (optical pumping of the cavity by the flashtubes), one of the cavity mirrors is obscured by an optical switch (often a Pockel's or Kerr cell). At the point of *maximum* population inversion, the optical switch is opened, and a large energy pulse is emitted as soon as laser action restarts. In the case of the JK 2000 laser used for these experiments, two pulses are required for it to operate correctly. The first pulse is used to pump the oscillator cavity. This pulse is also passed through a delay unit and used to pump the amplifier cavity. The second pulse is used to Q-switch the Pockel's Cell fitted in the oscillator cavity[28]. The delivery of the laser illumination occurs a short time after the Q-switch pulse is received. Since the laser illumination is used like the high speed flash of a camera to freeze the motion of the rotating disc, the Q-switch pulse must be accurately synchronised to a specific point in the disc rotation cycle. This requires *anticipating* where another point in the rotation cycle will be, so that the laser *fire* pulse may be issued (1.31ms in advance). The system developed by Heaphy addressed the problem in a novel way, which is described in the next section.

[28]The manufacturer of the laser specifies a fixed separation of 1.31ms between the two pulses.

3.1.1.2 Electronic Control Unit (ECU)

As already noted, the original control unit developed by Heaphy was not documented. The author investigated the electronic circuit, resulting in the following description. A shaft encoder is used to generate timing information about the rotational position of the rotating disc. This information normally consists of two signals, the first with 120 pulses per revolution, and the second with a single reference pulse per revolution. This timing information is fed into the electronic control unit, which consists of three electronic counting circuits: designated counters 1, 2 and 3 (see Figure 21). Counter 1 is a three digit BCD *up only* device used for counting the incoming timing pulses, counter 2 is a seven digit BCD *up/down* counter, coupled to a 10MHz square wave oscillator circuit. The third counter is a two digit BCD *up/down* counter used for generating the Q-switch pulse. This counter also counts the incoming timing pulses. The output of counter 1 is decoded twice, each decoder being variable over the entire count range (0-999), the variation produced by thumbwheel switch settings. The two decoded pulses are designated *A* and *B*. Pulse *A* is used as an activate signal for counters 2 and 3, pulse *B* is used to switch counters 2 and 3 from *count up* to *count down* mode. It is also used to reset counter 1 to zero. Counter 2 is decoded twice, both decoders being active only when the counter is in *count down* mode. The first decoded value is designated *C* and is used to generate the laser fire pulse. This decoder is also variable by means of thumbwheel switches over the entire count range of counter 2 (0-9999999). The second decoded value arises when counter 2 reaches zero (designated pulse *D*), and is used to initiate electron beam blanking in the TV camera. It is also used to reset counter 2. Counter 3 works just like counter 2, except that it counts the timing pulses. It is decoded at zero in *count down* mode, and the decoded output (designated pulse *E*) is used to Q-switch the laser, and reset counter 3. The system operation is shown diagrammatically in Figure 22 and by flowchart in Figure 23. Operation is initiated with a start signal supplied by the operator by means of a pushbutton. The control system waits for the reference pulse from the rotating disc (t = 0), then counter 1 starts counting the timing pulses from the disc. When counter 1 reaches the preprogrammed value *A*, counter 2 is started in up mode, counting the 10MHz clock signal. Pulse *A* also starts counter 3 in up mode counting the incoming timing pulses. In the meantime, counter 1 is still counting the incoming timing pulses. When counter 1 reaches the preprogrammed value *B*, counters 2 and 3 are switched into count down mode and counter 1 is reset and stopped. The decoder *C* is now enabled because counter 2 is operating in count down mode, and will activate when the count reaches the preprogrammed value set on the thumbwheel switches. The output of decoder *C* is amplified and used to generate the laser fire pulse[29]. When counter 2 reaches zero, an

[29]Amplification is necessary because the input controls for the laser are not TTL compatible.

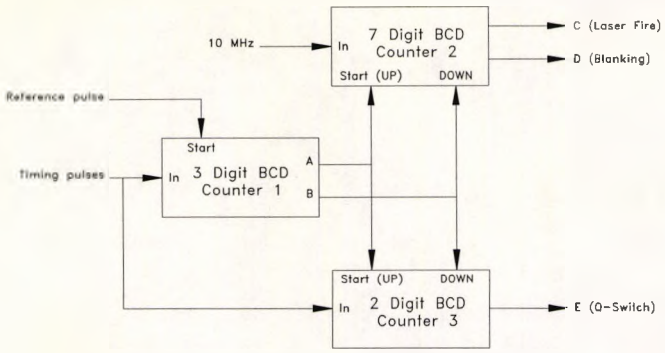


Figure 21: Block diagram of prototype ECU

output pulse is generated and used in conjunction with a small control circuit to blank the scanning electron beam of the TV camera (section 3.1.1.4). Counter 3 reaches zero at approximately the same time as counter 2, since the profiles of the two counts form similar triangles. When counter 3 reaches zero, the zero decoder output (pulse *E*) is amplified and used to Q-switch the laser. The pulse *E* is used to Q-switch the laser in preference to the pulse *D*, since *E* is generated physically by one of the shaft encoder pulses, and is therefore more likely to represent the exact position of the disc than the *D* pulse (which is generated by the 10MHz clock). Amplification of the laser fire and Q-switch pulses occurs via a DS3686 chip, so that the pulses are in the range: 0-15V. The input Q-switch pulse is coupled directly into the high-voltage stage of the Pockel's Cell driver unit, enabling highly accurate control over Q-switch firing. The direct drive of the Pockel's Cell enables control over the high voltage

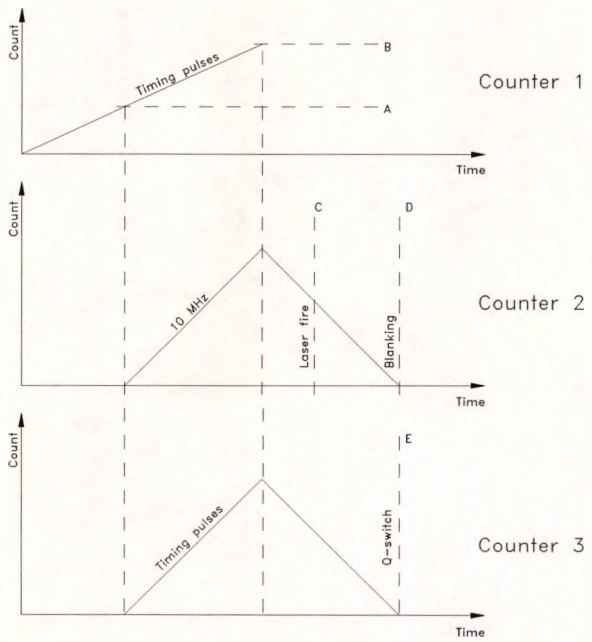


Figure 22: ECU counter operation

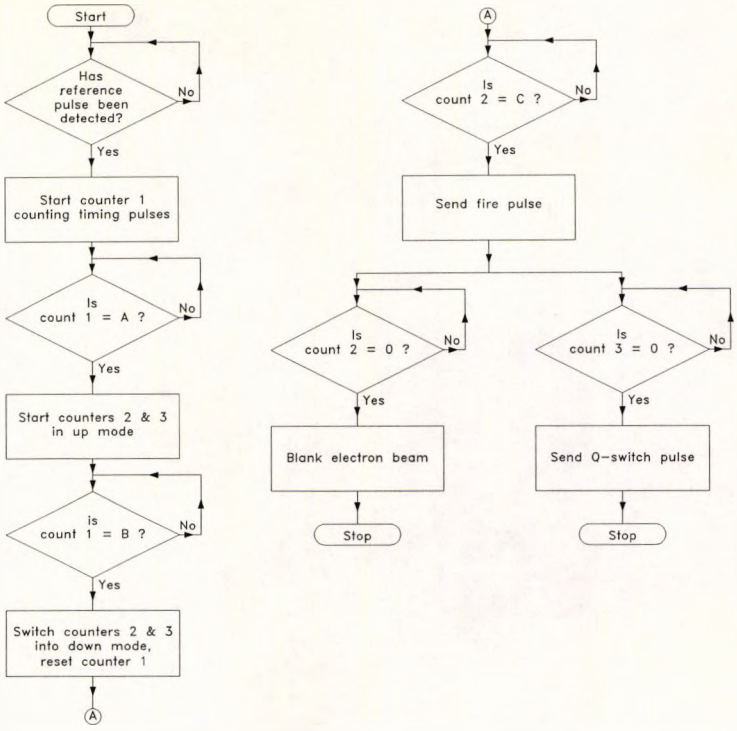


Figure 23: ECU operation flowchart

feed to the Cell without the additional time delay caused by the low voltage electronics of the normal driver. Consider the example shown in Figure 24. Suppose the component is rotating at 5,000rpm. In this example, the thumbwheel settings would be programmed: $A=005$, $B=017$ and $C=0013100$. The angular difference between A and B is the same as the angular difference between B and E (and D since they almost overlap), which in this instance is 1.256rad. It can be seen that the *peak* value of counter 2, which is counting real time, is the time taken for the disc to rotate from A to B, and is therefore an accurate measure of the rotational speed of the disc. Using this measurement (in this example, counter 2 would peak at about 0024000, which is 2.4ms), it is possible to produce the C pulse with great accuracy[30]. The shape of the ESPI fringes and the degree of correlation is dependent on the accuracy of the Q-switch pulse only. It should be noted here that as the rotational speed increases, the separation of the A and B pulses must be increased at certain critical points. This is because for a given separation, the time taken for the disc to rotate by that separation *reduces* as the speed *increases*. If the time reduces below the value programmed into the C decoder, then pulse C will never be produced, hence the laser will never receive the fire instruction.

[30]Incidentally, the accuracy to which the C pulse is developed will not affect the shape of the ESPI fringes, only the quality. This is because the time difference between the laser fire and Q-switch pulses only affects the output power of the beam. This in turn may have an effect on the temporal and spatial coherence, and possibly the wavelength.

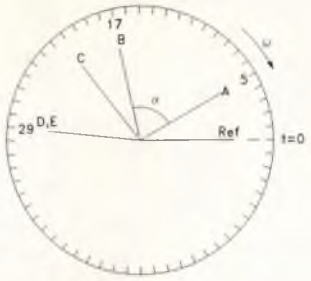


Figure 24: Timing example

3.1.1.3 Shaft encoder and timing considerations

The electronic control system generates all the synchronisation pulses necessary to capture correlated speckle patterns from a disc in rotation. The quality of the timing pulses is crucial to the accuracy of the system. Early versions of the shaft encoder required cutting slots around the circumference of the specimen disc (normally 60 or 120), and making one of the slots deeper than the others giving the single reference pulse (see section 1.3.1). Image 12 on Page 53 is a plan photograph of the early shaft encoder, and Image 13 (Page 54) shows a front view photograph of the rig, revealing the slots around the circumference of the disc. The two HeNe lasers that form the shaft encoder are to the left of the rotating disc. The slots form an optical shaft encoder through which HeNe beams are passed into photodetectors. The photodetectors are mounted close to the rotating disc and the electrical waveform is amplified locally and transmitted to the electronic control unit via coaxial cables. In this case, the disc forms both the encoder and specimen under test. The accuracy of the speckle registration is determined solely by the quality of the shaft encoder timing pulses, the reference pulse serving only to start the counting process[31]. In an effort to *reduce* the optical rise time of these pulses, a lens is used to focus the HeNe beam to a point, in order

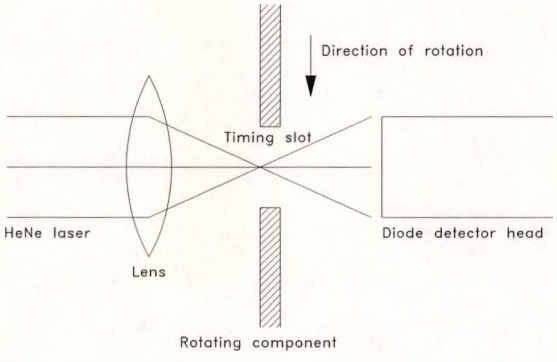


Figure 25: Timing pulse improvement

[31] Initially, the deeper slot of the reference pulse caused problems of stability at the higher rotational speeds, since the specimen was out of dynamic balance, and attempts to balance it proved difficult, since at very high rotational speeds, even slight errors cause major vibrational problems.

to produce an almost instantaneous optical cutoff, as shown in Figure 25. The local mounting of the diode photodetectors and amplifier electronics caused several problems, due to the electrical transmission of digital data pulses through several metres of coaxial cable. Transmission using voltage instead of current caused the link to be more susceptible to external electromagnetic interference. Also, the signal is 'spread' at the termination, a common effect when square wave data is passed through long cables [Horowitz and Hill, 1980], causing the positional repeatability of the rising edges of the pulses to reduce, thereby reducing the accuracy to which speckle registration can be achieved. Additionally, the mechanical means by which the detector/amplifier and laser launching system is constructed made the whole setup susceptible to vibrations, resulting in random optical misalignment between the photodetector and HeNe beams. This added 'jitter' to the pulses, producing random rotational misalignment of the speckle patterns.

3.1.1.4 Camera blanking

Before discussing blanking, it is necessary to explain some of the basics of interlaced video. The CCIR standard defines an interlaced raster scanning technique that eliminates flicker when the raster image is displayed. The horizontal scan lines which make up the frame are divided into two *fields*. The even field consists of the all the even numbered lines, starting with zero (the top line), and the odd field contains all the odd lines. Interlaced raster scanning results in the display of one field at a time. First, all the lines of the even field are displayed in succession, followed by all the lines of the odd field. The sequence repeats continuously, producing the raster image. Interlacing is not detected by the viewer, since the fields appear on the screen at a rate which exceeds average human perception.

Camera blanking was briefly mentioned in section 3.1.1.2, and is necessary because at the instant of laser Q-switching, the scanning electron beam of the video camera could be at any point in the scan cycle, and could be scanning either of the two interlaces. If the beam were allowed to remain scanning, and the image were digitized by the framestore at the start of the next even interlace, a sharp reduction in brightness would be observed at the point in the image where the beam was at the instant of Q-switching. This is because the scanning beam effectively deletes the information on the vidicon face plate as it scans. Switching off the beam at the instant of Q-switching results in a more uniform intensity distribution across the image.

The signal generated when counter 2 reaches zero (section 3.1.1.2) is fed to a latching circuit which *switches off* the scanning beam until the start of the next *even* frame. When the laser illumination is delivered, the phosphor coating of the TV cathode ray tube is used to store the

speckle pattern until the next *even* frame pulse. One problem which occurs with this system is an uneven intensity distribution of the two interlaces. The odd interlace is always scanned 10ms after the even interlace. The resulting decay of the odd interlace results in an average intensity that is much lower than the even interlace (this problem was overcome with the modified image capture system described in section 3.2.1.4).

3.1.1.5 Frame capture and subtraction

The original image processing system used by Preater [1984a] for the recording and subtraction of speckle images consisted of a KGM camera coupled to a video disc storage device. The output of the system was fed to a high resolution reel-to-reel video tape recorder for fringe image capture. The fringe pattern was stored as a single 'frame of interest', and was viewed with the video recorder in still frame mode. This system was later replaced by a Vinten FS4 framestore and Jackson Speckle Camera [Preater, 1986b]. The new system offered specialised picture processing for speckle type images, but, as previously, the output was stored on video tape, and viewed in much the same way as the video disc. The FS4 system was a 512x512 framestore offering digitization to 4 bits/pixel (16 grey levels). The FS4 could process the images by high pass filtering prior to digitization, and full wave rectification prior to D/A conversion. Low pass filtering of the image before display was also possible (for an explanation of the electronic processing necessary for good quality ESPI fringes, refer to: Slettemoen [1977]; Wykes *et al.*, [1981]; Jones and Wykes [1981]).

3.1.1.6 Electromagnetic Interference

As mentioned earlier, the original system operated reliably at certain well defined speeds, but would not operate at all over a wide range of speeds. After an extensive investigation into why this occurred, it was found that the triggering of the JK 2000 laser was the cause. The firing sequence of the JK 2000 laser is shown in Figure 26. The JK 2000 laser used for these experiments is a twin cavity system. The oscillator cavity is fitted with two inter-cavity

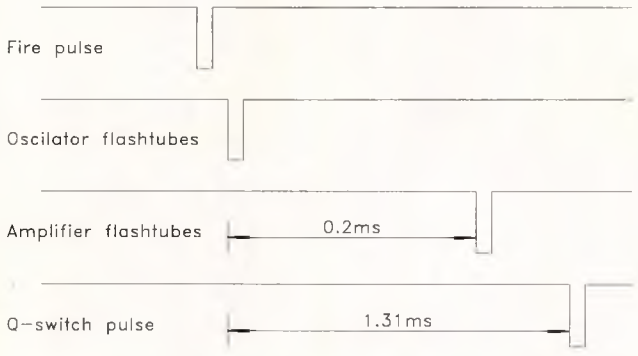


Figure 26: JK 2000 firing sequence

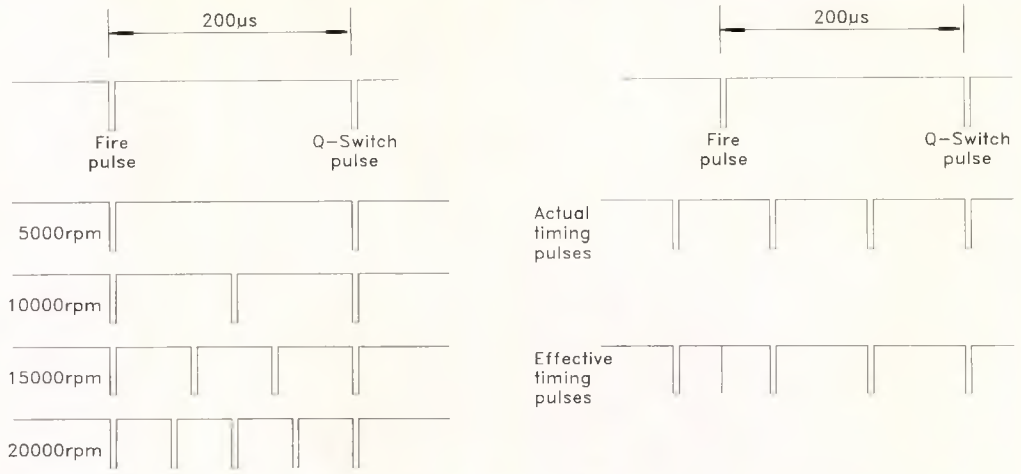


Figure 27: Interference, Correct operation (left), Incorrect operation (right)

etalons, and an inter-cavity Pockel's cell for Q-switching. The fire pulse initiates the firing process. A short time after this pulse is received by the laser, the flashtubes of the oscillator cavity are energised. The same pulse is passed through a variable delay device, and is used to energise the flashtubes of the amplifier cavity. The variable delay unit is usually set to produce a delay of 200μs, causing the amplifier cavity to be pumped 200μs after the oscillator. The electrical process by which the flashtubes are energized consists of applying a 2.2kV potential across the ends of the tubes and then injecting a 15kV breakdown voltage. This breakdown voltage causes the electrical resistance of the tubes to reduce, quickly enabling the large current associated with the 2.2kV potential to flow. The breakdown process causes a large amount of spurious electrical interference to be generated. The voltages measured in some parts of the enclosed ECU at a distance of several metres from the laser are of the order of 10V.

Since interference is prominent over the period of laser triggering, any *count* of timing pulses would almost certainly be in error. Hence, counter 3, which produces the Q-switch pulse, cannot be relied upon to produce repeatable results. Interestingly, it is the *repeatable* 200μs delay which caused the electronic control system to operate correctly at some speeds but not at others. This is because at certain speeds, the incoming timing pulses *overlapped* with the interference, as shown in Figure 27. A small range of speed variations close to the critical speeds could also be tolerated due to the finite width of the base of the timing pulses. Variations of about $\pm$200rpm of the critical speed would normally enable repeatable fringe patterns to be obtained.

3.1.2 Mechanical subsystem

The prototype mechanical subsystem consists basically of the support for the drive motor, and the support for the speckle interferometer. A diagram of the mechanical support system is given in Figure 28. The drive motor is mounted on a large concrete block (approximately 700kg). The block acts as a damper, absorbing the vibrations from the motor, which is rigidly coupled to it. The block is isolated from the floor on expanded polystyrene. Other isolation materials were tried, for example sorbathane rubber, but proved less effective than polystyrene. The optical components were mounted separately from the drive system, in an attempt to prevent vibrations from the drive system affecting the interferometer. The constituents of the speckle interferometer were all mounted together on an optical table, which was isolated from the floor by sorbathane rubber mounts. The pulsed laser was mounted on a separate support, several feet from the concrete block and optical table. Image 12 shows a plan photograph of the concrete block and optical table. The shaft encoder lasers are shown on the left of the image. The two HeNe laser beams are reflected off mirrors, and directed through slots cut in the perimeter of the disc. The shaft encoder cables can also be seen[32]. Image 13 shows a front view photograph of the optical system, original shaft encoder, and TV camera. The white test specimen is a perspex disc partially covered

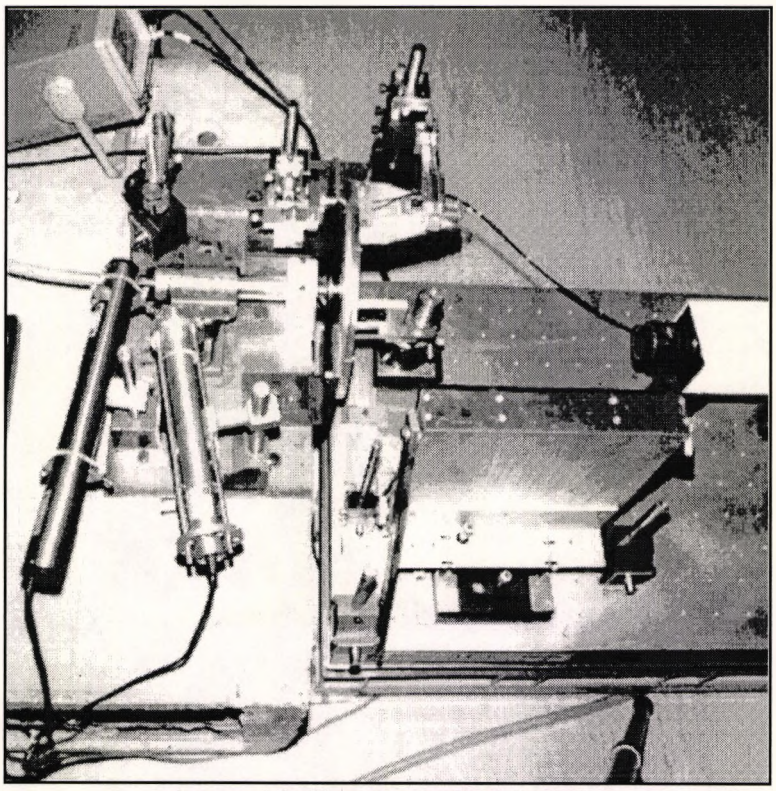


Image 12: Plan view of original rig

[32]In this image, fibre optic transmission of the shaft encoder pulses was used.

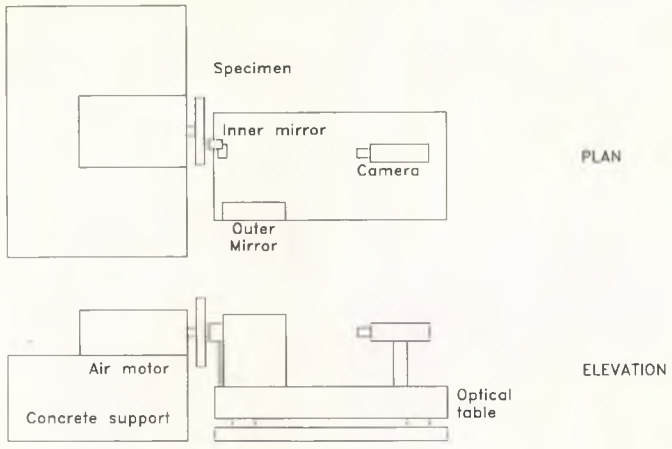


Figure 28: Mechanical support

by a shroud. The curved mirror to the left is the outer cylindrical mirror. The large base partially covering the lower front of the specimen is the inner mirror mounted on a series of translation, rotation and tilt stages. The stand which obscures the top right section of the test specimen is the mount holding the optical fibres of the shaft encoder. The TV camera (left foreground) is situated so as to view the left hand side of the component. Image 14 on Page 57 shows a photograph of the laboratory operating area. The pulsed ruby laser is mounted on a trolley (right background). The periscope mirrors (section 3.1.3.1) can be seen in front of the exit aperture of the laser (see Figure 29). The white cabinet behind the laser is the power supply unit and the control boxes on top of the cabinet are the drivers for the amplifier and oscillator flashtubes, the etalons and Pockel's cell. The test rig can be seen in the foreground.

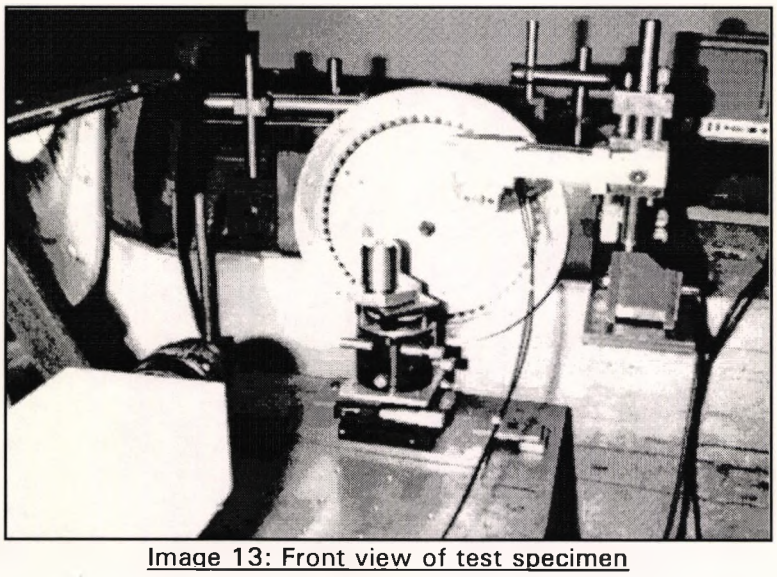


Image 13: Front view of test specimen

3.1.3 Optical subsystem

The optical subsystem developed by Preater was introduced in section 1.3.1, and a discussion of the theory was presented in section 2.1.2.1. Figure 17 in Chapter 2 shows details of the illumination delivery to the specimen surface. In addition, this section discussed the other constituents of the optical system, which interface with the radially sensitive speckle interferometer of Figure 17.

The pulsed laser beam is expanded using a diverging lens, and is steered to the interferometer by means of a periscope (see Figure 29 and Image 14). The periscope is used because the laser mounting is physically higher than the optical table. The expanded, height adjusted beam is then aimed onto the cylindrical mirror optical system directly, as shown in Figure 30. The alignment of the optical components poses a serious problem, since slight misalignment would result in severe errors in the resultant fringe patterns. Also, to align the pulsed laser is inherently difficult, due to the fact that the beam is only visible for an extremely short period of time.

3.1.3.1 Alignment of the pulsed laser

To align the pulsed laser with the speckle interferometer, Preater used a HeNe laser together with two adjustable mirrors. The mirrors were 'doglegged' in front of the diverging lens such that the HeNe beam *appeared* to be originating from the same point as the pulsed beam, as illustrated in Figure 31. By adjusting both mirrors, the spatial position of the beam could be altered. One problem with this technique is that it is not easy to determine whether the *vector* defining the direction of the pulsed beam is the same as that defining the HeNe beam. Therefore, angular adjustment of the periscope mirrors is impossible, allowing scope for a potential error of the incident wavefront on the speckle interferometer (since it may be tilted with respect to the interferometric horizon). Continuing with the alignment procedure used by Preater, the spot for the HeNe is positioned at the *extrapolated* intersection of the inner

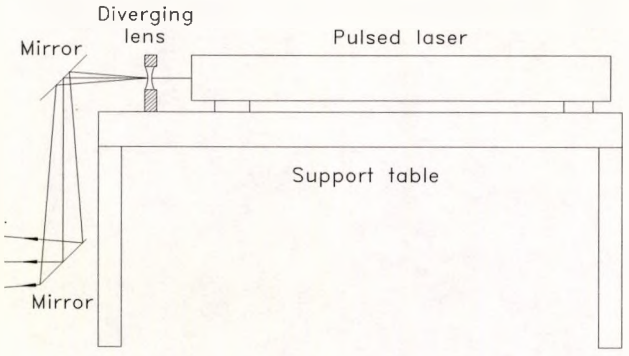


Figure 29: Periscope mirrors

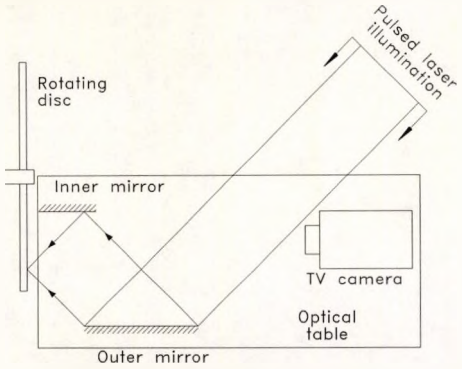


Figure 30: Original optical delivery

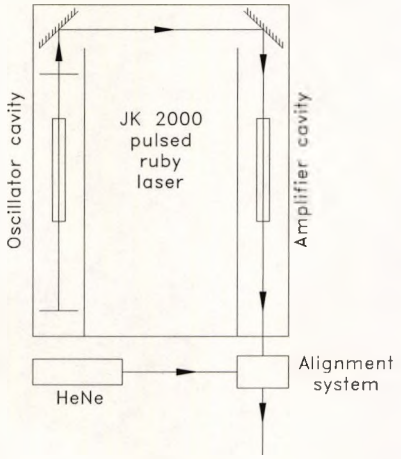


Figure 31: Alignment of the pulsed laser

mirror, the horizontal radius through the axis and plane of the rotating specimen. It is then moved using the adjustable mirrors, to determine whether the incident and reflected spots follow the *same* path. Adjustment of the various optical components allows this condition to be met, and the interferometer is then considered aligned.

3.1.3.2 Addition of carrier fringes

The system used by Preater to add carrier fringes to the fringe pattern involved rotating the inner cylindrical mirror in the *xz* plane. The inner mirror was mounted on a rotary stage which could be tilted in any plane, and rotated in the *xz* plane. Rotation required the operator to approach the rotating component, and turn the rotary knob of the tilt stage *very slightly*. Thus, repeatable fringe patterns were almost impossible to obtain, since the degree of rotation could not be accurately estimated. Also, the design of the stage holding the inner mirror intrinsically had *tilt* associated with rotation. The rotation of this mirror led to additional errors, due to the fact that it was non-planar, causing the geometry of the cylindrical mirror

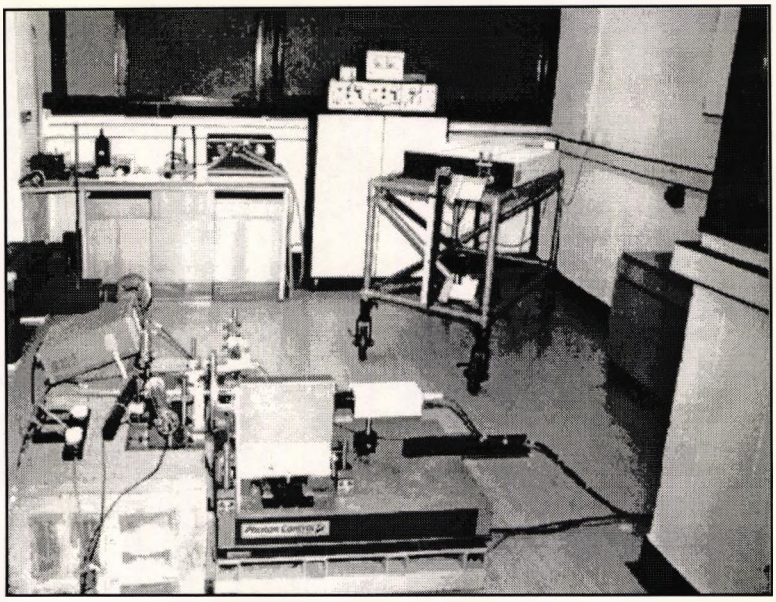


Image 14: View of laboratory

optical system to be distorted. This is illustrated in Figure 32, where the position of the mirrors along the *x* axis is scaled for clarity. Figure 32 (left) shows the position of the mirrors when in correct alignment, with no rotation of the inner mirror. After rotation (right diagram), it is obvious that only a *single plane* through both mirrors remains geometrically correct. This has the effect of altering the *radius of curvature* of the fringe patterns, as shown in Image 15, which illustrates fringes generated by rotation of the inner mirror (the dark patch in the middle of the image is a hole drilled through the specimen). The white lines on the image are concentric circles, drawn using the computer, indicating the expected shape of the carrier fringes. The corrected carrier fringes, obtained using the modified optical interferometer described in section 3.2.3.2, is shown in Image 16. These two images were taken using different specimens rotating at different speeds.

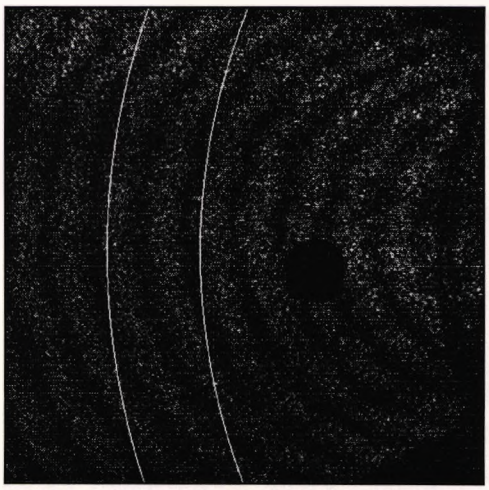


Image 15: Incorrect carrier fringes

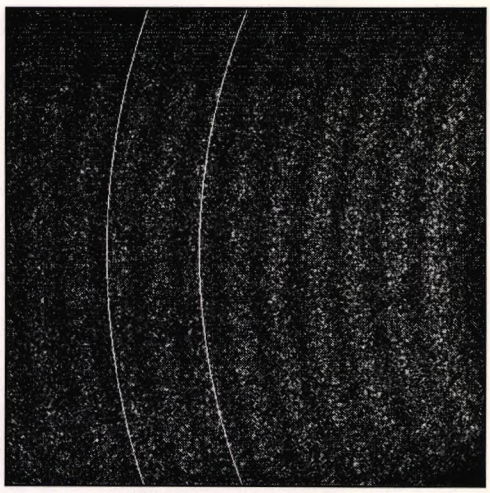


Image 16: Correct carrier fringes

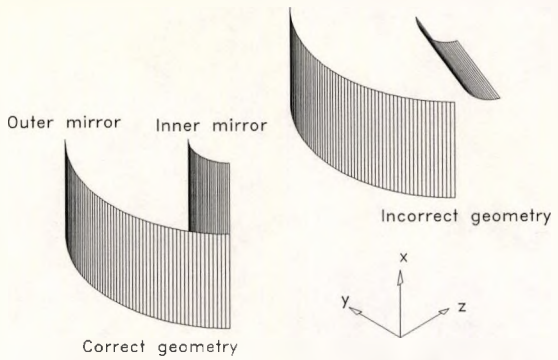


Figure 32: Cylindrical misalignment

3.2 Modified system

3.2.1 Electronic subsystem

The redesigned ECU is coupled to a PC compatible computer, and Imaging Technology VS100 framestore, to produce a completely new electronic subsystem, as illustrated in Figure 33. The modified system is considerably more flexible than the previous system, primarily due to the incorporation of the computer. The main advantages of using the modified control system are listed below:

- It is operated under full computer control. The experimental parameters can be programmed into the computer, which captures and stores the speckle images.
- More repeatable results can be obtained, since the amount of tilt added is under computer control[33].
- The analysis procedure is far more efficient, since the computer captures, stores and processes all data, without conversion from another storage format (eg. video tape).
- A centralised control provides a safer working environment for personnel operating the equipment. Personnel are no longer required to be in the vicinity of the operating test rig.

3.2.1.1 Electronic Control Unit (ECU)

The original control unit was poorly constructed, and was not in a form which could be easily modified. Hence, a new control unit was designed and built, providing an ideal opportunity for the electronics to be significantly improved. The main modifications were the incorporation of computer control, and immunity to electromagnetic interference. The operation of some parts of the system is fundamentally the same as in the previous unit, with the exception of the method of generating and transmitting the fire and Q-switch pulses of the laser. A block

[33]However, the system used is by no means perfect, since positional feedback from the motor is unavailable.

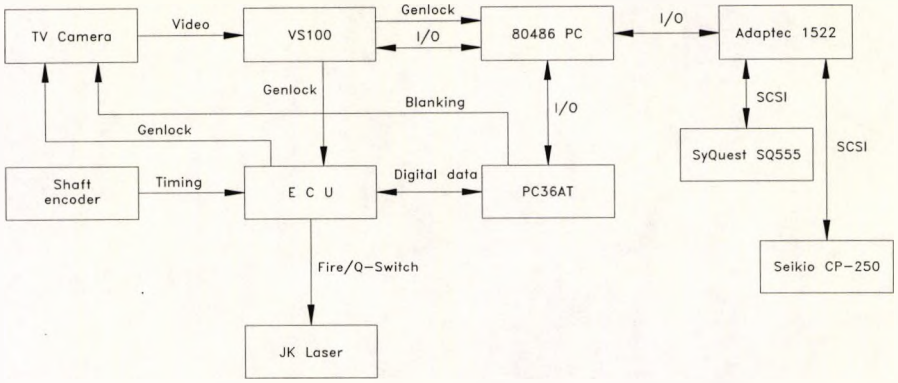


Figure 33: Modified electronic system

diagram of the modified ECU is shown in Figure 34. The VS100, PC36AT and Adaptec 1522 are third party hardware cards, fitted to the computer, and are therefore indicated as separate items in the diagram.

3.2.1.1.1 Theory of operation

The basic principle of the electronic control unit remains unchanged. Design modifications (see Appendix D for circuit block diagrams) have enabled the overall number of integrated circuits to be reduced, and those which remain are invariably faster, and consume less power. The new design generates and transmits the fire and Q-switch pulses using a method which suits the hostile electrical environment. A diagram illustrating the operation of the new control unit is shown in Figure 35, Figure 36 is a flowchart of its operation. The explanation of the operation should be compared with section 3.1.1.2, which gives a detailed description of the operation of the ECU counting mechanism. Counter 3 (section 3.1.1.2) has been removed, since previously, the generation of the Q-switch pulse required counting disc timing pulses *during* the period of laser firing and Q-switching. The new system tackles the problem of interference in a conventional way. The *C* pulse of Figure 35 causes all *inputs* to the electronic control unit to be connected directly to the 0V rail until the *D* pulse is generated (see the enable/disable circuit in Figure 34), eliminating electrical interference during that period. When the *D* pulse is produced, a new circuit is enabled (see Figure 34 and Figure 37) which generates the Q-switch pulse on the *next* timing pulse. The *D* pulse also disconnects the input of the ECU from the 0V rail, thereby switching the timing pulses back on. The inverted enable *Q* pulse is ANDed with the inverted disc timing pulses[34] to produce the Q-switch pulse, which is shown in Figure 37.

[34]Incidently, the new electronic control unit is capable of handling any number of timing pulses per revolution, but in practice, 60, 120 or 180 pulses are normally used.

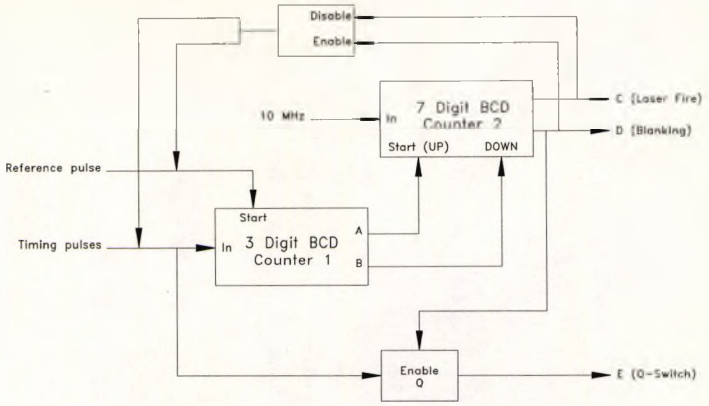


Figure 34: Diagram of modified ECU

3.2.1.1.2 Laser pulse transmission

The TTL pulses generated within the electronic control unit must be delivered to the laser, which is several meters away. The laser requires pulses in the voltage range 0-15V, rather than TTL, so the ECU pulses must be amplified. The previous system (section 3.1.1.2) used a DS3696 chip to convert the TTL pulses, and then transmit them via coaxial cables to the laser. The DS3696 is a relay driver chip, and is therefore unsuitable for high speed work. Also, the coupling signals between the ECU and laser require isolation in order to separate digital and analogue grounds. The latter no doubt added to the interference problems associated with the laser, and as a result it was decided to redesign the method of pulse delivery to the laser. It was not thought necessary to use optical fibre transmission, but a current loop rather than voltage loop was considered essential, as was optical isolation between the ECU and laser. A Hewlett-Packard 6N137 dual opto-isolator was selected because it was the highest speed device available at the time. The diodes of the device were placed in a current loop, as shown in Figure 38. This had the effect of reducing the influence of airborne interference on the signal.

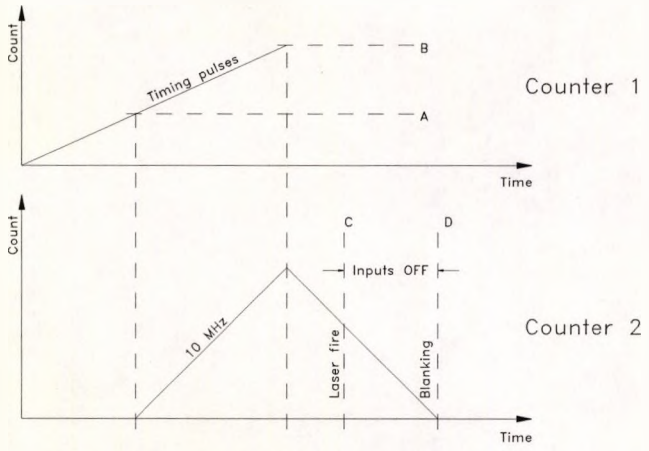


Figure 35: ECU counter profiles

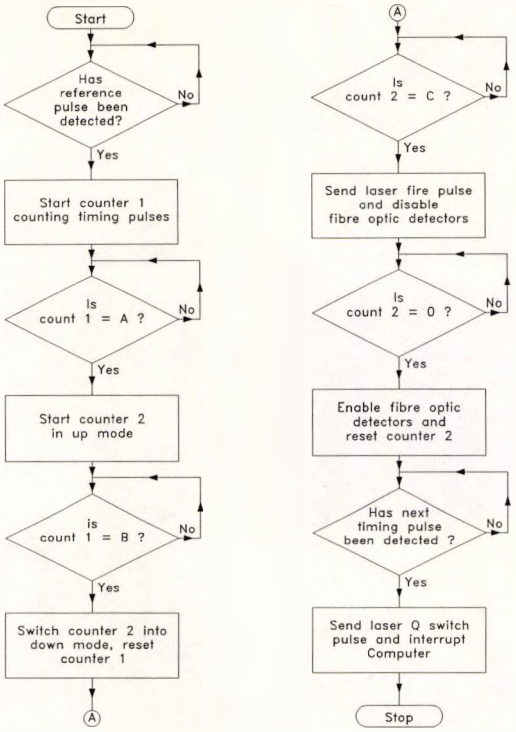


Figure 36: Modified ECU flowchart

3.2.1.1.3 Computer control

The introduction of a computer interface was appropriate, since the frame capture system was incorporated into the computer (section 3.2.1.4). Computer control was achieved by replacing the thumbwheel inputs of the ECU with programmable latches. This enabled a 'plug-in' replacement for the thumbwheels to be built. Each of the 13 thumbwheel switches[35] stores a 4 bit BCD number, and was replaced by a 74HCT173 (quad D-type latch). The chip select of each 74HCT173 is generated by a 74HCT154 (4 to 16 decoder), which is connected to the PC36AT board in the computer. A diagram of one of the 13 thumbwheel replacement circuits is shown in Figure 39. The 74HCT154 chip select and

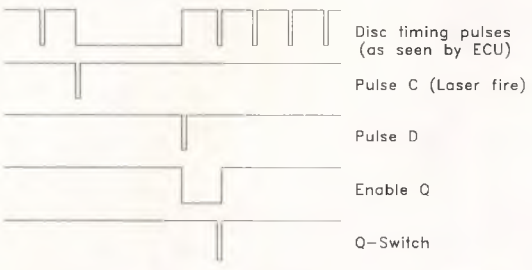


Figure 37: Enable pulse timing diagram

[35] 3 each for decoders *A* and *B*, and 7 for decoder *C*.

BCD address (Non Inverted)				Decoder output destination
A	B	C	D	
0	0	0	0	Initiate image acquire process
0	0	0	1	Unused (used on Vinten FS4)
0	0	1	0	Decoder A - Units
0	0	1	1	Decoder A - Tens
0	1	0	0	Decoder A - Hundreds
0	1	0	1	Decoder B - Units
0	1	1	0	Decoder B - Tens
0	1	1	1	Decoder B - Hundreds
1	0	0	0	Decoder C - 0.1μs
1	0	0	1	Decoder C - 1.0μs
1	0	1	0	Decoder C - 10μs
1	0	1	1	Decoder C - 100μs
1	1	0	0	Decoder C - 1ms
1	1	0	1	Decoder C - 10ms
1	1	0	1	Decoder C - 100ms
1	1	1	1	Unused

Table 1: ECU programming table

enable are held low, so the decoder is permanently decoding the address bus. The value of N in Figure 39 is between 2 and 14; function 0 is used to initiate the firing process (previously operated manually with a pushbutton). The programming table is shown in Table 1. The computer software compiles the address and data information. This information, together with the enable pulse are sent to the ECU via a 24 line I/O controller (Amplicon

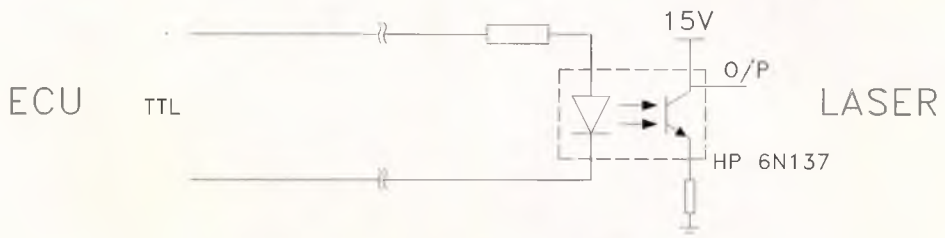


Figure 38: Laser pulse delivery

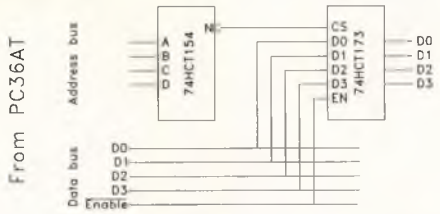


Figure 39: Computer interface

Liveline PC36AT) fitted in the computer. The *complete* table of data is sent prior to each fire operation because it was found that the electromagnetic interference sometimes corrupted the data in the latches. The data is sent in reverse logic[36] BCD, to remain compatible with the data format of the thumbwheel switches, which also uses this format. The computer software acquires the speckle image using the VS100 framestore (section 3.2.1.4). Complications caused by the operation of the framestore meant that hardware interrupts were needed to ensure the capture of the correct interlace (for an explanation of interrupts, see Tischer [1989]). The *D* pulse (section 3.2.1.1.1) was used to supply the interrupt. A flow chart of the operation of the computer software is given in Figure 40. The capture program is initiated by the operator pressing one of the keys on the computer keyboard. Once started, the registers of the ECU are programmed with the positional information (values *A*, *B* and *C*). A start instruction (function 0 from Table 1) is then issued, and external interrupts are enabled. When the ECU generates the interrupt, the program issues a modified snap instruction (section 3.2.1.4) to the VS100 (the modified snap instruction grabs the next *frame*, as opposed to *field*), and blanks the scanning beam of the camera. Maskable interrupts are disabled, so that the computer does not fail to detect the frame pulse whilst executing a secondary interrupt routine. The computer then executes a 'tight loop', each pass of which examines the registers of the VS100, in order to determine when the next *frame* pulse is generated (the moment at which the image will *start* to be digitized by the VS100). When this pulse is detected, the scanning beam is unblanked, interrupts are enabled, and the computer executes a loop waiting for an interrupt to be generated by the VS100, indicating the end of the first field. When the interrupt is received, the input gain of the VS100 is boosted (see section 3.2.1.4), and the operator is asked if the image should be stored[37]. A positive response will store the image under a unique name, on the designated file store device (usually the hard disk of the computer).

[36]For example: 9 is represented by 1001 in BCD, and 0110 in reverse logic BCD.

[37]The image is *still* being digitized at this point, but this operation is independent of the computer, and is completed in a few milliseconds.

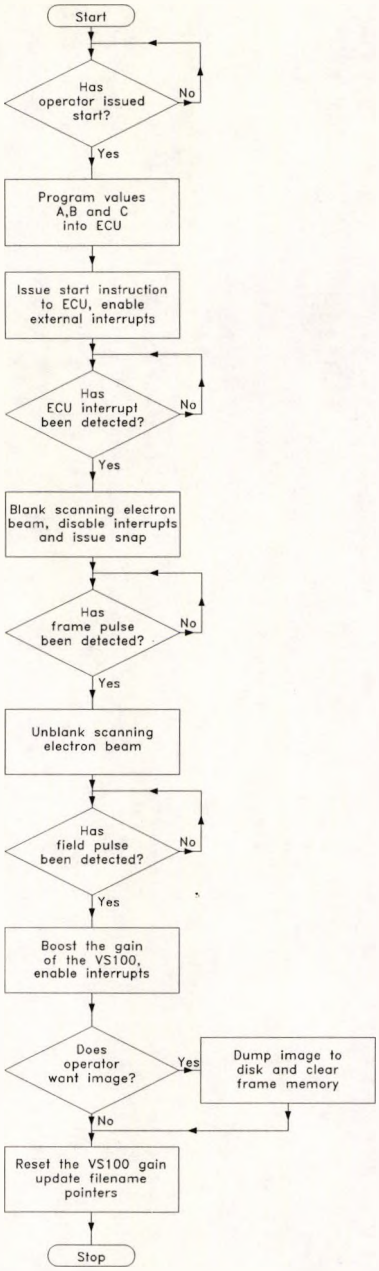


Figure 40: Image capture flowchart

3.2.1.2 Shaft encoder

The shaft encoder has been modified several times over the duration of this research project. Although the original encoder produced highly accurate pulses with well defined rising edges, it was not suitable for an industrial environment, since it required cutting slots in the perimeter of the specimen disc. Also, at higher drive speeds, the physical construction of the encoder produced inferior timing information from the rotating specimen. Therefore, several improved designs were tested, some of which are discussed.

The first modification concerned the method of signal transmission from the encoder to the electronic control system. In the previous system, this was accomplished by means of a voltage signal along coaxial cables (section 3.1.1.3). The large electromagnetic interference in the laboratory (likely to be even larger in an industrial environment), advocated the use of optical transmission. In an optical fibre, the enormous bandwidth results in almost no spreading of the optical signal, and total insulation from EI. The photodetectors and amplifiers were moved into the electronic control unit, resulting in a reduction of the physical distance travelled by the TTL pulses. Initially, the optical fibres were placed in the same position as the diode detector head, and the light from the HeNe lasers was launched into them. This system worked well for a period of time, but when the higher speed tests were performed, the vibrations of the rig caused the laser light to become decoupled from the fibres. The system was redesigned to compensate for this, and is shown diagrammatically in Figure 41, Figure 42 and photographically in Image 17. An etched, optically coded disc is mounted on the rear end of the motor shaft, through which laser beams are chopped, producing timing information. One advantage of this system is that the specimen no longer needs timing slots around the perimeter. The removal of the slots reduces the windage from the disc, and also simulates an actual spin test more realistically (obviously slots cannot be cut around the perimeter of an industrial test specimen). The two HeNe lasers are replaced with 3.5mW diode lasers, and are mounted into a single plastic holder. This holder also retains the focusing lenses and the terminated ends of the optical fibres. A section through plastic holder, showing one of the two launching systems is illustrated in Figure 42. The diode laser and lens are held rigidly in position within the holder by means of an interference fit and grub screw. The position of the fibre optic can be adjusted to optimise the output pulses, and is then locked firmly. Optimisation is performed by examining the direct output of the photodetectors prior to Schmitt triggering. The pulses are optimised for *minimum rise time* rather than *peak value* (the two do not necessarily coincide). Once the system is optimised, it becomes insensitive to vibrations, since the lasers, lenses and fibres all move together.

3.2.1.3 Camera blanking

Camera blanking was explained in section 3.1.1.4. The previous frame capture system (Vinten FS4 - section 3.1.1.5) provided interface signals which allowed a circuit to be constructed to blank the camera. The introduction of a new framestore resulted in the loss of these signals, hence a new scheme for camera blanking was needed. This was achieved by using one of the output lines of the PC36AT, connected to a voltage convertor circuit which changed the TTL signals into the range: 0 and -2.3V, which is the range necessary for use with the beam blank input of the Jackson Camera. The computer code written to grab the images has a built-in routine to generate the blanking pulse. As can be seen from

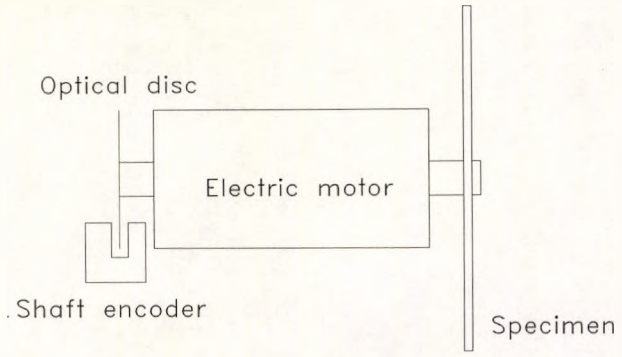


Figure 41: Modified shaft encoder

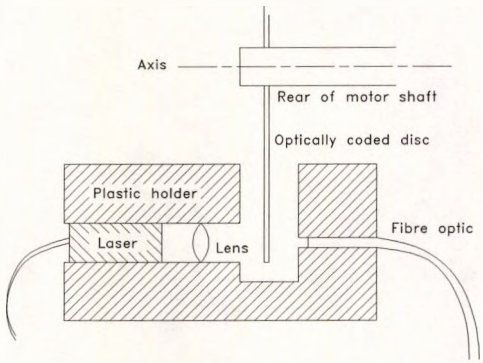


Figure 42: Modified encoder

Figure 40, the software blanks the beam *before* issuing the modified snap instruction (Appendix B, section B.4) to the VS100, and unblanks the beam on detection of the next *frame* pulse. Once issued, the modified snap instruction, which puts the framestore into acquire mode, does not require any further action from the host computer, which is free to wait for the *frame* pulse in a tight loop. Interrupts are disabled at this point, so the host computer does not fail to detect the frame pulse, since otherwise it could be called upon to service a *second* interrupt. The detection of the frame pulse occurs on the leading *edge*, but image digitization occurs on the trailing *edge*, which is almost 1ms later. Therefore, sufficient time is available for the unblanking operation.

3.2.1.4 Frame capture system

Since the frame capture system used on the previous design provided no obvious interface with a host computing system (section 3.1.1.5), it was decided to replace it with a computer based image processing unit. An Imaging Technology VS100 768/2 board was fitted to the PC (see Imaging Technology [1987]). The VS100 was chosen for several reasons, the most important of which was to allow software interchange with Rolls-Royce, who operate several

ITEX[38] based frame capture systems. The VS100 768/2 has 1 Mbyte of frame memory with 12 bits per pixel. The memory is organised into two pages, each with a standard resolution of 768x512 pixels when used with a CCIR compatible video source. Image digitization is to 8 bits (256 grey scales), the remaining 4 bits per pixel used for *image overlays*. The framestore has a variety of synchronisation methods, using either the internal PLL, or direct TTL master/slave. The PLL provides the easiest method of interface with a standard video source, since it strips the video synchronisation information from the signal, and locks to it. However, for highly accurate work, this is inadequate, since PLLs have a tendency to 'wander' around the signal, and in some cases, do not lock onto the signal for some time [Horowitz and Hill, 1980]. Direct drive provides a superior method of synchronisation, although in the case of the VS100, an additional problem arises. The VS100 is fitted with a *trigger* input, which allows a TTL pulse to force the framestore to execute a 'snap-on-frame' command[39]. However, when the VS100 is configured for *direct drive* synchronisation, the trigger input *cannot* be used. This means that the instruction to acquire the frame at the instant of pulsed laser Q-switching *must* come from the PC (software), and not the ECU (hardware). The consequence is that the PC must operate in *real time*, which is difficult, since the DOS operating system is constantly issuing interrupts to the CPU. Also, the snap instruction of the VS100 is a snap-on-*field* rather than a snap-on-*frame*.

Another problem encountered with both the Vinten frame capture system and the VS100 is the *intensity decay* of the odd interlace. When the laser illumination is generated, the scanning electron beam of the camera is switched off, and the system pauses until the start of the next *even* interlace before digitizing the image into memory. The odd interlace *always* suffers an additional 10ms delay before digitization begins, and therefore its average intensity is substantially lower than the even interlace[40]. This could be equalised by scanning the frame memory, and by multiplying the pixels on *odd* lines by a scaling factor until the average intensity of the two interlaces is similar. However, this approach does not yield additional information, since the processing occurs after A/D conversion. The solution was found using the input amplifier of the VS100. The image capture software holds *two* gain values, one for each interlace. Initially, the first gain value is programmed into the VS100. When image acquisition begins, the program waits until the next *field* pulse (the end of the acquisition of the even interlace), and instantly reprograms the input gain. This has the required matching

---

[38]ITEX is an image processing link library, optionally supplied by the manufacturer of the framestore. The library links into the Microsoft C compiler, and provides function calls to perform many commonly used image processing tasks.

[39]*Snap* is the ITEX function which causes the VS100 framestore to grab a single frame (both interlaces), and store it in the currently selected page.

[40]Typically, the average intensity of the odd interlace is 80% lower than the even interlace.

effect. When image acquisition is complete, the input gain is reset to its initial level (refer to Figure 40).

3.2.1.5 Data storage

Data storage is a problem when using a computer to acquire the speckle images. Typical Intel based computers come supplied with a 180MB hard disk drive, which is wholly inadequate for storing the output data from the interferometric system. One 512x512 image requires 256KB of disk storage, and a *single* fringe pattern requires two speckle patterns (768KB total). The two dimensional Fourier transform of a fringe pattern (explained in detail in section 4.2) requires 4MB of disk space, the inverse transform also requires 4MB of disk space. Once the wrapped phasemap is generated, the real/imaginary data of the Fourier transform can be deleted, as can the modulus part of the inverse transform, freeing 6MB of space. However, if the image is to be reanalysed, deletion of the real/imaginary data requires that the Fourier transform be recalculated. The unwrapped phasemap requires a 2MB data file, which allows the wrapped phasemap data to be deleted, leaving the overall disk space the same. In spite of the various file deletions during the analysis procedure, the various image and data files for a single fringe pattern occupy over 3MB of space. A compression routine was written to convert the double precision data files to single precision, freeing 1MB per fringe pattern. Therefore, a 180MB hard disk will only store the analysed data from 60 images, assuming no other programs are on the disk. Much larger hard disks are available, but can prove costly. Also, the relative unreliability of hard disks is sufficient to consider it irresponsible to place all valuable data on a single drive, which could easily be lost in a single incident. Therefore, a more intelligent data storage scheme was used. The computer was fitted with an Adaptec SCSI card, and a 44MB removable hard disk device was connected to the SCSI interface. A 250MB tape streamer was also coupled to the SCSI, providing a secure long term storage medium. The operation of both devices enables a sensible data storage regime to be implemented, providing both high speed access to data (on the 44MB cartridges) and secure long term archives (250MB tapes). One other very important point is that it is essential to keep track of data files on the disks and tapes, and to do this efficiently, a professional file tracking system (FTS) is required. The ARC/SOLO package was found to have one of the best FTS systems, and was used to archive all data.

3.2.2 Mechanical subsystem

3.2.2.1 Reduction of windage effects

It is found that the windage from the rotating specimen causes the optical table to vibrate at the high rotational speeds, because the end of the table was initially placed under the specimen disc. The table was moved away from the rotating specimen, and a baffle was

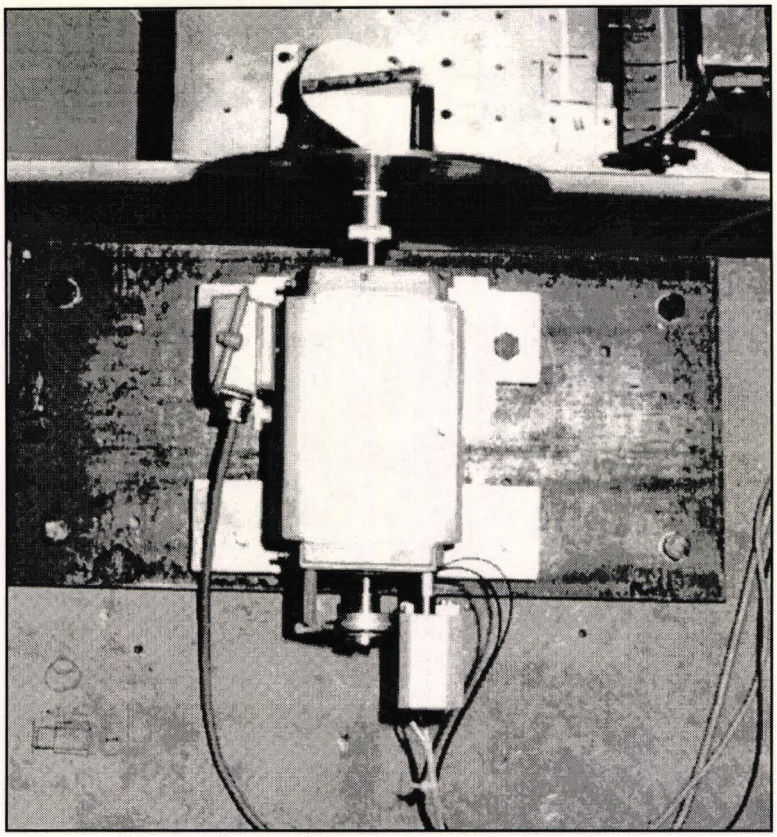


Image 17: Plan view of updated rig

positioned to direct the flow of air away from the surface of the table. This is shown diagrammatically in Figure 43, and photographically in Image 17. It should be noted that the baffle does not cover the face of the specimen, since this would block the surface to be measured. Also, the baffle does not extend to the floor, since this would prevent air from escaping below. A front view of the baffle that indicates direction of air flow is shown in Figure 44. The base of the air baffle is below the level of the support for the optical table. This means that the exhaust air is prevented from causing the optical table to vibrate. It was established that the introduction of the baffle improved the repeatability of the measurement system at the high rotational speeds (up to approximately 14,000rpm)[41]. Image 17 shows the current rig system. The HeNe lasers forming the shaft encoder have been removed, together with the fibre optic cables. The new shaft encoder can be seen on the lower edge of the image (at the rear of the electric motor).

3.2.2.2 Increased rigidity of optical mounts

The relative movement between the optical components is a common cause of problems with interferometric systems. The presence of an electric motor makes the requirement for *rigid*

[41] It is worth noting that in an industrial spin test facility, the operating environment is *evacuated*, so problems arising from windage vibration will not occur.

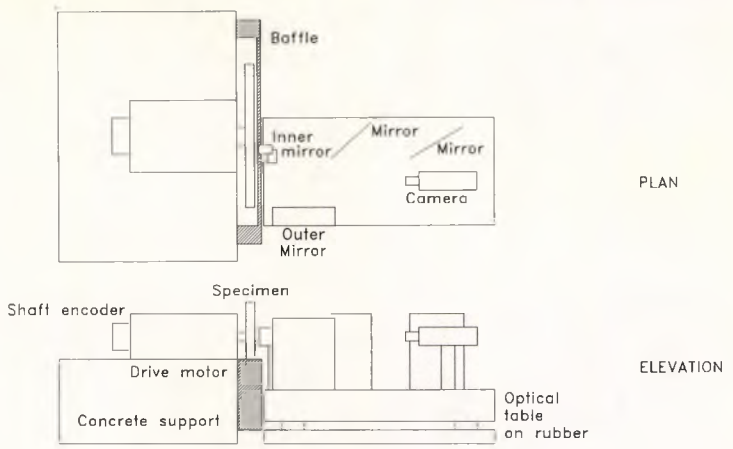


Figure 43: Rig with air baffle

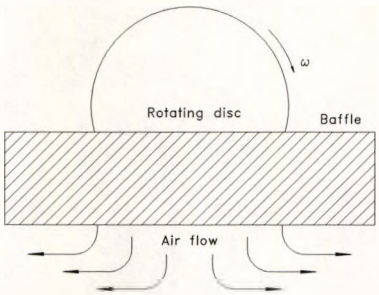


Figure 44: Air baffle

optical mounts essential, since the large vibration amplitudes of the drive system cause corresponding vibrations in the immediate environment. To reduce the movement of the optical components, it was proposed to sacrifice adjustability of the components in favour of rigidity. The inner mirror translation, rotation and tilt mounts were replaced by a *solid* mount, with no means of adjustability (all the various adjustments could be achieved in other ways). The outer mirror was modified, so that once it was in position, it could be locked by 4 tie bars to the optical table. Image 18 shows a front view photograph of the current cylindrical mirror system. The solid mountings of the inner and outer mirrors can be seen.

3.2.3 Optical subsystem

The basic modification to the optical subsystem is the insertion of two plane mirrors in advance of the beam incidence on the twin cylindrical mirror system. This is shown in Figure 45. The inner mirror *overhangs* the optical table to allow air to flow through the space between the table, and the support for the drive system. The pulsed laser is no longer directed straight onto the outer cylindrical mirror, but instead is first reflected from the plane

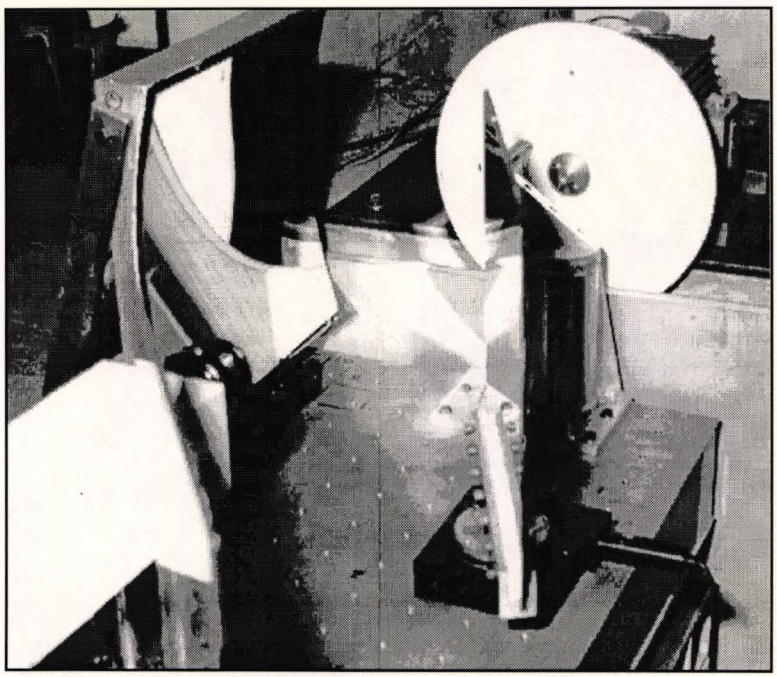


Image 18: Front view of test specimen

mirrors prior to incidence on the cylindrical mirror system[42]. The second plane mirror (tilt mirror), is mounted on a high resolution rotatory stage which is driven by a DC motor. The motor is under computer control, and can be driven in both directions. The tilt mirror is used to add carrier fringes in preference to the inner mirror. Tilting the plane mirror preserves the geometry of the twin cylindrical mirror system, and generates carrier fringes with the correct radius of curvature, as explained in section 3.1.3.2.

3.2.3.1 Alignment with the pulsed laser

The alignment method used by Preater suffered from one major drawback. To align the pulsed laser with the rest of the speckle interferometer, an alignment system had to be placed in front of the exit aperture of the pulsed laser and itself aligned, as shown in Figure 31. It then had to be removed before the results of realignment could be established (because it blocked off the pulsed laser beam). A system was required which could be used without interfering with the pulsed beam, and which needed to be aligned once only. Therefore, a HeNe laser was mounted in an adjustable holder and fitted to the rear of the pulsed laser on the amplifier cavity side, as shown in Figure 46. The HeNe beam passes through the *semi-reflecting* mirror, and along the amplifier cavity, through the amplifier ruby rod, and out of the exit aperture. The HeNe laser is rotated in its holder to produce *maximum* intensity at the output

[42]In fact, the first plane mirror has no effect on the optical system, and is only included so that the laser equipment can be located conveniently in the laboratory.

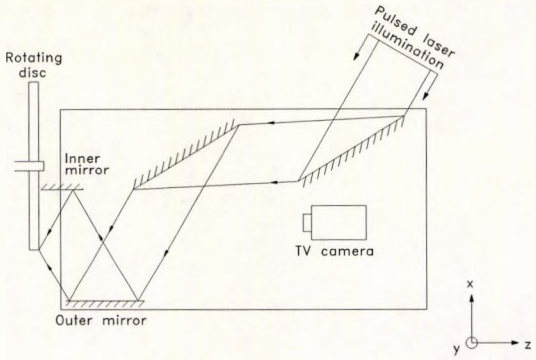


Figure 45: New optical delivery

aperture[43]. Initially, the HeNe beam is aligned so that it passes at a distance of 50mm from the base of the chassis, and 50mm from the side (the manufacturer's specification for the position of the pulsed beam). Then, more accurate alignment of the pulsed and HeNe beams is performed, by means of burn paper, using an iterative process, with a target placed close to, and far from the exit aperture. Once the two beams are sufficiently well aligned, the HeNe beam is used to align the remaining optical components of the speckle interferometer. A hinge with a central hole is fitted to the exit aperture of the laser. A piece of burn paper is placed over the hole and the pulsed laser is fired, with the power reduced, such that it barely marks the paper. Using a pin, a small hole is made in the centre of the burn. The HeNe alignment beam passes through the small hole forming a spot that can be used for alignment. The first task in the alignment procedure is to ensure that the periscope mirrors (see Figure 29 on Page 55) are positioned correctly. This is achieved by placing a plane mirror marked with a small spot at the height of the axis of the rotating component, onto the optical table. The face of the mirror is at a right angle to the surface of the optical table, which is levelled using a spirit level. By removing the diverging lens and arranging the alignment beam to be at normal incidence to the alignment mirror, a spot is seen on the front face of the pulsed laser. By

A	B	Description
0	0	Disabled (forward)
0	1	Disabled (reverse)
1	0	Enabled (forward)
1	1	Enabled (reverse)

Table 2: Tilt motor programming table

[43]This is because the cavity of the laser is polarisation sensitive.

altering the height of the *lower* periscope mirror and the angle of *both* mirrors, the laser spot on the alignment mirror can be arranged to coincide with the mark on the mirror, and the spot on the front face of the laser can be made to coincide with the emergent beam. When this condition is realised, the periscope is *correctly* aligned, and the remainder of the speckle interferometer can then be aligned. The centre of the inner mirror is aligned with the axis of the disc by adjusting the *height* of the optical table. Once this is correct, the table is shifted, such that the plane of the specimen is perpendicular to the plane of the surface of the table (with the table level). This is achieved using a square and spirit level. The outer cylindrical mirror is positioned so that the reflective surface is 254mm from the axis of the disc (the mirror has a radius of curvature of 508mm). This mirror can be tilted in the *xy* and *yz* planes by micrometer adjustments[44]. The tilt in the *yz* plane is adjusted to zero, again using the spirit level. To adjust the tilt in the *xy* plane, the HeNe alignment laser is used. The diverging lens at the exit aperture of the laser is replaced in position, and the hinge across the aperture is opened. This allows the full HeNe alignment beam to diverge and to be viewed on the stationary specimen. A circular stop is placed close to the diverging lens, on the exit side, such that only off-axis rays are allowed to pass. The outer cylindrical mirror can then be tilted in the *xy* plane until the focus of the outer rays is coincident with the axis of the specimen (refer to section 6.1.1 for more information). The distance between the mirror and the axis must be rechecked after this is performed, before the outer mirror is locked in position. The inner mirror is then replaced and adjusted, such that the front face is 52mm from the axis (52mm is the radius of curvature of the mirror). The inner mirror is mounted on a rigid base with no adjustment facility. The base has slots for the locking bolts, and can therefore be moved in the *x* direction only. The remainder of the alignment procedure simply ensures that the centre of the illumination beam arrives at the extrapolated intersection of the inner mirror, the horizontal radius of the specimen, and the specimen surface. This is achieved by removing the diverging lens, and closing the hinge across the exit aperture of the laser. The vertical position of the spot should be in the appropriate location if the alignment procedure is performed correctly. The horizontal position is adjusted by rotating either of the plane mirrors mounted on the optical table in the *xz* plane.

3.2.3.2 Correct addition of carrier fringes

It was indicated earlier that the method of tilt used in the early system led to errors in the *shape* of the carrier fringes (section 3.1.3.2). It was established that the destruction of the geometry of the twin cylindrical mirror system was to blame, as shown in Figure 32. To overcome this problem, a plane mirror, mounted on a high resolution rotary stage (Newport

[44] *xy* is the plane of the specimen.

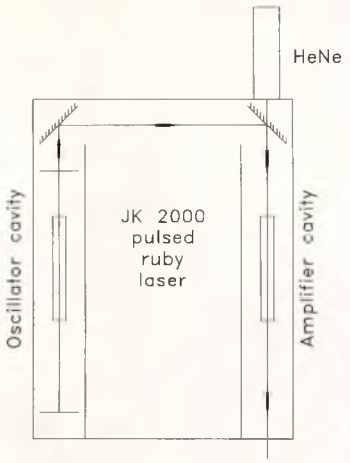


Figure 46: Pulsed laser alignment

M471), driven by a DC drive motor (Newport 860A), was incorporated into the interferometer. The plane mirror was mounted vertically on the rotary stage, as shown in Figure 47. This stage was incorporated into the interferometer as shown in Figure 45. The tilting of the plane mirror results in a tilt of the wavefront in the *xy* direction, the height of the beam remaining constant. The DC motor was used because it was considerably cheaper than a precision stepped drive. Two of the I/O lines of the PC36AT card in the PC are used to drive the DC motor. The lines control the direction[45] and power of the motor. Table 2 is the programming table for the drive motor. The improvement to the shape of the carrier fringes can be seen in Figure 32.

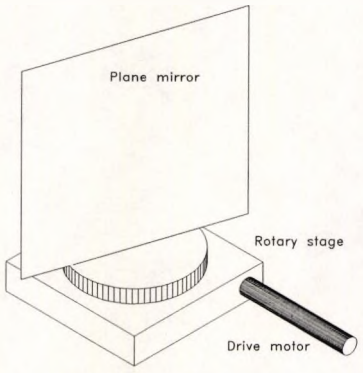


Figure 47: Tilt mirror mounting

[45]Controlled with a relay which reverses the polarity of the supply lines.

4 FRINGE PATTERN ANALYSIS

4.0 Fringe analysis

Fringe analysis is the interpretation of the fringe patterns generated by interferometric measurements. The result of an interferometric measurement is often a complex fringe field, contaminated by a large amount of noise. Computer algorithms have been devised to present the output data in a variety of formats which are easy to interpret. These algorithms are usually designed to be immune to noise contamination and to be operable by the non-specialist. A typical fringe analysis system comprises three main elements: (a) a detector which forms the interface between the interferometer and analyser, (b) an image acquisition system (framestore) and (c) a processor (normally a host computer). The detector is often a CCD or tube camera. The image acquisition system is basically a two-dimensional sampler, which converts the analogue video signal of the detector into binary numbers, to be analysed by the processor.

Equation [50] is a re-write of Equation [6] on Page 6, which is the basic equation for two beam interferometry, where the vector $\vec{r}$ represents the spatial coordinates (x,y).

$$I(\vec{r}) = A(\vec{r}) + B(\vec{r})\cos[\phi(\vec{r})] \qquad [50]$$

The intensity is the only data available from the detector, but as is clear, there are three unknown parameters, therefore the equation has no analytical solution. The basis of fringe analysis is to extract the phase information from the cosine function of Equation [50]. Many fringe analysis schemes have been devised for different types of application, as presented in Figure 48. Table 3 on Page 82 is a summary of features for the different fringe processing techniques in common use.

4.1 Overview of fringe analysis techniques

Several reviews of automated fringe analysis have been published, those found to be useful were Creath [1986], Reid [1986], Kreis [1987a], Kreis [1992] and Sirkis *et al.* [1992]. An earlier reference [Fienup, 1982] compares the extraction of phase information from intensity data, with the use of gradient search methods. Robinson [1987] details some of the developments in holographic and speckle interferometry in the UK, and includes a section describing the status of data analysis techniques up to 1987. Another recommended article

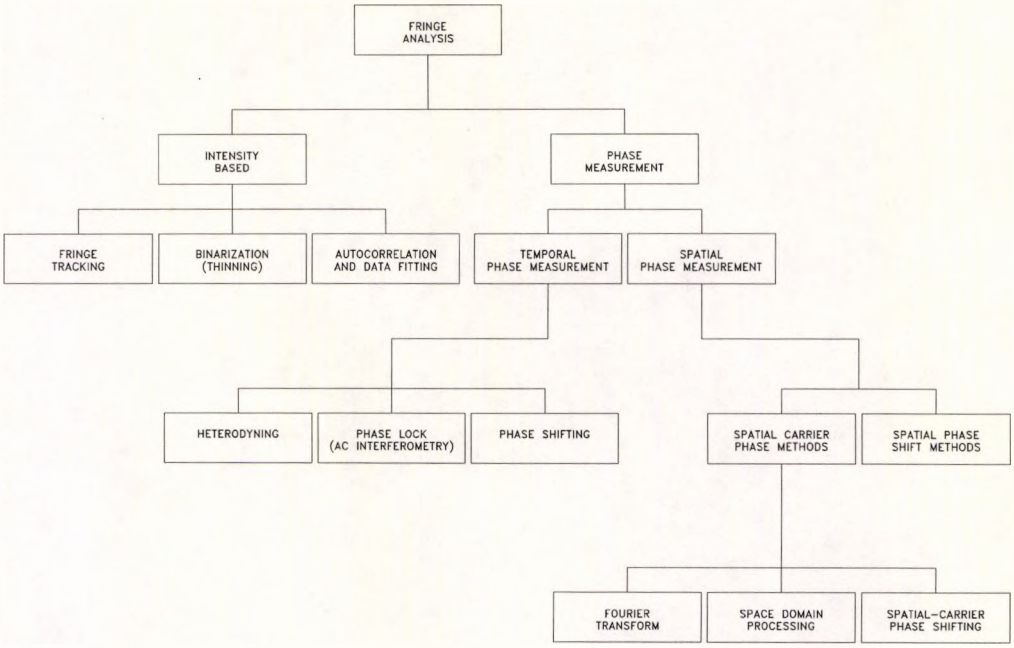


Figure 48: Fringe analysis techniques

that discusses phase measurement interferometry is Creath [1988]. Schwider [1990] takes the reader through the various advanced fringe evaluation techniques, describing some applications of each.

4.1.1 Intensity based analysis

In intensity based analysis, the phase information of the fringe pattern is normally found by searching the image for positions of a certain intensity, normally selected as points of *maximum* or *minimum* intensity. Although Robinson [1983] has developed several interesting applications of intensity based fringe analysis, a more commonly used method is *fringe tracking* [Reid, 1986]. In fringe tracking [Funnell, 1981; Becker and Yu, 1985; Button *et al.*, 1985], enhancement of the image is normally performed *prior* to analysis. Once enhanced, the general technique involves detecting *and following* intensity maxima (or minima) and then *skeletonizing* the pattern. Some of the more common problems encountered with fringe tracking are considered by Hunter and Collins [1989]. Binarization and thinning work by applying a running binary threshold or using an erosion thinning routine to narrow the fringes. Once thinned, fringe connectivity and numbering is carried out, followed by polynomial fitting [Kujawińska, 1992b]. Kujawińska [1992b] explains that the autocorrelation and data fitting techniques operate by matching a least-square curve or using non-linear regression to estimate the fringe function, based upon initial estimates for the coefficients. These routines

are less sensitive to noise, but are computationally expensive. All the intensity based methods suffer from large inaccuracies when the images are contaminated by noise, and do not solve the sign ambiguity problem associated with interferometers [Reid, 1986].

4.1.2 Phase measurement

Phase measurement methods [Creath, 1988; Takeda, 1990] operate by making a *direct* measurement of the *optical path difference* between two interfering wavefronts, at points covering the interference pattern. It is necessary for the fringe pattern to be modified for this to occur, which can be done in various ways, for example, a mirror can be tilted, or a polariser rotated. The modified fringe patterns can be recorded sequentially (Temporal phase measurement) or simultaneously (Spatial phase measurement).

4.1.2.1 Temporal phase measurement

By far the most accurate phase measurement technique is *heterodyne interferometry* [Massie *et al.*, 1979; Massie, 1980; Reid, 1986]. Heterodyne interferometry is an electro-optic method with an accuracy of up to *one thousandth* of a fringe. The wavelength of the reference beam is electronically altered with respect to the object beam, using a Bragg cell or acousto-optic modulator. Mathematically, Equation [50] is modified and becomes:

$$i(\vec{r},t) = A(\vec{r}) + B(\vec{r})\cos[\phi(\vec{r}) + 2\pi\delta v\, t] \qquad [51]$$

where δv is the frequency shift between the interfering beams. Upon recombination in the image plane, a beat frequency occurs between the beams, with a phase equal to the phase difference of the interfering beams. If the fringe field is subsequently scanned with a square law detector, the required phase difference is extracted (see Figure 49 taken from Kujawińska [1992b]). The phase of a whole image is then generated by scanning the detector across the interference field, and measuring the phase relative to a reference. Heterodyne techniques can

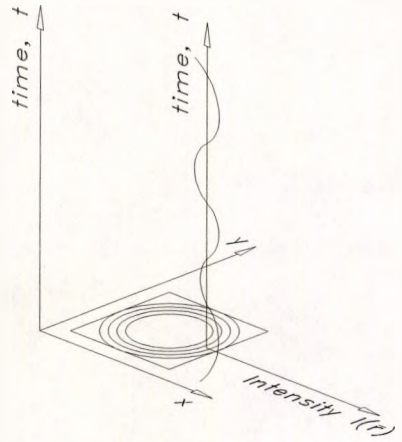


Figure 49: Heterodyne method

be applied to any kind of interferometry, for example dual reference beam holographic interferometry [Dändliker and Thalmann, 1985]. However, the technique has several drawbacks, primarily the need for extreme experimental conditions (such as rigorous vibration isolation), a slow processing time, and sophisticated electronics [Kwon, 1987].

The *Phase lock* method requires the optical signal to be detected and processed by frequency multipliers and up/down counters [Johnson *et al.*, 1979]. A phase modulator is placed in one arm of the interferometer, and is excited sinusoidally, with an amplitude of less than $\lambda/2$. A detector is scanned across the fringe pattern, and a complicated analysis process, using information about the scan position, the amplitude of the excitation, and the gain of the system, allows the two-dimensional unwrapped phase to be determined. It is claimed that the system has a phase resolution of $\lambda/100$, and requires optics of lower optical quality than those normally utilized in interferometry.

Temporal Phase shifting is often referred to as *quasi-heterodyne interferometry* [Brunning *et al.*, 1974; Creath, 1988] since it requires the successive recording of interference fringe patterns[46], as shown in Figure 50 [Kujawińska, 1992b]. It may be applied to any interferometer which can adjust the phase of one of the interfering wavefronts [Dändliker and Thalmann, 1985; Robinson and Williams, 1986; Kerr and Tyrer, 1987]. Temporal phase shifting modifies Equation [50] in a similar way to heterodyning:

$$I(\bar{r}) = A(\bar{r}) + B(\bar{r})\cos\left[\phi(\bar{r}) + \frac{2\pi k}{N}\right] \qquad k=1,\ldots,N \quad N>3 \qquad [52]$$

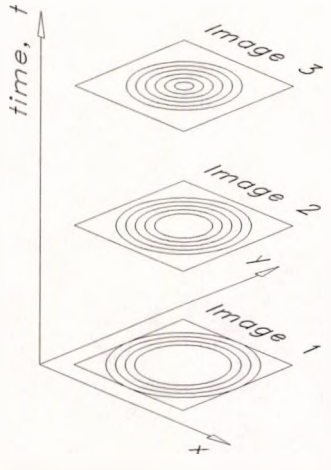


Figure 50: Temporal phase shift method

[46]Phase shifting is basically the discrete version of heterodyning.

Since the equation has three unknown parameters, then three phase stepped images are required to determine the unknowns. The stepping of the reference beam is normally achieved using a mirror mounted on a piezoelectric translator (PZT). The phase steps are normally equal, but Greivenkamp [1984] obtained accurate results with arbitrary phase steps. The equal phase step implementation generally involves recording three interferograms, each with the reference phase shifted by $2\pi/3$. Techniques have been developed where more than three interferograms are recorded [Creath, 1985; Nakadate and Saito, 1985]. These techniques result in greater phase accuracy at the expense of computational effort. Kerr *et al.* [1989] describe a technique which requires only two phase steps. The same group also describe a technique which requires only a single phase step [Santoyo *et al.*, 1988].

An elegant solution to the problem of object instability whilst recording the interferograms in phase shifting interferometry is described by Vikhagen [1990]. The *scanning phase shift algorithm* allows the specimen under examination to *drift slowly* during the acquisition of between 10 and 20 images. A simple routine computes for each pixel the maximum and minimum values. When the drift has undergone a complete 2π cycle, the phase angle of all valid pixels can be calculated. The accuracy of phase shifting interferometry has been investigated by several authors, those found most useful are Kinnstaetter *et al.* [1988], Brophy *et al.* [1990] and Creath [1991].

Kujawińska [1992b] notes that these methods of phase extraction are less vulnerable to stationary noise, have the ability to define the interferogram boundary, and solve the sign ambiguity problem. They have a typical accuracy in the range of 100^{-1} - 1000^{-1} of a fringe, and are relatively easy to apply. However, they cannot analyse dynamic events, and are very sensitive to phase shifting errors.

4.1.2.2 Spatial phase measurement

Spatial phase measurement methods record simultaneously all the information necessary to produce a phasemap from the interferogram. The phase can be retrieved from a single fringe pattern with a spatial carrier (spatial carrier phase measurement), or from three (or four) phase shifted interferograms, separated in space (spatial phase shift method).

The *spatial phase shift method*, illustrated in Figure 51, is described by Smythe and Moore [1984] and Kwon and Shough [1985], and has been employed in holographic interferometry by Kujawińska and Robinson [1988]. In this example, three *spatially separate* wavefronts are produced by placing a diffraction grating in the path of the object wavefront. The diffraction orders (0 and ± 1) interfere simultaneously with the reference beam. The

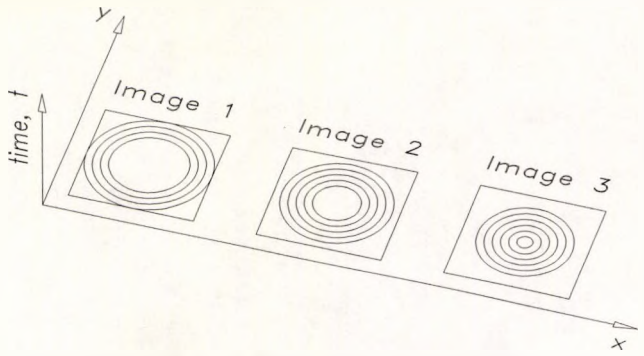


Figure 51: Spatial phase shift method

phase shifts are generated by shifting the diffraction grating. A similar technique was used with ESPI fringes, and is presented by Kujawińska *et al.* [1989a]. The technique has two major disadvantages: the first is the problem of alignment. Three spatially separate wavefronts must be aligned with three cameras to subpixel accuracy (or three separate regions of the same camera's photosensitive surface). Additionally, the *quality* of the wavefronts is relatively low in comparison to other interferometric techniques, therefore, high quality imaging optics are required.

Spatial carrier phase methods operate by introducing a tilt or carrier frequency into the fringe field, and encoding the phase information into the carrier. The modulation of the carrier (which is often the deviation of the fringes from linear and equally spaced) can be removed by analysis of the pattern in the spatial domain [Womack, 1984], frequency domain [Takeda *et al.*, 1981] or a combination of both [Shough *et al.*, 1990].

The *Fourier transform* method of fringe analysis is one frequency domain approach to the extraction of the phase data from a spatial carrier image. However, this method of analysis was also used to extract the phase data from the speckle correlation fringes described in this thesis, and is treated in greater depth in section 4.2. A close relative of the Fourier transform method, using the one-dimensional Hilbert transform, is presented by Zweig and Hufnagel [1990]. It is claimed that this technique is highly accurate, and computationally efficient. A simplified version of the Fourier transform method is described by Macy [1983]. Macy fits three adjacent points in the image to the first three terms of the Fourier series. Computation of the Fourier coefficients enables the phase value at that point to be extracted. Mertz [1983] measures the phase in a similar way, using three adjacent data points, and applies a complex convolution filter to the time domain data, electronically, in real time.

Womack [1984] considers three different methods of phase extraction by spatially processing a fringe pattern with tilt. The *Quadrature Multiplicative Moiré*, *Sinusoidal Window* and *Complex Exponential Window* algorithms operate by separating the information of interest in the *frequency* domain, and *convolving* with a digital filter in the spatial domain. The type of digital filter, and the way it is used allows the three methods to be classified as double-sideband low-pass, double-sideband high-pass and single-sideband high-pass respectively. Womack points out that the application of a digital filter tends to give rise to errors in the recovered phase, especially near the edges of the fringe pattern.

Shough *et al.* [1990] describe a technique which is similar in many respects to the procedure described by Ichioka and Inuiya [1972]. *Carrier frequency phase shifting* can be thought of as a combination of the Fourier transform and the phase shifting algorithms. The application of a large amount of tilt, providing a spatial carrier frequency, allows the phase at all the detector points to be computed in real time, by taking the differences between three sequential pixels, and calculating the arctangent. This technique can be applied to dynamic phenomena, and employs the principal advantages of both phase shifting and Fourier transform analysis.

	Number of fringe patterns per frame	Real time method	Inherent image enhancing	Inherent phase inter-polation	Sign detection (auto)	Domain detection (auto)	Accuracy achievable	Experi-mental requirement	Detector resolution required	Complexity of processing	Dynamic event analysis
Intensity methods	1/1	NO	NO	NO	NO	NO	LOW	LOW	R_o[a]	MEDIUM	NO
Heterodyne methods	SINGLE DETECTOR[b]	NO	NO	YES	YES	YES	VERY HIGH	HIGH	SINGLE DETECTOR	HARD-WARE	NO
Phase shifting ● **Temporal**	min 3/3	PARTLY	YES	YES	YES	YES	HIGH	HIGH	R_o	LOW	NO
● **Spatial**	3/1	YES	PARTLY	YES	YES	YES	LOW	MEDIUM	$3R_o$	LOW	YES
Fourier transform method	1/1	PARTLY	YES	YES	YES	PARTLY	HIGH	LOW	min $2R_o$	HIGH	YES
Carrier frequency phase shifting method	1/1	YES	YES	YES	YES	YES	HIGH	LOW	min $2R_o$	LOW	YES

Table 3: Comparison of fringe pattern analysis methods (Kujawińska [1992a])

[a] - R_o is the detector resolution required for fringe pattern detection.

[b] - The possibility of using an image dissector camera is not considered here.

4.2 Fourier transform fringe analysis

The Fourier transform is one of the most widely used transforms in the science of image processing. Some other transforms that exist are the Walsh, Hadamard, Hartley, Discrete Cosine and Hotelling. To begin the introduction to Fourier transform fringe analysis, a discussion of the one-dimensional continuous Fourier transform is presented.

The Fourier transform represents a mapping from one *domain* to another. Essentially, the Fourier transform generates an additional representation of the function under consideration. To move back and forth between the domains, the forward Fourier transform and inverse Fourier transform equations are used. In the context of fringe analysis, the Fourier transform is simply an efficient computational tool for accomplishing certain manipulations of data, since the same result could be generated in the spatial domain[47].

Let $f(x)$ be a continuous function of a real variable x. The Fourier transform of $f(x)$ is denoted by $\mathcal{F}\{f(x)\}$ and is defined by the equation:

$$\mathcal{F}\{f(x)\} = F(u) = \int_{-\infty}^{+\infty} f(x) e^{-2\pi i x u} dx \qquad i = \sqrt{-1} \qquad [53]$$

The inverse Fourier transform can regenerate $f(x)$ from $F(u)$:

$$\mathcal{F}^{-1}\{F(u)\} = f(x) = \int_{-\infty}^{+\infty} F(u)\, e^{2\pi i u x} du \qquad [54]$$

Although $f(x)$ is defined as real, the Fourier transform of $f(x)$ will generally be complex:

$$F(u) = R(u) + i\, I(u) \qquad [55]$$

where $R(u)$ and $I(u)$ are the real and imaginary parts respectively. Equation [55] can be expressed as shown in Equation [56]:

$$F(u) = |F(u)| e^{i\phi(u)} \qquad [56]$$

where

$$|F(u)| = \sqrt{R^2(u) + I^2(u)} \qquad \phi(u) = \tan^{-1}\left[\frac{I(u)}{R(u)}\right] \qquad [57]$$

The magnitude function $|F(u)|$ is called the Fourier spectrum of $f(x)$, and $\phi(u)$ is the phase angle. The square of the spectrum is often called the power spectrum or spectral density. The

[47] Computation in the spatial domain would increase *considerably* the processing power required.

variable u is referred to as the frequency variable. The Fourier transform is linear, so scaling is the same in both domains, and the transform of the sum of the functions is equal to the sum of the individual transforms:

$$\mathcal{F}\{h(x) + g(x)\} = \mathcal{F}\{h(x)\} + \mathcal{F}\{g(x)\}$$
$$\mathcal{F}\{ah(x)\} = aH(u) \qquad [58]$$

In the spatial domain, the function $h(x)$ may have several symmetries which can lead to relationships between $H(u)$ and $H(-u)$. Table 4 gives a summary of such relationships [Press *et al.*, 1988]. These symmetries can in many cases increase the efficiency of computational routines, and often reduce the amount of memory space necessary for data storage. The *first* entry in the table is employed in Fourier transform fringe analysis since the fringe data is *purely real* (it is taken from a frame capture system), and generally neither even nor odd. When $h(x)$ is real, the Fourier transform is a special type of complex sequence called *conjugate symmetric* or *Hermitian*. This means that for every point in the positive frequency space, a conjugate point exists in the negative frequency space that bears exactly the same information. Destruction of the Hermitian property by selective filtering in the Fourier transform domain allows the extraction of phase information from real data. Some further properties of the Fourier transform are now discussed.

If...	**then...**
$h(x)$ is purely real	$H(-u) = H^*(u)$
$h(x)$ is imaginary	$H(-u) = -H^*(u)$
$h(x)$ is even	$H(-u) = H(u)$ (even)
$h(x)$ is odd	$H(-u) = -H(u)$ (odd)
$h(x)$ is real and even	$H(u)$ is real and even
$h(x)$ is real and odd	$H(u)$ is imaginary and odd
$h(x)$ is imaginary and even	$H(u)$ is imaginary and even
$h(x)$ is imaginary and odd	$H(u)$ is real and odd

Table 4: Fourier transform symmetries

The symbol '⇔' is used to indicate transform pairs. If

$$h(x) \Leftrightarrow H(u) \qquad [59]$$

is a transform pair, then the following relationships exist:

'Spatial scaling' $$h(ax) \Leftrightarrow \frac{1}{|a|} H\left(\frac{u}{a}\right) \qquad [60]$$

'Frequency scaling' $$\frac{1}{|b|} h\left(\frac{x}{b}\right) \Leftrightarrow H(bu) \qquad [61]$$

'Spatial shifting' $$h(x-x_o) \Leftrightarrow H(u)\, e^{2\pi i u x_o} \qquad [62]$$

'Frequency shifting' $$h(x)\, e^{-2\pi i u_o x} \Leftrightarrow H(u-u_o) \qquad [63]$$

Consider two functions $h(x)$ and $g(x)$ and their corresponding Fourier transforms $H(u)$ and $G(u)$. The convolution of h and g, denoted by $g * h$ is defined by:

$$g * h \equiv \int_{-\infty}^{+\infty} g(\tau)\, h(x-\tau)\, d\tau \qquad [64]$$

It can be shown that the convolution of g and h ($g * h = h * g$) can be computed from the *convolution theorem*:

$$g * h \Leftrightarrow G(u)\, H(u) \qquad [65]$$

The Fourier transform of the convolution is the product of the individual Fourier transforms. The correlation of two functions, denoted as $Corr(g,h)$, is defined by:

$$Corr(g,h) \equiv \int_{-\infty}^{+\infty} g(\tau + x)\, h(\tau)\, d\tau \qquad [66]$$

It can be shown that the correlation of g and h (a function of x often referred to as the *lag*) can be computed from the *correlation theorem*:

$$Corr(g,h) \Leftrightarrow G(u)\, H(-u) \qquad [67]$$

If the two functions g and h are the same, the correlation becomes the autocorrelation. The autocorrelation of a function g can be computed from the *Wiener-Khinchin theorem*, so Equation [67] becomes:

$$Corr(g,g) \Leftrightarrow |G(u)|^2 \qquad [68]$$

Finally, the total power contained in a signal is the same, whether it is computed in the spatial or Fourier transform domain. This is known as *Parseval's theorem*:

$$Total\ Power \equiv \int_{-\infty}^{+\infty} |h(x)|^2 dx = \int_{-\infty}^{+\infty} |H(u)|^2 du \qquad [69]$$

4.2.1 The sampling process and the DFT

Sampled data signals are defined only at discrete instants in time, and arise whenever a *continuous* function is recorded *intermittently*[48]. It is impossible to import a continuous signal into a digital computer, therefore any input data must first be converted into a stream of numerical values (this process is referred to as *sampling*). In the majority of cases, the sampling instants are equally spaced, the time difference between successive samples being a measure of the *sampling frequency*. If the sampling frequency is too low, information about the detailed fluctuations of the continuous waveform will be lost; if it is too high, an unnecessarily large number of samples will have to be stored and processed. The required sampling rate is given by the 'sampling theory' or Nyquist rate [Bracewell, 1985], which states:

> "A continuous signal which contains no significant frequency components above f hertz may in principle be recovered from its sampled version, if the sampling interval is less than $1/2f$ seconds."

This is stated mathematically as follows:

> If a continuous function $h(x)$ is sampled at an interval of Δ and the function is bandlimited to frequencies smaller in magnitude than u_c (in other words $H(u) = 0$ for $|u| > u_c$), then the function $h(x)$ is completely determined by its samples h_n. The function $h(x)$ is given explicitly by the formula:

$$h(x) = \Delta \sum_{n=-\infty}^{+\infty} h_n \frac{\sin[2\pi u_c(x - n\Delta)]}{\pi(x - n\Delta)} \qquad [70]$$

Difficulties arise if the continuous function is *not* bandlimited to *less* than the Nyquist critical frequency. In this case, the spectral power which is outside the range $-u_c < u < u_c$ is spuriously

[48] Such signals have achieved greater popularity following the increased use of computers and digital electronics.

moved into that region. This is known as aliasing. Any frequency component outside the range $[-u_c,u_c]$ is falsely translated into that region by the very act of sampling [Bracewell, 1985; Press *et al.*, 1988]. The implications of sampling for Fourier transform fringe analysis are basically that the components of the carrier frequency resolved in the directions of the detector elements must be such that there are at least *two samples per fringe* in both directions. If this condition is not met, aliasing occurs. This point will be discussed in greater detail later in the chapter.

4.2.1.1 One-dimensional DFT

The *discrete* Fourier transform gives an *estimate* of the *continuous* Fourier transform for a given number of points. Suppose an array of real data has N consecutive sampled values:

$$h_k \equiv h(t_k) \qquad t_k \equiv k\Delta \qquad k=0,1,2,...,N-1 \qquad [71]$$

With N input numbers, only N output numbers can be evaluated, so it follows that the Fourier transform should be evaluated only at the discrete values:

$$u_n \equiv \frac{n}{N\Delta} \qquad n = -\frac{N}{2},...,\frac{N}{2} \qquad [72]$$

The extreme values of n correspond to the upper and lower limits of the Nyquist critical frequency. The Fourier transform integral is approximated by a discrete summation:

$$H(u_n) = \int_{-\infty}^{+\infty} h(x)\, e^{2\pi i u_n x} dx \approx \Delta \sum_{k=0}^{N-1} h_k e^{\frac{2\pi ikn}{N}} \qquad [73]$$

From Equation [73], the discrete Fourier transform of the N points h_k is:

$$H_n \equiv \sum_{k=0}^{N-1} h_k e^{\frac{2\pi ikn}{N}} \qquad [74]$$

The discrete Fourier transform maps the N complex numbers of the input sequence (the h_k's) to N complex numbers in the Fourier transform domain (the H_n's) and is independent of any dimensionless parameter, such as the time scale Δ. The one-dimensional discrete inverse Fourier transform is given by:

$$h_k = \frac{1}{N}\sum_{n=0}^{N-1} H_n e^{\frac{-2\pi ikn}{N}} \qquad [75]$$

Similarities between this equation and the forward Fourier transform equation indicate that with a slight modification to the input sequence, the same computer code can be used to

compute both the forward and inverse transforms. Often, all that is required is to invert the sign of the imaginary component of the complex sequence, transform, scale by N, and invert the output sequence.

4.2.1.2 Two-dimensional DFT

Many of the techniques used in one-dimensional analysis have a direct equivalent in two-dimensions. Assuming a square array of samples are to be transformed, the two-dimensional discrete Fourier transform pair is given by [Gonzalez and Wintz, 1987]:

$$F(u,v) = \frac{1}{N}\sum_{x=0}^{N-1}\sum_{y=0}^{N-1} f(x,y)e^{\left[\frac{2\pi i(ux+vy)}{N}\right]} \qquad [76]$$

for $u,v = 0,1,2,..,N-1$, and

$$f(x,y) = \frac{1}{N}\sum_{u=0}^{N-1}\sum_{v=0}^{N-1} F(u,v)e^{\left[\frac{-2\pi i(ux+vy)}{N}\right]} \qquad [77]$$

for $x,y = 0,1,2,..,N-1$. The discrete Fourier transform pair given in Equations [76] and [77] can be expressed as:

$$F(u,v) = \frac{1}{N}\sum_{x=0}^{N-1} e^{\left[\frac{2\pi iux}{N}\right]} \sum_{y=0}^{N-1} f(x,y)e^{\left[\frac{2\pi ivy}{N}\right]} \qquad [78]$$

for $u,v = 0,1,2,..,N-1$, and

$$f(x,y) = \frac{1}{N}\sum_{u=0}^{N-1} e^{\left[\frac{-2\pi iux}{N}\right]} \sum_{v=0}^{N-1} F(u,v)e^{\left[\frac{-2\pi ivy}{N}\right]} \qquad [79]$$

for $x,y = 0,1,2,..,N-1$. This property is called *separability*, the principle advantage of this property is that $F(u,v)$ or $f(x,y)$ can be obtained in two steps by successive application of the *one-dimensional* Fourier transform or its inverse. The two-dimensional function $F(x,v)$ is produced by taking a transform of each row of $f(x,y)$ and by multiplying the result by N. The desired function $F(u,v)$ is then generated by taking a transform along each column of $F(x,v)$[49]. Computation of the one-dimensional transform is simplified by using a *Fast Fourier Transform* (FFT) algorithm [Bracewell, 1985; Press *et al.*, 1988]. The FFT algorithm drastically reduces the number of floating point computations, by storing commonly used results. The algorithm has a greater impact as the size of the array to be transformed increases. Typical savings in computational effort for a one-dimensional FFT of length N are shown in Table 5

[49]The same result would be obtained if the transform order were reversed.

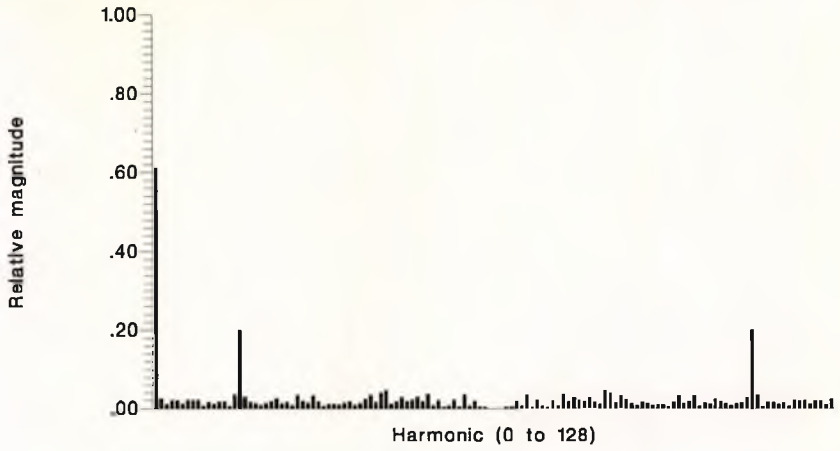
[Gonzalez and Wintz, 1987]. Since the one-dimensional FFT is also used for computation of the two-dimensional Fourier transform (applied to rows then columns, or visa-versa), an even greater impact is obtained from its usage.

4.2.1.3 Sequence reordering

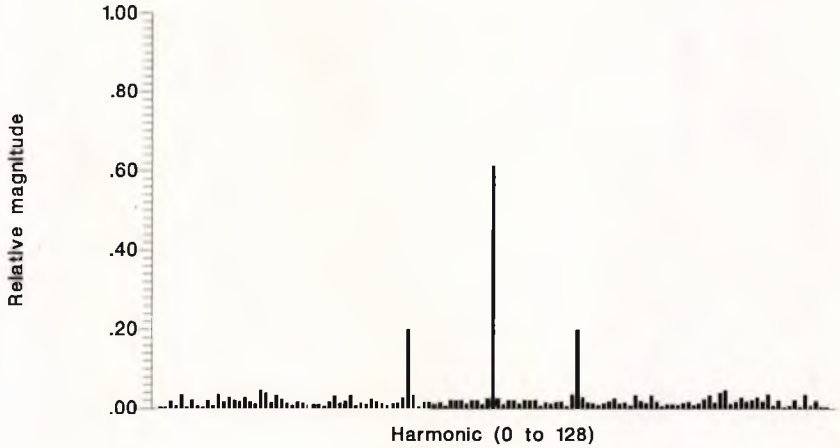
When the Fourier transform of a linear sequence of data is computed, the zero frequency falls on the first data point in the array. The array contains one period of the Fourier transform, but compared with conventional representations, it is shifted by $N/2$ (N is the length of the array). In order to design filters in the Fourier domain, it is useful to display the magnitude of the Fourier transform with the zero frequency in the centre of the array (shift the origin by $N/2$), since the spectrum is then easier to visualise. Consider the one-dimensional example shown in Graph 3. The top diagram shows a typical result of a 128 point Fourier transform of a sequence of data, the reordered sequence is shown in Graph 4. The transformation of the origin is easily accomplished by the multiplication of the data $f(x)$ prior to transformation by $(-1)^x$. For a two-dimensional sequence, the function $f(x,y)$ is multiplied by $(-1)^{x+y}$ [Gonzalez and Wintz, 1987]. The origin shift does not affect the magnitude of the Fourier transform.

N	N^2 (Direct FT)	$N\log_2 N$ (FFT)	Computational Advantage
2	4	2	2.00
4	16	8	2.00
8	64	24	2.67
16	256	64	4.00
32	1,024	160	6.40
64	4,096	384	10.67
128	16,384	896	18.29
256	65,536	2,048	32.00
512	262,144	4,608	56.89
1,024	1,048,576	10,240	102.40
2,048	4,194,304	22,528	186.18
4,096	16,777,216	49,152	341.33
8,192	67,108,864	106,496	630.15

Table 5: Computational advantage of using the FFT



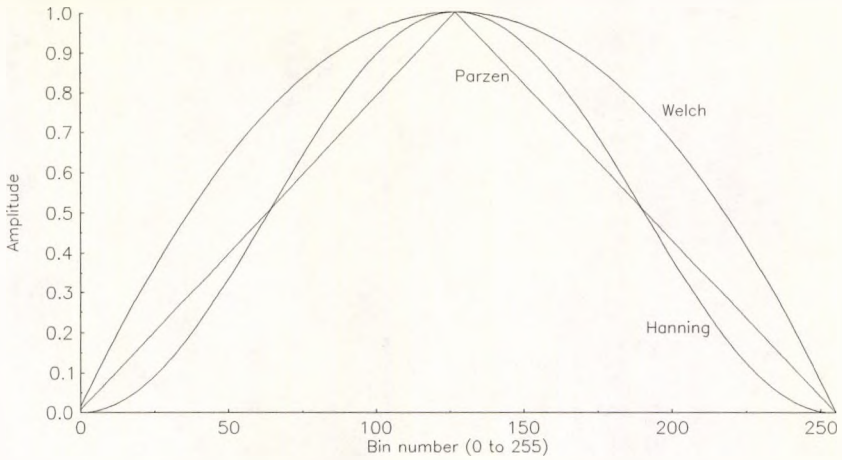
Graph 3: Reordering a sequence (before)



Graph 4: Reordering a sequence (after)

4.2.1.4 Windowing in the spatial domain

The application of a window in the spatial domain is often referred to as *data weighting*. A weighting window is applied to the *spatial* domain because the Fourier transform is a *periodic* transformation. The one or two-dimensional section under consideration is simply *one period* of an infinite sequence of data [Bracewell, 1985]. The two-dimensional case is shown diagrammatically in Figure 52, with the hatched region at the centre of the figure representing the array under consideration (the 512x512 image or similar). The Fourier transform perceives this as replicating infinitely in all directions, so the array represents a single 'tile' in an infinite grid. In other words, the tile on the right of the array is a replication of the array itself, and therefore the *left* side of the array must equal the *right* side for there to be no edge mismatch. Similarly, the *upper edge* of the array must equal the *lower edge*. It is not sufficient simply



Graph 5: One dimensional data weighting functions

to copy the edge values, since this would result in errors occurring further inside the array when transformation takes place. The normal technique which is used to make the array periodic is to multiply the data by a *windowing function*, which gradually reduces the values to zero towards the edges. Once the values at the perimeter are zero, no mismatch occurs and the Fourier transform is then considered to be a single period. Some one-dimensional data weighting functions are shown in Graph 5.

A *rectangular* window (no window) has the value 1 for all bin numbers. The triangular shaped window is called a 'Parzen window' with the definition[50]:

$$W_k = 1 - \left| \frac{k - 0.5(N-1)}{0.5(N+1)} \right| \qquad [80]$$

where N is the length of the array (in this case 255) and k is an integer $0 \leq k \leq 255$. The steeper window with rounded ends at the bottom is called a 'Hanning window' with the definition:

$$W_k = \frac{1}{2}\left[1 - \cos\left(\frac{2\pi k}{N-1}\right)\right] \qquad [81]$$

The 'Hamming window' is similar to the Hanning, but does not reach zero at the array ends. The third window from Graph 5 is the 'Welch window' with the definition:

$$W_k = 1 - \left(\frac{k - 0.5(N-1)}{0.5(N+1)}\right)^2 \qquad [82]$$

The applied window will modify the Fourier transform of the data, since it is multiplied in the

[50] A 'Barlett window' has a similar definition to the Parzen window.

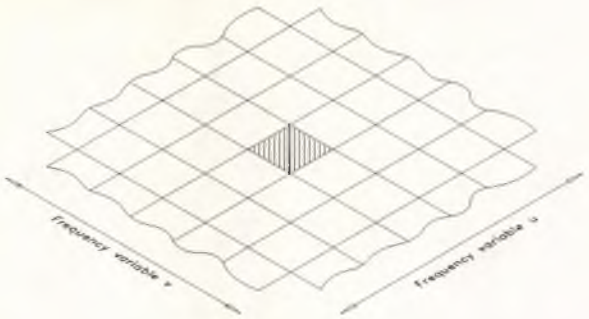


Figure 52: Periodic nature of 2D DFT

spatial domain. Multiplication in the spatial domain is equivalent to *convolution* in the Fourier domain (Equation [65]). This is another reason why the data should be weighted prior to Fourier transformation. Since the window function is convolved with the data, *no* weighting function[51] convolves the data with a function which has sharp discontinuities at the edges. The Fourier transform of the rectangular function has substantial components at high frequencies. Other windows which offer different characteristics are discussed by Nuttall [1981]. The construction of two-dimensional windows is relatively straightforward. Huang [1972] shows that if $w(x)$ is a 'well-behaved', symmetrical one-dimensional window, then $W(x,y)$ will be a 'well-behaved' two-dimensional window, where:

$$W(x,y) = w(x)\sqrt{x^2 + y^2} \qquad [83]$$

4.2.1.5 Filtering in the Fourier transform domain

The application of a filter in the transform domain can be rather complex. It must be appreciated that a multiplication applied to the *transform* domain (the application of a filter window), is equivalent to a *convolution* in the spatial domain (this duality was presented without proof in section 4.2). The most common types of filter to be applied in the Fourier transform domain are the 'ideal' filters. These filters are zero everywhere except in the

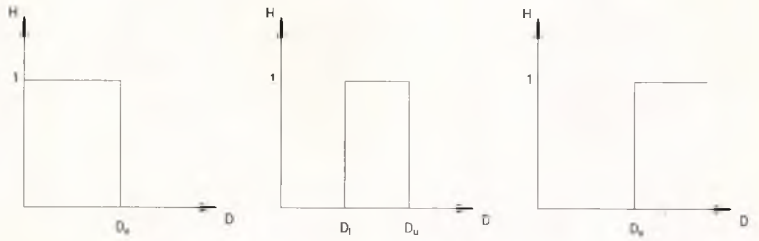


Figure 53: Ideal filters

[51] 'No weighting function' is actually a *rectangular* window, since this is 1.0 for all values inside the range, and 0.0 for all values outside the range.

passband, where they are unity. Figure 53 shows three 'ideal' filters; the left is a *low pass* filter with cutoff D_o, the centre is a *bandpass* with upper and lower cutoffs D_u and D_l respectively, and the right is a *highpass* filter. The lowpass filter has the definition:

$$H(u) = \begin{cases} 1 & |u| \leq D_o \\ 0 & otherwise \end{cases} \qquad [84]$$

The bandpass filter is defined:

$$H(u) = \begin{cases} 1 & D_l < u < D_u \\ 0 & otherwise \end{cases} \qquad [85]$$

and finally the highpass filter is defined:

$$H(u) = \begin{cases} 1 & |u| \geq D_o \\ 0 & otherwise \end{cases} \qquad [86]$$

Although these filters are simple to program, they suffer from the fact that the edges have sharp transitions. These sharp cutoffs cannot be realised in practice, and this type of filter is often referred to as 'noncausal'. The necessary and sufficient conditions that a frequency response characteristic $H(u)$ must satisfy in order that the resulting filter will be causal (realisable) are given by the *Paley-Wiener* theorem [Wiener and Paley, 1934]:

> If $h(n)$ has a finite energy and $h(n) = 0$ for $n < 0$, then:
>
> $$\int_{-\pi}^{\pi} |\ln |H(u)|| \, du < \infty \qquad [87]$$
>
> Conversely, if $|H(u)|$ is square integrable and if the integral in Equation [87] is finite, then we can associate with $|H(u)|$ a phase response $\Theta(u)$, so that the resulting filter with frequency response:
>
> $$H(u) = |H(u)| e^{j\Theta(u)} \qquad [88]$$
>
> is causal.

An important conclusion drawn from the Paley-Wiener theorem is that the magnitude function $|H(u)|$ may be zero at *some* frequencies, but cannot be zero over any finite *band* of frequencies, since this would make the integral infinite. Consequently, any ideal filter cannot be causal. However, in digital electronics, such filters can be applied to stored data. The application of an ideal filter characteristically causes 'ringing' in the spatial domain. This is because the Fourier transform of the filter function has severe sidelobe leakage, which is convolved with the recovered spatial data. To reduce the ripples in the spatial domain, a filter

with a *smoother* characteristic is required. An example of a smooth filter is the Butterworth lowpass filter:

$$H(u) = \frac{1}{1 + 0.414\left[\frac{D(u)}{D_o}\right]^{2n}} \qquad [89]$$

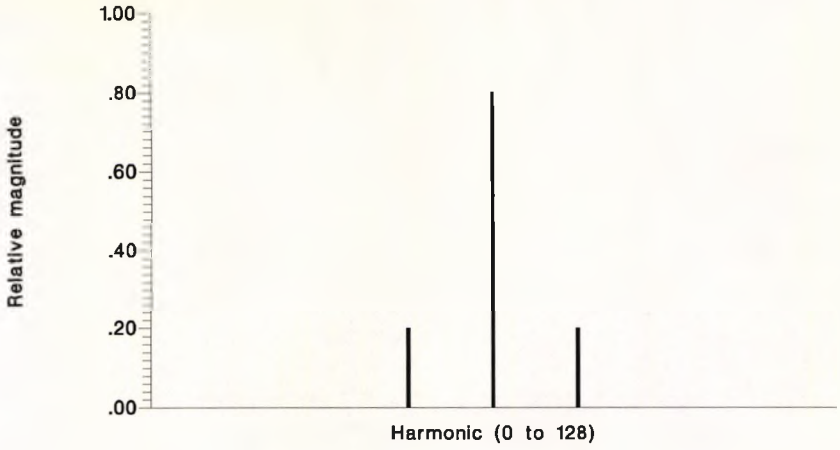
Unlike the ideal lowpass filter, the Butterworth lowpass filter does not have a sharp transition which establishes a clear cutoff between the passband and the stopband. This filter has a *defined* cutoff ($H(u) = 1/\sqrt{2}$ when $D(u) = D_0$) which is not zero. Depending upon the order of the filter (which is given by n), it can allow a fairly large amount of high frequency information to pass.

4.2.1.6 Spectral leakage

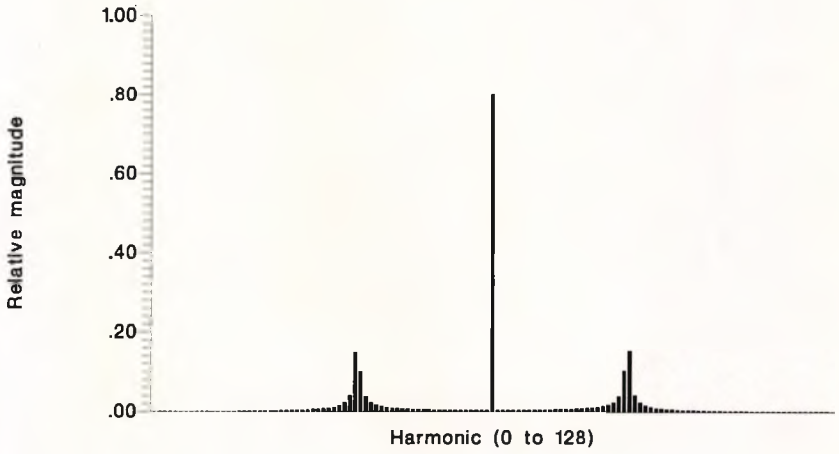
One of the problems associated with filtering in the Fourier transform domain is the spectral leakage. Spectral leakage occurs when a 'strong' harmonic occurs *between* the discrete 'bin' points in the DFT space. The following example illustrates the leakage problem. Consider the equation:

$$y(x) = 0.8 + 0.2\sin\left[\frac{2\pi x}{n}\right] \qquad [90]$$

Suppose the equation is evaluated at 128 equally spaced points ($0 \leq x \leq 127$), and the Fourier transform of the equation is calculated for different values of n. If n is a multiple of 2, then an *integer* number of cycles will occur in the record length, and no leakage will occur from the spectral point corresponding to the sine wave. This is shown in Graph 6, which is a 128 point DFT with $n = 8$. If the value of n is not a power of 2, then leakage occurs, as shown in Graph 7, which has $n = 5$. Graph 6 corresponds to 16 fringes, hence the spectral peaks appear at locations 48 and 80 in the 128 point transformation. Graph 7 corresponds to 25.6 fringes, so the spectral peak would be at locations 38.4 and 89.6 respectively. The energy of the spectral lines corresponding to the sine wave has been reduced and spread across several frequency components in Graph 7, so the peak amplitude is reduced from 0.2 to 0.1501 at locations 38 and 90 (the closest locations to the actual peak). Notice the 'skirts' of the spectral information, which extend relatively far from the actual peak. Truncation of the small components of the skirt at the edge of the transform region causes additional errors, and is considered in more detail in Chapter 6.



Graph 6: DFT of Equation [90] with $n = 8$



Graph 7: DFT of Equation [90] with $n = 5$

4.2.1.7 Noise and the DFT

Noise is defined as *the difference between the actual and detected signal*. It can be either additive or multiplicative, wideband or narrowband. The degree of noise contamination will limit the overall accuracy to which useful information can be extracted from a signal spectrum. The discrete Fourier transform handles relatively large amounts of noise before becoming ineffective, as pointed out by Green [1990]. It is beyond the scope of this thesis to conduct an in-depth investigation into the noise characteristics of the Fourier transform, and any further references to this topic will be in the context of error analysis (Chapter 6).

4.2.2 Fourier transform analysis with a linear carrier

The Fourier transform method of fringe analysis was first reported by Takeda *et al.* [1982]. The paper proposed considering a two-dimensional fringe field to be made up of slices, any

of which could be independently analysed using a one-dimensional Fourier transform[52]. Macy [1983] extended the method to two-dimensions by considering the entire fringe field as made up of slices, each slice being processed again using a one-dimensional Fourier transform. The method was advanced further by Bone *et al.* [1986] to enable two-dimensional processing in the true sense, with the use of a two-dimensional Fourier transform, which is the method under consideration in this section. Several reviews of the Fourier transform techniques have been published, the most useful of which were found to be Kreis [1986], Kreis [1987b], Kreis [1988], Choudry and Kujawińska [1989], Kujawińska *et al.* [1989b], and Kujawińska and Wójciak [1991].

Spik [1987] modified the method to allow non-square and non-rectangular fringe fields to be examined, by supplementing the fringe pattern with a matched sinusoidal function. This routine was suitable for good quality fringes, but deteriorates when the signal-to-noise ratio is decreased. A superior algorithm, proposed by Roddier and Roddier [1987], uses an existing method of extrapolation[53] for fringe data, to reduce the phase errors at the edges of the recovered phasemaps. However, the improved algorithm still operates well in low noise conditions. Kreis [1986] describes a technique of sign determination using two orthogonal filtering schemes, with each filter passband occupying half of the data array space[54]. The two resulting phasemaps are unwrapped together and used to determine the sign. Although this technique appears extremely useful, it can only be applied to low noise fringes, due to the use of a wideband Fourier filter. This is pointed out by Huntley and Benckert [1992a,b] who use the filtering method with speckle correlation fringes, which have been 'cleaned up' with a correlation fringe averaging algorithm. Green *et al.* [1988] and Green [1990] have studied the effects of increasing levels of random additive noise, and increasingly complicated phase function, to images analysed with the Fourier transform method. They conclude that the Fourier transform method of fringe analysis is robust in the presence of signal-independent additive noise, provided that the phase function is *slowly varying*[55]. Under conditions of no noise, the phase function could vary at up to 30% of the carrier without any problem.

Malcom *et al.* [1989] and Burton and Lalor [1989] consider some of the problems linked with using the discrete Fourier transform (DFT), sampling and windowing in the Fourier domain. The implications of sampling are basically that the components of the carrier frequency

---

[52]The mathematical theory is presented later in this chapter.

[53]A Fourier transform based iterative algorithm developed by Gerchberg and Saxton [1972].

[54]So, the first filter is the $+u$ half-plane (right hand half of the array), the second filter is the $+v$ half-plane (lower half of the array).

[55]For example, when the variations of the phase function are about 5% of those introduced by the spatial carrier, then the Fourier transform method gives good reconstructions with a signal-to-noise ratio as low as 2.0.

resolved in the directions of the detector elements must be such that there are at least *two samples per fringe* in both directions. If this condition is not met, aliasing occurs. However, Bone *et al.* [1986] and Greivenkamp [1987] have shown that in some cases, the carrier frequency may exceed the Nyquist frequency without any serious problems. A prior knowledge of the experiment allows the aliased frequencies to be mapped into unused areas of the frequency domain.

Huntley [1986] compares the use of the two-dimensional Fourier transform with the two-dimensional Walsh transform for the analysis of double exposure speckle photographs. It is found that the Walsh transform is much faster to compute than the Fourier transform, but that it tends to be less reliable when the modulation of the fringes reduces. However, for high modulation, the accuracy of the two techniques is similar. Huntley [1989a] compares the two-dimensional Fourier and Walsh transforms with the one-dimensional integration and autocorrelation methods, using computer generated speckle photography fringes. Kreis and Jüptner [1989] consider some of the effects of filtering in the spatial frequency domain. The consequence of filter orientation and cutoff frequencies is considered, and experimental results used in illustration. The accuracy of the Fourier transform method of fringe analysis is discussed thoroughly in section 6.3.

Returning to the theory, consider a general fringe pattern imaged by a suitable image-sensing device. Assume the device has a linear transfer function and that all pixels respond in the same way. If the optical stage is free from abberations, the spatial intensity distribution may be written (ignoring noise) [Roddier and Roddier, 1987]:

$$g(\vec{r}) = a(\vec{r}) + b(\vec{r})\cos(\phi(\vec{r})) \qquad [91]$$

The vector $\vec{r}$ reflects the spatial coordinates (x,y). The functions $a(\vec{r})$ and $b(\vec{r})$ are the background and modulation terms respectively, and $g(\vec{r})$ is the spatial intensity distribution imaged by the sensor. The information of interest is the function $\phi(\vec{r})$, which is the phase distribution. If one of the interferometer mirrors is tilted slightly, Equation [91] becomes:

$$g(\vec{r}) = a(\vec{r}) + b(\vec{r})\cos(2\pi\vec{f}_o.\vec{r} + \phi(\vec{r})) \qquad [92]$$

where the vector $\vec{f}_0$ is called the spatial carrier frequency. This is in fact nothing more than a two-dimensional adaptation of a standard one-dimensional wave processing technique. An analogy would be the modulation of a radio wave signal. The information of interest (eg. audio) is made to modulate a carrier wave signal. Modulation of the amplitude of the carrier (AM), frequency (FM) or phase (PM) allows the signal of interest to be positioned at a specific region of the frequency spectrum. Demodulation of the carrier allows the

information to be retrieved. The *fringe pattern* represents an amplitude and phase modulated sinusoid, the recovery of the function $\phi(\vec{r})$ being a demodulation process. Simple trigonometric identities allow Equation [92] to be written in the form:

$$g(\vec{r}) = a(\vec{r}) + c(\vec{r})\,e^{2\pi i \vec{f}_o \cdot \vec{r}} + c^*(\vec{r})\,e^{-2\pi i \vec{f}_o \cdot \vec{r}} \qquad [93]$$

where the function $c(\vec{r})$ is given by:

$$c(\vec{r}) = \frac{1}{2} b(\vec{r}) e^{i\phi(\vec{r})} \qquad [94]$$

and $c^*(\vec{r})$ is the complex conjugate of $c(\vec{r})$.

If the rate of variation of the phase function is 'slow' compared to the spatial carrier[56], then the Fourier transform technique can be used to extract it. Denoting the two-dimensional Fourier transform of a function with a capital letter, the Fourier transform of Equation [93] is given by:

$$G(\vec{R}) = A(\vec{R}) + C(\vec{R}-\vec{F}_o) + C^*(-\vec{R}-\vec{F}_o) \qquad [95]$$

where the vectors $\vec{R}$ and $\vec{F}_o$ represent the spatial frequency coordinates (u,v) and the coordinates of the carrier frequency respectively. The function $g(\vec{r})$ consists of real positive numbers if the fringe field is stored in a digital image processing device. The Fourier transform of a real positive sequence is a particular type of complex sequence called conjugate symmetric or Hermitian (see Table 4) with the basic property:

$$G(\vec{R}) = G^*(-\vec{R}) \qquad [96]$$

It can be seen from Equation [95] that in the Fourier domain, the spatial frequency information will consist of three distinct regions, the function $A(\vec{R})$ centred on the origin and containing the background and low frequency information. The functions $C(\vec{R}-\vec{F}_o)$ and $C^*(-\vec{R}-\vec{F}_o)$, are offset from the frequency origin by $|\vec{F}_o|$, and contain the phase information. If $c(\vec{r})$ is a bandlimited function with cutoff frequency f_c, and $|\vec{F}_o| > f_c$, then $c(\vec{r})$ may be determined unambiguously. The application of a suitable filter in the Fourier domain allows either $C(\vec{R}-\vec{F}_o)$ or $C^*(-\vec{R}-\vec{F}_o)$ to be removed, thereby destroying the Hermitian nature of the data. It is unimportant which of the two functions is filtered out, since they contain the same information. Conventionally, the *conjugate* function is always filtered out, together with the function $A(\vec{R})$. The filtering process is discussed in more detail later in the chapter.

---

[56] See Green [1990] for details of the ratio of required phase to spatial carrier.

As an example, consider the fringe pattern shown in Image 19. This example is of a linear carrier fringe field with a large discontinuity in the centre of the image. The fringes were generated by tilting one of the mirrors of an in-plane ESPI system. The central 64x64 points of the two-dimensional Fourier transform modulus are shown in Figure 54 (the DC peak has been scaled in this diagram). The application of a filter in the Fourier domain, as explained earlier, allows one of the 'fringe peaks' to remain, as shown in Figure 55. The computation of the inverse two-dimensional Fourier transform of the data remaining in Figure 55 results in the 'wrapped phasemap' shown in Image 20[57]. The greyscale representation of the wrapped phasemap[58] indicates principle phase (0 to 2π), where black represents 0, and white 2π. A *binary mask*, shown in Image 21, is applied to the image, to distinguish the valid and invalid data regions. This mask was generated using a standard image thresholding technique, and was 'tidied up' using the PC mouse. The wrapped phasemap with the invalid data masked is shown in Image 22. As stated, Image 19 was generated by tilting one of the mirrors of an in-plane electronic speckle pattern interferometer. These fringes therefore contain no useful information, and are the two-dimensional spatial carrier represented mathematically in Equation [92]. The application of a load to the specimen would modulate (distort) these fringes, and can be measured by comparing the tilt fringes with the modulated tilt fringes.

[57]Note the 'filling' of the discontinuous region with phase data. The reason for this is explained in section 4.2.4.

[58]Refer to section 4.3 for a discussion of wrapped and unwrapped phase data.

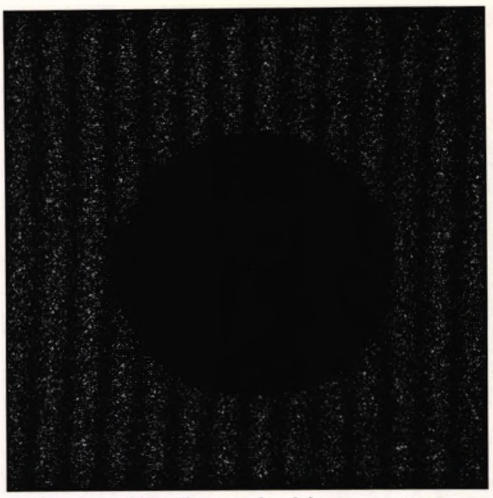


Image 19: Example fringe pattern

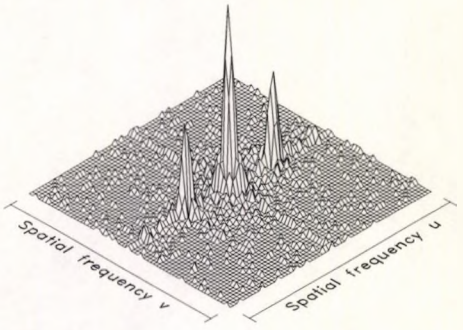


Figure 54: 2D FFT of Image 19

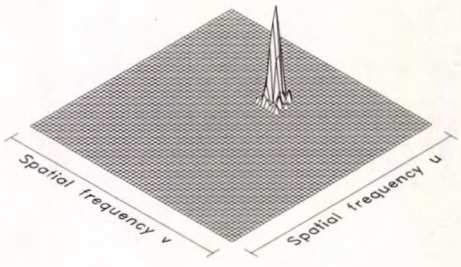


Figure 55: Filtered spectrum

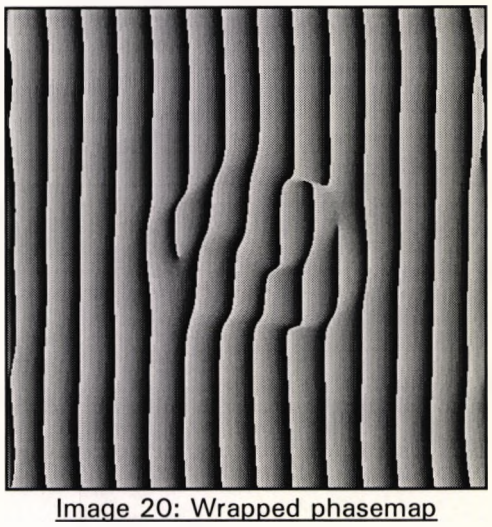


Image 20: Wrapped phasemap

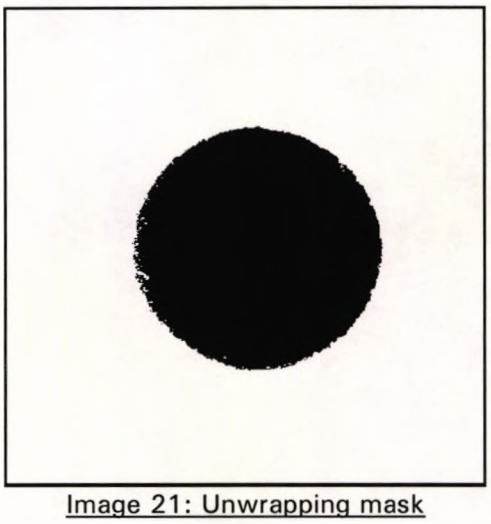


Image 21: Unwrapping mask

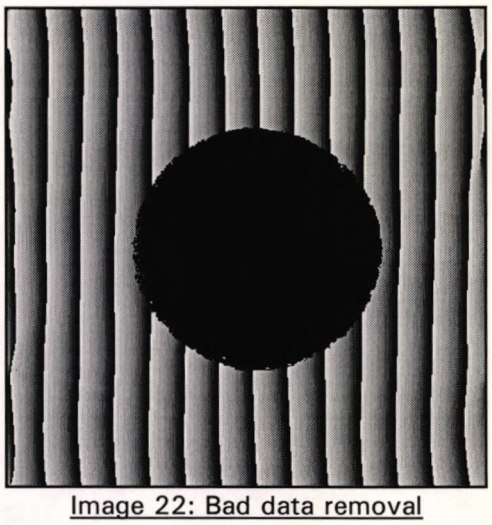


Image 22: Bad data removal

After filtering, the function $C(\vec{R}-\vec{F}_o)$ remains. This function contains both the phase and the spatial carrier term $\vec{F}_o$. The carrier term must be removed to yield correct phase information. Removal can take place in either the spatial or spatial frequency domains, which is dealt with in the following two sections.

4.2.2.1 Tilt removal in the spatial frequency domain

Takeda *et al.* [1982] removed the carrier phase by translating the function $C(\vec{R}-\vec{F}_o)$ to the frequency origin, yielding $C(\vec{R})$, and then by computing the inverse Fourier transform, as illustrated in Figure 56. This method suffers from three main problems which limit the accuracy to which the phase may be determined:

- the fringes must be linear and equally spaced for the translation to be possible.
- an integral number of fringes must be added by the tilting process in order for the spatial carrier frequency to equal an integer.
- the amount of tilt must be determined accurately.



Figure 56: Tilt removal in the Fourier domain

Since the method proposed by Takeda *et al.* was one-dimensional, only one component of the heterodyning frequency could be removed. Also, the carrier frequency and scan direction had to be chosen so that the other component was zero. The mathematical reasoning behind this idea is relatively straightforward. From Equation [95], the application of a filter in the frequency domain can remove the low frequency background variation $A(\vec{R})$ and the function $C^*(-\vec{R}-\vec{F}_o)$. The remaining function after filtering, $G'(\vec{R})$ is given by:

$$G'(\vec{R}) = C(\vec{R}-\vec{F}_o) \qquad [97]$$

Whilst still in the Fourier domain, the bundle of information containing the function $C(\vec{R}-\vec{F}_o)$ can be translated by $\vec{F}_o$ to the frequency origin, yielding the new function $G''(\vec{R})$:

$$G''(\vec{R}) = C(\vec{R}) \qquad [98]$$

Computation of the inverse two-dimensional Fourier transform of Equation [98] gives:

$$g''(\vec{r}) = c(\vec{r}) \qquad [99]$$

Equation [94] shows that the modulation and phase terms are now available. It follows:

$$\phi(\bar{r}) = \tan^{-1}\left[\frac{Im[c(\bar{r})]}{Re[c(\bar{r})]}\right] \qquad [100]$$

Where *Re* and *Im* are the real and imaginary operators respectively. The modulation may also be extracted:

$$b(\bar{r}) = 2|c(\bar{r})| \qquad [101]$$

4.2.2.2 Tilt removal in the spatial domain

Bone *et al.* [1986] arranged the interferogram so that some region was free from fringe information, and computed the amount of tilt in this region using a least-squares fit to an inclined plane. The tilt was then removed by direct subtraction of the plane (see the upper diagram of Figure 57). One of the drawbacks of this method is that the carrier fringe field may not be uniform over the entire frame. This could be the case if the response of the imaging device was not uniform throughout the active area. Another method of tilt removal, discussed by Green [1990], is the multiplication of the unwrapped phase data by a conjugate exponential function[59]. However, this method requires a highly accurate measure of the amount of tilt, which can be both difficult, and prone to error. One method used to overcome this problem is examined by Huntley and Field [1989]. The tilt is removed in essentially the same way as Bone *et al.*, except that instead of *calculating* the tilt from an unused area of the interferogram, it is *measured* by recording the *carrier* field prior to deformation. This means that the carrier fringe pattern need not contain an integral number of fringes across the field, nor must they be equally spaced. This method involves twice the number of forward

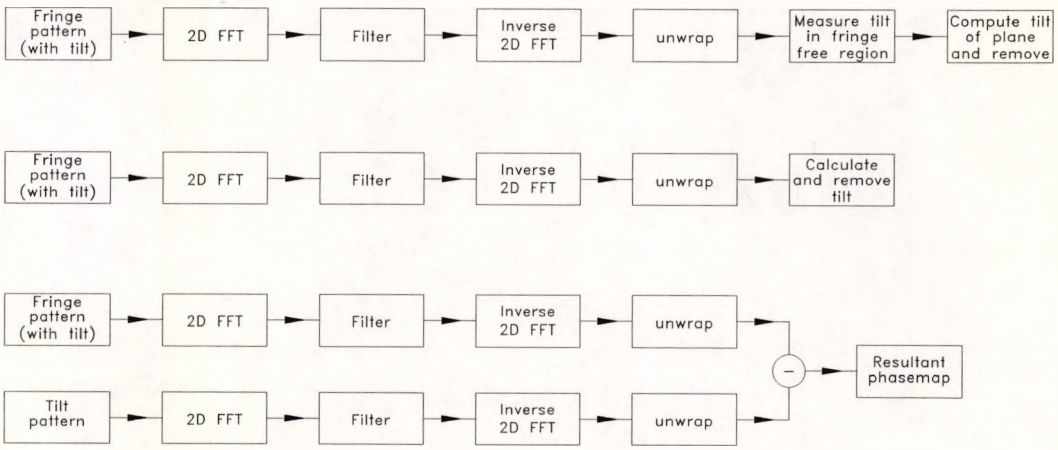


Figure 57: Three methods of tilt removal in the spatial domain

[59]Refer to Equation [63].

and reverse Fourier transform operations, since the process must be applied to two images instead of one, for each test. However, a tilt value for each pixel location is computed *uniquely*. This process is illustrated in Figure 57 (lower diagram). The analysis is similar to the previous section, except that the data is *not* translated in the Fourier transform domain. The filter applied in the spatial frequency domain yields the function $G'(\vec{R})$ (Equation [97]). The function $g'(\vec{r})$ is computed by application of the inverse two-dimensional Fourier transform to function $G'(\vec{R})$ forming (again, refer to Equation [63]):

$$g'(\vec{r}) = c(\vec{r})\, e^{2\pi i \vec{f}_o \vec{r}} \qquad [102]$$

As stated, if the carrier frequency term $\vec{f}_o$ can be measured or calculated (for example by measuring the tilt angle of the mirror), then multiplication of the function $g'(\vec{r})$ by the conjugate exponential would give the function $g''(\vec{r}) = c(\vec{r})$, (the same as result as obtained in Equation [99]), and the modulation and phase terms would be available. However, in many cases it is either not possible or extremely difficult to obtain a reliable estimate for $\vec{f}_o$. Therefore, using the *carrier pattern* alone to compute the tilt phase is the most versatile algorithm, although it is computationally inefficient. The carrier phase, once computed, is subtracted from the modulated phase, resulting in the final phasemap (Figure 57). Once the function $c(\vec{r})$ is obtained, extraction of the phase information is identical to that used in section 4.2.2.1 (Equations [99] - [101]).

4.2.3 Fourier transform analysis with a sectored concentric carrier

The experimental system used in this research programme generates curved, instead of linear fringes. The mathematical treatment of the Fourier transform method of fringe analysis is basically the same as described in section 4.2.2. The main difference however, is that the spatial carrier frequency is *not* constant when various directions through the fringe pattern are considered (when working in a cartesian coordinate system). A simple change of coordinate system is not easy to effect, since this would require the computation of the two-dimensional Fourier transform in cylindrical coordinates.

Consider Equation [92], if the tilt added to the interferogram is generated using a non-plane mirror, then the spatial carrier frequency vector $\vec{f}_o$ will vary with position. If the unit vectors along the x and y axis are denoted by $\vec{i}$ and $\vec{j}$ respectively (Figure 58), then:

$$\vec{f}_o = p\,\vec{i} + q\,\vec{j} \qquad [103]$$

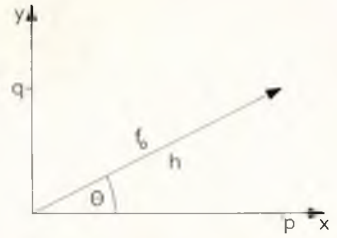


Figure 58: Radial carrier

where:

$$p = h.\cos\theta \qquad q = h.\sin\theta \qquad h = \sqrt{p^2+q^2} \qquad [104]$$

Suppose that the added tilt generates fringes which are concentric circles (or sections of concentric circles). Then as the angle θ is altered, the value of h remains constant if the origin of the coordinate system is aligned with the centre or extrapolated centre of the concentric fringes. This means that the *magnitude* of the tilt remains the same as different *angles* through the fringe pattern are considered. Introducing polar coordinates into the Fourier transform pair and defining the two-dimensional discrete Fourier transform of $f(x,y)$ as $F(u,v)$, we have:

$$x = h.\cos\theta \qquad y = h.\sin\theta \qquad u = \omega.\cos\phi \qquad v = \omega.\sin\phi \qquad [105]$$

So, the transform pair $f(x,y)$ and $F(u,v)$ are transformed to $f(h,\theta)$ and $F(\omega,\phi)$ respectively [Gonzalez and Wintz, 1987]. It can be shown by direct substitution in the discrete two-dimensional Fourier transform that as the angle θ is varied, a corresponding variation in the angle ϕ occurs, but ω remains unchanged. Hence, a concentric or sectored concentric carrier fringe field generates a circle or 'crescent' around the zero frequency origin, the radius of which is proportional to the amount of tilt, as shown in Figure 59. In Figure 59, the upper diagram is an example of a fringe pattern that *could not* be analysed using the Fourier transform method of fringe analysis. This is because the method relies on *destroying* the Hermitian nature of the data, which is impossible here, since any point in the Fourier domain cannot be said to be part of C or C^* (see section 4.2.2). Also, had the fringes in the lower example been of a higher radius of curvature, such that the right hand side of the image would form a *diameter* through the fringes, then this image also could not be analysed using Fourier transform methods for the same reason as the upper image. This is stated as:

> "The centre of sectored concentric fringes must fall beyond the limits of the fringe field in order to adequately separate the Hermitian data in the Fourier domain."

Ru *et al.* [1988, 1989] have used both the two-dimensional Fresnel transform and the two-dimensional Fourier transform to analyse circular fringe patterns. Their use of the Fourier

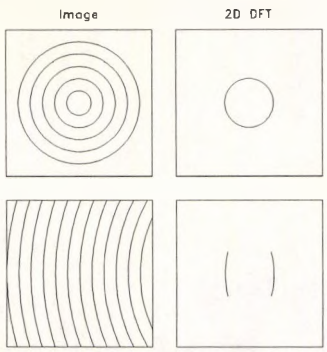


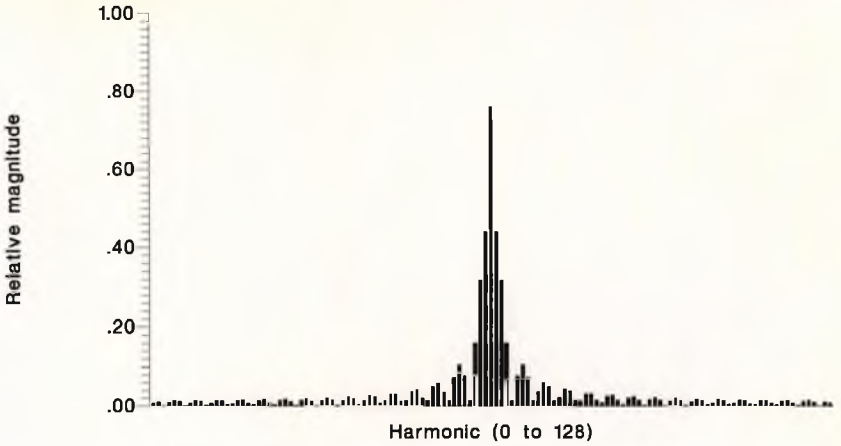
Figure 59: Fringes and their 2D DFT's

transform [Ru *et al.*, 1989] appears somewhat ambiguous, since it is unclear whether the computations were performed in cartesian or polar coordinates. Also, they appear to have made the assumption that the fringe field is perfectly symmetrical about the vertical, and have reconstructed only *one half* of the phase map. This would mean that two different phasemaps would be obtained depending upon which of the functions C or C^* is filtered out (see section 4.2.2), which obviously cannot be correct for the most part. The application of this method of analysis to ESPI type fringes would almost certainly fail, due to the large amount of background noise (speckle) and the use of an extremely tight Fourier filtering window. Computation of the two-dimensional Fourier transform of sectored concentric fringes using cartesian coordinates means almost inevitably that the removal of the spatial carrier must be performed in the spatial domain. Removal in the Fourier domain would require 'shrinking' of the fringe information towards the zero frequency, a problem fraught with practical difficulties when applied to the discrete Fourier transform case.

4.2.4 Incomplete fringe fields

One of the major problems with the Fourier transform method of fringe analysis arises when there is a *discontinuity* within the fringe field. A discontinuity is a region within the fringe field which contains no fringe information, or a region with a sudden change of fringe frequency. Examples of these are shadows, shock waves in flow patterns, and physical surface features which result in 'dead' zones. A discontinuity represents a rapid change in conditions, and will therefore be 'rich' in high frequency components [Lynn, 1973]. The Fourier transform of a discontinuity will cause 'ripples' to occur in the frequency domain, the amplitude of which will increase towards the edge of the discontinuity. In one-dimension, this is illustrated by Graph 8, which shows the ripples occurring in the Fourier transform domain after computing a 128 point transform of the pulse function:

$$y(x) = \begin{cases} 1 & 16 \le x \le 112 \\ 0 & \textit{otherwise} \end{cases} \qquad [106]$$



Graph 8: Ripples from a discontinuity

In order to reconstruct accurately the pulse function from its Fourier transform, the *high frequency* information would be required in to shape the rapidly rising edge of the pulse. Hence, a wideband Fourier filter would be employed to retain such information. In relation to fringe analysis, the data close to a discontinuity will be less reliable than the rest of the data. It is worth noting that the boundaries of the field also form a discontinuity, as explained in section 4.2.1.4. Furthermore, the method employed to reduce the errors at the edges of the field *cannot* be applied to regions inside the field. The following diagrams illustrate the ringing effect of a discontinuity within the fringe field. Image 23 shows a field of 12 vertical cosine fringes. Image 24 shows the two-dimensional Fourier transform of Image 23 (logarithmically scaled). Image 25 shows the same data as Image 23, but with a large circular discontinuity (radius of 100 pixels) at the centre. Image 26 represents the Fourier transform of Image 25, showing the 'ripples' in the Fourier domain. Image 27 shows the same data with a medium discontinuity (radius 50 pixels). Image 28 shows the Fourier transform of Image 27.

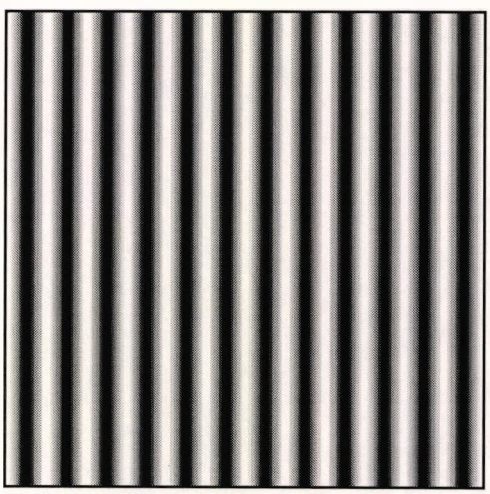


Image 23: Simulated cos fringes

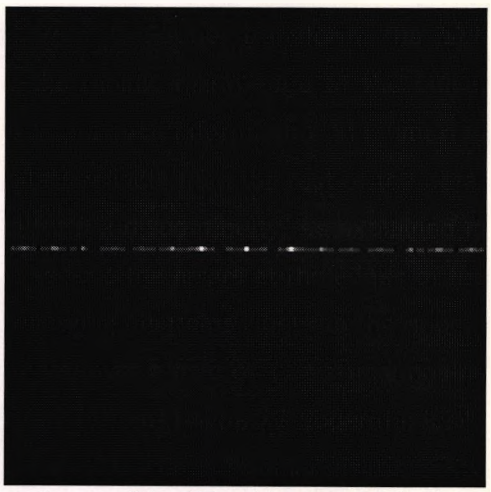


Image 24: FFT of Image 23 (x4)

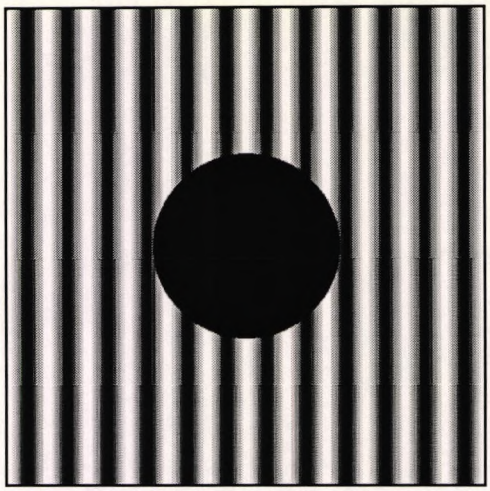


Image 25: Large discontinuity

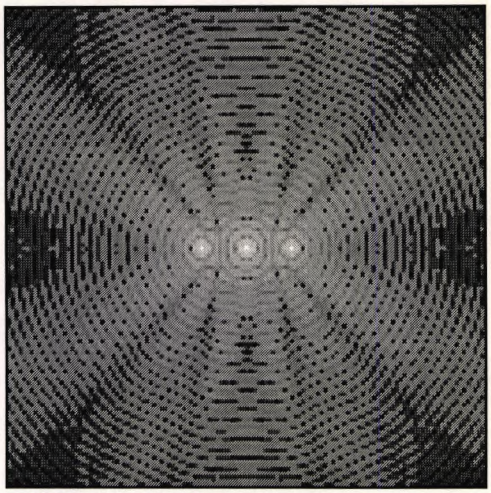


Image 26: FFT of Image 25 (x4)

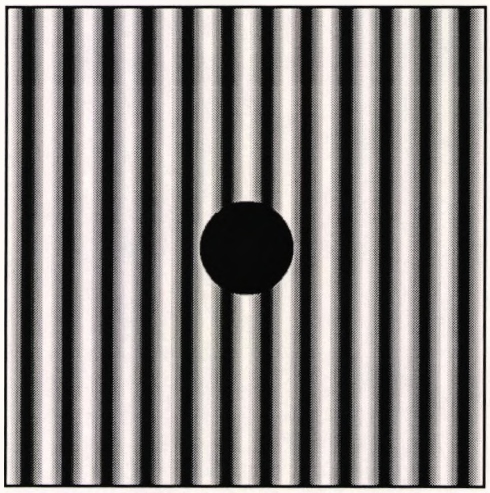


Image 27: Medium discontinuity

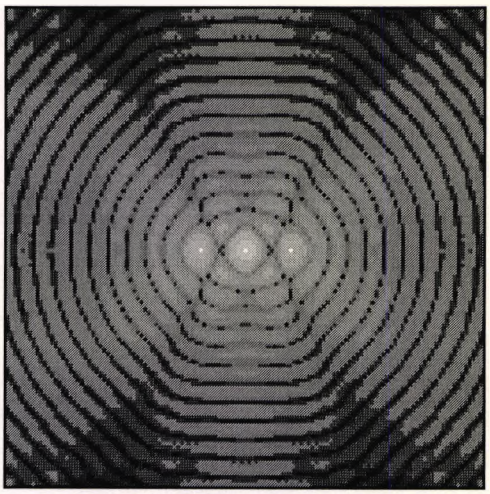


Image 28: FFT of Image 27 (x4)

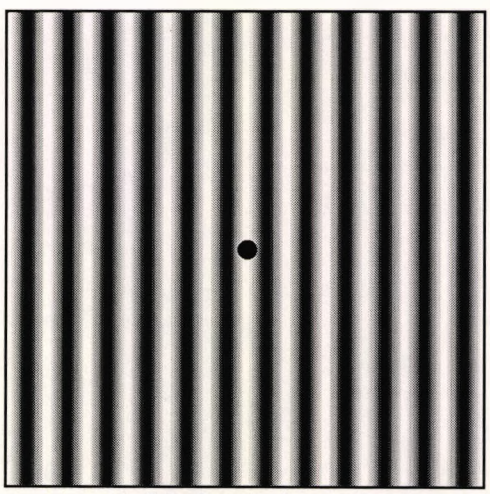


Image 29: Small discontinuity

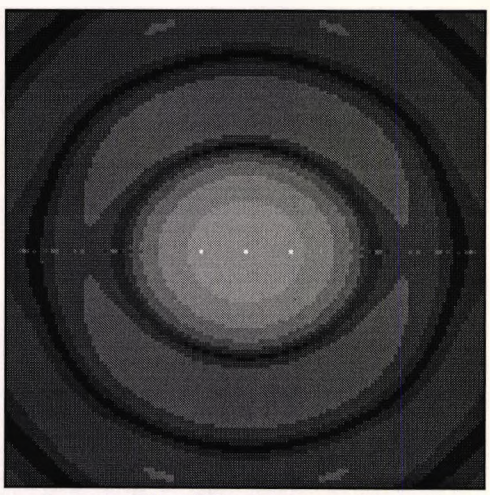


Image 30: FFT of Image 29 (x4)

Discontinuities which are very small in comparison to the array size can also generate large amounts of ringing. This is shown in Image 29, which has a small discontinuity (pixel radius of 10) at the centre. Image 30 is the two-dimensional Fourier transform of Image 29. Several methods have been proposed to overcome this problem, but none appear successful in dealing with noisy speckle fringes. The most straightforward method involves copying the data from the edges of the discontinuity into the 'bad' region. A more sophisticated method is based upon the technique of error energy reduction [Gerchberg and Saxton, 1972]. The Gerchberg Saxton iterative algorithm for analytical function extrapolation has been employed by Roddier and Roddier [1987] to replace the data lost by shadows in a telescope (the iterative nature

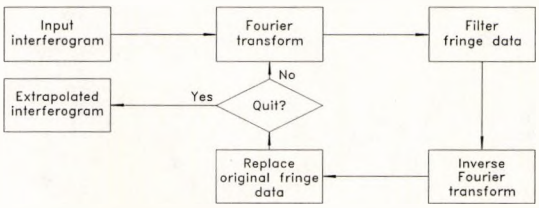


Figure 60: Gerchberg Saxton algorithm

of the algorithm is shown in Figure 60). It consists of moving back and forth between the Fourier transform and spatial domains. On each pass of the algorithm, the *original* fringe data is replaced in the image, but the erroneous data is unaltered. The difference between the actual data and the extrapolated regions (the error energy) reduces on each iteration. Typically, three or four iterations result in a reasonable extrapolation for low noise fringes. Image 31 shows the extrapolation of a simulated fringe pattern with a large discontinuity (Image 25) after only a single iteration of the algorithm. Three iterations of the algorithm result in the reconstruction displayed in Image 32. The reconstruction is good providing the fringes have a low noise content.

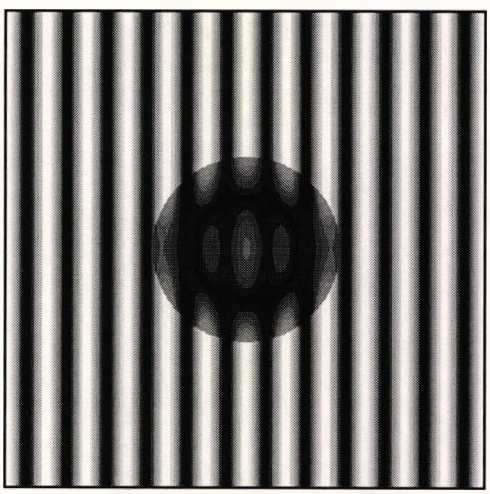


Image 31: Image 25 + 1 iteration

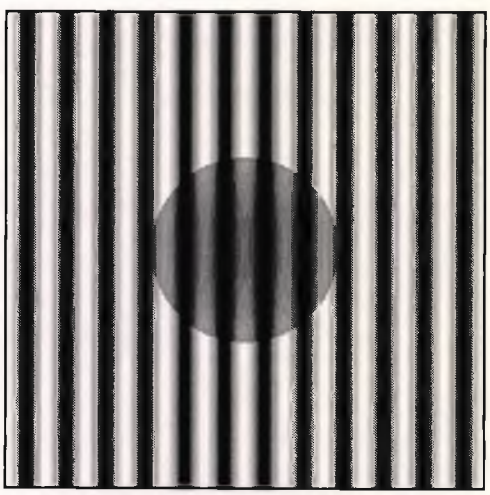


Image 32: Image 25 + 3 iterations

4.2.4.1 Domain detection

A general fringe field with a carrier frequency, but without noise, was represented by Equation [92] on Page 97. The term $b(\bar{r})$ is a measure of the local contrast of the fringes, and can be used to determine if valid fringe information exists at a particular pixel location. To measure the local fringe modulation, a thresholding technique could be applied, such as:

$$\begin{array}{lll} \textit{if} & b(\bar{r}) \geq T & \textit{Valid} \\ \textit{if} & b(\bar{r}) < T & \textit{Invalid} \end{array} \qquad [107]$$

The Fourier transform method automatically generates the fringe modulation data as a by-product of the phase extraction process, as indicated in Equation [101]. Although this technique seems useful, in the case of electronic speckle pattern interferometry, the use of very tight Fourier transform filters causes edges to be 'smeared' due to the loss of high frequency information. Another interesting method, described by Paler and Bowler [1986][60], uses Gabor filters for determining the fringe pattern carrier frequencies. Fringes are detected by a convolution of the Gabor sine and cosine filters with the image. A variation in the filter frequency and orientation is required before the convolution, and results in a peak in the graph of Gabor energy for valid fringe data. The presence on this peak indicates valid fringe information, the fringe direction and frequency are the same as the filter. This type of fringe detection scheme works on the actual image data of the fringes, unlike the previous technique.

4.2.5 Subpixel manipulations

The degree of correlation between two speckle patterns is reduced if one of the patterns undergoes a rigid body shift with respect to the other. In this case, the correlation can be increased by performing a subpixel shift [Tian and Huhns, 1986; Slud, 1988] of one of the patterns, prior to correlation. The following example shows the result of a subpixel translation. Image 33 shows a fringe pattern formed from two speckle patterns, one physically shifted with respect to the other. The Fourier transform of Image 33 is shown in Figure 61. The two 'lobes' corresponding to the fringe information can barely be resolved. A *linear* subpixel interpolation and shift applied to one of the speckle patterns, results in the fringe pattern shown in Image 34, with the Fourier transform shown in Figure 62. In this case, the speckle pattern was shifted by 1.53 pixels to the left, since the physical shift was to the right.

[60] See also Bowler and Paler [1986].

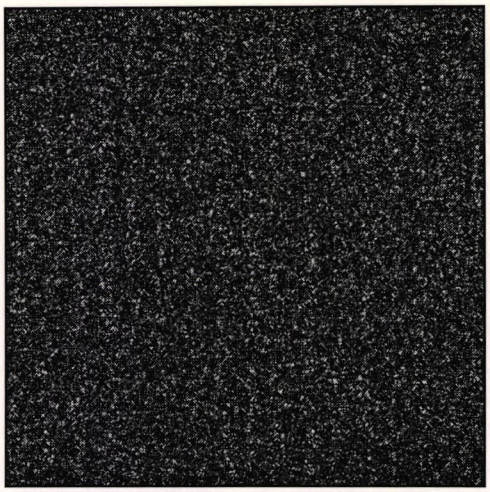


Image 33: Uncorrelated image

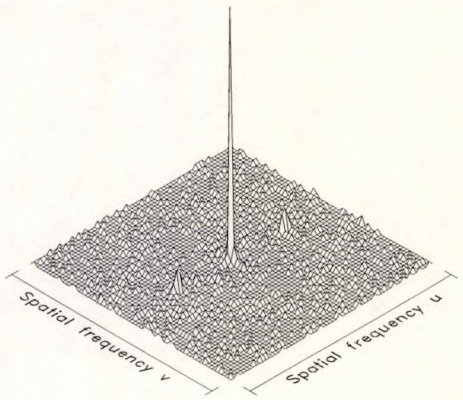


Figure 61: FFT of Image 33

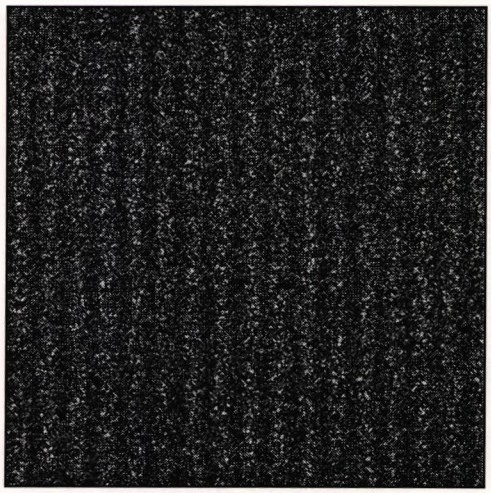


Image 34: Correlated image

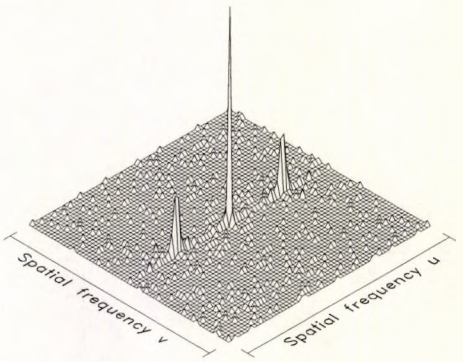


Figure 62: FFT of Image 34

4.3 Phase Extraction

The extract of the phase data from a fringe field is the ultimate aim of the Fourier transform method of fringe analysis (as explained in section 4.2.2). Equation [100] describes the basis for the phase retrieval. The use of an *arctangent* function in this computation results in a 'wrapped' phasemap, in which all the phase values are in the principal range ($-\pi$ to π).

4.3.1 Wrapped phase

As stated, the problem of wrapped phase arises from the use of an arctangent function in the computation of the phase. Any value of the phase outside the principal range ($-\pi$ to $+\pi$) will be mapped by the arctangent function, back into the principal range. For example, consider Figure 63, which shows the wrapped phase (lower) for the function $\phi(x) = 8\pi x$ over the range $0 \leq x \leq 1$ (upper). The wrapped phase is offset by π, so the principal range is transformed

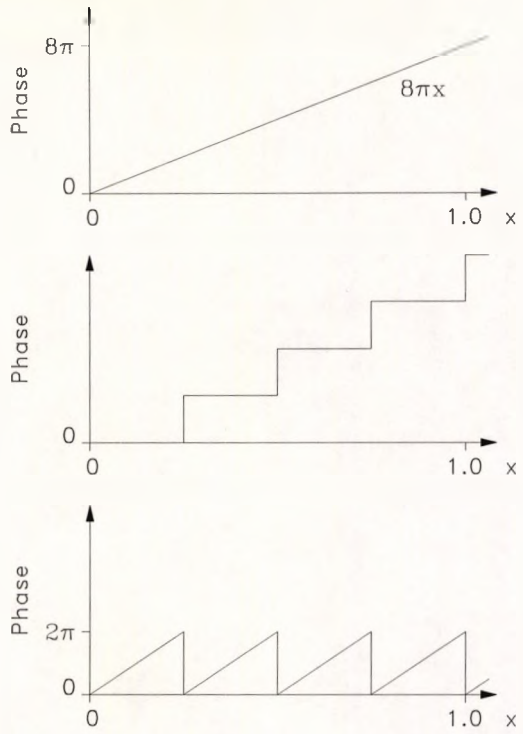


Figure 63: Wrapped phase

(0 to 2π). Discontinuities can be seen in the phase when it approaches 2π. The problem of phase unwrapping (section 4.3.2) involves the construction of a function which allows the discontinuities to be removed. For example, the function shown in the middle of Figure 63 is known as the offset phase function [Takeda *et al.*, 1982].

All fringe analysis phase extraction methods, and several 'apparently' unrelated technologies, generate wrapped phase. Several authors have reported ways of unwrapping the phase for many different applications, since it is not limited to interference fringe analysis. The problem is common when a phase modulated sinusoid with a large degree of modulation, is analysed.

4.3.2 Phase unwrapping

A typical approach which is often used to unwrap phase (*Shafer's algorithm*) is to compute the principal values using an arctangent routine, and then to unwrap by adding or subtracting multiples of 2π to the principal values, until all the discontinuities are removed [Tribolet, 1977]. The algorithm relies upon detecting the discontinuities, which is accomplished by comparing adjacent values. Whenever the difference is greater than a specified threshold, a discontinuity is present. It is pointed out that correct phase unwrapping can only be achieved if the sampling rate is sufficiently high, such that any rapid changes in the phase are not confused with discontinuities. In other words, the Nyquist sampling limit

must apply to the phase in order for it to be recoverable. If the fringes are sampled with less than two samples per fringe, the phase cannot be unambiguously recovered. Tribolet [1977] proposed an algorithm for use with speech, seismic and lunar data. This 1D homomorphic signal processing technique arose from the need to compute the complex cepstrum[61], which used information from both the derivative of the phase and principal phase value. This adaptive numerical integration technique worked by selecting the best phase value from a selection of several possibilities at each point. The selection is performed by using an estimate of the phase from numerical integration of the phase derivative. Osten and Höfling [1990] review some of the basic methods of phase unwrapping, in addition to discussing some of the problems associated with the sampling theorem, object discontinuities, noise and unsteady phase fields.

Itoh [1982] discusses the phase unwrapping problem with reference to fast implementation on a digital processor. He concludes that the *phase tracking algorithm* [Mertz, 1979,1981] can be implemented using three simple operations; differentiating, wrapping and integrating, and that realization and execution on a digital processor is possible in almost real time. The technique used by Takeda *et al.* [1982] is based on a standard method of unwrapping. It involves scanning along each row in turn. When the phase difference between a pixel and its predecessor is greater than π, 2π is either added or subtracted from all pixels in the remainder of the row. Although this method is computationally very efficient, the immunity to noise is extremely poor. If a single pixel in the row is invalid (erroneous), then all the remaining pixels in that row are also affected.

The *Cellular-Automata* method of phase unwrapping was proposed by Ghiglia *et al.* [1987], and is more robust than Shafer's algorithm, but computationally prohibitive. Cellular automata are simple, discrete mathematical systems that can exhibit complex behaviour resulting from the collective effects of a large number of cells, each of which evolves in discrete time steps according to simple local rules [Wolfram, 1983]. The algorithm typically requires hundreds of iterations, each iteration involving the entire image. The paper includes an example showing 512 principal valued samples, which is finally unwrapped after 3468 iterations involving the entire data set. The increased computer power available to small computer users may eventually make this algorithm viable.

Another robust algorithm, proposed by Gierloff [1987], subdivided the array into small regions, each of which contained no phase ambiguities. These regions were then phase

[61] The inverse Fourier transform of the log of the Fourier transform of a sampled data signal.

shifted with respect to one another to minimise the number of inconsistent boundaries. This is the basis of one of the most popular methods of phase unwrapping, developed by Towers *et al.* [1989], which is a path independent technique called the *tile unwrapping algorithm*. In this technique, the domain of the fringe field is subdivided into tiles[62], each of the same size. Each tile is processed independently, and if the consistency of the phase is sufficient across the tile, then it is accepted for further processing, otherwise it is discarded. A 'minimum weight spanning tree' is then used to connect the tiles together.

Another algorithm, proposed by Huntley [1989b], overcomes many of the error spread problems associated with conventional row/column unwrapping techniques, and is also computationally efficient. Huntley argues that the unwrapped phasemap of a two-dimensional phase field should be unique. In other words, whichever unwrapping route is chosen through the phase field, the resultant phasemap should always be the same. Error propagation in conventional row/column techniques is dependant upon the order in which the map is unwrapped. The algorithm developed by Huntley computes barriers across which unwrapping is prohibited, and is therefore compatible with any unwrapping strategy. Brown [1991] presents a similar phase unwrapping system developed for complicated automotive structures, which contain many sheared phase fringes. The *rectilinear path phase unwrapping algorithm* is similar in some respects to the noise immune algorithm of Huntley, since it performs a consistency check around very small segments in the phase map (typically 2x2 regions) and then unwraps along a path based upon the results of the check. It therefore decides the route through the data based upon 'micro rules' rather than 'macro rules'.

The *flood unwrapping algorithm* developed by Vrooman and Maas [1989] relies on invalid pixels being marked prior to unwrapping. The unwrapping system then 'floods' from a start point, around the invalid regions until the entire field is unwrapped. This algorithm is discussed in the next section.

4.3.2.1 Flood unwrapping algorithm

The flood unwrapping algorithm is presented by Vrooman and Maas [1989]. It receives special attention here because it is the technique used to unwrap the phase maps in this thesis. A more detailed explanation of this algorithm is given in the thesis of Maas [1991a], from which Figure 64, and the basis of the following description are taken.

---

[62]Towers *et al.* explain that since the most distorting effects are localised, a regional based approach offers many advantages over a global based unwrapping system.

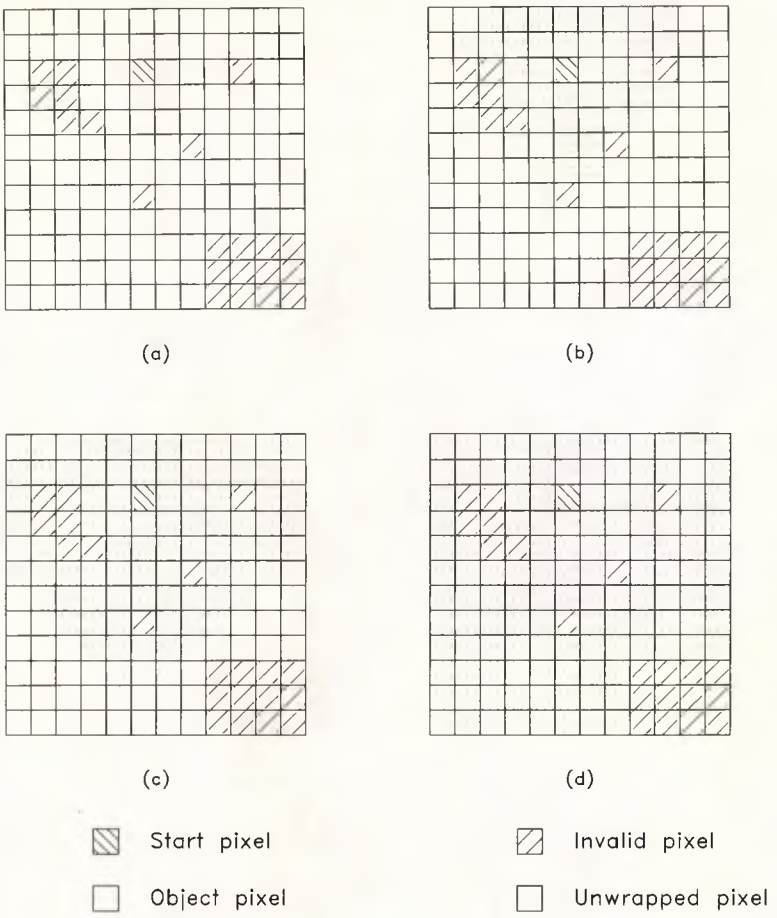


Figure 64: Flood unwrapping algorithm

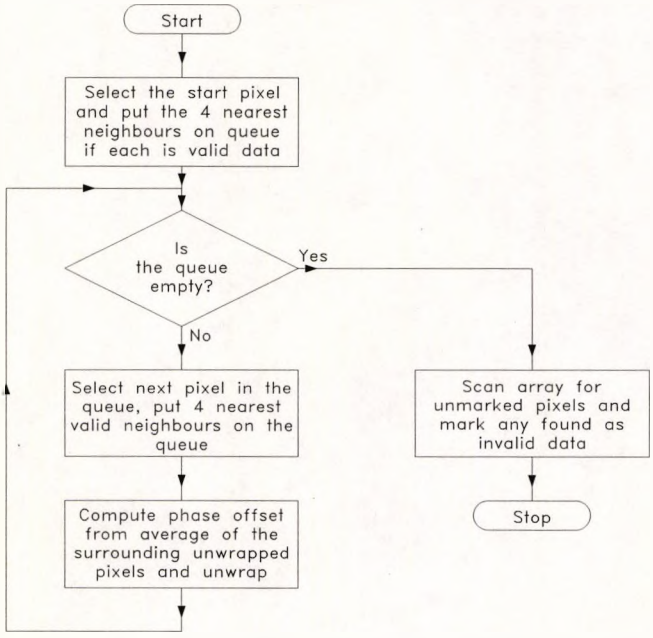


Figure 65: Flood unwrapping algorithm flowchart

The flood unwrapping algorithm is built upon a one-dimensional queue structure. A start pixel is located within the field to be unwrapped, the areas of invalid (bad) data having been previously flagged. All other pixels are unwrapped with reference to this pixel. The coordinates of the four adjacent neighbours of the start pixel are placed in the queue if they are not flagged as invalid (Figure 64a). The first of these four pixels is taken from the queue and unwrapped by comparing it with the average of all its valid neighbours (up to four pixels if all are valid). If the pixel needs adjusting, 2π is either added to or subtracted from the pixel until the average phase value of all the unwrapped pixels in a 3x3 neighbourhood is less than π, in which case the current pixel is marked as unwrapped. The next pixel at the output side of the queue is taken as the 'current pixel'. The pixel coordinates of new valid pixels surrounding the current pixel are placed at the input end of the queue, and all data is moved to the output side by one location. The process continues until the queue is of zero length, in which case the entire field is unwrapped (Figure 64d). Any regions which do not have at least one pixel width route into them will be excluded from the unwrapping. Any such regions must either be marked as invalid or unwrapped independently. A flowchart of the flood unwrapping algorithm is shown in Figure 65. Continuing with the example initiated on Page 100, the application of the flood unwrapping algorithm to the wrapped phasemap shown in Image 22 produces the unwrapped phasemap shown in Image 35, with a 3D representation of the greyscale phase displayed in Figure 66 (the data has been 'flipped' left-to-right for display purposes. This is the case for all the 3D unwrapped plots included in this thesis).

4.4 Displacement data extraction

The extraction of strain data from the phase data was discussed in section 2.2. It must be noted that the fringe analysis system described here will only provide the radial strain, the tangential (or hoop) strain cannot be measured. The radial displacement is proportional to the

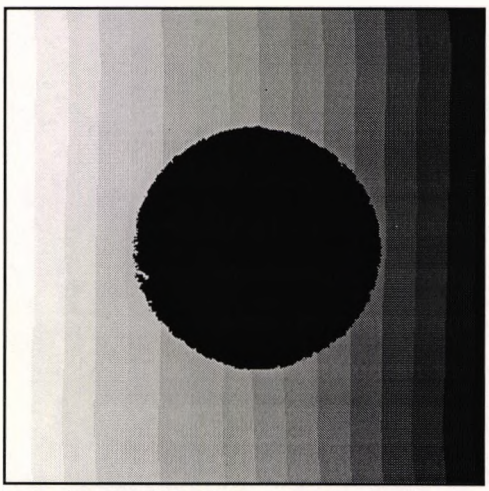


Image 35: Unwrapped phase

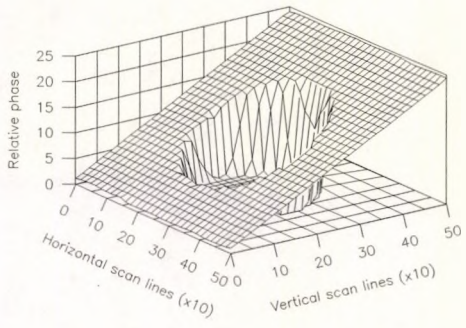


Figure 66: 3D Plot

phase in a radially sensitive in-plane interferometer (section 2.1.2.1). Once the relative phase has been extracted, multiplication by the sensitivity vector converts the phase to displacement. In the case of the rotating specimen tests, the magnitude of the sensitivity vector is constant at all pixel locations (since it is given by the wavelength and incidence angle only). The direction of the vector is found by referencing the centre location of the specimen disc. The gauge length over which the strain is to be measured is translated to a pixel count (using the ratio of the number of pixels per metre), and the displacement data from those pixels, starting from a desired location, and in the direction of the sensitivity vector, is recorded. A linear least-squares fit is applied to the data, to obtain the best fit line, and the gradient of the line is measured. The physical change in the displacement between the ends of the line is divided by the distance between the ends of the line, giving a direct measure of the strain.

4.5 Computer software

The computer software developed for this research project was written using the Microsoft C compiler (version 6.0), and later the Microsoft C++ compiler (version 7.0). The software was developed to run under the Microsoft DOS (MS-DOS) operating system (version 5.0), and to interface specifically with the Imaging Technology VS100 768/2 frame store. An image processing link library (ITEX version 2.0) was used to interface with the frame store. The hardware interface instructions to the electronic control unit were issued via an Amplicon Liveline PC36AT card. The software is not compatible with either ANSI or UNIX standards, since specific DOS calls are used extensively. Also, the large amount of data generated in the computation of a two-dimensional Fourier transform requires the use of extended memory (see Appendix A, section A.3), which is unique to DOS based machines. Additionally, the software is incompatible with the WINDOWS operating system.

The software philosophy used is that of the *parent/child* approach. Each application is written as a separate 'stand alone' program, to which parameters are transferred using the DOS command line interpreter. For example, to read an image from the disk into the framestore, the program 'READIMG' is used, which requires two parameters: the image name and the image page, to load into. The program is unloaded from the memory upon completion of its task. This approach allows a 'parent' program to 'spawn' other programs in much the same way as a main program calls subroutines or functions, and has many advantages over the use of a large program with many subroutines:

- At any one time, there are only two relatively small programs in the computer memory. Thus, each application can allocate more memory.

- The modification of a child program does not require the recompilation of the rest of the suite (crude object orientated programming).
- The child program can be run alone, which is useful for debugging.
- Simple DOS batch files can be created to perform repetitive tasks.

In the following few sections, only the most important computer programs are discussed, since over 300 programs were written for the project, but most performed rather trivial tasks. A detailed knowledge of the IBM AT type computers is required to understand the terminology, the fundamentals of which are described in Appendix A.

4.5.1 Computation of forward 2D DFT

No software existed to compute large two-dimensional Fourier transforms on a PC at the time this software was developed, thus a routine was written explicitly to perform the task, the flowchart of which is shown in Figure 67. To make the routine viable, RAM memory rather than disk had to be used to store intermediate variables[63]. A simple calculation for a 512

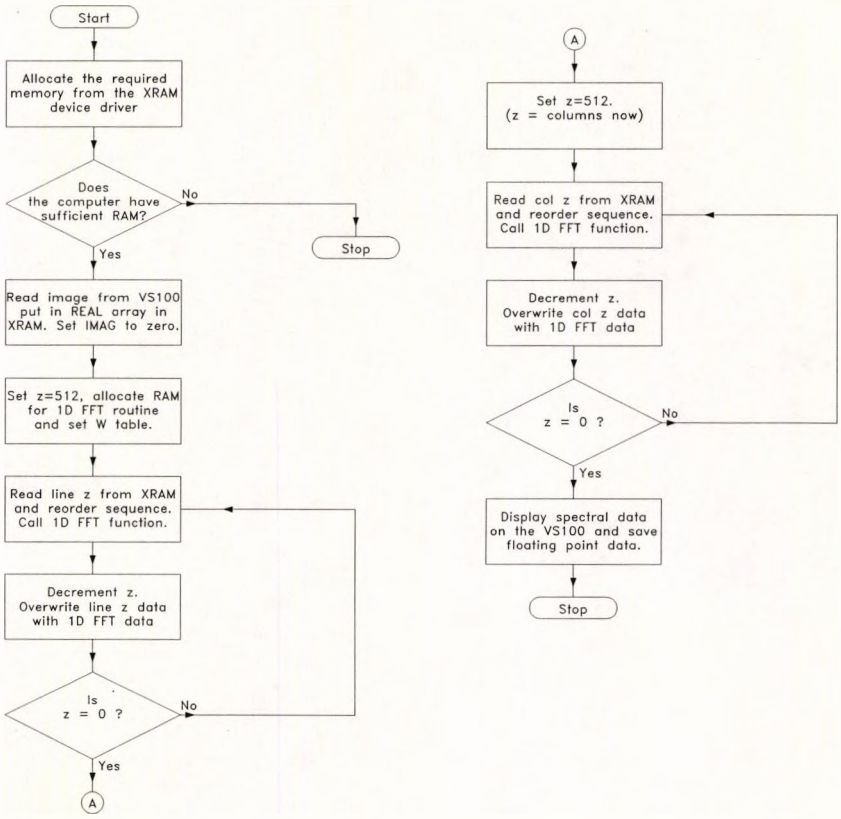


Figure 67: Forward Fourier transform program flowchart

[63] A single forward 512 square two dimensional Fourier transform would require over one half million disk I/O operations. Random access memory is at least 10,000 times faster than disk.

square two-dimensional Fourier transform yields the amount of RAM memory required for storage. A 512 square array is 262,144 points, and at each point, the Fourier transform yields a real and imaginary floating point number. For Microsoft C, 8 bytes are required per double precision floating point number. So, the total memory required to store the data is 262,144 x 8 x 2 = 4,194,304 (exactly 4MB). Single precision floating point was initially used, but it was found to give slight errors[64], the actual significance of which was not determined. Section 4.2.1.2 explains how the two-dimensional Fourier transform can be computed by using a one-dimensional fast Fourier transform algorithm. The one-dimensional algorithm is presented in Appendix B, section B.1. Appendix A, section A.3 explains the extended memory addressing used on 80x86 computers.

Data storage in extended memory causes the execution speed of the program to reduce (as compared with data storage in conventional memory). Also, the computation of the rows of the Fourier transform is considerably faster than the computation of the columns, because the extended memory is treated like a *linear* data array. Two 2MB blocks of extended memory are opened, referred to as REAL and IMAGinary in Figure 67. The 512x512 data array for one of the extended memory blocks is shown in Figure 68; each square represents 8 bytes. To read one row of data, two calls to the extended memory driver with the length set to 4,096 bytes (since 512 x 8=4,096) are all that is required (one for real and one for imaginary). However, to get a column of data, 1,024 calls to the extended memory driver with the length set to 8 bytes are required (since the vertical data points are separated by 512 values). Each call of the extended memory driver causes the processor to be mode switched, which is time consuming.

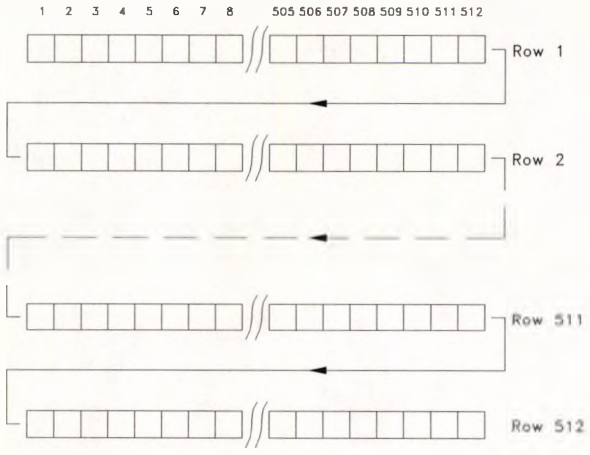


Figure 68: Extended Memory structure

[64]When an image is transformed then inverted, it should result in exactly the same image. However, when the recovered image was subtracted from the original, a null field did not remain.

The offset pointer for any double precision data point in the extended memory is:

$$Offset\ pointer = (long)x*8L + (long)y*4096L \qquad [108]$$

where $0 \leq x,y \leq 511$, and are the coordinates of the required double precision data point value. The offset pointer points to the start byte in extended memory of a single data point or row of data points. The 'L' after the numbers is standard C terminology for a number stored in long format.

Returning to the description of the program (flowcharted in Figure 67), the initialization process checks the available memory on the computer. If there is less than 4MB of extended memory available, or more specifically less than two 2MB blocks available[65], the program terminates. If the test passes, it then converts the image in the VS100 into double precision and stores this in the REAL block in the XRAM. The IMAGinary block is zeroed. The first pass of the program reads the row data sequentially from the XRAM. Alternate points are negated to give half period reordering (see section 4.2.1.3). The one-dimensional fast Fourier transform algorithm is applied to the data. The transformed data (which is now complex) is copied to the extended memory, overwriting the row under consideration. When all rows of the image have been transformed, the program transforms the columns. The complex column data is read from the extended memory, transformed, and overwrites the same memory space in extended memory. Once the complete transform is computed, the spectral density is computed and displayed on the VS100. Many image spectra decrease rapidly as a function of increasing frequency and their high frequency terms have a tendency to become rather obscured when displayed in image form. For this reason, two spectra are computed and displayed in pages 0 and 1 of the VS100. The first is the standard spectrum scaled to fit the dynamic range of the framestore (this spectrum is $|F(u,v)|$). The other is called the *logarithmic spectrum*, and compensates for the display difficulties. The logarithmic spectrum is defined as:

$$D(u,v) = \log(1 + |F(u,v)|) \qquad [109]$$

Equation [109] preserves zero values in the frequency plane since $D(u,v)=0$ when $|F(u,v)|=0$. It should be stressed that the Fourier transform data is in no way altered, only the method of displaying the data is changed. All of the Fourier spectra shown in this thesis were processed using Equation [109] unless otherwise stated. Once the spectral density is displayed, the operator can manually apply a frequency space filter using the system mouse.

---

[65]Some advanced memory management systems will allocate 'fragmented' memory as a single block. However, this type of memory is not recommended for this application. Therefore, the program checks for the largest blocks rather than absolute available RAM.

4.5.2 Filtering in the Fourier domain

The VS100 framestore has four *overlay planes*, thus every pixel in the frame memory can be marked with sixteen different 'flags'. The overlay planes of the VS100 are used to flag points to be included in the passband of the Fourier domain filter. The points in the REAL and IMAGinary arrays, which correspond to points *inside* that passband, remain unchanged, those *outside* are multiplied by zero. Although complex filters were described earlier in the chapter (section 4.2.1.5), it was found that for the very *tight* Fourier filters used in speckle type images, the difference between an ideal passband filter and some of the more complex filters was insignificant. The extent of the window is determined by the operator, using the PC mouse and a library of standard shapes. The window is constructed *around* the required frequency space information, as shown in the typical Fourier domain filter of Figure 69.

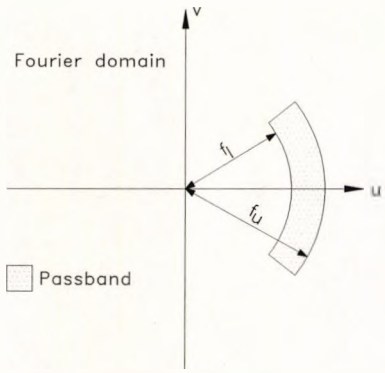


Figure 69: Typical Fourier window

An example of *loose* filtering is shown in the following diagrams. Image 36 shows a typical fringe pattern from a rotating disc. The 3D plot of the modulus of the Fourier transform is shown in Figure 70. The application of a 'tight' Fourier filter produces the spectrum shown in Figure 71. The wrapped phasemap, computed from the filtered spectrum, is shown in Image 37. It is worth noting that since the filter removes high frequency information, then the discontinuity (hole) in the fringe field is almost completely smoothed out. A less tight filter, producing the spectrum shown in Figure 72, allows a greater proportion of the high frequencies to pass. The resultant wrapped phasemap is shown in Image 38. Notice that the hole is now starting to reappear, due to the introduction of higher frequencies in the passband.

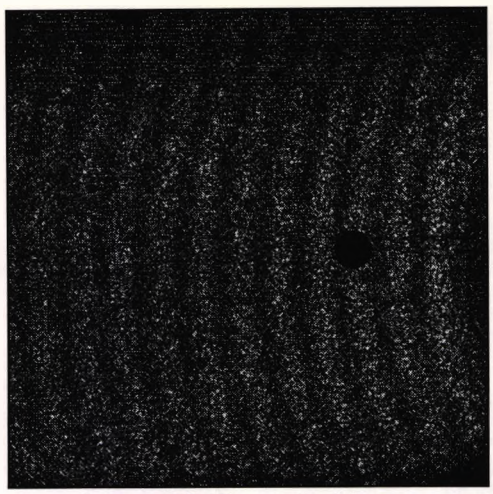


Image 36: Example fringes

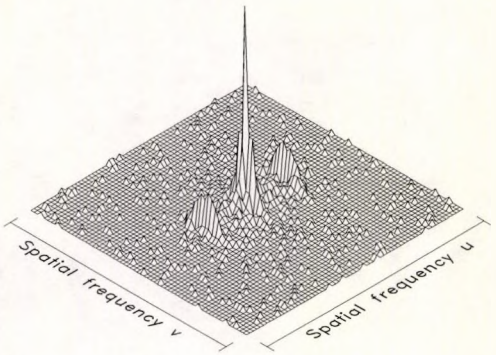


Figure 70: 2D FFT of Image 36

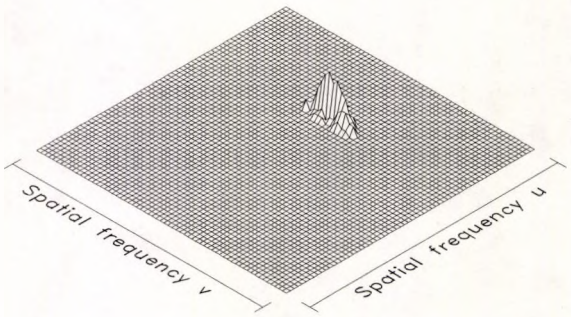


Figure 71: Tight filter (1)

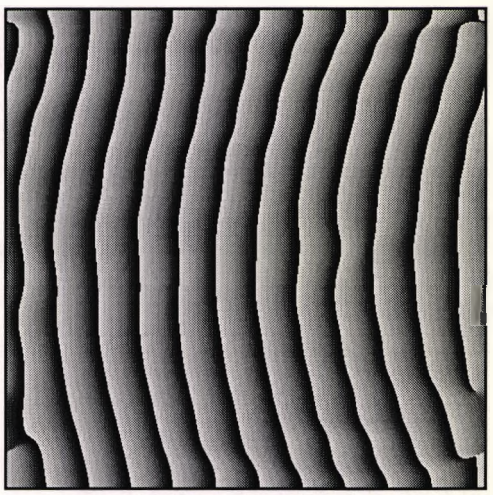


Image 37: Unwrapped phase (1)

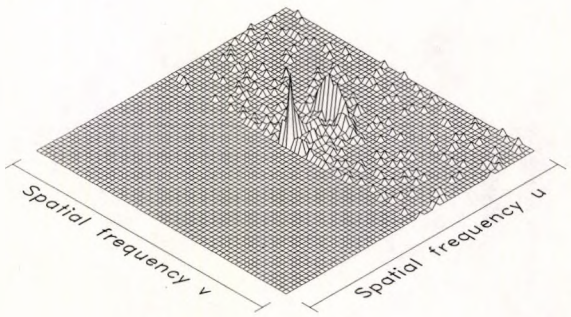


Figure 72: Loose filter (2)

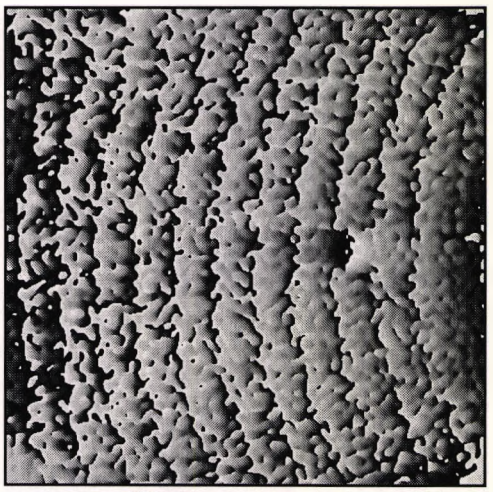


Image 38: Unwrapped phase (2)

4.5.3 Computation of inverse 2D DFT

The computation of the inverse 2D DFT is substantially faster than the computation of the forward transform, because the Fourier filtering process reduces considerably the number of *columns* which need to be transformed, and therefore increases the execution speed of the program. The process of inverse transformation uses the same one-dimensional fast Fourier transform algorithm as the forward transformation (see section 4.2.1.1). A flowchart of the program is shown in Figure 73. Initially, the program ensures that the data in the extended memory blocks is valid, and that a Fourier transform filter has been applied to it. Once this

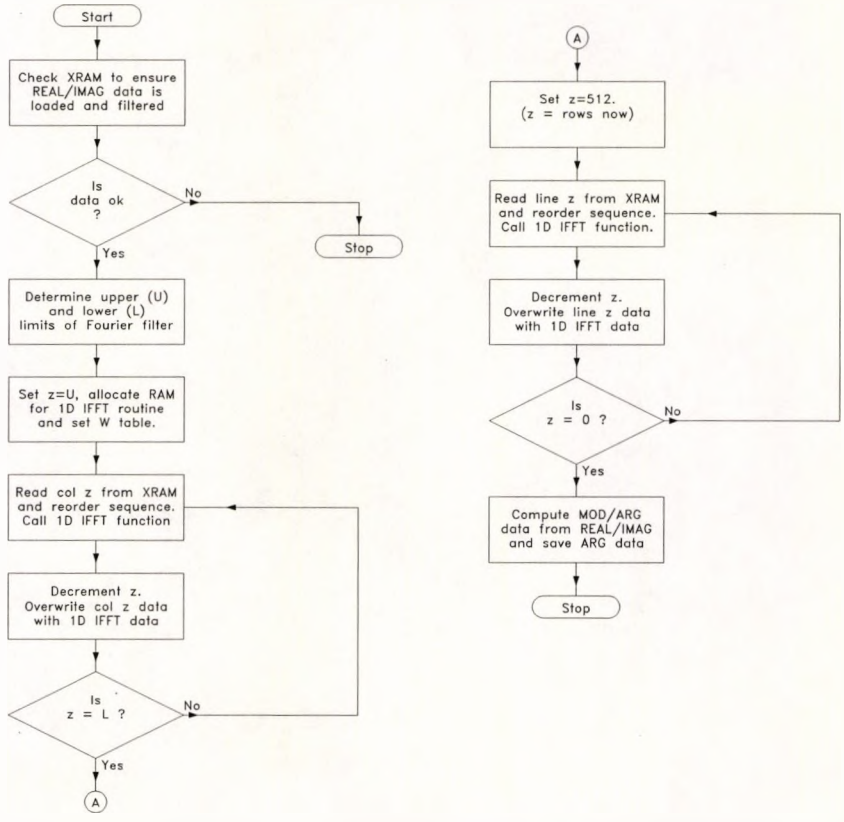


Figure 73: Inverse Fourier transform program flowchart

is complete it checks all the columns, and those which do *not* have a filter overlay 'flag' in them are zeroed. The program determines the upper (U) and lower (L) limits of the horizontal extent of the filter, since only the columns between L and U need to be processed. The complex column data is read sequentially from the extended memory for all the columns which *do* have a filter overlay 'flag' in them (between L and U). The imaginary component of each column is negated and the inverse fast Fourier transform algorithm applied, after which sequence reordering is then applied. The transformed data overwrites the columns in the extended memory. The second pass of the inverse routine reads *all* the rows sequentially and

transforms them (again negating the imaginary component of each number). Finally, the real/imaginary data of the inverse transformation is converted to modulus/argument data using normal complex number theory. It is noted here that the *argument* data is computed from the ratio of the imaginary to real components:

$$Arg = \tan^{-1}\left[\frac{\Im}{\Re}\right] \qquad [110]$$

which is the same as Equation [100], hence the origin of the wrapped phasemap. The wrapped phase data is scaled and displayed on the VS100 screen.

4.5.4 Phase unwrapping

The basic flowchart for the flood unwrapping program is shown in Figure 65. Initially, the program checks the extended memory for the ARGument data generated by the inverse Fourier transform program. If this data is unavailable, the program terminates, otherwise it asks the operator for the threshold value to be used for determining if a phase discontinuity exists, which is normally π. It then performs a raster search of the data field to discover if any regions of invalid data have been previously 'flagged'. If it fails to find any, it prompts the operator for any invalid regions to be marked. The PC mouse is used to 'paint' erroneous regions, which will be excluded from the unwrapping procedure. An advanced 'paint' program was written which allows various 'brush' sizes, fills and shapes to be used. Once this is complete the program asks the operator for the start pixel location. This can be entered either as pixel coordinates in the VS100 coordinate system, or by using the computer mouse to point to a location on the screen. If the start location is unsatisfactory[66], the program asks the operator to select another point. Once under way, it performs a double precision floating point unwrap of the data in approximately 6 minutes[67]. The unwrapped phase data is scaled and displayed on the VS100 monitor, the double precision data being saved on hard disk.

4.5.5 Speckle image quality determination

The main program which captures the speckle patterns from the rotating disc has a routine to give the operator an indication of the 'quality' of the speckle pattern image for each fire. This is necessary because the JK 2000 pulsed laser is notoriously inconsistent, suffering from large energy fluctuations from fire to fire, resulting in large intensity variations in the speckle patterns. The correlation of two speckle patterns is higher if the images are of close average intensity [Jones and Wykes, 1977; Wykes, 1977]. Various attempts were made to define a

---

[66] It could be that the start point is too close to some invalid data, or inside an invalid region.

[67] This is for a 512x512 data field with no bad data, running on a 33MHz 80486 with 128K cache and 16MB of RAM.

parameter which gave the best correlation fringes, which was finally found to be the percentage of the image which contained black pixels. Originally, the percentage of black pixels on the *even* lines only was used, since the odd interlace was much darker than the even interlace (section 3.1.1.4). However, when the software to equalise both interlaces was implemented (section 3.2.1.4), the image quality parameter was altered to compute the percentage of the black pixels in both interlaces. Care is taken to avoid 'dead' lines at the top and bottom of the screen, since these are always black. Also, the parameter is ignored if large 'dead zones' are in the field of view, since these tend to desensitise the measurement.

The reason why the parameter is a good measurement of 'quality' is introduced on Page 28. The speckle patterns obey negative exponential statistics (Graph 1), therefore, the largest number of values in any given greyscale will be black (greyscale 0 in the VS100), which will make it the most sensitive measure of brightness fluctuations.

4.5.6 Disc centre coordinates

The coordinates of the centre of the rotating disc must be computed in the coordinate system of the framestore, in order to differentiate the phase data radially. To enable this, a fine line was drawn along the radius of the disc. Illumination with ordinary light allows several images of the line in *different* angular positions to be taken. Once the required number of images are stored, the user is asked to mark two points on the line in *each frame*, using the computer mouse. For each line, the program generates an equation and then solves *all possible* combinations of intersection (2 lines have 1 solution, 5 lines have 10 solutions, and so on). The average value of the solutions is computed to give the coordinates of the disc centre. The coordinates will be outside the numerical range of the framestore axis ($0 \leq x,y \leq 1023$). This does not cause a problem, since the centre coordinates are only used to compute the *direction* of the radial vector within the framestore range.

4.5.7 Camera calibration

Calibration of the camera and framestore is achieved by establishing a relationship between the object under examination and the discrete image stored in the VS100. It is important to be able to map between the two domains with relative ease. It should be realised that a 3D to 2D transformation (object space to image plane), is a many-to-one mapping, and as such, the reverse mapping is not possible. Imaging an object in the plane of examination and computing the number of pixels that the object occupies provides a good estimate of the magnification.

If an object of length L metres occupies N pixels in the frame memory, then for a 512x512 image array with square pixels, the imaging area will be:

$$\textit{Imaging area} = \left[\frac{512L}{N}\right]^2 \quad m^2 \qquad [111]$$

Of course, the accuracy to which an object can be measured by the computer is often limited, so many measurements of different known features in an image are necessary.

5 RESULTS

5.0 Results

Simulated test data was used for the detection of software errors. The test data, which often consisted of computer generated 'ideal' cosine fringes, with various amounts of random noise, was useful in the detection of a considerable number of coding 'bugs'. However, some of the more subtle coding errors, which remained undetected in the simulations, necessitated the use of real interferometric data. It is for this reason that the static tests of section 5.1 (and many more unpublished tests) were conducted, in order to ascertain the existence of additional problems with the acquisition system, correlation or Fourier transform software.

As stated, in order to determine the effectiveness of the computer processing system for the measurement of radial in-plane strain from a rotating specimen, a series of static tests was conducted. In these tests, many of the experimental parameters could be controlled with great precision, and alternative methods of measurement could easily be incorporated, for comparison purposes. The Fourier transform method of fringe analysis has no 'in-built' rules about the type of fringe pattern it is required to analyse, and consequently the use of a plane mirror electronic speckle pattern interferometer is a realistic simulation test. The signal-to-noise ratio, fringe density and sensitivity are all similar to the radially sensitive in-plane system[68]. The use of a simple flat plate tensile specimen, equipped with strain gauges, and subjected to axial loading, is considered sufficient to determine the worthiness of the software.

Section 5.2 contains results from a rotating specimen, at different rotational speeds, and subjected to various accelerations. Previous specimens were used with the experimental rig, but at the time of testing, no reliable data storage medium existed, and the numerical image data was deleted to provide storage space on the PC disk[69]. The incorporation of a SCSI interface, with a removable hard disk and tape backup now overcomes this shortcoming.

---

[68]Only the shape of the fringes, and therefore the shape of the Fourier filter, is significantly different.

[69]The results are stored in photographic format, which cannot be analysed with the computer software, and are therefore not included in this thesis. Attempts were made, without success, to rescan the images into the computer.

5.1 Results from static specimens

5.1.1 Experimental apparatus

The schematic diagram of the static in-plane measurement system is shown in Figure 74. The video camera is a COHU type 4990 HAD interline transfer CCD with a resolution of 752x582 pixels[70]. It is mounted on a linear translation stage to permit increased correlation of the images to be obtained when the specimen is strained. The laser illumination, provided by a 30mW HeNe, is spatially filtered from a distance of approximately 0.8m, prior to incidence on the specimen surface, causing it to diverge slightly[71]. A diagram of the first specimen (without a central hole) is shown in Figure 75, and the second specimen (with a hole) in Figure 76. The material used for both specimens was 99.1% aluminium alloy (material code S1C). Both specimens were fitted with two strain gauges, one on each side (Figure 77), and a pair of dummy gauges were fitted to a piece of similar material, to eliminate thermal effects. The active gauges were calibrated by hanging the specimen vertically, and applying known loads. The initial wiring configuration is shown in Figure 78 (left), which is setup to measure bending[72]. The gauges were of type FLA-1AS-11, with a gauge length of 1mm, a resistance of $120 \pm 0.3\Omega$, and a factor of 2.17. The Wheatstone bridge measuring device was a Measurements Group 3800 Wide Range Strain Indicator. The output voltage of the strain indicator was set to 4V in order to prevent thermal heating of the gauges. Once it was established that bending and thermal effects were not a problem[73], calibration of the gauges was performed, using the configuration shown in Figure 78 (right).

A Vickers hardness test was performed on the material to ascertain the mechanical properties more accurately. The Vickers hardness (HV_5) was found to be approximately 45, which inferred that the material was *fully hardened* S1C, with a 0.2% proof stress of approx.

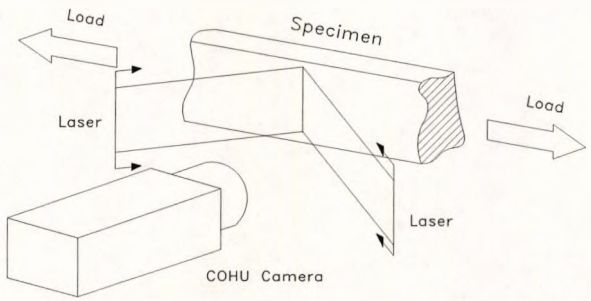


Figure 74: Optical measurement system

[70]Pixel cell size is 8.6x8.3μm.

[71]The error introduced by divergence is discussed in Chapter 6.

[72]The active gauges fitted to the specimen are designated *A*, the dummy gauges *D*.

[73]The maximum measured strain due to bending, over the experimental measurement range, was $\pm 5\mu$strain.

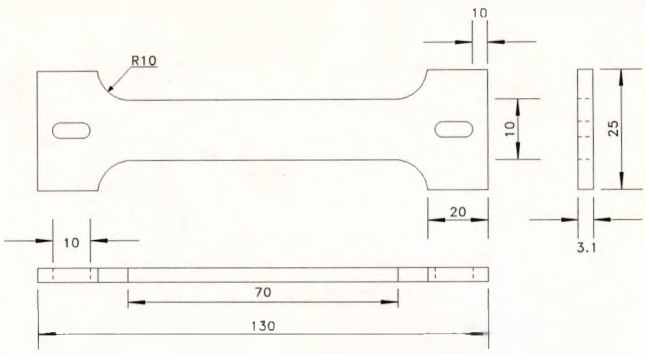


Figure 75: Specimen without hole

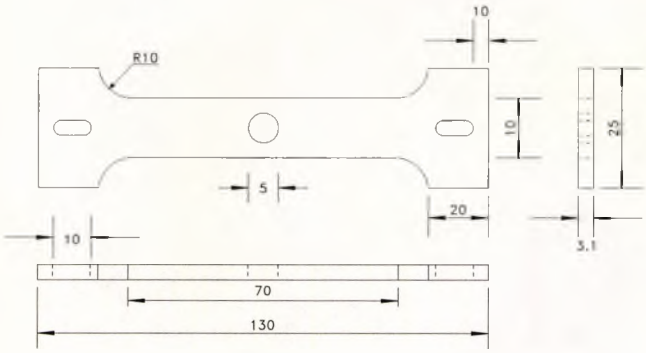


Figure 76: Specimen with central hole

135MPa, and an ultimate tensile strength of 150MPa. The modulus of elasticity, found from standard tables, is $68.2 \times 10^9 N\ m^{-2}$. One of the surfaces of the specimen was painted with a matt white paint to maximise the amount of scattered laser illumination. The paint used was manufactured by Automotive Chemical Ltd, and was paint number UN 1950.

The specimens were placed in a purpose built loading rig, which is shown in Image 39. The rig could only apply tension to the specimen, by tightening the bolt at the bottom of the loading system. The specimens are held in the loading jaws by means of 'pins' through the

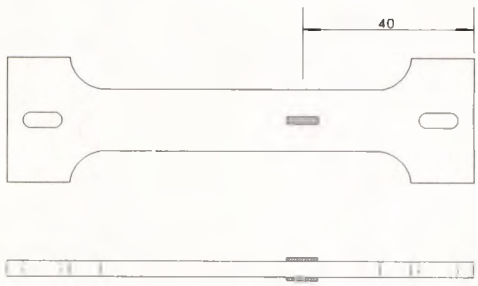


Figure 77: Strain gauge configuration

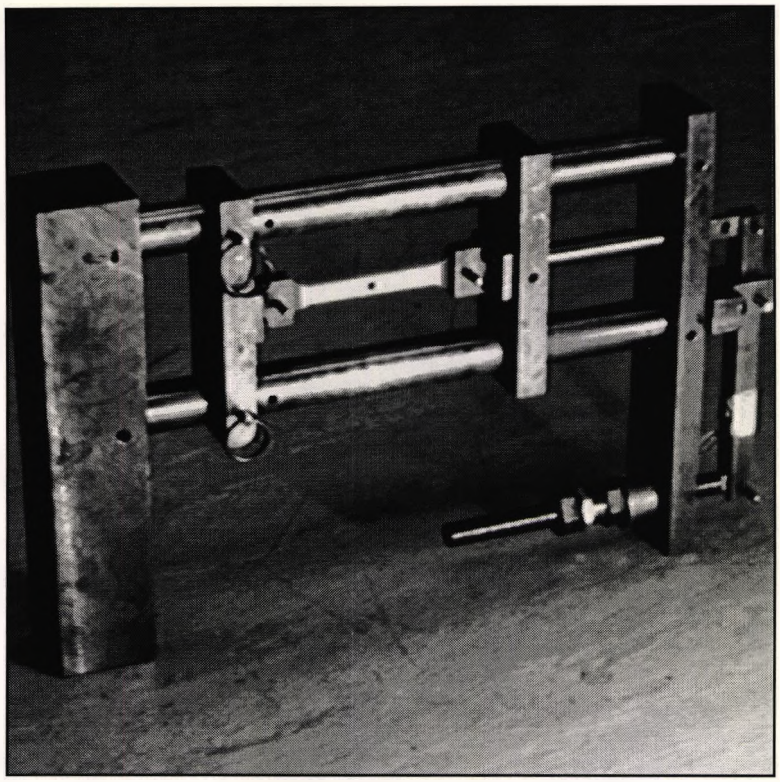


Image 39: Static loading rig

slots. During interferometric testing, the entire system is fixed to an optical table, so that vibrational movements do not disturb the fringe patterns. The optical table is fixed to a concrete mounting. The interferometric system is located in a small room, isolated from external air currents and ambient light.

5.1.2 Experimental procedure

The following description is applicable to the test of both specimens. After gauge calibration, the specimen was mounted in the tensile test rig and a small load applied to remove any slackness in the grips. A larger load was then cycled onto the specimen to ensure that all pins

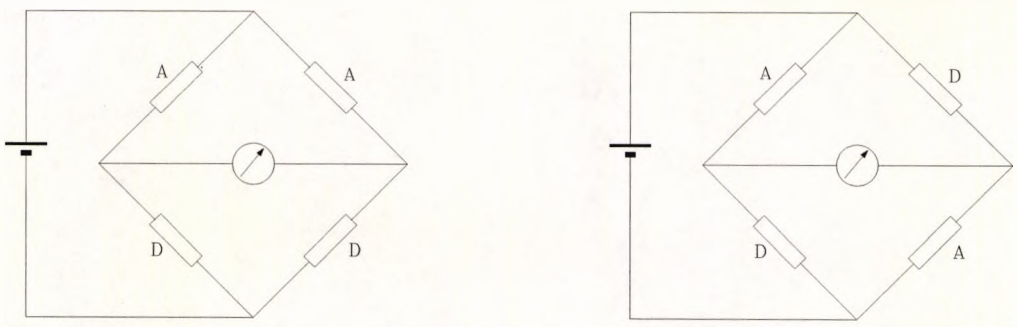


Figure 78: Strain gauge configurations: Bending (left), strain (right)

'bed in'. The specimen load was then adjusted so that it remained in a state of tension[74]. The camera was located close enough to the specimen to ensure that the image filled the entire image space of the VS100. The image was precisely focused using white light and a large aperture. The HeNe beam was then aligned onto the specimen, with the spatial filter removed. An accurate assessment of the incidence angle was obtained by 'glancing' the fine HeNe beam along a rule, and using a protractor to measure the angle between the rule and the specimen normal. The spatial filter was replaced and aligned. An image of the speckle pattern was obtained on the monitor, and the input gain of the VS100 set to 1.0. Real time carrier subtraction fringes from the specimen were obtained by tilting one of the interferometer mirrors. The gain of the camera was adjusted to optimise the contrast of the fringes. At this stage, the system was ready for use.

With the operator and computer located in a separate room, the rig was left for several seconds to allow the air surrounding the specimen to settle[75]. A reference speckle pattern was captured and stored on the PC hard disk. The VS100 was then switched into real time subtraction mode, and one of the interferometer mirrors tilted. The real time subtraction fringes on the monitor enabled the operator to select a precise carrier fringe pattern. The VS100 was then reset and a second speckle image captured. A load was applied to the loading frame, taking great care not to disturb any of the interferometric components. The reading from the strain gauge indicator was noted down, and after allowing the surrounding air to settle, an image of the speckle pattern was recorded. This procedure was repeated for further loads applied to the specimen.

The strain gauge readings were recorded for increasing load, and compared with the decreasing load, to establish if the specimen was subjected to excess load during the tests. In both of the tests described, the specimen was not subjected to excess load.

Since these tests were to determine the suitability of the Fourier transform software, the overall range of the measurements, and the fringe sensitivities were chosen to be similar to those expected from the rotating system.

---

[74]The reference speckle pattern must be recorded with the specimen in a state of tension, since in a relaxed state, rigid body motions are likely to occur when the load is applied.

[75]This procedure of leaving the air to settle was adopted prior to capturing all images.

5.1.3 Tensile tests

5.1.3.1 Flat plate tensile specimen without hole

Image 40 shows a steel rule placed in the object plane of the test specimen, and imaged using the camera. Several measurements from this image established that the inspection area was approximately 80.64mm^2, a single pixel was found to be equal to approx. 17.5μm (1mm $\approx$ 57 pixels). The angle of illumination, measured from the surface normal, was determined to be approx. 58°. Using Equation [15] from Page 31, the fringe sensitivity, for a HeNe laser ($\lambda = 628$nm) was calculated to be 0.38μm fringe^{-1}. A carrier fringe pattern, shown in Image 41, was recorded by tilting one of the interferometer mirrors, then the applied load increased in three increments, of 57μstrain, 110μstrain and 156μstrain, measured using the strain gauges[76]. The camera was operated with a numerical aperture of $f8$, and the gain was adjusted to produce an optimum video signal.

The fringe patterns, wrapped and unwrapped phasemaps[77], and loading phase fields for the tests are shown on Pages 132 to 135. An array of 'optical strain gauges' was used to determine the plane strain at 56 locations covering the image. The program 'STRAIN.EXE', which was written for this work, was employed to compute the strains. The gauge lengths were approximately 1mm (57 pixels), and the distance between them was 1mm vertically, as shown in Figure 86 (drawn to the same scale as the images). The plane strains for the various optical gauges, under the measured load increase of 57μstrain, are shown in Table 6. Table 7 and Table 8 contain the results for the higher load tests.

It can be seen from the fringe patterns that 'tilting' of the specimen occurred during the tests. This was due to the loading rig, which was designed for non-metallic specimens, requiring smaller loads than aluminium, was found to be slightly flimsy for this application. It was practically impossible to obtain correct axial loading of the specimen. It is for this reason that higher loads were not applied to the specimen, since the fringe patterns skewed by an unacceptable amount. Also, the expected loads from the rotating system were of this order, and it was considered satisfactory to restrict the range to less than 200μstrain.

---

[76] The gauges are on the right hand side of the images.

[77] It should be stressed that the 3D representations of the unwrapped phasemaps are 'flipped' horizontally (with respect to the vertical scan lines), for presentation purposes. Also, they are scaled to the same vertical scale.

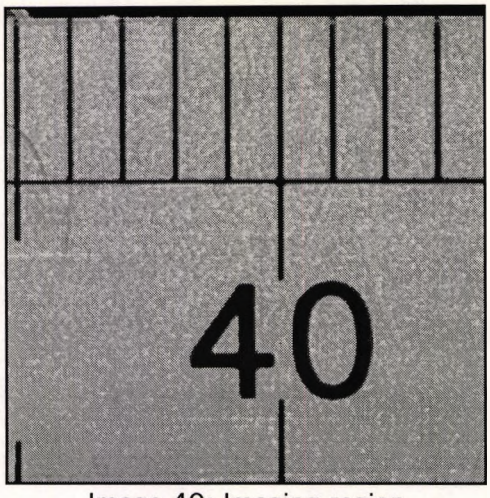


Image 40: Imaging region

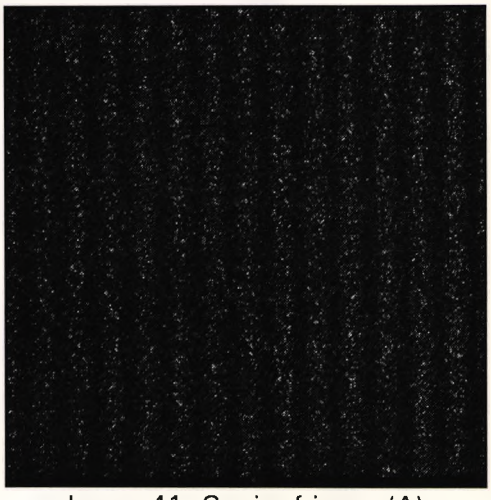


Image 41: Carrier fringes (A)

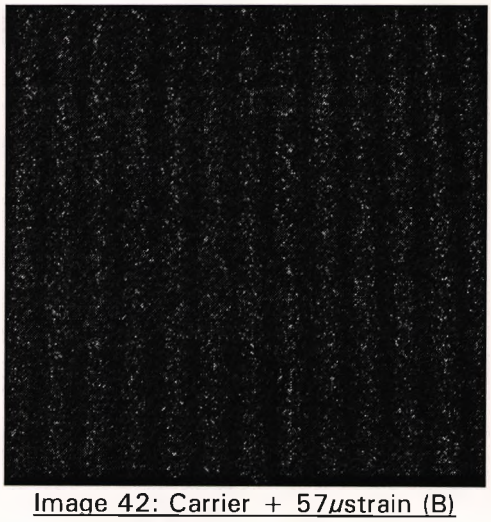


Image 42: Carrier + 57μstrain (B)

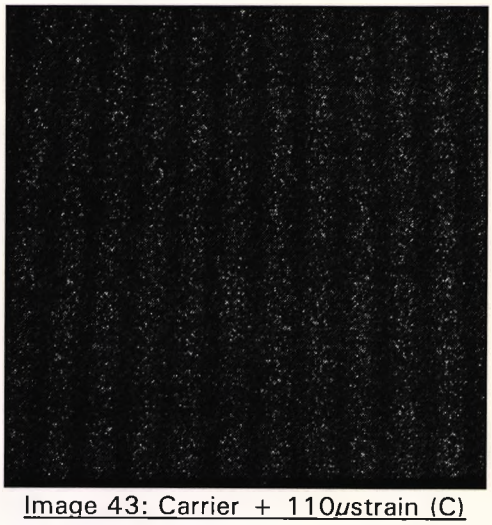


Image 43: Carrier + 110μstrain (C)

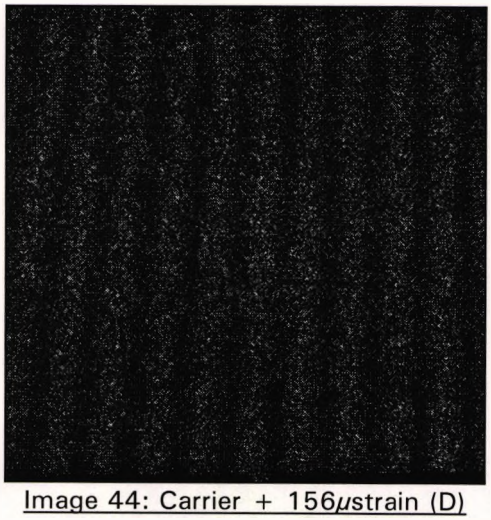


Image 44: Carrier + 156μstrain (D)

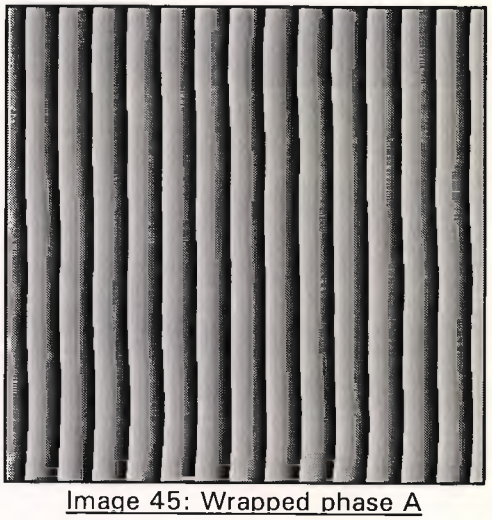


Image 45: Wrapped phase A

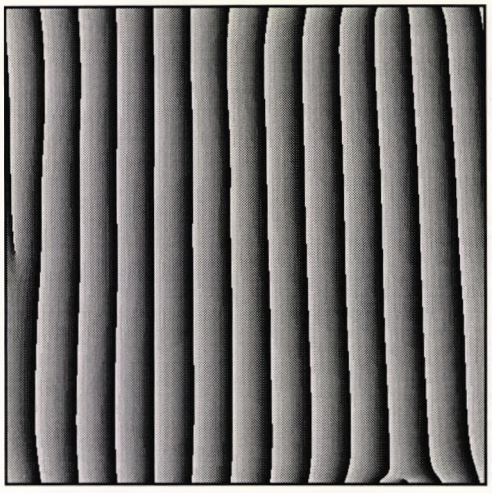


Image 46: Wrapped phase B



Image 47: Wrapped phase C

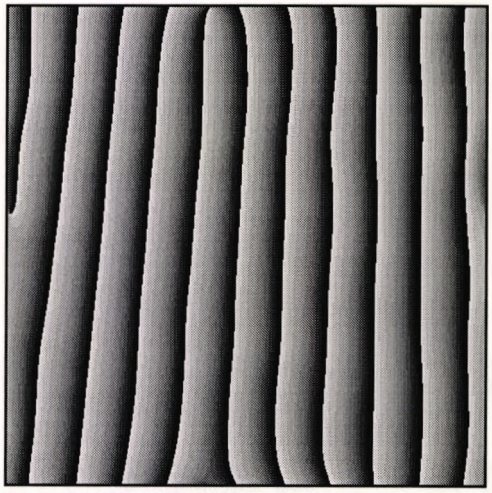


Image 48: Wrapped phase D

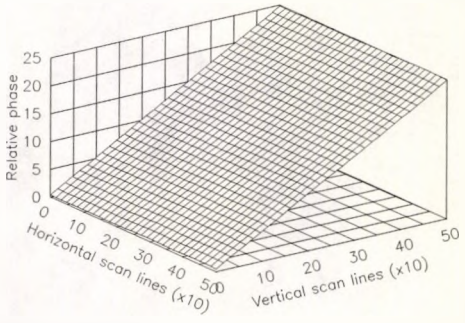


Figure 79: Unwrapped phase A

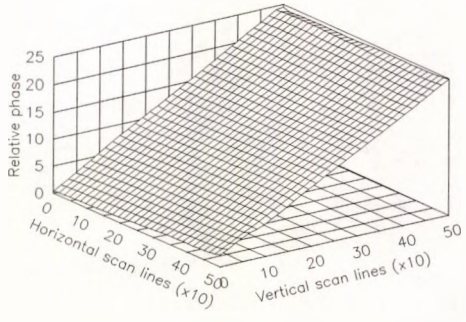


Figure 80: Unwrapped phase B

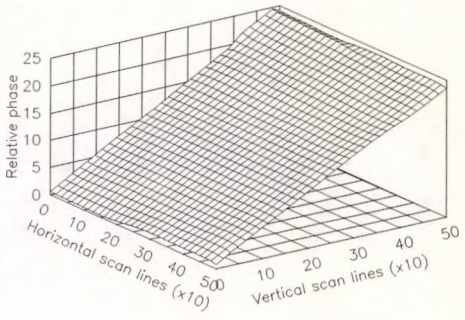


Figure 81: Unwrapped phase C

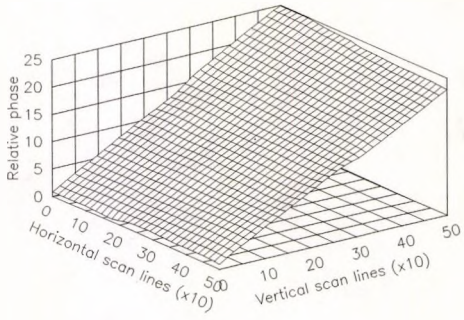


Figure 82: Unwrapped phase D

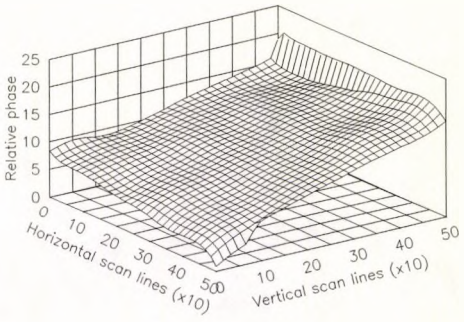


Figure 83: Phase B - Phase A

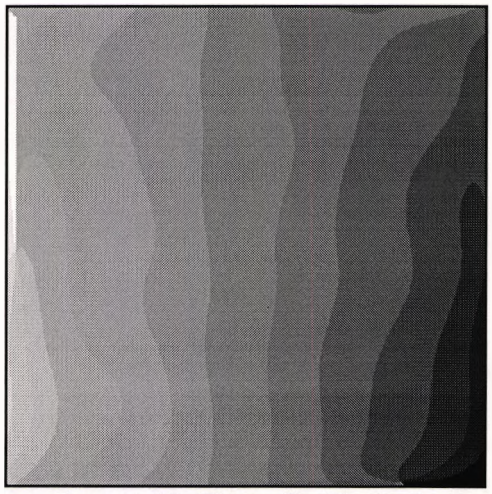


Image 49: Phase B - Phase A

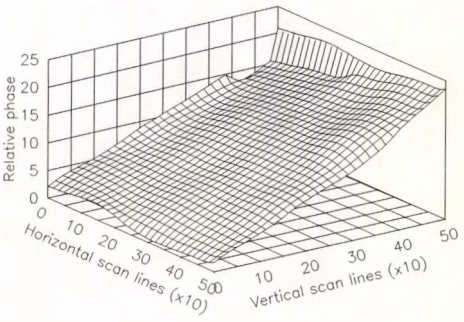


Figure 84: Phase C - Phase A

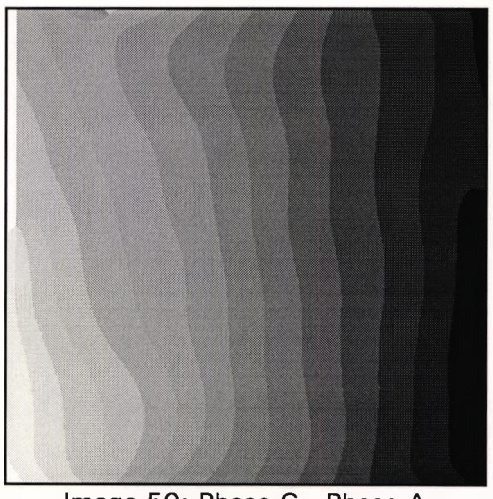


Image 50: Phase C - Phase A

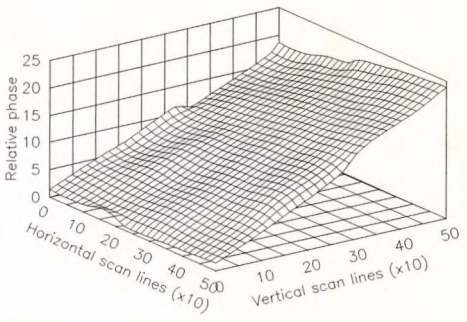


Figure 85: Phase D - Phase A

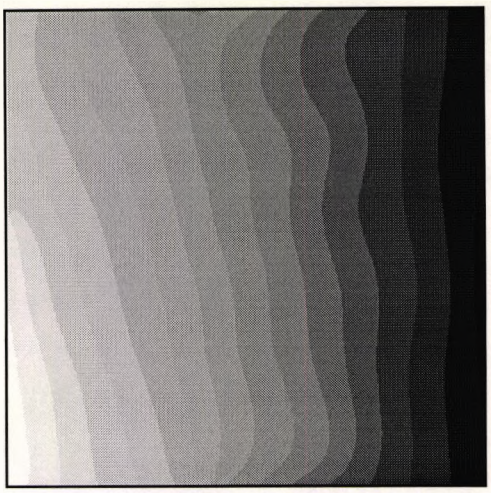


Image 51: Phase D - Phase A

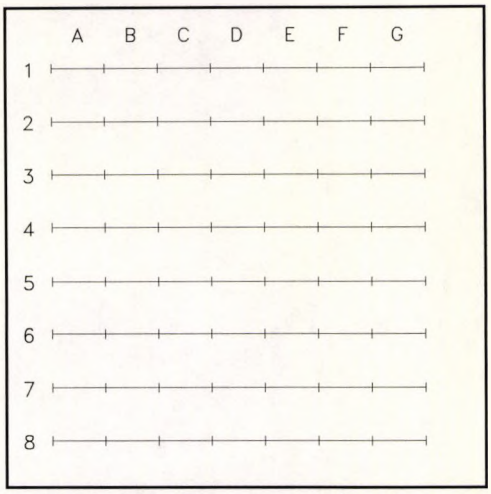


Figure 86: Gauge array locations

	Optical strain gauge (reading in μstrain)						
	A	B	C	D	E	F	G
1	34.1	31.4	37.8	45.1	55.2	25.3	30.1
2	24.5	43.6	46.1	57.2	56.6	48.7	46.4
3	42.7	46.3	51.1	57.6	56.6	61.3	57.7
4	52.3	46.1	51.9	52.7	59.5	57.6	53.5
5	68.2	28.3	54.8	53.2	57.3	51.5	52.9
6	75.2	41.1	63.8	52.5	62.0	57.7	55.9
7	72.2	59.5	86.2	56.7	70.1	65.8	58.4
8	71.2	60.5	86.2	61.8	68.4	79.1	60.2

Table 6: Strain measurements for 57μstrain load increase

	Optical strain gauge (reading in μstrain)						
	A	B	C	D	E	F	G
1	66.2	76.9	71.6	79.3	97.4	92.2	90.8
2	84.1	71.7	90.8	102.5	108.3	108.1	102.4
3	84.6	68.8	93.7	101.7	108.2	104.5	105.9
4	97.7	81.4	95.7	112.9	106.2	106.5	107.5
5	118.1	72.5	90.9	117.0	105.3	109.2	100.1
6	119.9	88.9	92.7	111.0	109.8	112.4	105.3
7	118.9	103.1	125.0	123.9	108.2	110.1	113.2
8	104.9	108.5	145.4	123.2	101.8	126.4	115.2

Table 7: Strain measurements for 110μstrain load increase

	Optical strain gauge (reading in μstrain)						
	A	B	C	D	E	F	G
1	115.5	105.9	114.5	129.9	138.0	97.1	103.7
2	116.3	101.4	148.1	152.6	162.3	159.6	148.5
3	123.6	122.4	143.5	157.7	146.4	147.1	148.1
4	133.0	129.8	153.5	162.3	157.2	151.7	149.2
5	157.4	130.6	149.5	144.9	154.6	151.4	149.3
6	166.4	132.8	150.8	156.8	145.5	149.9	145.2
7	175.6	155.5	162.5	150.6	149.6	174.9	165.3
8	164.2	149.2	177.5	151.9	139.8	189.5	175.3

Table 8: Strain measurements for 156μstrain load increase

To look at the results in a little more detail, consider the situation of perfect plane axial loading of the specimen. In this case, with a gauge length of 1mm, a load of 57μstrain, the resulting extension over the gauge length would be 57nm. If the Fourier transform software determined the plane strain *exactly*, then for a fringe sensitivity of 0.38μm fringe^{-1}, the measurement accuracy would be approximately 7^{-1} of a fringe. This figure is more than reasonable, and in fact the accuracy is expected to be *at least* 20^{-1} of a fringe (Chapter 6). However, it can be seen that if the Fourier transform accuracy is 20^{-1} of a fringe, then the smallest strain which can be determined is 18μstrain (for a fringe sensitivity of 0.38μm fringe^{-1}). Therefore, for the 57μstrain test, the system is operating quite close to the

measurement floor, and the results will be subject to higher errors (since the errors are quoted as a percentage of the load). The expected error on these measurements would be approximately 33% (if it is assumed that the Fourier transform software is operating at 20^{-1} of a fringe). With reference to Table 6, the 25 optical gauges in the rectangular range C2 to G6 have an average of 55.4μstrain, and a standard deviation of 4.4μstrain, and a peak error of 19%, indicating that for the region of gauges under consideration, the Fourier transform analysis software is operating with a accuracy of approximately 35^{-1} fringe. When considering the whole of Table 6, the average is 54.6μstrain, standard deviation of 13.3μstrain, and peak error of 51%. The large error is due to edge effects of phase data, resulting from abnormal truncation of the fringe field prior to Fourier transformation. Also, the error is quoted with reference to the strain gauge reading, which will itself be subject to errors. In some cases, the error on a strain gauge can be as high as $\pm 5\mu$strain, which would almost completely encompass all the errors in the range C2 to G6 of Table 6. Table 7 shows results for an applied load of 110μstrain[78]. When considering the data for this test, it is noted that the degree of fringe skewing is higher than the previous test, and therefore the errors in the skew region can be expected to be high (this is not to say that the specimen was not subjected to a high load in that region). With reference to Table 7, the region of 24 gauges in the rectangular range D2 to G7 have an average measurement of 108.3μstrain, a standard deviation of 5.1μstrain, and a peak error of 12%. The data for the entire range has an average value of 101.8μstrain, standard deviation of 16.0μstrain, and a peak error of 40%. The plane strain results for the applied load of 156μstrain are shown in Table 8. The 25 optical gauges in the rectangular range C2 to G6 have an average value of 151.4μstrain, a standard deviation of 5.2μstrain, and a peak error of 8%. The complete data set has an average of 146.2μstrain, standard deviation of 19.6μstrain, and a peak error of 37%.

In the determination of the optical measurements, the program 'STRAIN.EXE' uses linear regressional analysis to determine a best fit line to the data. In all the measurements presented in this section, the accuracy of the data fit (measured by r^2), was better than 0.96. The closer r^2 is to 1.0, the closer and more predictable the relationship between the variables.

Therefore, in summary, it can be seen that for relatively small loads, and in regions of reasonable fringe spacing, and without discontinuities in the image, the electronic speckle pattern interferometer, and Fourier transform fringe analysis software demonstrate measurements which are very close to the strain gauge. The situation for a fringe field with a central discontinuity is examined in the next section.

---

[78]As measured by the strain gauges.

5.1.3.2 Flat plate tensile specimen with hole

The specimen for this test had a central hole, which was half the width of the specimen (see Figure 76). Such a configuration, in a plane state of stress, has an exact analytical solution [Howland, 1930], which can be used for comparison purposes. A white light image of the area under investigation is shown in Image 52. The hole is 5mm in diameter, which when measured by eye using the framestore, has a diameter of approximately 273 pixels. Therefore, each pixel is approximately 18.3μm, and the area of the image is approximately 87.80mm^2. The angle of illumination, measured from the surface normal, was found to be approx. 58°, producing a fringe sensitivity, for a HeNe laser ($\lambda = 628$nm), of 0.38μm fringe^{-1}. The camera was operated with a numerical aperture of $f8$, and as in the previous test, the gain was adjusted to produce an optimum video signal. A carrier fringe pattern, shown in Image 53, was recorded by tilting one of the interferometer mirrors, then the applied load increased in four increments, of 54μstrain, 102μstrain, 153μstrain and 212μstrain, measured using the strain gauges[79]. The fringe patterns, wrapped and unwrapped phasemaps[80], and loading phase fields for the tests are shown on Pages 139 to 142.

An array of 'optical strain gauges' was used to determine the plane strain at 46 locations covering the image (excluding the central area). As in the previous section, the program 'STRAIN.EXE', was employed to compute the strains. The gauge lengths were approximately 1mm (55 pixels), and the distance between them was 1mm vertically, as shown in Figure 96 (drawn to the same scale as the images).

Image 67 is a representation of the discontinuity in the fringe field (the mask used to mark invalid data in the phasemaps). The modulus of the two-dimensional Fourier transform of Image 67 is shown in Image 68, and indicates the magnitude of the 'high frequency' ripples which are convolved with the phase data. The plane strain results for three of the tests are presented (Table 9 to Table 11), the final test was not analysed.

---

[79] The gauges are on the right hand side of the images.

[80] It should be stressed that the 3D representations of the unwrapped phasemaps are 'flipped' horizontally (with respect to the vertical scan lines), for presentation purposes. Also, they are scaled to the same vertical scale.

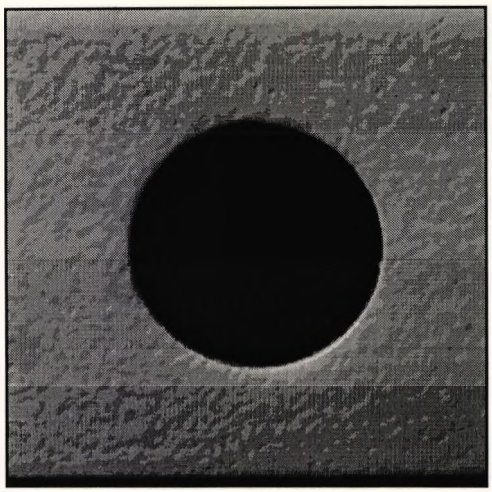


Image 52: Imaging region

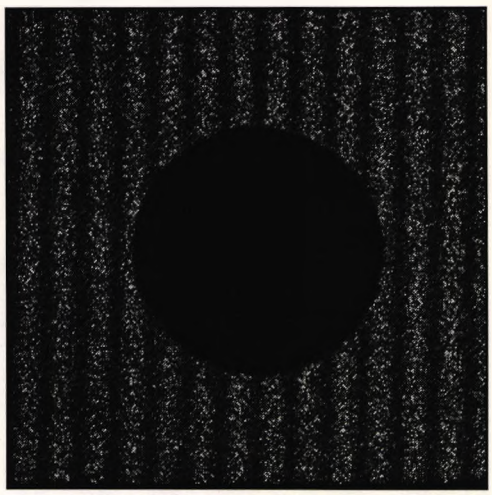


Image 53: Carrier fringes (E)

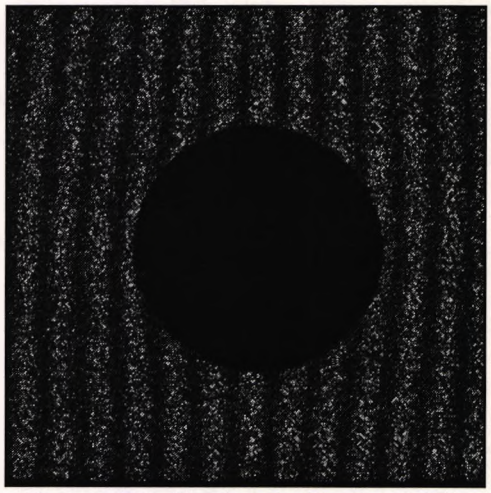


Image 54: Carrier + 50μstrain (F)

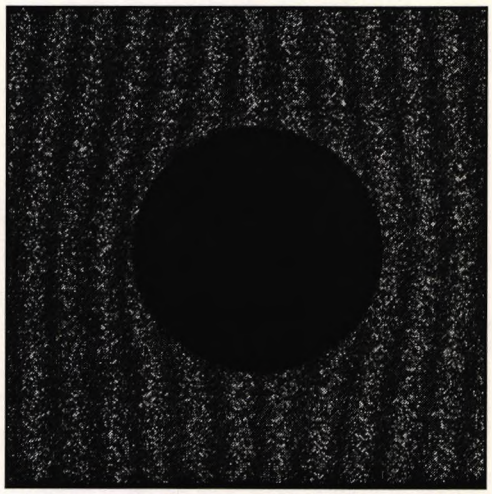


Image 55: Carrier + 100μstrain (G)

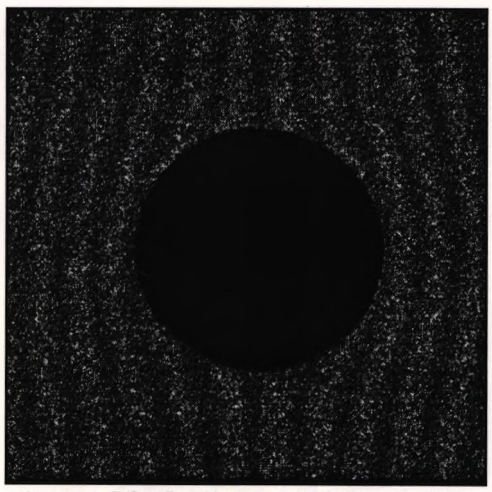


Image 56: Carrier + 150μstrain (H)

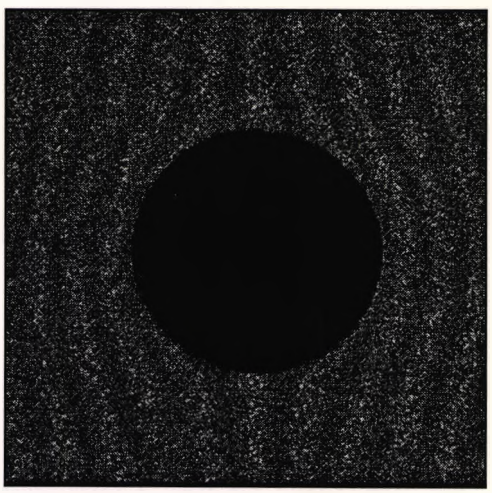


Image 57: Carrier + 200μstrain (I)

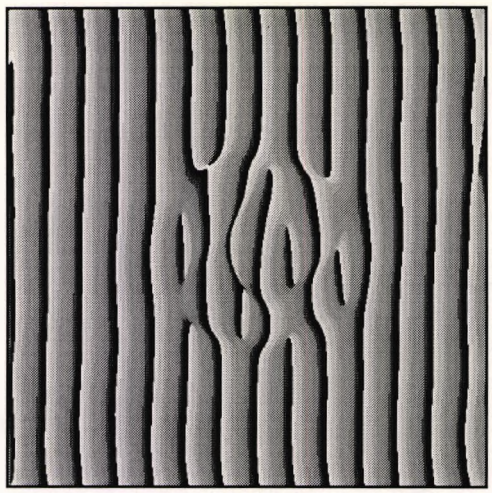


Image 58: Wrapped phase E



Image 59: Wrapped phase F



Image 60: Wrapped phase G



Image 61: Wrapped phase H



Image 62: Wrapped phase I

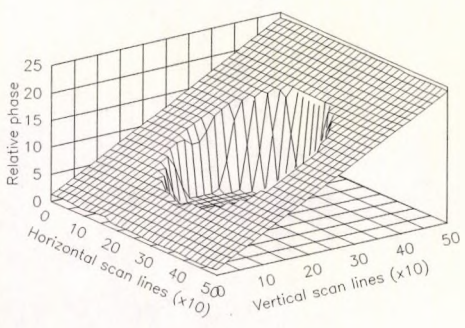


Figure 87: Unwrapped phase E

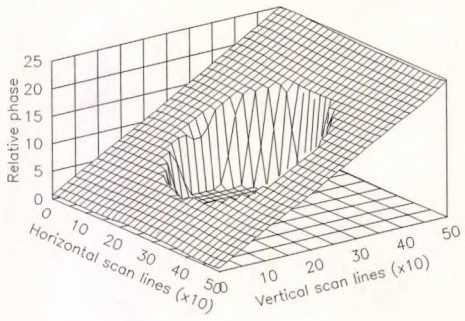


Figure 88: Unwrapped phase F

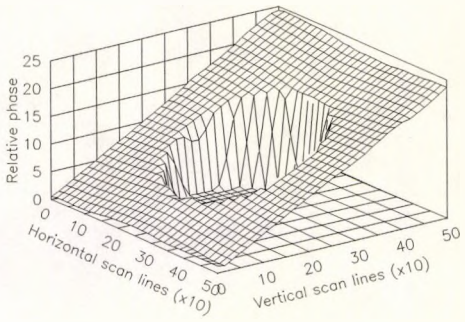


Figure 89: Unwrapped phase G

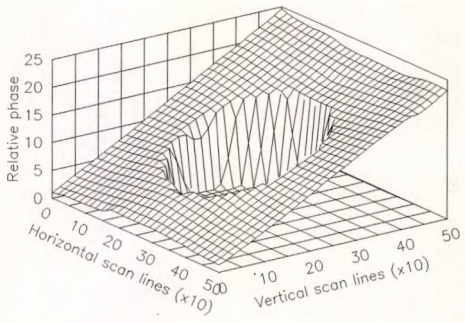


Figure 90: Unwrapped phase H

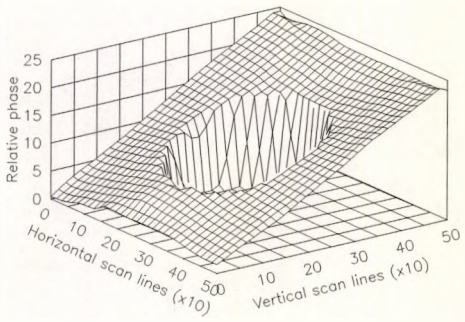


Figure 91: Unwrapped phase I

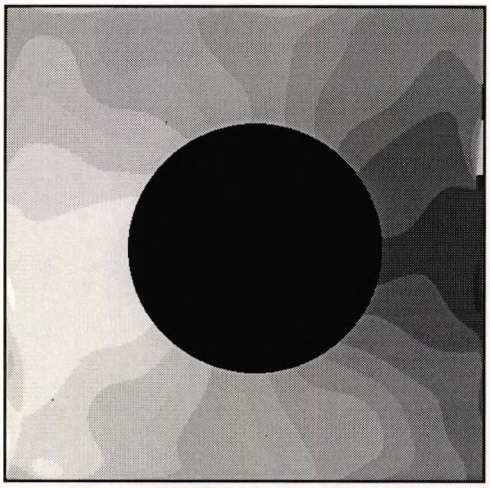


Image 63: Phase F - Phase E

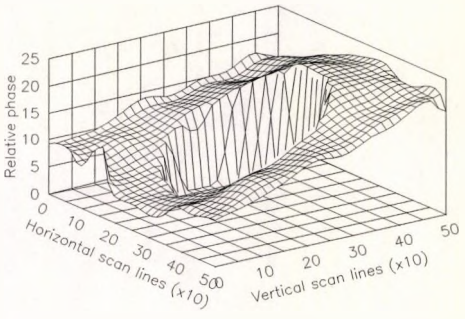


Figure 92: Phase F - Phase E

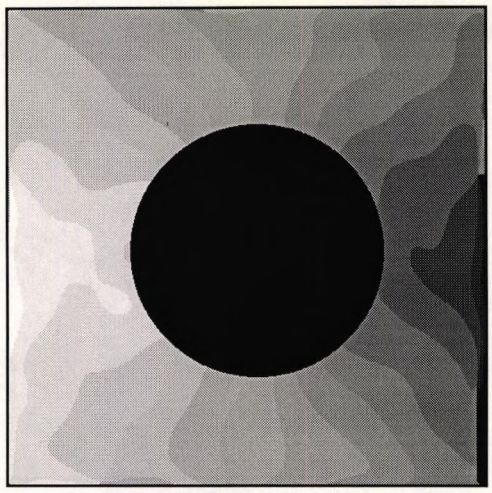


Image 64: Phase G - Phase E

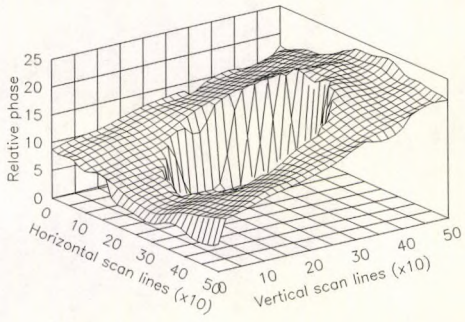


Figure 93: Phase G - Phase E

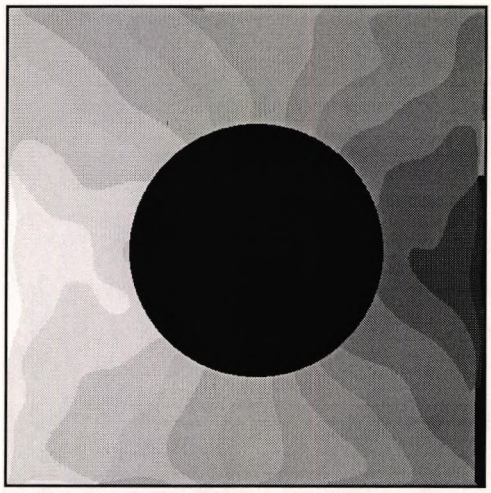


Image 65: Phase H - Phase E

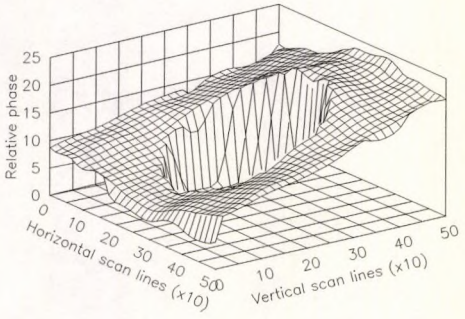


Figure 94: Phase H - Phase E

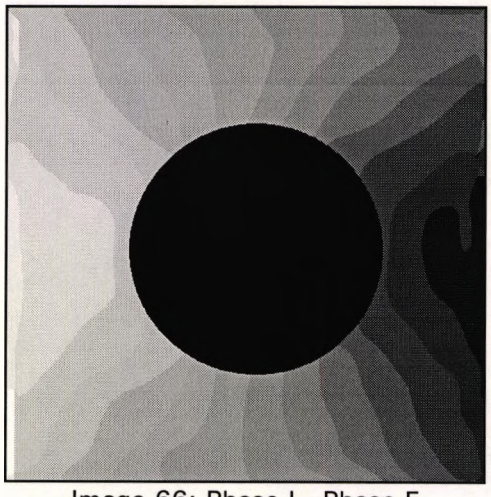


Image 66: Phase I - Phase E

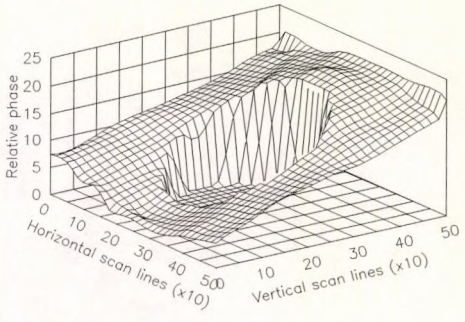


Figure 95: Phase I - Phase E

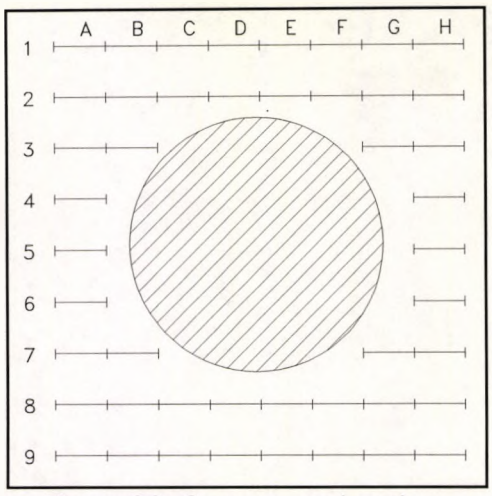


Figure 96: Gauge array locations

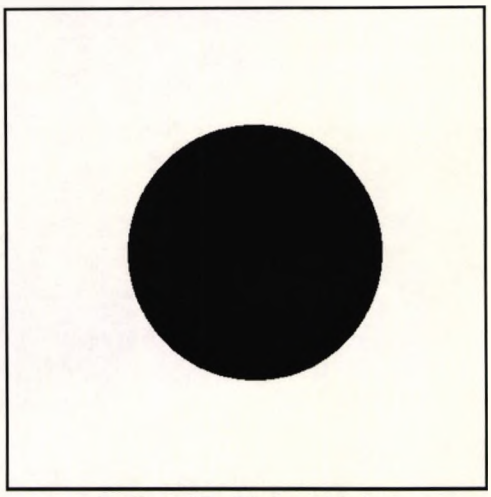


Image 67: Discontinuity

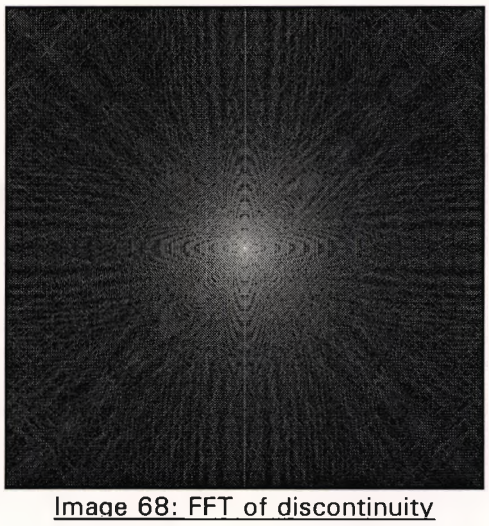


Image 68: FFT of discontinuity

Table 9 indicates the results of the 54μstrain test. It is clear that along the rows (1, 2, 8 and 9), no symmetry or consistency of readings is evident. For example, row 2 has a fluctuation of results from 0.3μstrain to 56.5μstrain. Similar fluctuations are evident for the other rows, and the columns. The higher load test results, shown in Table 10, and also those of Table 11, indicate similar errors. However, the greyscale images of the phase due to the increasing load (Image 63 to Image 66) appear to indicate the expected shape of the in-plane horizontal displacement [Howland, 1930]. What is not evident from these images, and can only be visualised when examining the phase data at a much closer level, is the 'ripples' in the phase, due to the hole (see section 4.2.4 for more information of the cause of the ripples). Image 68 shows the ripples in the Fourier domain resulting from the discontinuity. These ripples are convolved with the real/imaginary data of the 'complete fringe field' in the Fourier domain, therefore altering the magnitudes of the various frequency components of the

	Optical strain gauge (reading in μstrain)							
	A	B	C	D	E	F	G	H
1	54.9	1.6	25.6	17.5	26.9	30.1	22.7	3.5
2	47.1	0.3	32.2	28.3	56.5	22.9	29.4	14.0
3	24.2	14.7					27.6	7.8
4	0.2							17.5
5	14.1							7.1
6	0.6							26.2
7	12.6	18.6					24.7	13.9
8	42.9	17.4	51.1	43.2	47.4	8.9	54.8	24.8
9	29.1	41.9	45.6	10.4	41.8	18.9	45.3	42.7

Table 9: Strain measurements for 54μstrain load increase

	Optical strain gauge (reading in μstrain)							
	A	B	C	D	E	F	G	H
1	73.3	32.8	59.3	36.9	41.4	64.7	46.4	56.5
2	71.3	53.1	59.1	73.4	106.8	57.1	45.2	42.8
3	47.5	45.9					26.7	41.7
4	23.7							42.7
5	52.4							44.7
6	4.0							61.8
7	4.5	57.7					29.6	62.2
8	67.9	48.4	106.2	81.8	116.2	65.2	78.6	65.5
9	61.3	66.2	82.7	57.4	68.0	39.1	92.9	68.8

Table 10: Strain measurements for 102μstrain load increase

data. Those alterations of the magnitudes which are included in the passband of the Fourier filter are transferred back into the spatial domain, causing ripples in the phase. The extrapolation of data over the discontinuous region, using the Gerchberg/Saxton iterative algorithm, was tried, but appeared to make the phase information slightly worse. The ripples cause major problems when the linear regression algorithm of the program 'STRAIN.EXE' is used, and in many of the measurements presented, the value of r^2 is typically 0.5 or less, indicating a very poor fit to the data. When the value of r^2 is less than about 0.7, it can be

	Optical strain gauge (reading in μstrain)							
	A	B	C	D	E	F	G	H
1	108.8	78.1	63.0	64.0	63.8	85.9	79.4	81.7
2	101.8	74.0	113.1	102.8	144.7	95.1	69.4	97.9
3	62.7	58.4					54.5	37.5
4	24.4							74.7
5	47.7							29.9
6	64.6							83.6
7	66.0	29.7					57.3	91.7
8	99.5	80.7	151.2	122.8	153.5	103.1	111.4	111.1
9	126.0	120.0	111.3	78.9	93.4	70.0	116.9	118.2

Table 11: Strain measurements for 153μstrain load increase

assumed that the resulting measurements are meaningless. A change of the gauge length over which the measurements are made will affect the value of r^2, but may not affect the 'meaning' of the resultant information, since the errors in the phase are the same, irrespective of the number of data points used to make the measurements. Smoothing of the phase data, which was used successfully by Maas [1991a], is a technique which was not tried, but could be used to yield accurate data from the phase information. However, at locations very close to the discontinuity, the errors will be very large (of similar magnitude to the edge errors), and no amount of smoothing will yield useful information in this range.

It is concluded that the Fourier transform method of fringe analysis is not suitable for the measurement of phase data from fringe patterns with large discontinuities. However, during simulation tests, smaller discontinuities had a much smaller effect, assuming the measurement was made at a reasonable distance.

5.2 Results from rotating specimens

5.2.1 Experimental apparatus

Figure 97 shows the test specimen used for the following tests, which is mounted on a high speed three phase synchronous electric motor (Perske KNS 61.13-2 5kW, 380V, 18,000rpm @ 300Hz). The electric motor is driven by an invertor controller (Haynau FU4-11F), the combination of motor and controller enabling rotational speeds in excess of 20,000rpm to be attained. The FU4 employs a variable frequency PWM technique to generate the three-phase output, which allows a variation of the rotational speed of standard three-phase induction motors, whilst providing constant torque. The controller is fully programmable, and allows variable acceleration rates to be selected. Numerous acceleration ramp profiles are possible, but in all tests, a linear ramp was used. The controller is capable of holding a specified rotational speed to within ±10rpm, using a slip compensation facility. Also, the FU4 allows the magnetic fields of the motor to be energised with the motor stationary, thereby eliminating any slip during the initial period of the acceleration.

The cooling of conventional self-cooled three phase motors fluctuates with speed, and significantly affects the thermal loading of the motor at slow speeds. On the test rig, external cooling of the motor is achieved by placing fans on either side of the cooling fins, thereby rendering the cooling efficiency independent of the motor speed. Under these conditions, the motor can produce its nominal torque from 0.5A up to the nominal frequency.

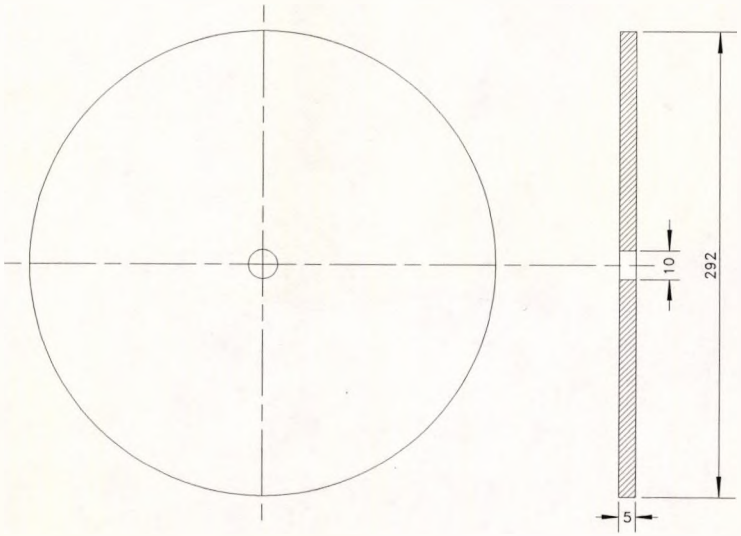


Figure 97: Test specimen

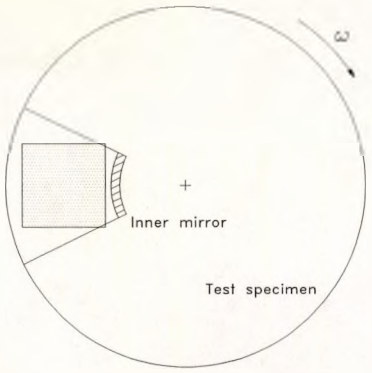


Figure 98: Region of interest

The aircraft alloy specimen of Figure 97, which has international material designation 7075 (BS specification 2L95, DTD 5124), was dynamically balanced by Rolls-Royce to within 1gmm, and is capable of withstanding the extreme forces of high speed rotation. The material has the following properties[81]:

- Modulus of Elasticity 70.0×10^9 N m^{-2}
- Poisson's Ratio 0.34
- Density 2.8×10^3 Kg m^{-3}
- Coefficient of linear expansion 23.5×10^{-6} /°C (20-100°C)
- Thermal Conductivity 130.0 W/m°C (0-100°C)
- Melting range 475-630°C

The specimen has several holes drilled through it, which are not indicated on the diagram. In all the test results presented in this thesis, one of the holes is in the field of view of the imaging system, so that during image acquisition, the operator can detect any errors in the counting electronics of the ECU. However, the hole is normally positioned away from the central region, so that errors in the Fourier transform analysis are less likely. The imaging region of the optical measurement system is shown in Figure 98, where the shaded area (which is not a critical parameter) represents the 512x512 array of the VS100. The exact position of the imaging area varies from test-to-test. It is possible to compute the real space location of any pixel in the image from the pixel-to-millimetre ratio and the centre coordinates of the disc.

The interferometric system is initially aligned with the test specimen, as described in section 3.2.3.1. This is a 'one-off' procedure which needs checking at weekly intervals[82]. To perform a typical test, the following start up procedure is used. The assorted pulsed laser sections are powered up, and the coolant is supplied to bring the operating temperature of

[81] Source: Aerospace Structural Metals Handbook, 1968.

[82] Various heavy components 'settle' slowly, and need inspecting regularly.

the closed loop flow to approximately 13°C (10-20°C is acceptable). The coolant flow is interlocked to the laser, and must be under pressure before the laser can be operated. The full energy of the laser is not required for testing, so the output is selected to be approximately 400mJ, corresponding to 2.10kV excitation of the oscillator cavity and 1.75kV excitation of the amplifier. It is found that a high voltage selection on the amplifier causes irregularities in the coherence of the wavefront, which may be related to the age of the laser. The camera, ECU, opto-isolators, and computer are all powered up. The computer automatically executes an initialization program, 'INITESPI.EXE', the execution command is stored in the 'AUTOEXEC.BAT' file. Finally, the shaft encoder lasers are supplied with power, and the motor invertor is switched on. The entrances to the laboratory are closed, and the safety interlock for the laser is energised[83]. The system can now be operated, but as a final safety precaution, a shroud is moved into position around the rotating specimen. The motor is rotated at a speed of about 4,000rpm, and the quality of the timing pulses is maximised, using the procedure described in section 3.2.1.2. This can also be termed a 'one off' operation, which must be checked weekly.

5.2.2 Speed variation tests

5.2.2.1 Experimental procedure

In order to capture images from the rotating specimen, the DOS program 'MAINPROG.EXE' is executed. This program performs all the control tasks necessary to capture, classify and store the speckle images on the disk. The program logs each image sequentially under a header name, and stores the time, date, position, gain, offset, speed and tilt mirror position with each image. Once the complete test capture is concluded, the program is terminated, and the program 'AUTOSUB.EXE' is used to effect all possible combinations of subtractions. The operator is requested to select those fringe patterns for analysis, which are stored under a new header (the original data set is unchanged). The selected images are passed on to the Fourier transform analysis programs for phase extraction. The forward transform program 'FFT2D.EXE' is used to compute the double precision 2D Fourier transform of the image, leaving the real and imaginary spectrum data in the extended memory of the computer. The program 'WINFILL.EXE' is then used to apply a Fourier filter to the data, to be used by the program 'IFFT2D.EXE', which computes the inverse 2D Fourier transform of the filtered data. Finally, the program 'BADPIX.EXE' is used to manually mark bad data region of the wrapped phasemap generated by 'IFFT2D.EXE', and the program 'FLOODUWP.EXE' is employed to unwrapped the double precision wrapped phasemap. The entire process is coded into a DOS

[83]This is a legal requirement for the operation of class 4 laser systems.

batch file (FFT.BAT) and takes approximately 8 minutes per image[84]. The program 'STRAIN.EXE' is utilised to compute the in-plane radial strain from the unwrapped phasemap. The program assumes that the centre coordinates of the disc have previously been computed using the program 'DISCCENT.EXE' (section 3.3.2), which stores them on disk. Also, the pixel-to-millimetre ratio is required for the computation of strain, and is determined using the procedure described in section 3.3.1. The 'STRAIN.EXE' program allows the user to specify a gauge length, and position a cursor on the screen with the mouse, producing the average radial strain at that point.

For a variable speed test, the specimen is accelerated to the reference speed and allowed to run at this speed for several minutes. This allows the specimen temperature, rig and the surrounding environment to settle into an equilibrium state. After a suitable period of time has elapsed, a series of speckle images are recorded at intervals of approximately 10s. It is necessary to record a series of reference speckle patterns, since the output power of the pulsed laser cannot be determined prior to firing, hence a series of images with several average intensity levels is preferable (data set *A*). In the case when the strain levels are likely to be relatively low[85], the tilt mirror is rotated slightly, and a further series of speckle images are recorded, with the specimen still rotating at the reference speed (data set *B*). The motor is then accelerated to the higher speed, and a set of speckle images is recorded at

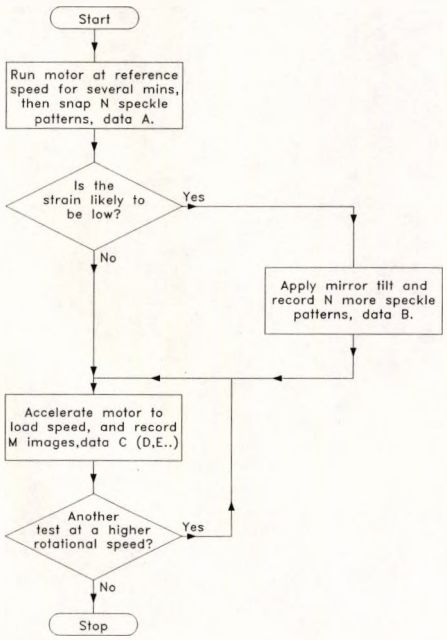


Figure 99: Flowchart of image acquisition procedure

[84]Using a 33MHz 80486 with 16Mbytes of RAM.

[85]Producing less than about five fringes across the image.

approximately 10s intervals (data set *C*). This process is shown diagrammatically in Figure 99. Further loads can be added in the same test (data sets *D*, *E*,..), and if the strain levels are high, they may be referenced to the tilted images directly, thereby eliminating the need for subtraction of a carrier pattern. In either case, the displacement phase is computed from:

$$\phi_{disp} = \phi_{C-B} - \phi_{B-A} \qquad \textit{With carrier}$$
$$\phi_{disp} = \phi_{C-A} \qquad \textit{Without carrier} \qquad [112]$$

where *C* is replaced by *D*, *E*,.. for the different data sets.

5.2.2.2 Results (low speed)

The first set of results is a speed change from 5,156rpm to 7,046rpm. The disc was accelerated to 5,156rpm (reference speed) in 12s, and after 289s, was accelerated to 7,046rpm. A series of reference and load images were recorded, at the times indicated in Table 12, and Figure 100. The fringe patterns, wrapped phasemaps and unwrapped phasemaps are shown on Pages 151 and 152. It is seen from the images that some skewing of the fringe patterns has occurred. This skew would render strain results measured remote from the horizontal axis less accurate, but has no effect on the accuracy close to the axis, since the phase gradient along this line is unchanged by the skew. The fringe sensitivity is 0.40μm fringe^{-1} (incidence angle of 60° to the normal, with $\lambda = 694$nm). The acceleration rate used for this test was 42rad s^{-2}.

	Reference speckle pattern time	Loaded speckle pattern time
Fringe pattern A	A1 (13s)	A2 (459s)
Fringe pattern B	B1 (128s)	B2 (309s)
Fringe pattern C	C1 (248s)	C2 (299s)
Fringe pattern D	D1 (277s)	D2 (530s)

Table 12: Capture times of the reference and load speckle patterns (A to D)

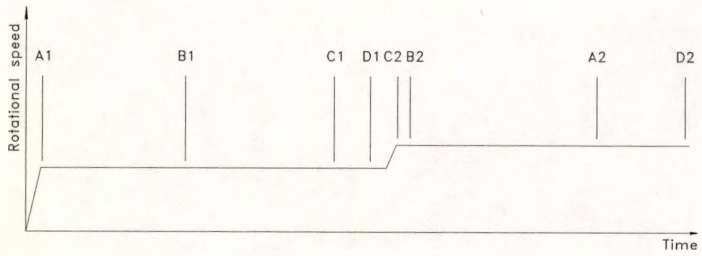


Figure 100: Diagrammatic representation of test schedule



Image 69: Fringe pattern A



Image 70: Fringe pattern B



Image 71: Fringe pattern C

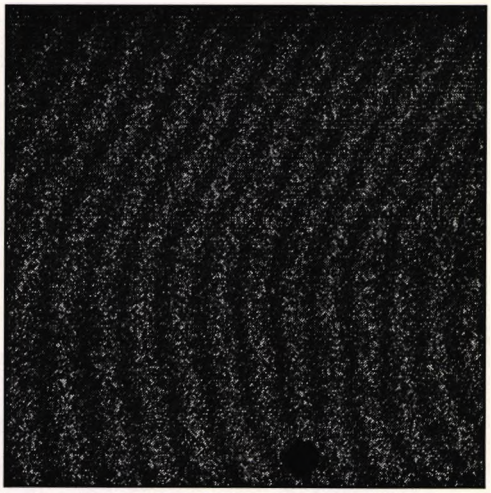


Image 72: Fringe pattern D

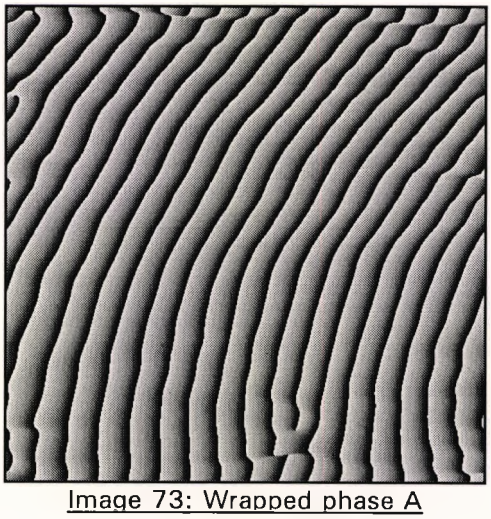


Image 73: Wrapped phase A

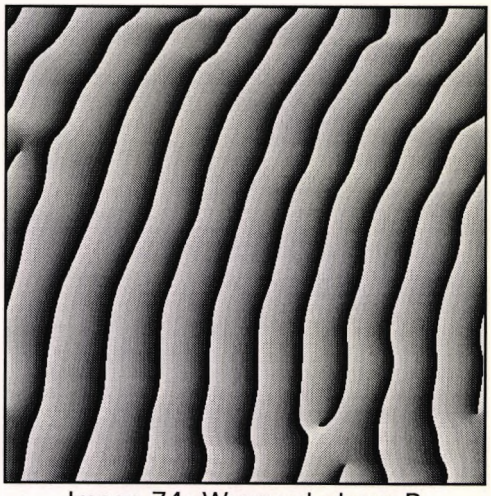


Image 74: Wrapped phase B



Image 75: Wrapped phase C

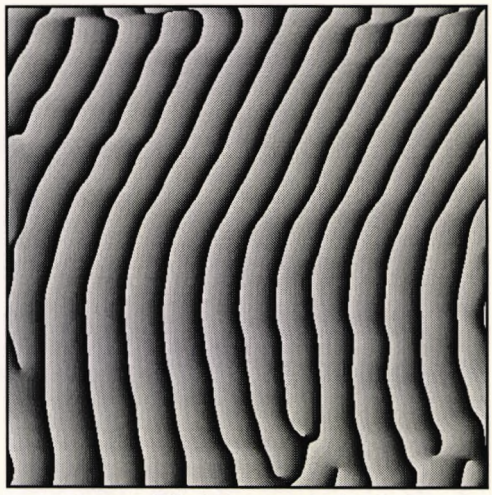


Image 76: Wrapped phase D

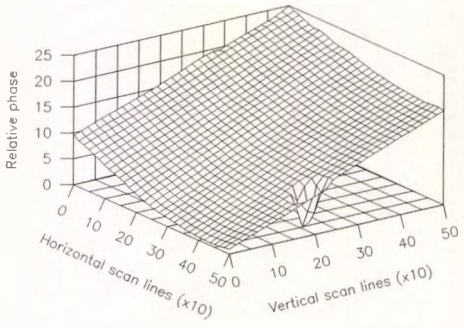


Figure 101: Unwrapped phase A

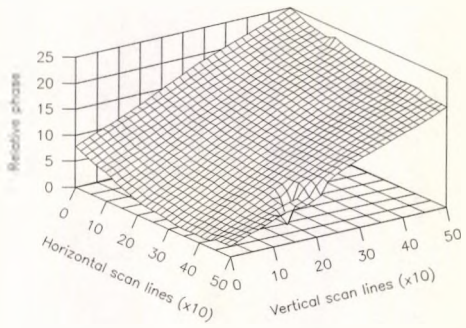


Figure 102: Unwrapped phase B

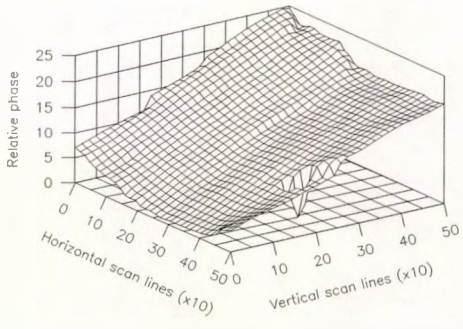


Figure 103: Unwrapped phase C

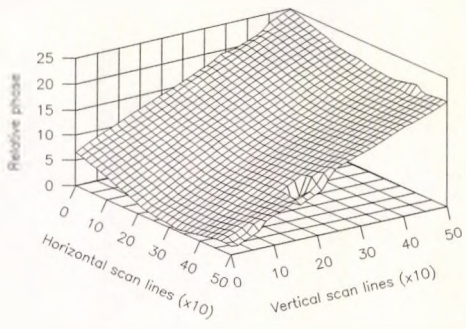


Figure 104: Unwrapped phase D

The fringe patterns show a time related change in the radial strain of the specimen. The numerical results for the radial strains at the 'optical strain gauge' locations shown in Figure 105 (which is drawn to the same scale as the images), are presented in Appendix C. Graph 9 is a plot of the measured radial strains for each fringe pattern against the radius, and also indicates the expected theoretical value (calculated from the equations presented in Chapter 2). Interestingly, all results are higher than those predicted by theory, with fringe pattern C representing the closest measurement. The 'fall-off' gradient of the measured strains is not as great as the theoretical calculations predict, indicating that the effect causing the deviation from the theory is greater at the outer edge of the specimen. The reference speckle pattern of fringe pattern C was taken over four minutes after the specimen reached the reference speed, and the load speckle pattern was recorded almost immediately after the specimen finished accelerating to the load speed. The reference and load speckle patterns of fringe pattern A are separated by a considerable time, and generate a fringe pattern which represents the largest deviation from the theory. Fringe patterns B and D are in between these extremes, both in terms of the measurement values and the speckle capture times.

These facts are consistent with windage heating of the specimen surface, since this would produce measured results which would always be greater than the theory. Windage heating is proportional to the fourth power of the radius, and would therefore cause a greater deviation from the theory at larger radii. Initially, creep was considered as a candidate for the effect, but the creep properties of the material are not consistent with these results. In order to ascertain if the effect under observation was windage heating, a speed change test with a much greater acceleration was performed, in order to minimise the heating of the specimen during the acceleration period.

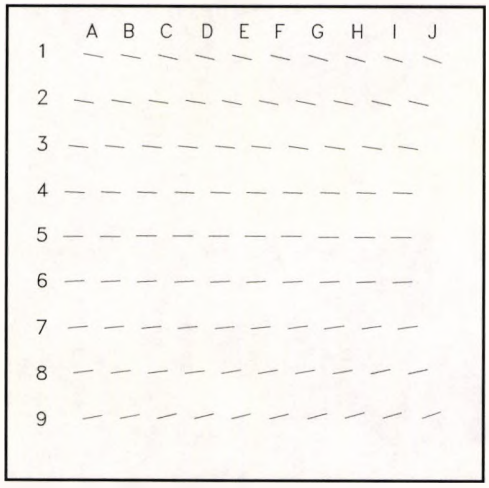
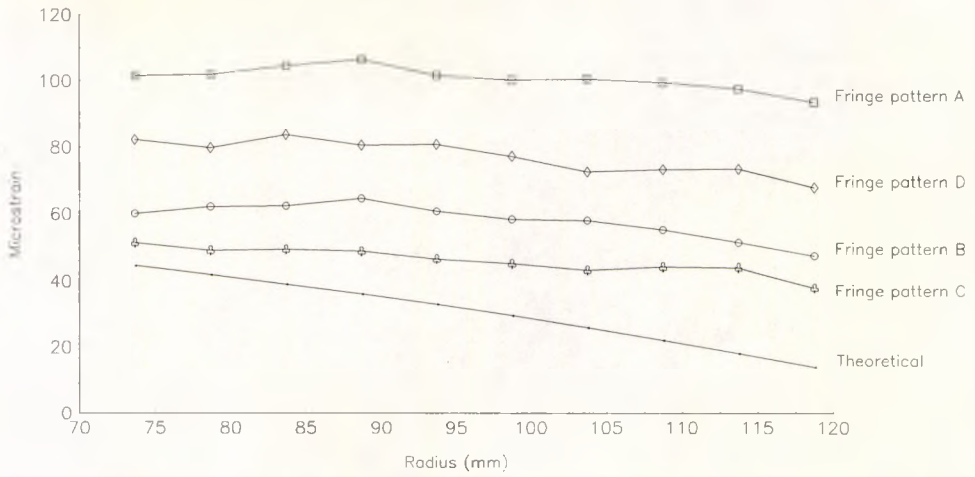


Figure 105: Optical gauge locations



Graph 9: Comparison of measured and theoretical radial strains

In the following high acceleration test, the acceleration rate of the disc was substantially increased in order to minimise the heating occurring during the acceleration period. Image 77 is a fringe pattern for a speed increase from 5,402rpm to 7,298rpm, after leaving the disc rotating at the lower speed for several minutes. The rapid acceleration from the lower speed (170rad s^{-2}) took less than a second, at which point the second speckle image was recorded. Image 78 is a fringe pattern for a similar test, with a speed variation from 7,298rpm to 9,764rpm. In both cases, the sensitivity and imaging region are the same as the previous test (sensitivity of 0.40μm $fringe^{-1}$).

A comparison between the theoretical prediction (ignoring windage) and the measured data for Image 77 (taken from the relevant table in Appendix C) is presented in Graph 10, which is plotted to the same scale as Graph 9. Graph 11 is a plot of the data computed from Image 78, and compared with theoretical data.

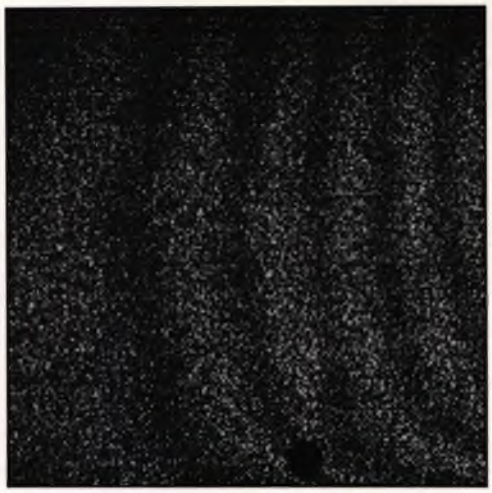


Image 77: Fringe pattern E

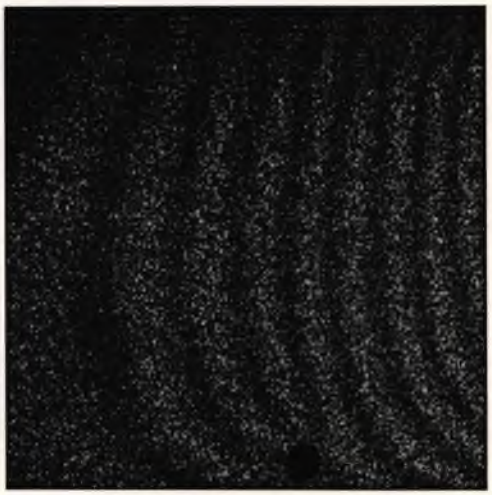


Image 78: Fringe pattern F



Image 79: Wrapped phase E



Image 80: Wrapped phase F

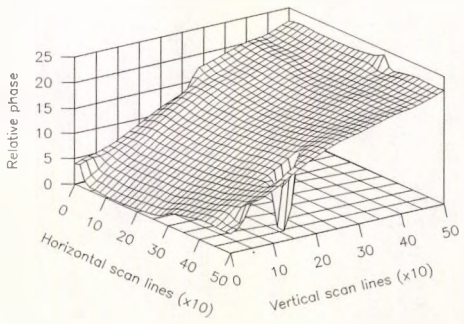


Figure 106: Unwrapped phase E

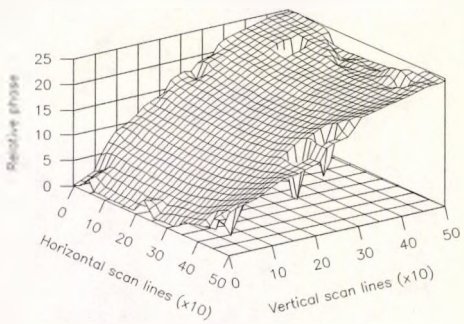
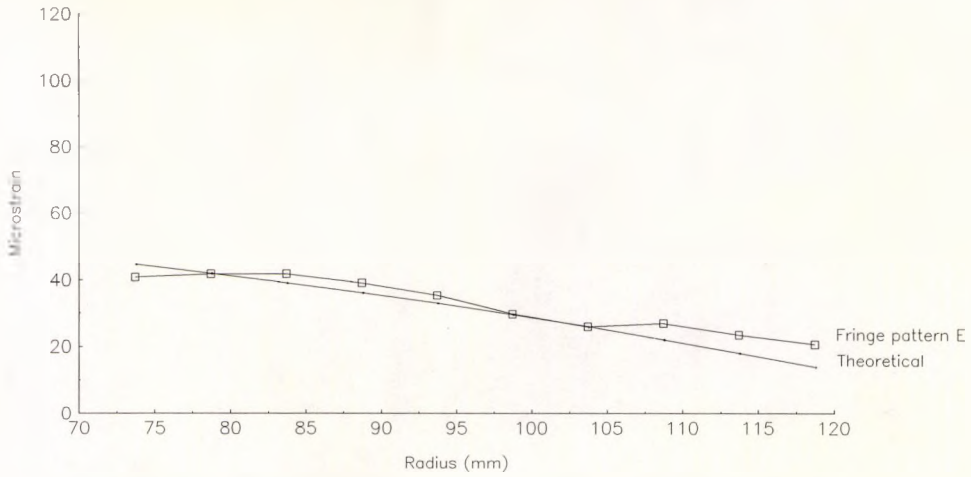
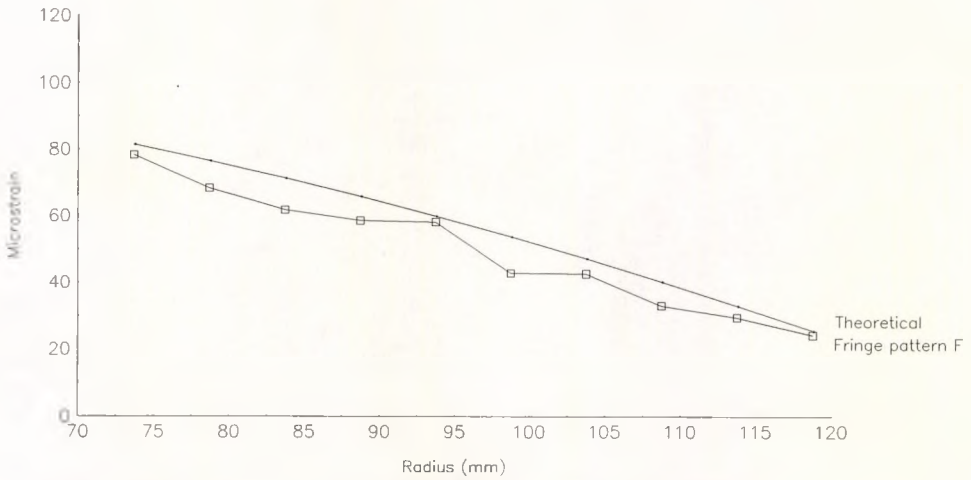


Figure 107: Unwrapped phase F



Graph 10: Radial strain for high acceleration rate (Fringe pattern E)



Graph 11: Radial strain for high acceleration rate (Fringe pattern F)

One of the problems with the prototype ESPI system developed by Preater, was that it was unable to correlate the images recorded at large differences in the speed of the specimen. The following test indicates that this problem is no longer of major significance. Image 81 is a fringe pattern generated by the correlation of a reference speckle pattern at 2,055rpm, and a load speckle pattern at 7,069rpm (a difference of 5,014rpm, at an acceleration rate of 42rad s^{-2}, with a fringe sensitivity of 0.40μm $fringe^{-1}$). The wrapped and unwrapped phasemaps are shown on Page 157, indicating that even very poor fringe images can be successfully analysed with the Fourier transform software. The optical strain gauge results at the locations indicated in Figure 105 are presented in Appendix C, and a comparison between the theoretical and measured results is shown in Graph 12.



Image 81: Fringe pattern G

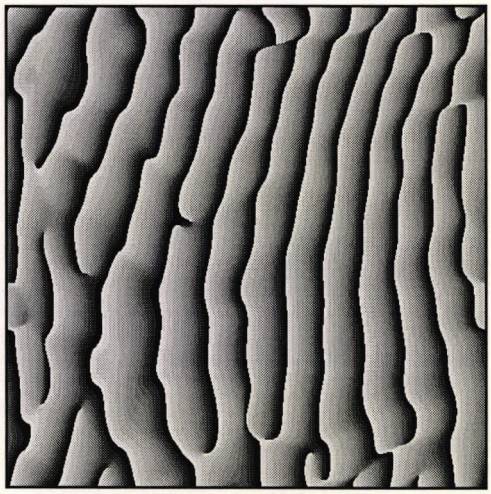


Image 82: Wrapped phase G

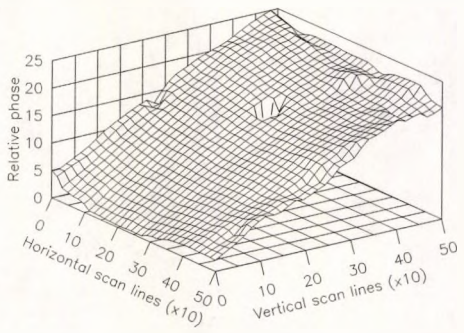
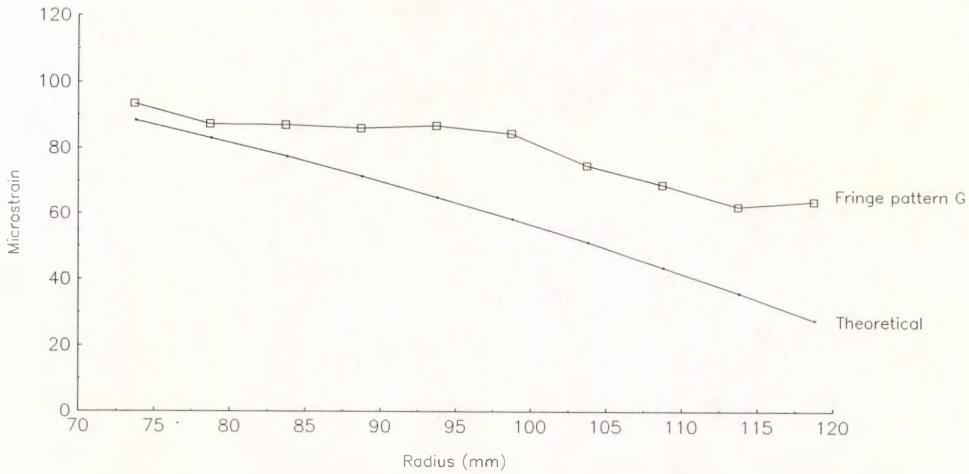


Figure 108: Unwrapped phase G



Graph 12: Comparison of measured and theoretical radial strains

5.2.2.3 Results (medium speed)

For the first test in this section, the specimen was accelerated to 10,180rpm at a rate of 42rad s^{-2}, and a series of four reference speckle patterns was recorded at the times indicated in Table 13. After 338 seconds, the specimen was accelerated to 12,192rpm, using the same rate of acceleration, and a speckle pattern was recorded at 342 seconds. Each of the speckle patterns at the reference speed was correlated with the speckle pattern at the higher speed, producing fringe patterns H to K shown on Page 159. The fringe sensitivity is 0.40μm $fringe^{-1}$. A diagrammatic representation of the test schedule is shown in Figure 109. The wrapped and unwrapped phasemaps are shown on Pages 159 and 160. The numerical results from the array of optical strain gauges shown in Figure 105 are indicated in Appendix C. Graph 13 is a comparison between the theoretical and measured radial strains. This graph clearly indicates that the differential strain between the two rotational speeds appears to be reducing as the *time* of the reference speckle pattern increases. This is consistent with the surface temperature of the specimen increasing with time, since the reference speckle patterns recorded at the higher speeds will 'contain' less of the strain due to heating.

	Reference speckle pattern time	Loaded speckle pattern time
Fringe pattern H	H1 (87s)	2 (342s)
Fringe pattern I	I1 (158s)	2 (342s)
Fringe pattern J	J1 (233s)	2 (342s)
Fringe pattern K	K1 (323s)	2 (342s)

Table 13: Capture times of the reference and load speckle patterns (H to K)

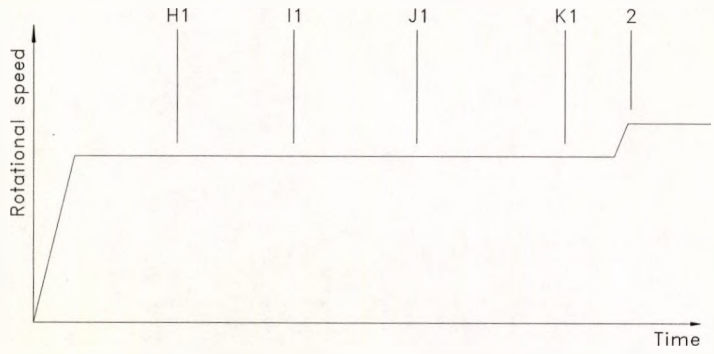


Figure 109: Diagrammatic representation of test schedule



Image 83: Fringe pattern H



Image 84: Fringe pattern I

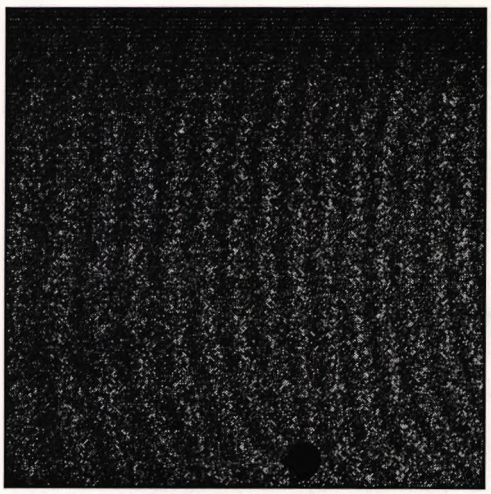


Image 85: Fringe pattern J



Image 86: Fringe pattern K

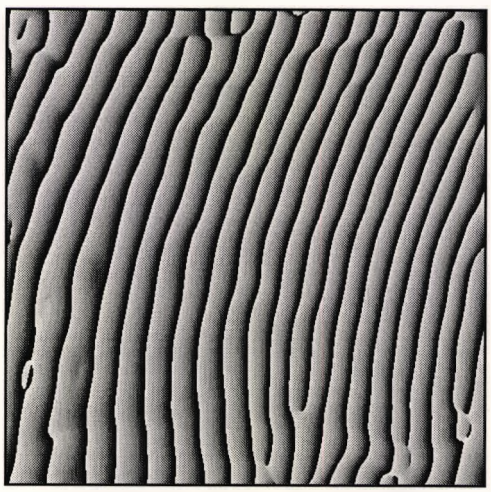


Image 87: Wrapped phase H

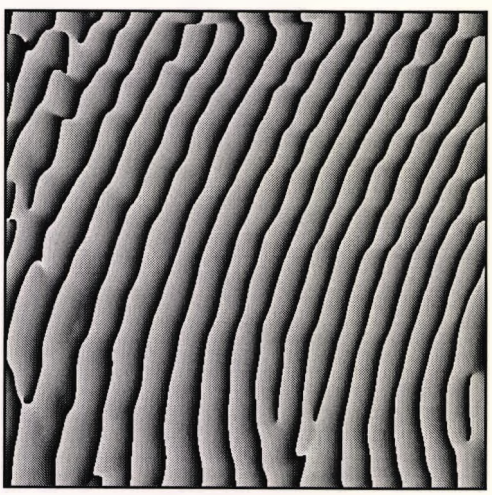


Image 88: Wrapped phase I

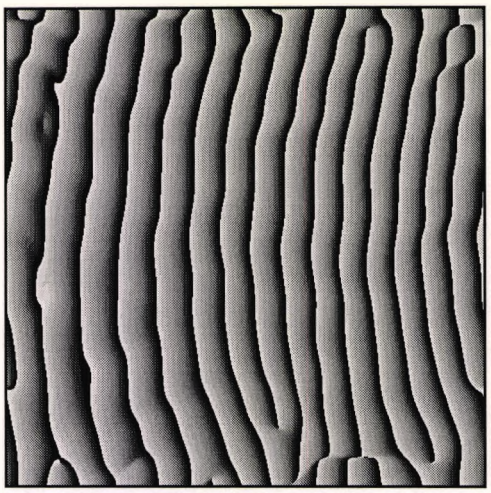


Image 89: Wrapped phase J



Image 90: Wrapped phase K

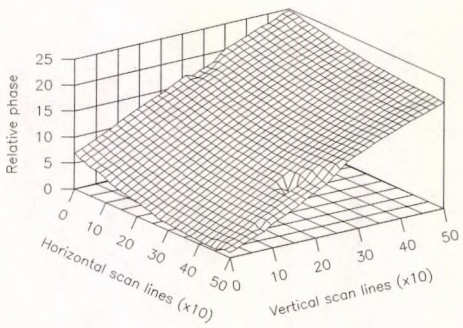


Figure 110: Unwrapped phase H

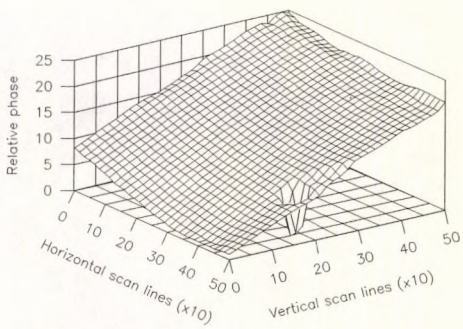


Figure 111: Unwrapped phase I

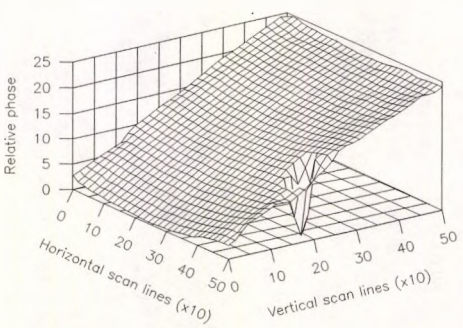


Figure 112: Unwrapped phase J

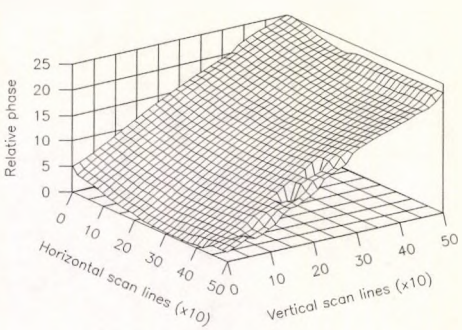
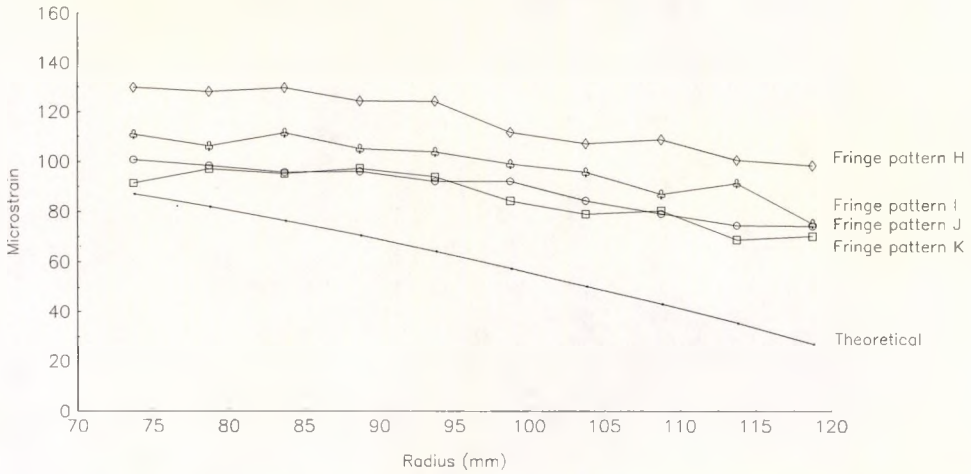


Figure 113: Unwrapped phase K



Graph 13: Comparison of measured and theoretical radial strains

In a similar test, the fringe patterns of which are shown on Page 162 (L to N), the speckle pattern capture schedule shown in Figure 114 was followed. The specimen was accelerated very rapidly (170rad s^{-2}) to the operating speed of 9,764rpm, and allowed to run for some time. A reference speckle pattern (marked 1 in Figure 114) was captured, and the specimen was accelerated at the same rate to a speed of 12,164rpm. It was allowed to run at this speed for 30 seconds, after which time 3 speckle patterns were recorded at 10 second intervals. As stated, the fringe patterns (L to N) are shown on Page 162, and the phasemaps on Pages 162 and 163. Numerical results from these images are contained in Appendix C. Graph 14 shows a comparison between the theoretical and measured radial strains from the fringe patterns. Clearly, the radial strain is still increasing, even 50 seconds after the acceleration is complete.

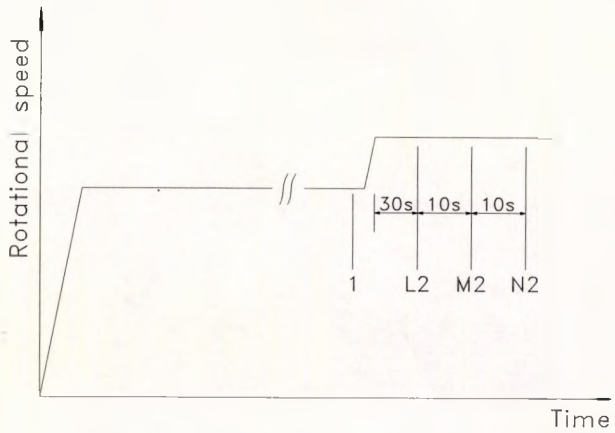


Figure 114: Diagrammatic representation of test schedule



Image 91: Fringe pattern L



Image 92: Fringe pattern M

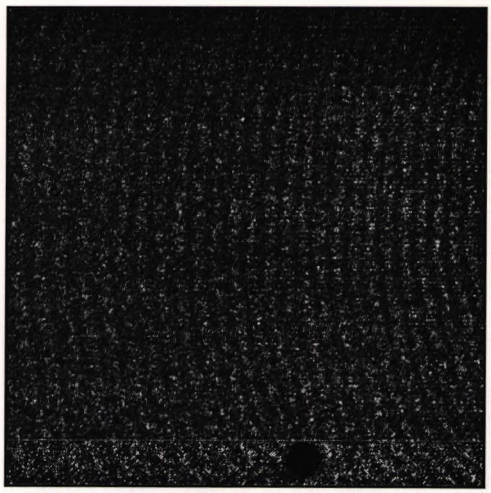


Image 93: Fringe pattern N

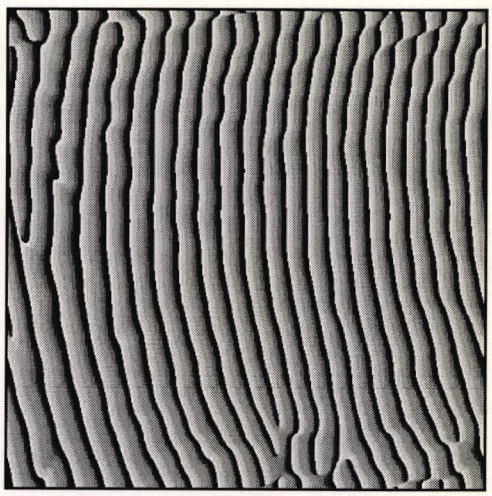


Image 94: Wrapped phase L

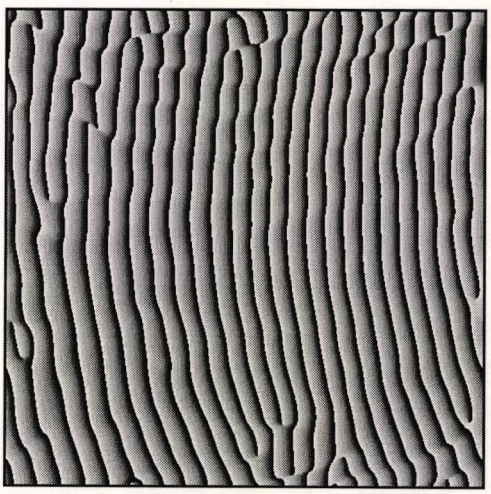


Image 95: Wrapped phase M



Image 96: Wrapped phase N

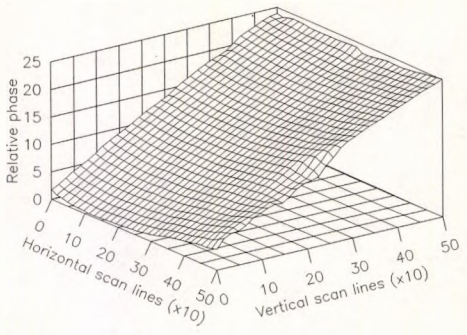


Figure 115: Unwrapped phase L

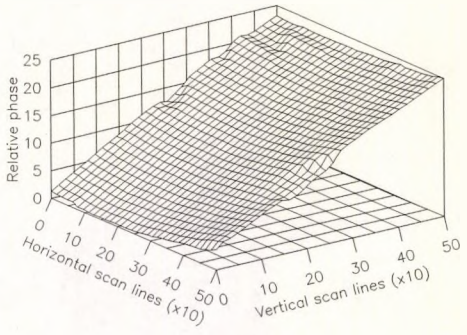


Figure 116: Unwrapped phase M

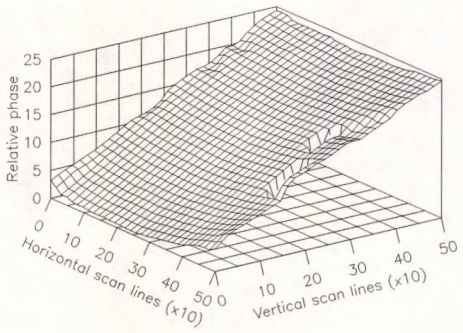
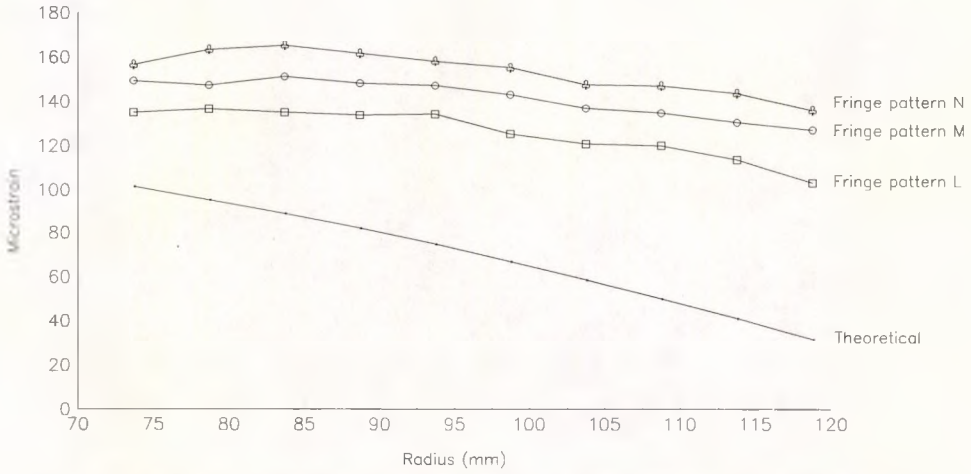


Figure 117: Unwrapped phase N



Graph 14: Comparison of measured and theoretical radial strains

In the final test described in this section, the sensitivity vector of the interferometer was altered from 0.40μm fringe^{-1} to 0.47μm fringe^{-1} (by varying the incidence angle of incidence from 60° to 48°). Image 97 is a fringe pattern generated by the correlation of a speckle pattern with the disc rotating at 10,200rpm, and a speckle pattern at 12,026rpm. The disc was driven at the reference speed for several minutes before the reference speckle pattern was recorded, then accelerated to the higher speed at a rate of 46rad s^{-2}. The load speckle pattern was recorded at the instant the specimen attained the higher speed. Image 98 is the wrapped phasemap computed from Image 97, the unwrapped map is shown in Figure 118. Appendix C contains the computed radial strain for the gauge location shown in Figure 105. Graph 15 is a comparison between the measured and theoretical values.



Image 97: Fringe pattern O

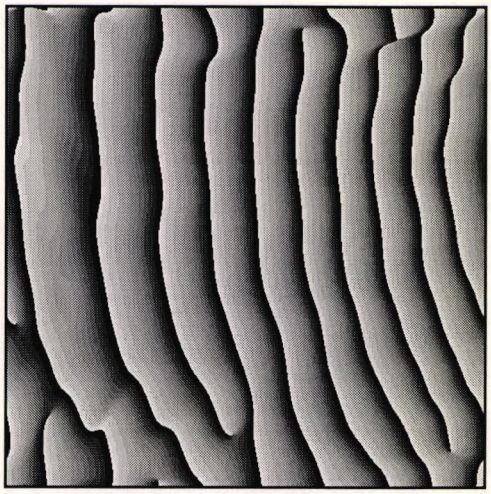


Image 98: Wrapped phase O

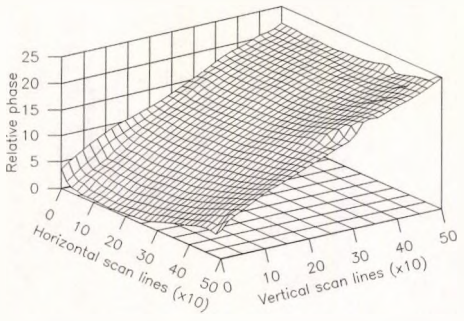
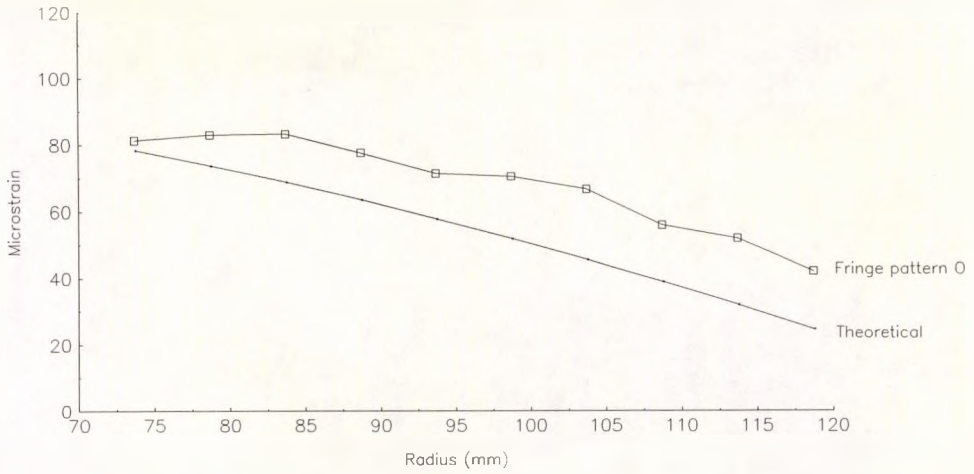


Figure 118: Unwrapped phase O



Graph 15: Comparison of measured and theoretical radial strains

5.2.2.4 Results (high speed)

Figure 119 indicates the test schedule of the first test in this section[86]. The specimen was accelerated at 42rad s^{-2} to 15,098rpm, and allowed to run at that speed for several minutes. A speckle pattern was recorded at the reference speed (referred to as 1 in the figure). The disc was then accelerated to 16,550rpm at the same acceleration rate, and 4 more speckle patterns were recorded at 10 second intervals. The correlation of the reference speckle pattern with the load speckle patterns produces fringe patterns P to S shown on Page 166. The wrapped and unwrapped phasemaps are shown on Pages 166 and 167. The computed radial strains, using the gauge locations shown in Figure 105, are presented in Appendix C. Graph 16 compares the theoretical and measured radial strains for fringe patterns P to S. As would be expected, a time related strain increase is clearly observed on the measurements, consistent with windage heating of the surface.

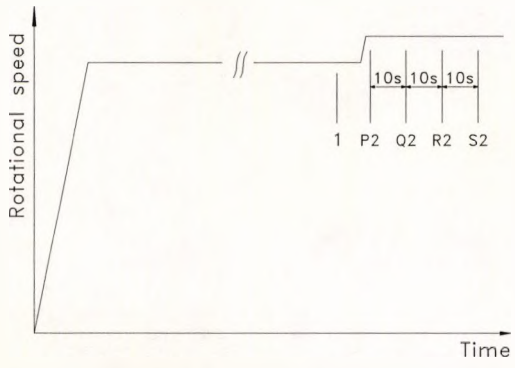


Figure 119: Diagrammatic representation of test schedule

[86]Note: The image for this test is of a different rotational position of the specimen, but the physical position of the image is the same as the previous tests.



Image 99: Fringe pattern P



Image 100: Fringe pattern Q

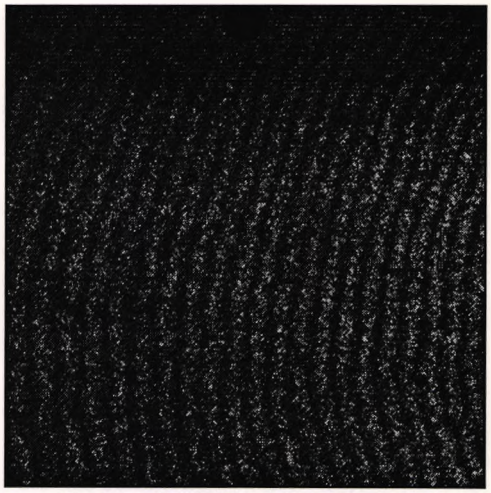


Image 101: Fringe pattern R



Image 102: Fringe pattern S

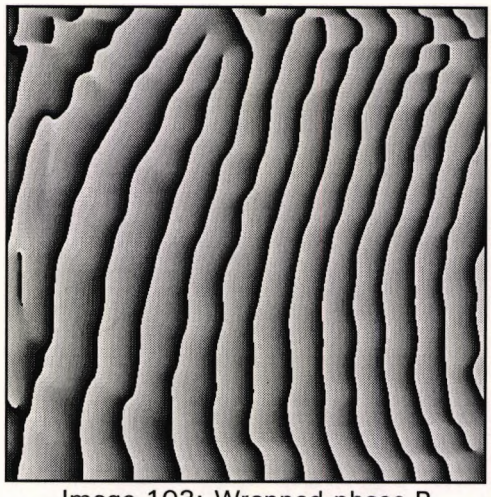


Image 103: Wrapped phase P

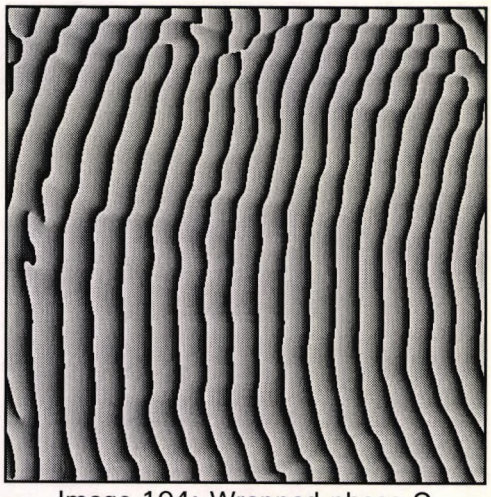


Image 104: Wrapped phase Q

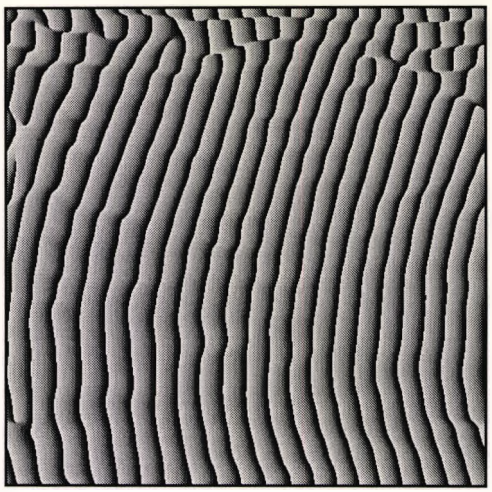


Image 105: Wrapped phase R

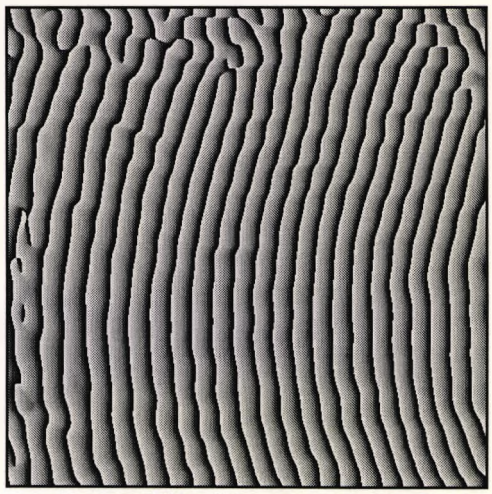


Image 106: Wrapped phase S

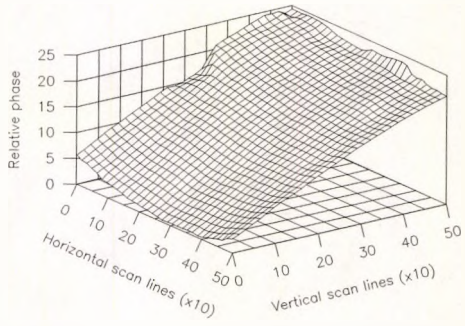


Figure 120: Unwrapped phase P

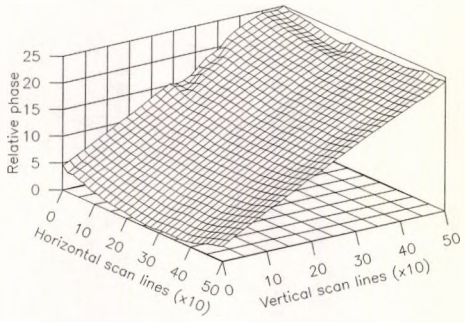


Figure 121: Unwrapped phase Q

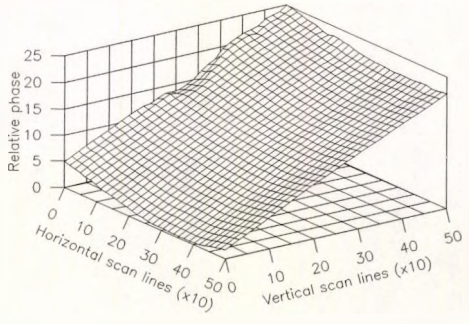


Figure 122: Unwrapped phase R

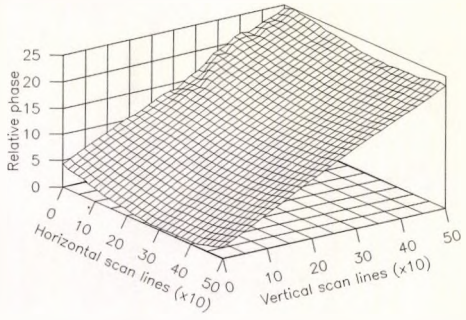
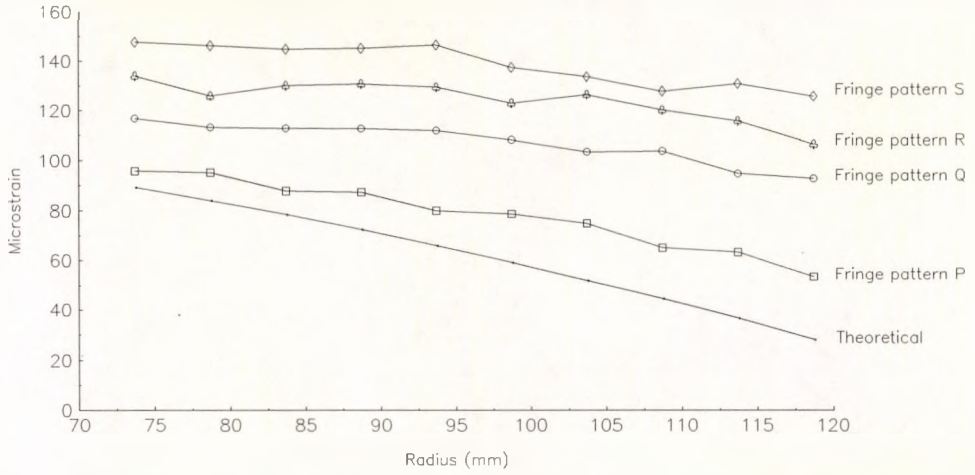


Figure 123: Unwrapped phase S



Graph 16: Comparison of measured and theoretical radial strains

5.2.2.5 Results (very high speed)

At very high speeds (greater than about 16,000rpm - a tip speed of 245m s^{-1}), the vibration of the drive rig causes significant problems for the interferometric system. For example, fringe patterns T and U on Page 169 are for a rotational speed increase from 18,047rpm to 19,054rpm (tip speed of 291m s^{-1}). The 'skew' of the fringes is now unacceptable, and no useful engineering information could be extracted from them. Fringes V and W on Page 169 were generated from speckle images recorded with the specimen rotating at a constant speed of 20,749rpm (tip speed of 317m s^{-1}). The correlation of speckle images recorded at a constant rotational speed should produce a 'null' image, but it can be seen that vibrational effects are now too large, and the fringes are no longer repeatable.

Fringes X and Y on Page 169 represent a couple of high contrast fringe patterns obtained from a test conducted at the fastest speed reported in this thesis. The specimen was accelerated to a rotational speed of 23,842rpm (tip speed of 364m s^{-1}) and a series of speckle images were captured. Fringe pattern X shown in Image 111 is a radial fringe pattern at the test speed, and fringe pattern Y is an image of a different rotational region of the specimen, again at 23,842rpm. No useful results were obtained at any speed over 16,550rpm (Page 166), but high contrast speckle correlation fringes are clearly achieved.



Image 107: Fringe pattern T



Image 108: Fringe pattern U



Image 109: Fringe pattern V

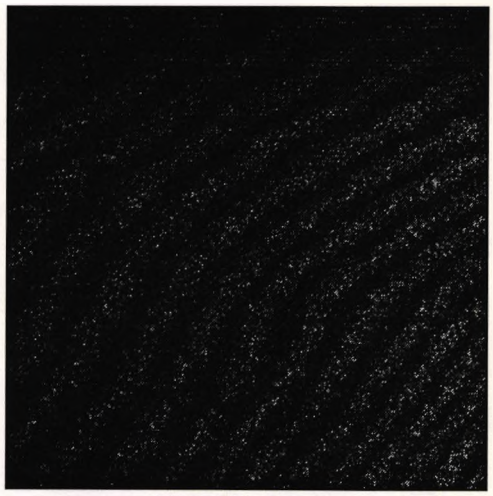


Image 110: Fringe pattern W

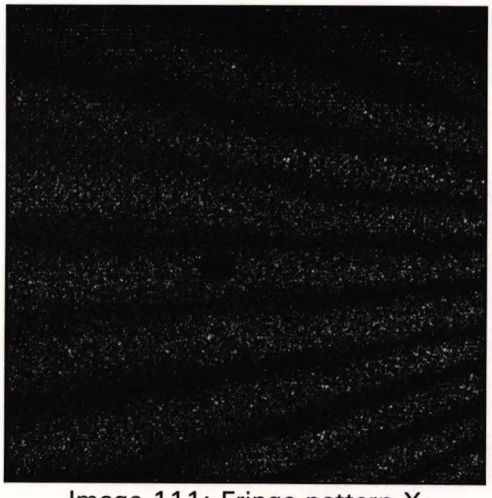


Image 111: Fringe pattern X



Image 112: Fringe pattern Y

5.2.3 Windage tests

The specimen disc is subject to surface heating, due to the friction (windage) of the surrounding air. Additional heating arises from the front bearing of the drive motor, which transmits heat to the specimen via the drive shaft. At rotational speeds below about 2,000rpm, the windage and bearing heat is small, even when running the specimen for extended periods of time, and does not cause any problems. At higher speeds, and test runs of longer duration, the heating effect becomes a factor which cannot be ignored.

The windage, which is not taken into consideration in the theoretical calculations of the radial strain described in section 2.3, will cause the disc to expand with time[87], and will result in the strain measurements calculated from the specimen being higher than those predicted by the theory. Absolute windage data from the speckle pattern interferometer is impossible to obtain, and therefore cannot be separated from the differential strain measurements presented in the previous section, for the following reasons:

- A stationary reference speckle pattern is unavailable to correlate with time delayed speckle patterns, recorded at the loading speed. Therefore, absolute levels of windage heating cannot be determined[88].
- It is impossible to separate the temperature rise resulting from the windage, from the transmitted heat from the drive bearing, so computer models cannot be used.

5.2.3.1 Experimental procedure

To observe the effects of windage heating, the specimen disc was accelerated from stationary to a fixed rotational speed. Upon attaining the required test speed, a reference speckle pattern was immediately recorded, and subsequent speckle images recorded at

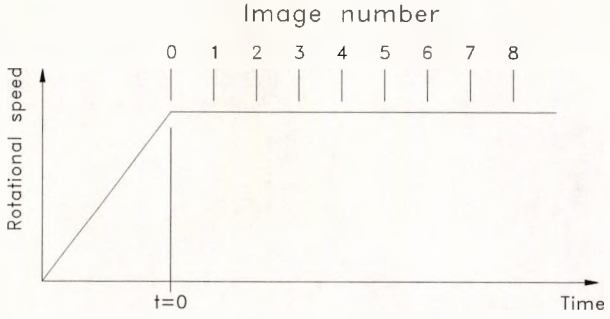


Figure 124: Windage test schedule

[87]Until an equilibrium state is attained.

[88]Also, speckle patterns recorded at slow rotational speeds (eg. 600rpm), which exhibit insignificant windage heating, do not appear to correlate with images taken at the high speeds.

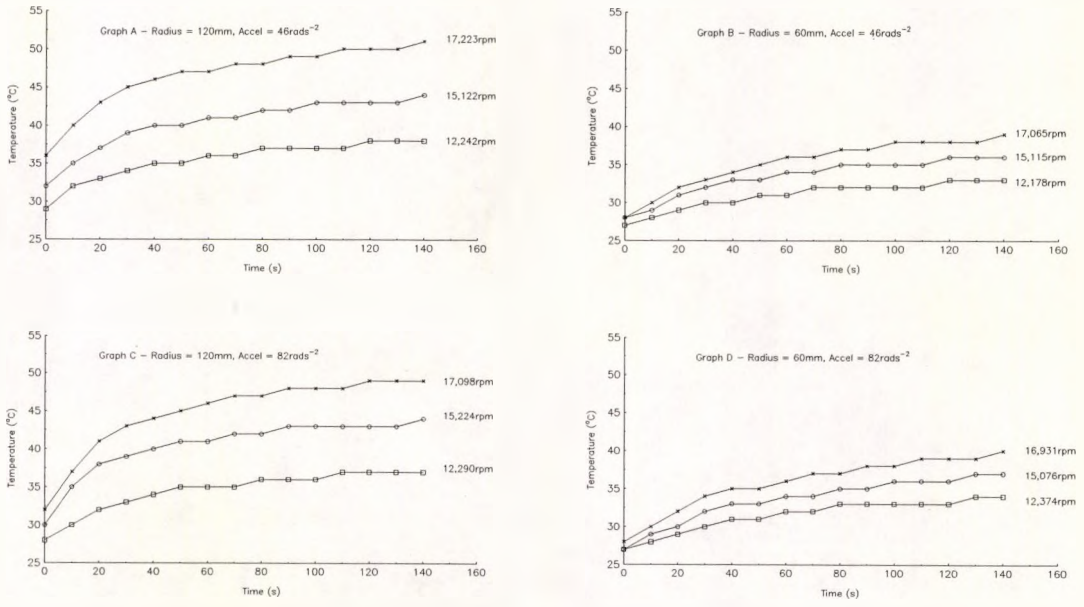
approximate 10s intervals, as shown in Figure 124. For simplicity and comparison purposes, the time at which the specimen achieves the test run speed is referred to as zero.

To establish the genuine heating of the specimen, at two different radial positions, and two acceleration levels, an infra-red (IR) sensor was placed close to the front surface (the same surface imaged by the interferometer), and the temperature recorded as a function of time. The IR sensor had a fixed emissivity of 0.85, which corresponds to the general emissions of everyday materials. The emissivity of white paint is approximately 0.78, and so the absolute measurement of the temperature is probably subject to an error. However, the error is constant, and since the profile of the temperature curve is the primary interest here, the sensor was considered satisfactory for this purpose.

In each test, the specimen was allowed to settle at an ambient temperature of 27°C. It was then accelerated to the operational speed, using an acceleration rate of either 46rad s^{-2} or 82rad s^{-2}. Upon attaining the test speed, the temperature was recorded at 10s intervals, for a 140s duration. The IR measurement device indicated the temperature to the nearest °C, with an accuracy of ±0.5°C.

5.2.3.2 Results

The measured rise in surface temperature, at radii of 60mm and 120mm, and rotational speeds of approximately 12,000rpm, 15,000rpm, and 17,000rpm is shown in Graph 17. As would be expected, the temperature is higher at the larger radius, since the tangential



Graph 17: Measured temperature change at 60mm and 120mm

velocity, and therefore the air friction, is greater. Also, the rate of temperature rise is greater for the higher acceleration rate. This is an expected result, since a higher rate of acceleration leads to less heating incurred during the acceleration period[89], and therefore a greater temperature rise is required, to attain the equilibrium temperature, which is independent of acceleration.

Returning to the interferometric results, the correlation of various combinations of the speckle images allows the changing behaviour of the heating to be followed. The average deformation across the image was obtained by counting the number of fringes crossing a horizontal line through the specimen axis. Obviously, the Fourier transform fringe analysis software could have been used to determine the point strains at different radii, at different times, but the number of images which would require processing, for a single test run, is prohibitive[90]. Speckle correlation fringes, acquired from the specimen rotating at various speeds are presented on Pages 173 to 179. The tests speeds were:

- Test 1 4,991rpm 42rad s^{-2}
- Test 2 10,080rpm 42rad s^{-2}
- Test 3 10,012rpm 21rad s^{-2}
- Test 4 14,822rpm 42rad s^{-2}
- Test 5 14,884rpm 86rad s^{-2}
- Test 6 14,931rpm 21rad s^{-2}
- Test 7 17,394rpm 42rad s^{-2}

The 'Corr' in the image captions indicates which speckle images in the sequence were correlated. For example, Corr(0,4) represents the subtraction of images 0 and 4. The caption also contains the time differences of the images, a single number if the reference speckle pattern is image 0, otherwise the time of both images. The sensitivity is 0.40μm $fringe^{-1}$.

Graph 18 on Page 180 indicates the number of fringes across the image for various rotational test speeds, showing a definite increase in the average strain with time and speed. The initial reference speckle pattern is correlated with itself, producing a 'zero' fringe number for the first data point. The total number of fringes is a direct indication of the average strain across the 'gauge length' of the image. An equilibrium state is clearly reached by the specimen. Graph 19 indicates a similar results, but for a roughly constant speed (approx. 10,000rpm), attained at different acceleration rates. Graph 20 is similar to Graph 19, but for a speed of approx. 15,000rpm.

---

[89]This is evident by examining the y axis intersection of Graphs A and C. The 'starting' temperature, measured from when the specimen attains the test speed, is higher for the lower acceleration rate.

[90]A single test run may consist of 150 images, each requiring about 13 minutes to analyse completely. Therefore, continuous processing for 1.4 days would be required.



Image 113: Corr(0,1) - 10s
(Windage test 1)



Image 114: Corr(0,2) - 31s
(Windage test 1)

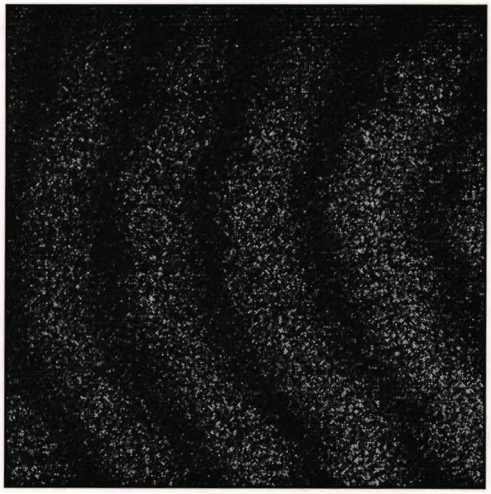


Image 115: Corr(0,3) - 41s
(Windage test 1)

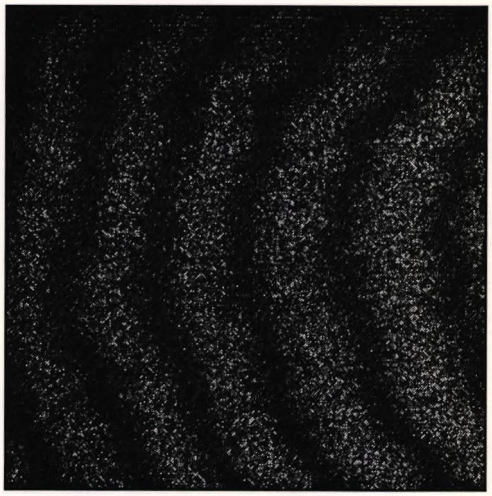


Image 116: Corr(0,4) - 51s
(Windage test 1)

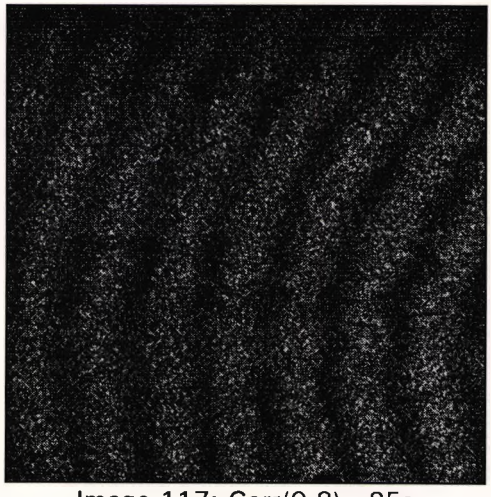


Image 117: Corr(0,8) - 95s
(Windage test 1)

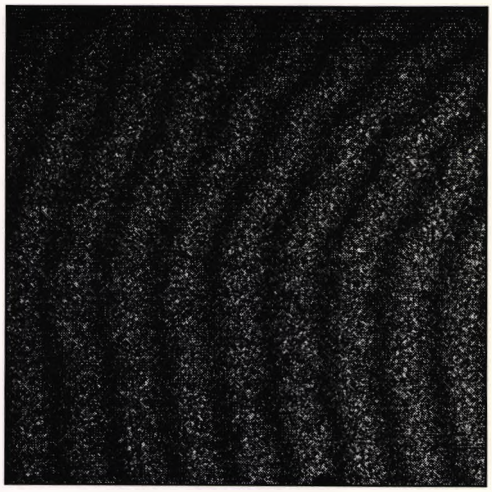


Image 118: Corr(0,13) - 150s
(Windage test 1)



Image 119: Corr(0,2) - 19s
(Windage test 2)



Image 120: Corr(0,3) - 29s
(Windage test 2)



Image 121: Corr(0,4) - 38s
(Windage test 2)



Image 122: Corr(0,5) - 48s
(Windage test 2)

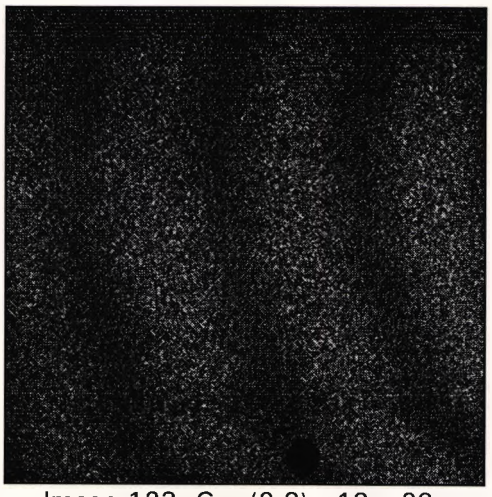


Image 123: Corr(2,3) - 19s, 29s
(Windage test 2)

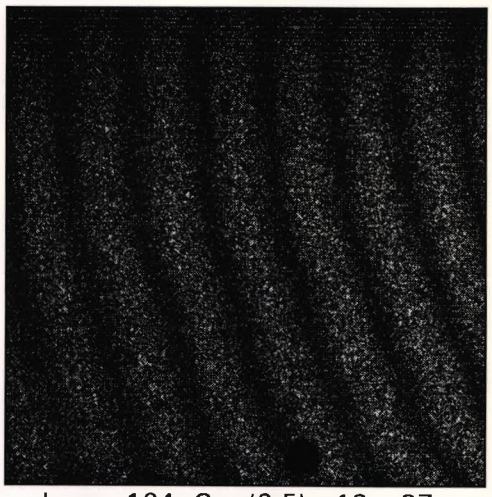


Image 124: Corr(2,5) - 19s, 37s
(Windage test 2)



Image 125: Corr(0,1) - 10s
(Windage test 3)



Image 126: Corr(0,2) - 20s
(Windage test 3)

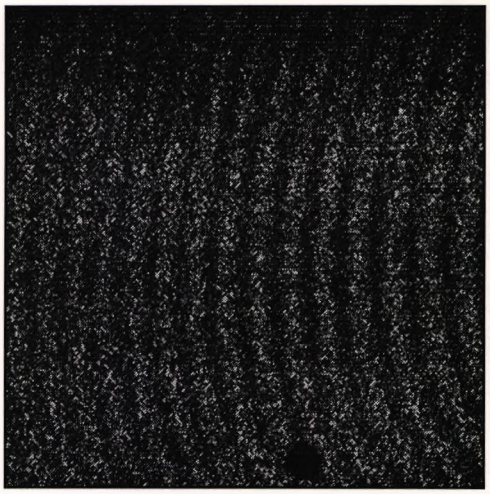


Image 127: Corr(0,4) - 39s
(Windage test 3)

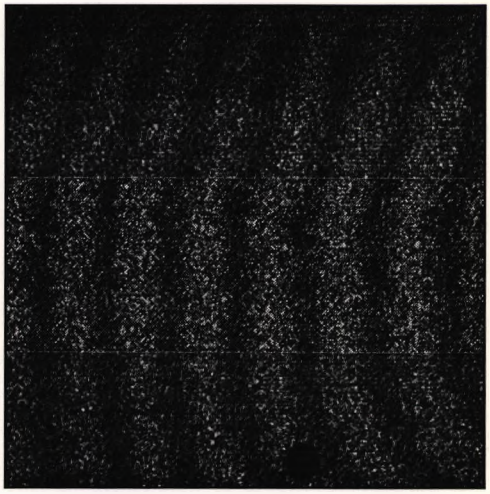


Image 128: Corr(1,3) - 10s, 29s
(Windage test 3)

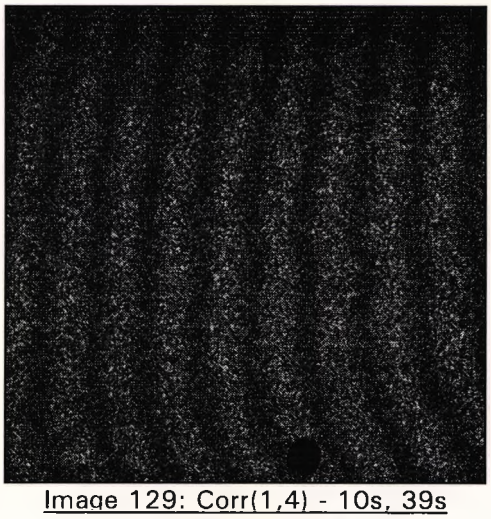


Image 129: Corr(1,4) - 10s, 39s
(Windage test 3)



Image 130: Corr(0,1) - 10s
(Windage test 4)



Image 131: Corr(0,2) - 19s
(Windage test 4)



Image 132: Corr(0,3) - 29s
(Windage test 4)

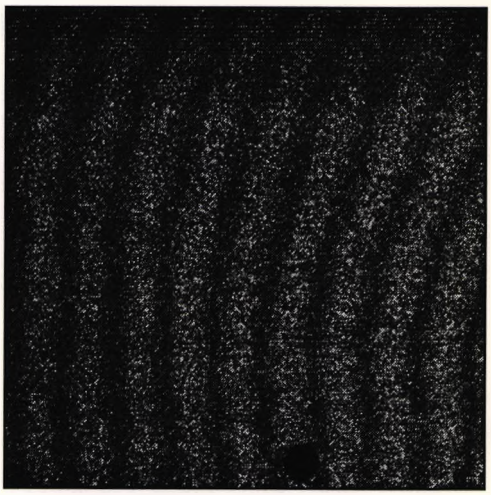


Image 133: Corr(1,2) - 10s, 19s
(Windage test 4)

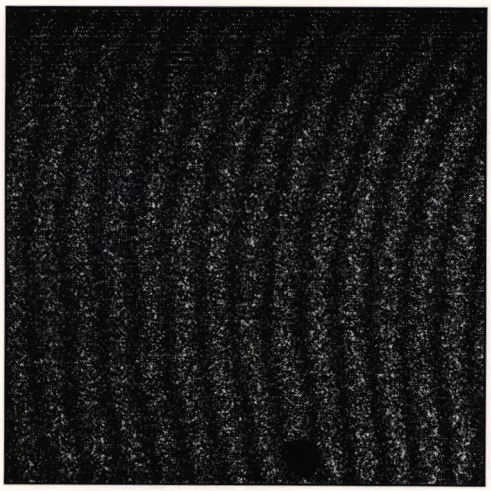


Image 134: Corr(1,3) - 10s, 29s
(Windage test 4)

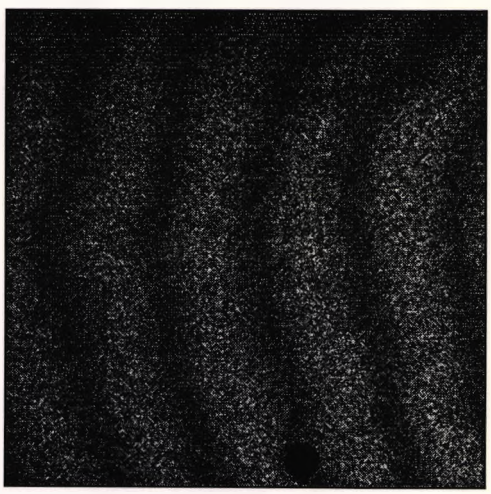


Image 135: Corr(2,3) - 19s, 29s
(Windage test 4)



Image 136: Corr(0,1) - 10s
(Windage test 5)

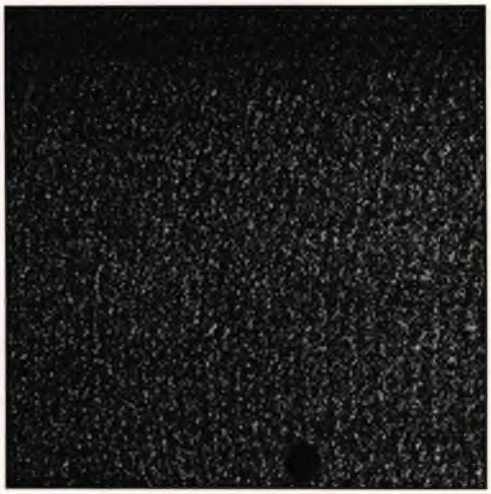


Image 137: Corr(0,2) - 20s
(Windage test 5)

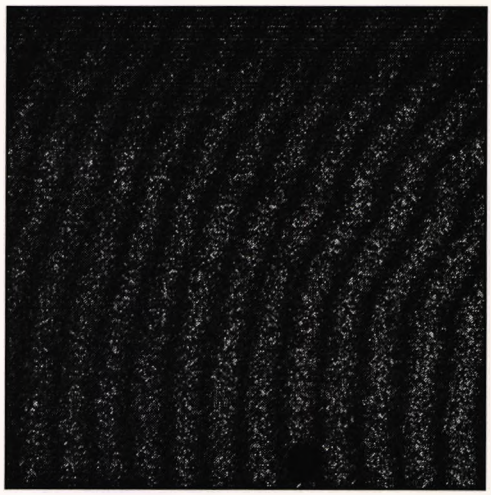


Image 138: Corr(1,2) - 10s, 20s
(Windage test 5)



Image 139: Corr(1,3) - 10s, 29s
(Windage test 5)



Image 140: Corr(1,4) - 10s, 39s
(Windage test 5)

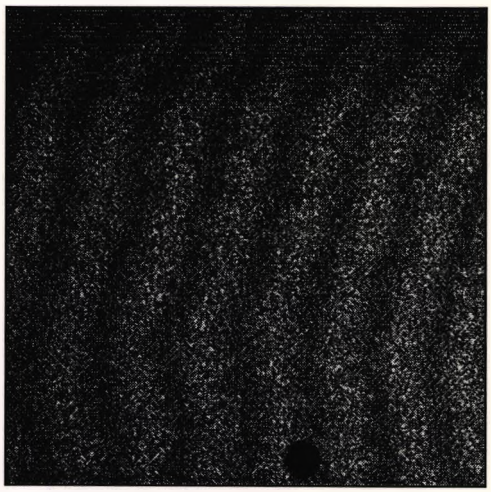


Image 141: Corr(3,5) - 29s, 49s
(Windage test 5)



Image 142: Corr(0,2) - 9s
(Windage test 6)

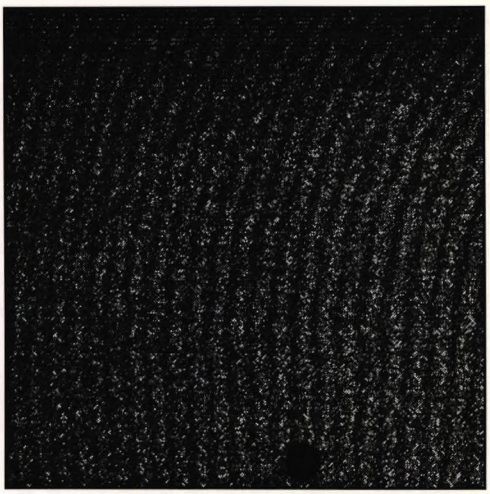


Image 143: Corr(0,3) - 28s
(Windage test 6)

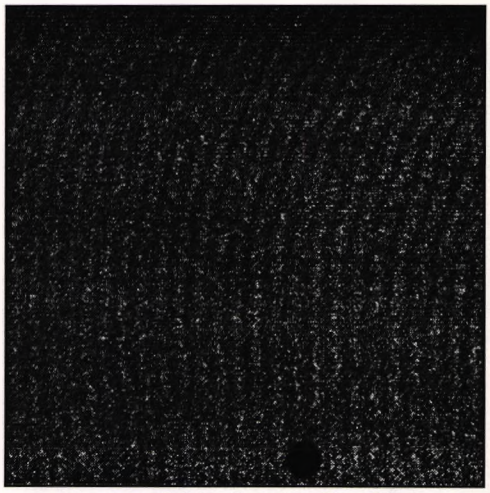


Image 144: Corr(0,4) - 38s
(Windage test 6)



Image 145: Corr(1,4) - 9s, 38s
(Windage test 6)



Image 146: Corr(1,5) - 9s, 48s
(Windage test 6)



Image 147: Corr(3,4) - 28s, 38s
(Windage test 6)



Image 148: Corr(0,1) - 9s
(Windage test 7)

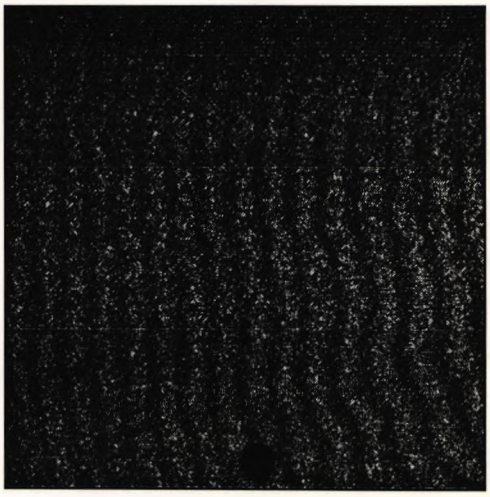


Image 149: Corr(1,2) - 9s, 18s
(Windage test 7)

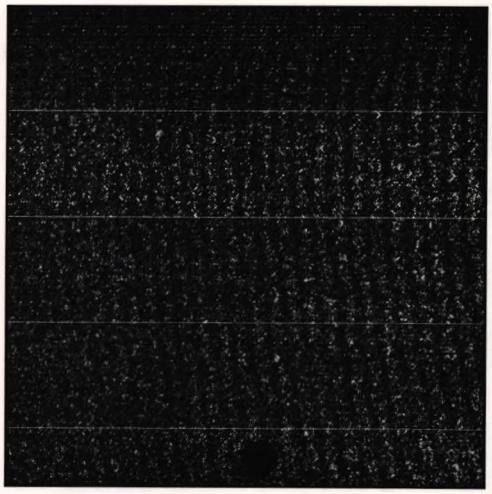


Image 150: Corr(1,3) - 9s, 31s
(Windage test 7)

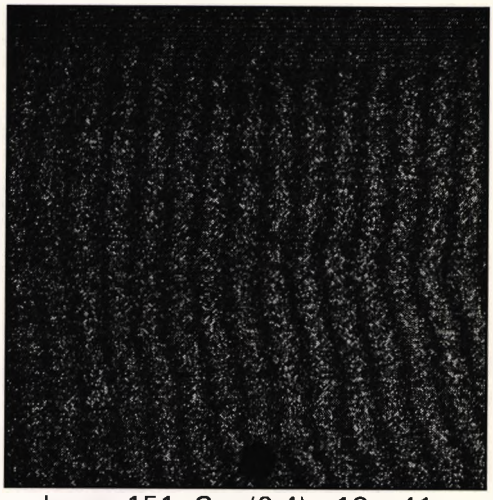


Image 151: Corr(2,4) - 18s, 41s
(Windage test 7)

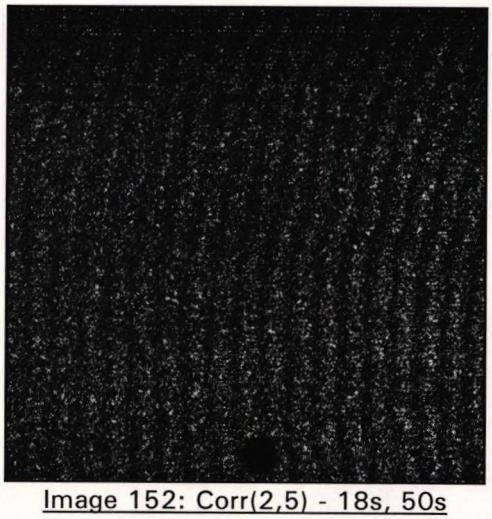
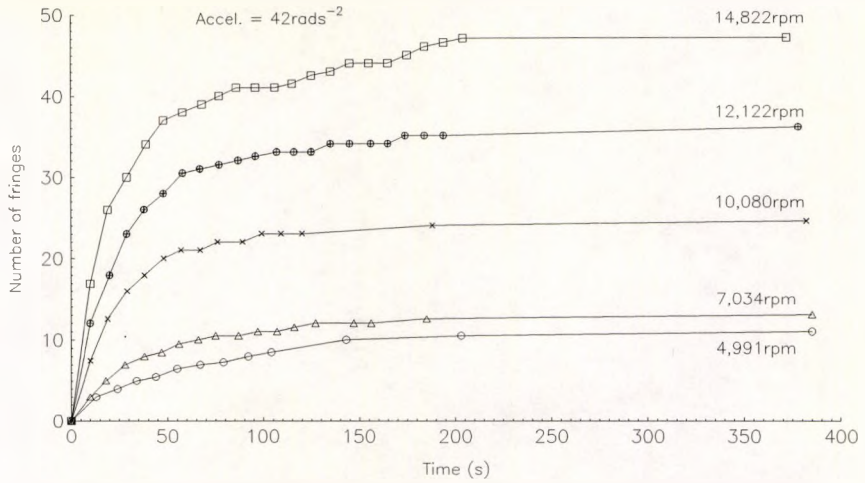
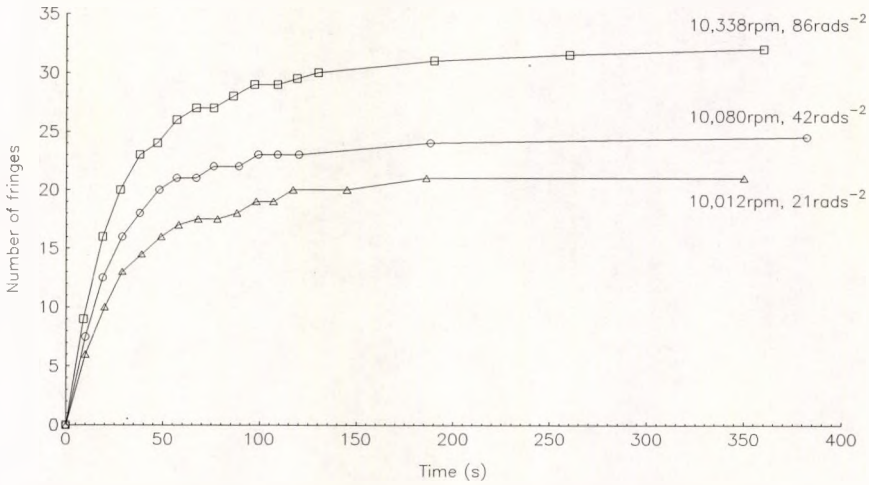


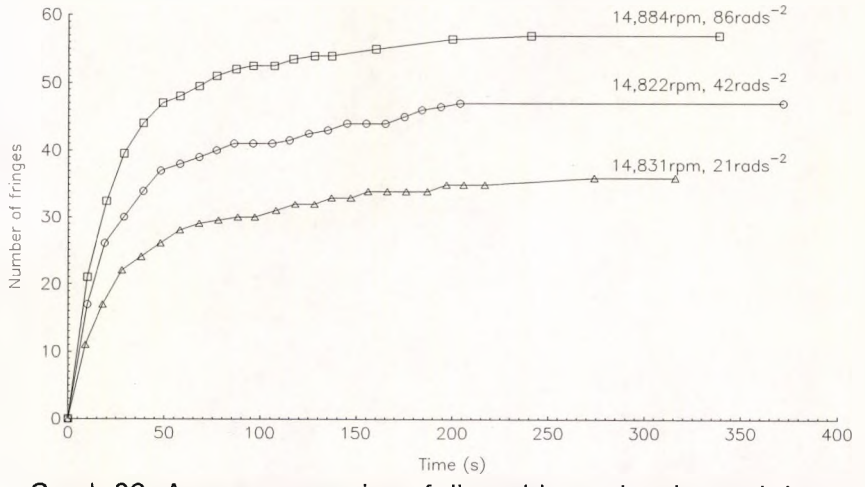
Image 152: Corr(2,5) - 18s, 50s
(Windage test 7)



Graph 18: Average expansion of disc with speed and time



Graph 19: Average expansion of disc with acceleration and time



Graph 20: Average expansion of disc with acceleration and time

5.2.3.3 Computed windage expansion

To determine if the windage tests are a reasonable estimate of the windage heating, the average temperature rise of the specimen is calculated from the windage test fringe patterns. The coefficient on linear expansion of the material is 23.5×10^{-6} /°C, which translates to a linear expansion[91] of 1μm for a temperature rise of 0.57°C. With reference to Graph 18, It can be seen that for a rotational speed of 12,122rpm, the ultimate[92] number of fringes seen across the gauge length of the screen is 36, which for a sensitivity of 0.40μm fringe^{-1}, represents an average temperature rise of 8.2°C. However, it can be seen from Graph 17(b) that the ultimate measured temperature change attained at 60mm radius is 5°C. At 14,822rpm (again refer to Graph 18), the ultimate number of fringes obtained is 48, representing an average temperature rise of 10.9°C. Graph 17(b) indicates a temperature rise of approximately 8°C. The computed temperature change is greater than the measured temperature change, since the majority of the measurement average is taken at a radius of greater than 60mm, which is at a higher temperature.

This method of comparing the data is approximate, and is only useful to determine if the agreement is within an order of magnitude. Obviously, there is a temperature gradient across the specimen, which is seen in the fringe patterns as a non-uniform field of fringes (see also Graph 17). The averaging procedure effectively transforms the gradient to linear, thereby introducing a major error. However, as stated, such a comparison is sufficient for the case described.

[91] The unit length is approximately 75mm, which is the width of the screen.

[92] Here, ultimate indicates the number at the end of the record cycle, not the physical ultimate.

6 ERRORS

6.0 Sources of error

6.1 Sensitivity vector error

6.1.1 Contribution due to optical system abberations

The twin cylindrical mirror optical system shown in Figure 11 (Page 23) suffers from a spherical aberration of mirror M_2. A spherical (or cylindrical) mirror will bring axial and peripheral rays to different focal points[93]. The degree of spherical aberration increases for rays distant from the axis, as the cube of the distance. The outer mirror used in the speckle pattern interferometer described in this thesis is the same one as used by Preater in the early experiments (described in Chapter 1). The mirror was constructed by selecting a piece of quality plate glass with a nominal thickness of 10mm, which was bent into an arc by allowing it to 'slump' into a mould (after heating). This technique was used since it is inexpensive.

A diagram of the theoretical mirror aberration is shown in Figure 125, a zoom of the focal region in Figure 126. Several mechanisms exist to overcome this aberration, for example Schmidt corrector plates [Smith and Thompson, 1988], but none were considered to be suitable for incorporation into the rig. However, it is noted that a paraboloidal reflector does not suffer from this aberration. A paraboloidal reflector, as shown in Figure 127, gives an

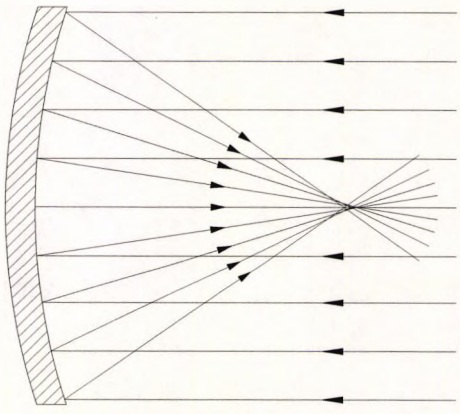


Figure 125: Spherical reflector

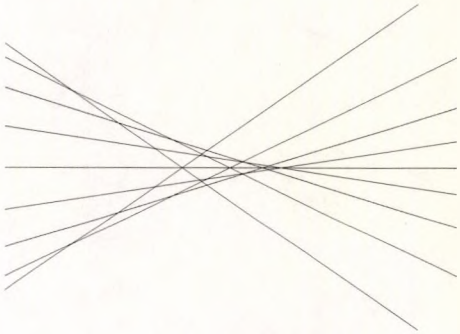


Figure 126: Zoom of Figure 125

[93]The 'focal plane' for a spherical mirror is a spherical surface with half the radius [Smith and Thompson, 1988].

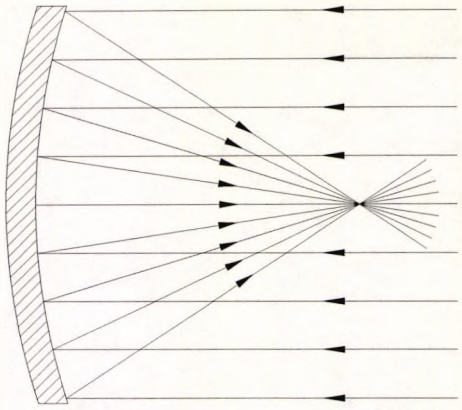


Figure 127: Paraboloidal reflector

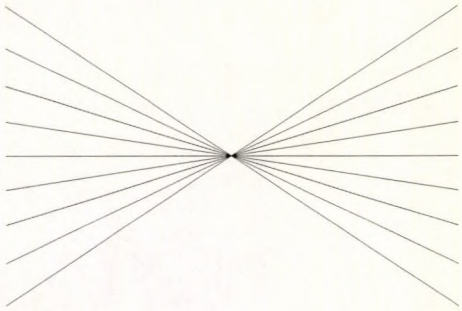


Figure 128: Zoom of Figure 127

exact focal point (in other words the optical path length from the incoming plane wavefront to the focal point is the same for all rays). The spherical aberration was made worse by the fact that the mirror was found to have a smaller radius of curvature than that specified to the supplier. The error at the extremities of the mirror was found to be approximately 2.5mm, which means the 'spread' distance shown in Figure 126 is significantly greater than it should have been. In the case of the mirror M_2, this spread was found to be approximately 12mm. The implications of the spherical aberration are two fold. Firstly, the alignment process discussed in section 3.2.3.1 becomes more difficult. Since only one 'focal point' can be placed on the axis of the rotating component, then only one pair of rays will be correctly aligned. It was considered wise to use the furthest intersection of rays possible from the surface of the mirror, since a parabola approximates a circle close to the axis. Hence, the regions close to the axis would suffer from very small errors. However, the errors at the extremities would be large. The second and perhaps more important implication of the spherical aberration is the alteration of the sensitivity vector of the interferometer. This can be understood with reference to the following three diagrams, which are drawn to scale. In Figure 129, a single ray is shown passing through the optical system. Since mirror M_2 does not reflect it along the path of the radius of mirror M_1, it is reflected back from M_1 along a different path than the incoming ray. In Figure 130, a second ray has been added to enable interference to occur. In the overlap region of the rays on the surface of the rotating component, interference occurs at the point P, but the rays are skewed with respect to each other. Figure 131 shows a greater degree of skewing with respect to the initial incident ray. The sensitivity vector lies between the rays, along the bisector. It is evident that for a particular ray, *R* (Figure 129), the sensitivity vector *approaches* the ray vector as the distance from the surface of mirror M_1 *increases*. Additionally, the initial difference between these vectors is proportional to the height of the incident ray (1) above the axis. Along the

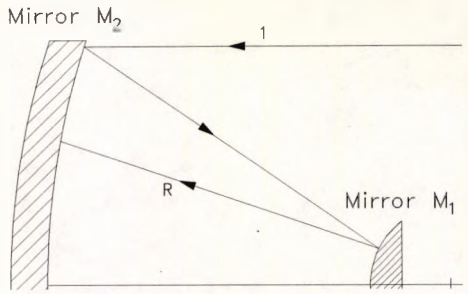


Figure 129: Off axis ray

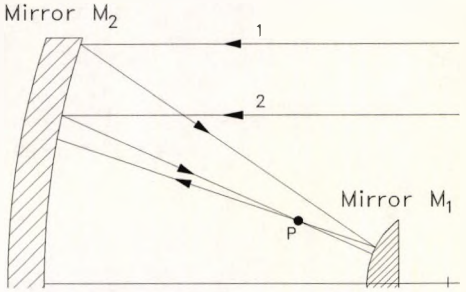


Figure 130: Additional ray

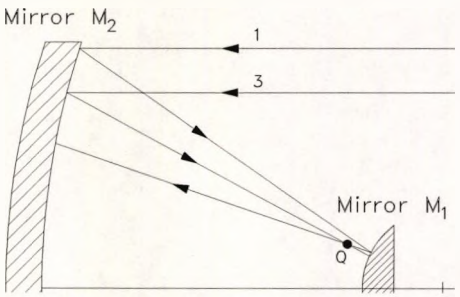


Figure 131: Another ray

horizontal line through the axis, the interferometer is correctly aligned. It can be concluded that off-axis rays will suffer a greater error in the *direction* of the sensitivity vector, and this error increases closer to the surface of the inner mirror. Also, since the sensitivity vector lies along the bisector of the incident and reflected rays, it rotates (counterclockwise) as the point under consideration is moved away from the inner mirror (M_1), along the path of ray *R*. This is because a different pair of rays interfere at each point, unlike the correctly aligned system, in which the same pair of rays interfere at all radial distances. This has the effect of 'flattening' the fringe patterns generated, by loading the specimen, since the fringes are perpendicular to the sensitivity vector. The value of the directional error is difficult to calculate, because the shape of the outer mirror is not spherical. A profile of the reflective surface of the mirror could have been conducted to generate the surface function, but this was considered meaningless, since the *exact* alignment of the two mirrors with respect to each is also difficult to gauge.

6.1.2 Contribution due to divergence of the laser beam

The standard in-plane interferometer of Leendertz [1970] operated with plane wavefronts. Any deviation from this system causes in-plane strain measurement errors. It must be remembered that the beam diverges into a *cone*, so that both the sensitivity vector magnitude, *and* direction will be subject to errors. The effect of the beam divergence on the

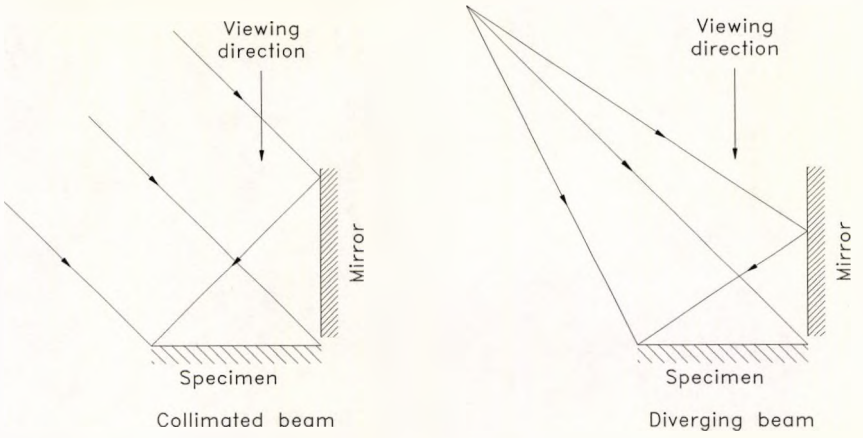


Figure 132: In-plane divergence error

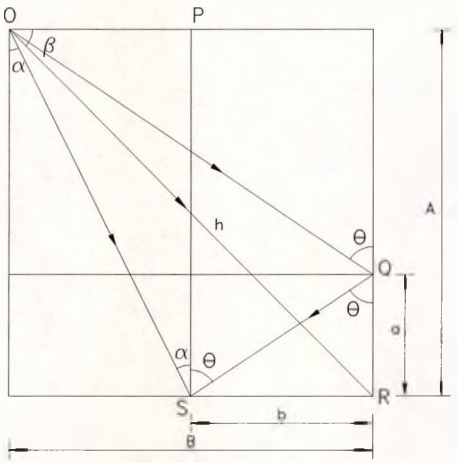


Figure 133: Geometrical representation (*xz* plane)

in-plane speckle pattern interferometer is shown in Figure 132. It is seen that the diverging beam causes the interfering rays to be incident on the specimen surface at different angles. The position of the incident beam on the plane mirror surface can be found from Fermat's Principle[94], and from this, the angle of incidence on the surface is easily determined. The divergence effect is worst at the edge of the field of view which is most distant from the mirror, since the angular difference of the interfering beams is greatest there. It is possible to calculate the effect on the magnitude of the sensitivity vector. Redrawing Figure 132 (right) to indicate quantities (Figure 133), it is clear that from $\angle$PSQ and $\angle$POQ, the angle of θ can be determined in terms of the lengths A, B, a and b. The angle θ is given by Equation [113] overleaf:

[94]Pierre Fermat, (1650): *"A light ray travelling from one point to another will follow a path such that, compared with nearby paths, the time required is either a minimum or a maximum or will remain unchanged".*

$$\frac{b}{a} = \tan\theta = \frac{B}{A-a} \qquad [113]$$

It can readily be shown that:

$$\tan\theta = \frac{B+b}{A} \qquad \tan\alpha = \frac{B-b}{A} \qquad \tan\beta = \frac{A}{B} \qquad h^2 = A^2 + B^2 \qquad [114]$$

To gauge some typical values, if the nominal angle of beam incidence, β, is 45°, then:

$$\theta = \tan^{-1}\left[1+\frac{\sqrt{2}b}{h}\right] \qquad \alpha = \tan^{-1}\left[1-\frac{\sqrt{2}b}{h}\right] \qquad [115]$$

where h is the distance over which the beam diverges, and b is the extent of the field of view. The fringe sensitivity for collimated illumination is[95]:

$$\textit{fringe sensitivity} = \frac{\lambda}{2\sin\theta} \qquad [116]$$

And for diverging illumination, at a distance b from R:

$$\textit{Divergent fringe sensitivity} = \frac{\lambda}{\sin\theta + \sin\alpha} \qquad [117]$$

For the system described in this thesis, the JK 2000 pulsed laser is diverged over a distance of approximately 4m, and the field of view is normally about 10cm. So, for nominal 45° illumination, the collimated fringe sensitivity (for $\lambda = 694$nm) is 0.4907μm fringe^{-1} and for diverging illumination, it is 0.4910μm fringe^{-1}. This is the worst case error (0.06%), since as the distance b decreases, so does the error. It can be seen that if the beam is diverged over a large distance, and the field of view is relatively small (see Table 14), then the error can be ignored. An experimental measurement system, described by Macarthur [1988], explains some of the practical problems encountered with beam divergence over a short distance. Macarthur describes errors of the order of 33% when using rapidly diverging illumination (0.2m), which is somewhat higher than indicated in this analysis, but Macarthur did not seem to realise that directional errors (which are considered below) would also occur, which could easily account for the increased error observed.

If a video camera images the situation of Figure 132 (right) in the direction indicated, and the raster scan direction aligned so that it is parallel to the sensitivity vector, then the condition illustrated in Figure 133 will be true for *any* scan line, and the *vertical* position of the scan line

[95] θ in this case is the angle of incidence of both interfering rays.

under consideration does not affect the *magnitude* of the vector[96]. However, as stated earlier, beam divergence also has an effect on the *direction* of the sensitivity vector. If the video image of the specimen surface is now considered, then for a standard plane mirror optical system, the geometry of which is shown in Figure 134[97] (the image is in the plane of the paper), it is a relatively trivial matter to derive an expression for the angular difference between the interfering beams ($\sigma+\eta$) in terms of the divergence distance (h), the height of the scan line (c), and the distance from the reflecting surface (b):

$$\sigma = \tan^{-1}\left[\frac{c}{h+b}\right] \qquad \eta = \tan^{-1}\left[\frac{c}{h-b}\right] \qquad [118]$$

The angle between the sensitivity vector and the horizontal (φ) is the deviation of the vector direction, from that produced by collimated illumination, and is given by:

$$\varphi = \frac{\eta - \sigma}{2} \qquad [119]$$

In this case, the nominal angle of incidence, which was important in determining the magnitude error, is of no consequence. Typical results, for a divergence distance of 4m, a field of view of 10cm and a worst case position[98], the deviation, φ, is 0.0358°. Additional results for different divergence distances are shown in Table 14. For all the in-plane ESPI systems described in this thesis, the divergence distance is large and the field of view is small, so the errors (for nominal illumination close to 45°) can be ignored, and the sensitivity vector can be considered to be indistinguishable from that produced by collimated illumination. For the twin cylindrical mirror system, any error in the direction of the sensitivity

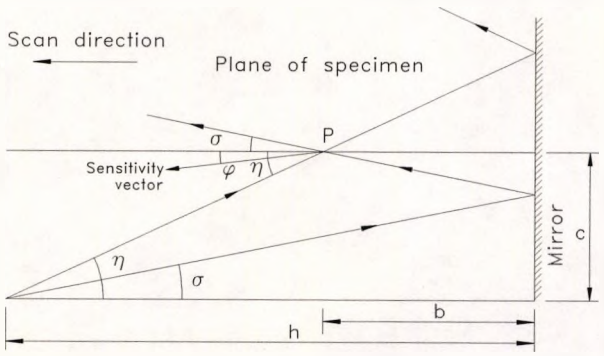


Figure 134: Plane mirror divergence (*xy* plane)

[96]Vertical in this context indicates the height of the scan line on the video image.

[97]In this illustration, the laser is diverged from the same height as the base line. In many real systems, the divergence height is chosen to be the vertical centre of the image.

[98]If a square image of the overlap area were made, the worst case position would be the extreme top left of the image, with b = 10cm and c = 10cm

Divergence distance (m)	Magnitude error (%)	Direction deviation (°)
4.0	0.047	0.037
3.5	0.061	0.047
3.0	0.083	0.064
2.5	0.120	0.092
2.0	0.188	0.143
1.5	0.335	0.255
1.0	0.757	0.573
0.5	3.117	2.287
0.4	4.975	3.562
0.3	9.257	6.264
0.2	23.626	13.282

Table 14: Error for plane system (45° nominal, 0.1m field of view and scan line)

vector due to divergence would inevitably be swamped by the error due to the spherical aberration of the outer mirror, and the magnitude calculation would be identical to the plane mirror setup. Also, it would be difficult to determine the effect of this error on the twin mirror cylindrical optical system since the focal position of the outer mirror cannot be determined accurately, again due to the aberration. Therefore, for all the cases under consideration in this thesis, the errors due to beam divergence can be ignored.

6.1.3 Contribution due to area determination

It is essential that the object plane dimensions of the image area under consideration be determined as accurately as possible. This was mentioned on Page 38, where three ways were suggested to compute the ratio of pixels to physical length (metres). In this work, only the first two of those suggestions were utilised. A white light image is taken of the specimen or a target located in the object plane. Some feature from the image, having known dimensions, is used to compute the dimensions of a pixel. An example of such an image is shown on Page 139, Image 52. In this example, a 5mm hole is imaged, and found to have an *average* diameter of approx. 273 pixels. However, slight burs on the edges of the drilled hole, or differences in the lighting of the image could yield a different measurement for the hole. According to Gonzalez and Wintz [1987], it is often possible to determine an edge to *at least* the nearest pixel, and so the assumption is made that the measurement is accurate to ± 1 pixel. Therefore, when choosing a gauge length for the strain measurements, a

compromise between the minimum number of pixels, and required length of strain measurement must be used. For example, if 10 pixels are used for the gauge length, then the length measurement may be subject to a ±10% error, whereas 100 pixels would reduce the error to ±1%. A suggested minimum number of pixels is approximately 40, reducing the length error measurement to a maximum of ±2.5%.

6.1.4 Contribution due to centre coordinate calculation

The method of determining the centre coordinates of the specimen disc in the coordinate system of the VS100 was discussed in section 4.5.6. In summary, a line is scribed on the disc and white light images of it in different rotational positions are recorded. The operator locates two points on each line in the image, using the computer mouse, and the equation of each line is computed, and used to solve for the crossover point, with respect to all the other lines. As mentioned earlier, a line in the VS100 memory will generally occupy more then one pixel width, and therefore selecting a point on it will only be accurate to approximately a single pixel. Consider Figure 135, in which a line is measured at two points, with heights y_1 and y_2 respectively, the distance between them of b. The vertical error in measuring the two points is E_1 and E_2, and the subsequent error in the cross point with the horizontal is E_H. If E_1 and E_2 are 1 (a measurement accuracy of 1 pixel), then it can be shown that:

$$E_H = \frac{b(y_1+y_2)}{(y_1+y_2)(y_1+y_2-2)-4y_1y_2} \qquad [120]$$

Typically, the horizontal axis will pass through the centre of the video image, so y_1 has a maximum value of 256. However, the VS100 has 768 horizontal pixels[99] (b), so some typical values would be $y_1 = 256$, $y_2 = 128$ and $b = 768$, resulting in a horizontal error, E_H,

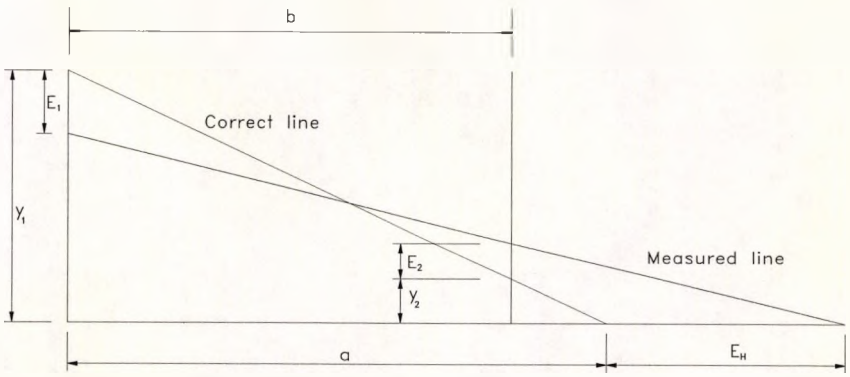


Figure 135: Error in measuring disc centre coordinates

[99]The VS100 768/2 has 768 horizontal and 512 vertical (square) pixels, even though 512x512 are normally used for processing. This is because the Fourier transform requires sample sizes which are powers of 2.

of about 18 pixels. It must be remembered that the horizontal axis would also need to be measured on the VS100, and this too is subject to a similar error. However, this means that the crossing point error of the two lines is subject to a vertical as well as horizontal error. If we assume, without proof, that the vertical error is of similar magnitude (in reality it is likely to be much less than the horizontal), then the measured centre coordinates can be said to lie within a circle of radius R_E, centred on the actual disc centre coordinate. For the typical results presented, R_E = 18 pixels. In practice, ten different images of the line are taken with the disc in different orientations, so the error will be reduced by a factor of about 3, indicating a peak error of about 6 pixels. If a typical imaging size is used, in which the field of view is 10cm (for 512 pixels), then the measured centre coordinate is within 1.2mm of the actual measurement. The deviation of the sensitivity vector due to a centre coordinate error will be greater, closer to the axis. The minimum radial value observable with the rig is 50mm (the radius of curvature of the inner mirror), so the worst case angle deviation will be about 1.4°. This is a rough figure based on a number of 'typical' figures, but serves to show that the deviation in sensitivity vector is relatively small if several measurements of the line in different orientations are made, at wide positions on the screen, using a zoom facility to position the ends of the line to the nearest pixel accurately.

6.1.5 Contribution due to incidence angle measurement

The sensitivity vector magnitude error is directly related to the accuracy to which the angle of incidence on the specimen surface can be determined. The method of measurement of the incidence angle is rather crude, and is shown in Figure 136. Using the undiverged laser beam[100], a long thin plate is moved close to the beam, and is shifted to be parallel, as shown. When the profile of the beam is barely visible on the plate surface, it is considered to be exactly parallel with the beam. The angle of the plate is then measured, with reference

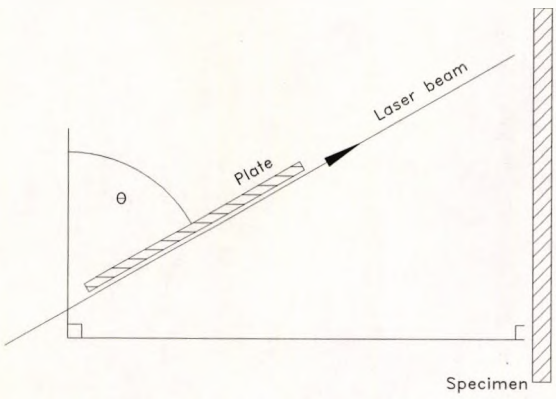


Figure 136: Method of incidence angle determination

[100]The HeNe alignment laser is used to determine the incidence angle of the pulsed laser.

to the specimen normal. The angle is measured either directly, using a protractor, or by drawing a line along the base of the plate, on a piece of paper, and using a right angle triangle to calculate the angle. It is estimated that this form of angle determination can indicate the incidence angle to an accuracy of $\pm 1°$, or better. The sine term of Equation [15] is modified by the inaccuracy, and the interferometer sensitivity becomes:

$$\textit{fringe sensitivity} = \frac{\lambda}{2\sin(\theta \pm 1)} \qquad [121]$$

For example, if the actual angle of incidence is 45°, then the true value of the sine term is 0.70711, and the values of the sine of $45 \pm 1°$ are 0.71934 and 0.69466, which gives a sensitivity vector variation (for a ruby laser) from 0.48μm fringe^{-1} to 0.50μm fringe^{-1} (the actual fringe sensitivity is 0.49μm fringe^{-1}). Therefore, for an incidence angle of 45°, a ruby laser, and an uncertainty of $\pm 1°$ on the incidence measurement, the error in the magnitude of the sensitivity vector is $\pm 2\%$. The magnitude of the error is dependent upon the nominal incidence angle, and since in-plane electronic speckle pattern interferometers only operate successfully in the incidence range 20° to 60°, then for a ruby laser, the peak error is approximately 5.5% (the difference between incidence angles of 19° and 20°). However, what must be remembered is that a small value of θ represents a 'steep' beam incidence with respect to the tangential surface vector, since θ is measured from the surface normal. Therefore, in many of the cases under consideration in the results section of this thesis, the operating incidence angle is well over 45°, and therefore the error is less than 2%.

6.1.6 Fringe field angular skew

When using the twin cylindrical mirror interferometric system, the spherical aberration of the outer mirror sometimes causes 'radial fringes' to be produced, an example of which is shown in Image 10 (on Page 35). The same effect that causes the radial fringes can 'skew' the concentric fringes, causing errors in the recovered phase data. The skew will normally occur about the horizontal centre line through the specimen axis, and will therefore have conjugate effects on points on either side of that line. In other words, the error will add to points on one side of the line, and subtract from points on the other side. Hence, if a measurement is made at a certain angle above the line, and the same angle below the line, then assuming all other factors have small errors, the average value of the two measurements should be a good estimate of the real measurement at each point. This scheme is used to analyse all the fringe patterns from the rotating specimen.

6.2 Data acquisition and processing

Data acquisition is the process of acquiring the optical information from the interferometer, and converting it into digital data, for analysis by the computer. The acquisition process involves several steps, each causing distortion to the data (noise)[101]. Noise can be defined as *"fluctuations which cause a difference between the estimated and true values of a signal"*. Noise analysis is a very complex subject, which is laden with assumptions and approximations. Therefore, the analysis presented in this section will be a simplification, and should serve only to give an indication of the magnitude of the errors resulting from the analysis system. The three main sources of noise in the acquisition system under consideration in this thesis are from the optical system, the camera and the sampler. A block diagram of the acquisition system is shown in Figure 137, in which each 'box' can involve several different processes. The data under consideration is obviously a two-dimensional intensity field, the distortion of which affects both the intensity information, and the spatial position. However, the spatial distortion is considered to be a constant, and is not discussed further. The intensity information is passed along the processing chain of Figure 137, becoming progressively more distorted as it passes to the right. Certain processes involve manipulation of the data without error[102] and these are obviously not considered.

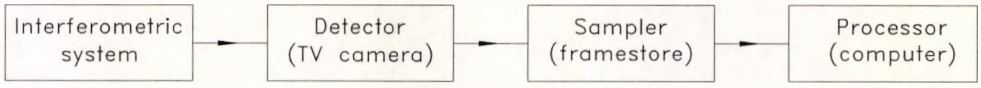


Figure 137: Acquisition system

6.2.1 Camera noise

The irradiance is recorded by a video camera, which has a signal-to-noise ratio of approximately 35dB (CCD cameras can be approximately 50dB). An estimate of the noise on the video signal can be obtained from the equation [Cohn and Pryputniewicz, 1990]:

$$N^2 = \left[\frac{W_d}{SNR}\right]^2 \qquad [122]$$

where W_d is the pixel electron well depth, and SNR is the signal-to-noise ratio. This is an important parameter when one is dealing with time averaged fringe systems, since many of the other noise sources (especially the electronic noise) are significantly reduced by the averaging procedure. However, it is important to remember that the fringes generated with

[101] In the PC, further errors are negligible, unless the programs have been coded clumsily, or software errors remain.

[102] For example, moving the data within the computer.

a 'double pulsed' ESPI system are two snapshots of the specimen in different loading conditions. In this case, the camera noise is 'frozen' into the image along with the other noise sources, and only reduces the correlation of the two speckle patterns if significant. It therefore reduces the signal-to-noise ratio of the fringes, but most importantly does not affect the shape of the fringe patterns. Without going through the complete analysis, this noise can be considered additive, and 'lumped' together with the other noises.

6.2.2 Quantization

The process of converting a discrete-time signal[103] into a digital signal by expressing each sample value as a finite (instead of infinite) number of digits, is called quantization. The error introduced by representing the continuous signal as a finite set of discrete values is called the *quantization error* or *quantization noise*. Following from Proakis and Manolakis [1988], the quantization error is defined as the difference between the actual value of a signal and the quantized value. The allowed values in the quantized digital signal are called quantization levels, and the distance between the levels (often given the symbol Δ) is called the quantization step or resolution. Most quantizers perform rounding, as shown in Figure 138, with a quantization error $e_q(n)$ limited to:

$$-\frac{\Delta}{2} \leq e_q(n) \leq \frac{\Delta}{2} \qquad [123]$$

Quantization always results in the loss of information due to the many-to-one mapping of samples at a distance of $\Delta/2$ from a certain quantization level. Therefore, quantization is both nonlinear and irreversible, and may be modelled as an additive noise corrupting the desired signal, as shown in Equation [124] overleaf:

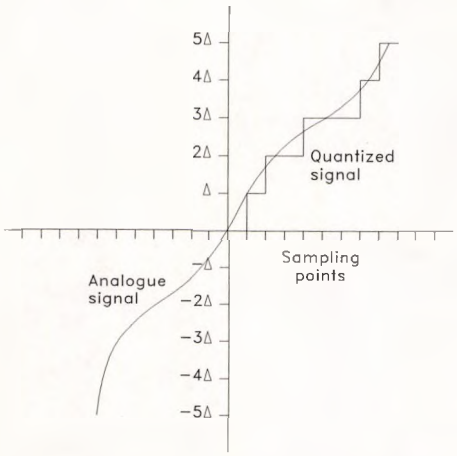


Figure 138: Rounding of signal samples

[103] An analogue signal which is sampled, but not digitized.

$$x_q(n) = x(n) + e(n) \quad [124]$$

where the quantization error is $e(n)$. The effect of the noise on the desired signal can be found by evaluating the signal to noise ratio (SNR), which is:

$$SNR = 10 \log_{10}\left[\frac{P_x}{P_n}\right] \quad [125]$$

where P_x is the signal power, and P_n is the noise power. Since the probability density function of the quantization noise is uniformly distributed over the region $[-\Delta/2, +\Delta/2]$, the mean value of the error is zero and the variance can be shown to be:

$$P_n = \frac{2^{-2b}}{12} \quad [126]$$

where b is the number of bits used to digitize the signal. The SNR is then:

$$SNR = 10 \log_{10}[p_x] + 10.8 + 6b \quad [127]$$

Each additional bit used to digitize the signal reduces the quantization noise power by 6dB or alternatively increases the signal to quantization noise power by 6dB. The VS100 framestore fitted to the computer digitizes the video signal to a resolution of 256 grey levels which is 8 bits. Therefore, the quantization noise power level is -58.8dB below the signal power level. This error can be regarded as negligible, as verified by Frankowski *et al.* [1989] who explain that for a 6 bit quantization, the error in the recovered phase is of the order of 1000^{-1} of the wavelength.

6.2.3 Speckle noise

As noted in section 2.1, when an optically rough surface is imaged using coherent illumination, random *phase* fluctuations in the object plane result in random *intensity* fluctuations in the image plane[104]. The transformation occurs due to interference between different waves originating from separate locations within the system's point spread function [Saleh and Rabbani, 1980]. In a practical coherent imaging system, as shown in Figure 14, the random phase noise of the surface, due to roughness, $\exp\{i\theta(x)\}$, is multiplied by the useful information from the surface, $\sqrt{s}(x)$, and if certain assumptions about the properties of the noise are made, then to a good approximation, the system may be modelled as shown in Figure 139. The detected intensity in the image plane is given by Equation [128]:

[104]Speckle also occurs in many other systems which require coherent imaging. For example Munson Jr. and Sanz [1984] describe speckle problems in synthetic aperture radar.

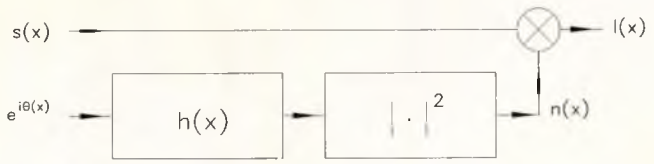


Figure 139: Speckle noise mathematical model

$$i(x) = s(x)|\, e^{i\theta(x)} \otimes h(x)|^2 \qquad [128]$$

where $h(x)$ is the coherent impulse response of the imaging system. Saleh and Rabbani [1980] point out that the speckle noise is multiplicative, and although this result had been obtained earlier by different researchers, it is disputed by Tur *et al.* [1982], who believe the approximations used are invalid for many cases. However, for the ESPI systems under consideration, it is sufficient to assume that the noise is multiplicative.

Goodman [1975] explains that when a speckle pattern is added to a coherent background, the probability density function of the intensity of a fringe pattern degraded by noise has a mean of:

$$\langle I(\vec{r}) \rangle = \langle I_N \rangle + I_s(\vec{r}) \qquad [129]$$

where I_N is the mean intensity of the speckle noise, and $I_s(\vec{r})$ is the fringe pattern signal (noise free), and the variance is given by:

$$\sigma_I^2(\vec{r}) = \langle I_N \rangle^2 \left(1 + 2\frac{I_s(\vec{r})}{\langle I_N \rangle} \right) \qquad [130]$$

This result is interesting, since the variance of the intensity increases as the fringe signal power increases. Therefore, there is a higher level of noise at the fringe maxima than at the fringe minima, an effect which is quite evident with speckle correlation fringes (the dark fringes are far less noisy than the bright fringes).

Several interesting methods have been devised to remove the speckle noise from images. Several examples, specific to electronic speckle pattern interferometers, are described by Varman and Wykes [1982]. Some of the methods in the paper seem interesting, but do not fully solve the speckle noise problem. A later publication by Paler and Bowler [1986], in which Gabor filters are applied to fringe separation appears to yield better results. The paper explains that many of the decorrelation methods developed to process images contaminated with speckle noise are inappropriate to ESPI images since the fringe modulation is dependent upon speckle correlation. Also, the Fourier transform methods developed are only partially successful since the frequency response of the fringe function is suppressed by that of the

speckle. The speckle reduction achieved from the use of Gabor filters appears to be very effective. Once the fringe pattern has been created, by the correlation of two speckle patterns, then noise removal schemes are more successful. A few interesting references to the techniques of speckle noise removal are: Jain and Christensen [1980], Lim and Nawab [1981], Maeda and Murata [1986].

6.2.4 Post processing (after acquisition and storage)

All mathematical operations are computed in the host processor using Microsoft C version 6.0. Double precision floating point data fields are generated for all non double precision data (for example an image would be converted to a double precision field). All mathematical manipulations are performed in double precision which is the natural typecast for the functions of the link library (no typecast conversion errors occur). The Microsoft C double precision values occupy 8 bytes of memory and have a range of 10^{-308} to 10^{308}. The mantissa has a precision of 15 digits. The compile options explicitly use the inline floating point library which means the programs only run on computers fitted with a math coprocessor. The 80x87 coprocessors compute values using the long double format (10 bytes) which are even more accurate than the double precision format. It is therefore considered that any errors due to the mathematical manipulation of the data are small in comparison with other errors.

6.3 Phase extraction errors

The accuracy of the Fourier transform method of fringe analysis has been investigated empirically by Macy [1983], who explains that if the Nyquist limit is obeyed (more than two pixels per fringe), then the RMS standard deviation of the phase reconstructed by the Fourier transform method from the true phase is about *one fiftieth* of the wavelength of the illumination. Kreis [1988] compares the Fourier transform method with several other phase extraction methods, but unfortunately does not use a carrier frequency. Green [1990] points out that this is incorrect, since adequate separation of the lobes in the Fourier transform domain cannot be achieved. However, Kreis obtains an accuracy of about *one twentieth* of a fringe, which is comparable to several other phase extraction techniques, and an order of magnitude greater than intensity based methods. The expected accuracy with a carrier frequency would be higher than that found by Kreis. Malcolm *et al.* [1989] report very small mean errors (0.01%) on the extraction of the radius of a simulated sphere using the Fourier transform method. Kujawińska and Wójciak [1991] have produced a very comprehensive reference to the sources of error encountered when using the Fourier transform method of fringe pattern analysis.

They list the main sources of error as:

- *Aliasing*, if the rate of sampling is too low (section 4.2.1).
- *Spectral leakage* of energy from adjacent frequency locations, due to inappropriate truncation of the data. This error is greatest at the edges (section 4.2.1.6).
- Errors due to incorrect filtering in the Fourier transform domain, especially when non-linear recording of the fringe pattern has been performed (section 4.2.1.5).
- The *picket fence effect*, which occurs if the input signal to the Fourier transform includes a frequency which is not a discrete frequency (section 4.2.1.6).
- The effects of random noise and spurious fringes in the fringe pattern.
- Errors due to incorrect determination of the domain, causing errors in the unwrapping algorithms (4.2.4).

It is pointed out that the elimination or reduction of some, or all of these errors depends upon several important factors, namely:

- Features of the interferometric image, such as the carrier frequency, the spatial bandwidths of the background, the information content, the gradient of the phase, the signal-to-noise ratio and the complexity of the fringe pattern domain.
- The physical acquisition of the data, such as the quality of the optical components, the resolution and quality of the detector, the quality of the laser, and the digitization process.
- Modification to the basic Fourier transform method of fringe analysis (ie the one proposed by Takeda *et al.* [1982].

If the basic assumptions regarding the Fourier transform method suggested by Takeda *et al.* [1982] are obeyed (sampling and domain), then an estimate of the expectation value of the RMS error in the retrieved phase is given by [Takeda *et al.*, 1982; Bone *et al.*, 1986; Chen *et al.*, 1991]:

$$E\{\delta\phi_{rms}\} = \delta_n \frac{\sqrt{\alpha/2}}{\pi m} \qquad [131]$$

where α is the ratio of the number of sample points in the passband of the filter (n), to the total number of sample points (N), δ_n is the rms value of the noise, and m is the mean modulation amplitude. Bone *et al.* [1986] state (without explanation) that if an optimum filter is applied to the spectrum, then the error resulting from inclusion of random noise frequency in the passband of the filter is approximately equal to the loss of important frequency components pertaining to phase information. They produce an estimate of the error in the retrieved phase under these optimum filtering conditions:

$$\{\delta\phi_{rms}\}_{est} = \delta_n \frac{\sqrt{2\alpha}}{\pi m} \qquad [132]$$

Kujawińska and Wójciak [1991] continue by explaining that refinements to the basic Fourier transform method of Takeda *et al.* [1982] can increase the accuracy of the retrieved phase:

- The use of the two-dimensional Fourier transform, permitting a considerable improvement in the discrimination between the required and unwanted spectral components.
- The application of a two-dimensional spatial window to the data, and the extrapolation of data over the complete image array, both of which significantly reduce the errors caused by inappropriate truncation of the data.
- Removal of the heterodyning frequency in the spatial domain rather than the Fourier transform domain, since the tilt is unlikely to result in an integer number of carrier fringes.
- Subtract errors caused by the experimental configuration. This must be performed prior to removal of the tilt.
- Obtain an accurate estimate of the fringe pattern domain.

The Fourier transform fringe analysis system described in this thesis does utilise many of the improvements suggested by Kujawińska and Wójciak [1991]. In the first part, a two-dimensional Fourier transform analysis is used, with sufficient detector resolution to ensure that aliasing does not occur[105]. There is normally no problem in domain determination, since the fringes of the rotating specimen regularly fill the entire data array of the VS100. However, small holes are sometimes drilled in the specimen to act as stress raising features, and the phase data in the region of these is considered less reliable than the rest of the data. No form of data weighting in the spatial domain is applied to the fringe data, since measurements near the edges of the phase array are not required for this application, and the substantial edge errors do not extend very far into the array [Green, 1990]. Kujawińska and Wójciak [1991] point out that it is preferable to remove the heterodyning in the spatial domain, rather than the Fourier transform domain, since the latter can only be shifted by integer amounts due to the discrete nature of the Fourier transform. This form of heterodyne removal is used in the analysis of the fringes in this thesis, but is a different approach to that suggested by Kujawińska and Wójciak, who recommend removal by multiplication of a conjugate exponential function or subtraction of an inclined plane, as shown in Figure 57. However, in the case of the speckle correlation fringes generated in this project, the tilt pattern consists of curved fringes, which are difficult to remove by a direct

[105] In the worst case, each fringe is sampled by about 17 pixels (30 fringes in a 512x512 array).

subtraction or multiplication method, since the heterodyning vector changes with position. A simpler method is shown in the lower diagram of Figure 57, and was taken from Huntley and Field [1989]. This method does require twice the number of Fourier transform operations, which increases the analysis time required for the operation. However, it does eliminate the problems associated with non-linear and unequally spaced tilt fringes. Contrast variations and noise are a significant problem with speckle correlation fringes, but much is made of the immunity of the Fourier transform to such effects. Kujawińska and Wójciak demonstrate that even with large contrast variations (50%) and considerable noise (standard deviation of signal and noise up to 20% of mean), accuracies of 1% of the peak phase shift are possible, using basically the same analysis configuration as described in this thesis. Kujawińska and Wójciak explain that for this type of configuration, the overall accuracy should be around *one fiftieth* of a fringe, but in reality a more often quoted figure on the accuracy of the Fourier transform method of fringe analysis is about *one twentieth* of a fringe. However, this figure is an overall accuracy of a typical Fourier transform fringe analysis system, and includes the substantial edge errors associated with truncation or data weighting. If the operator limits the measurement of the phase information to the centre[106] of the data array away from the edges, then an accuracy of *one fiftieth* of a fringe is quite simple to achieve.

6.4 Errors resulting from the mechanical system

6.4.1 Vibrations

Vibration of the specimen will cause fringe correlation errors, and if sufficiently large, may cause complete decorrelation of the speckle patterns. The test specimen represents a vibrating system with six degrees of freedom, but as far as the interferometer is concerned, the dominating effects will be the in-plane translations, since speckle correlation is relatively insensitive to out-of-plane translations, as stated in section 2.1.3.1. It was shown in section 2.1.2.1 that when the specimen is translated in-plane, then for a radially sensitive in-plane speckle interferometer, the result is a radial fringe pattern. The number of fringes is proportional to the magnitude of the translation. It is therefore reasonable to use the ESPI system itself to gauge the vibrational magnitude, assuming the optical table containing the interferometer components remains relatively unaffected by the vibrations of the drive system. To establish if this assumption is correct, an accelerometer was placed at various locations on the optical table, and measurements of the relative vibration of the table were taken at different rotational speeds. It was established that the vibration amplitude of the table was small - up to approximately 14,000rpm, after which it increased in proportion to the rotational speed. As expected, the dominant frequencies of the vibration were the driving

[106]Exclude the outer 15 - 20% of the array pixels.

frequency and harmonics, but certain natural frequencies, of low amplitude, were also detected.

The specimen disc was accelerated to a specific speed and allowed to run for several minutes, so as to reach a state of equilibrium. Several speckle images were recorded, without any change being applied to the system. Theoretically, the correlation of these images should result in a 'null' field, or characteristically dark image, if the relative position of the specimen is the same for both images. If an in-plane translation has occurred between the image captures, then radial fringes will be evident on the correlated image.

Experiments were conducted at various different speeds, and it was found that only a small proportion of the fringe patterns taken at speeds below 14,000rpm contained radial fringes. For those images which did contain radial fringes, the overall number of fringes was generally small (typically less than 3 fringes). The proportion of images containing radial fringes, and the number of fringes per image, increased significantly at higher speeds. At 20,000rpm, the majority of the images contained radial fringes, and the typical number of fringes was about 30. Since the high speed tests actually produce high contrast fringes, then the speckle images must be spatially close to each other at the time of laser triggering (well within the correlation criteria explained in section 2.1.3). Therefore, it can be concluded that:

- the maximum amplitude of the vibration is small enough to prevent the interferometer from becoming decorrelated

and/or

- the vibration of the specimen is cycle dependant, and it returns to the same approximate position on each rotational cycle.

A test which can establish which of the above is correct, is to run the specimen at a high rotational speed for some time, allow it to settle, then record several speckle patterns. A small increase in rotational speed should not alter significantly the correlation fringe pattern, but should change the frequency of the vibration. The transfer function of the mounting assembly will therefore be subject to a different excitation frequency, and will have a modified response, thereby altering the cycle dependant nature of the vibration. If the vibration amplitude is large enough to decorrelate the speckle patterns, then a significant number of the images will have no correlation (which can be established by computing the cross-correlation function). If the vibration is cycle dependant, then a consistently 'skewed' fringe pattern should be generated when speckle patterns are correlated.

Such a test was conducted with the capture of 100 images at speeds of 19,951rpm and 20,148rpm. All 4,950 possible combinations of correlation were examined[107], and it was established that 4,753 images had a reasonable degree of correlation. A later examination of the data showed that 2 of the images were subject to a counting error of the ECU, which caused the laser to trigger at an incorrect time (the number of correlations from 2 images is 197, which is the difference between 4,753 and 4,950). It is concluded that the vibration amplitude of the rig at approximately 20,000rpm, is sufficiently small so as not to decorrelate the speckle pattern interferometer.

Tobias and Arnold [1959] consider some of the vibrational problems associated with rotating discs. They explain that the vibration may be composed of nodal diameters, nodal circles, or a combination of both. However, nodal circles are rarely encountered in practice, and shall not be considered further, in order to confine the discussion to nodal diameters. For the case of a disc with perfect axial symmetry, the nodal diameters are arbitrary, and depend only on the initial conditions. When an imperfection exists, which is the case in all practical systems, the angular position of the nodes ceases to be arbitrary. In this case, only two nodal positions are then possible for each of the natural frequencies.

6.4.2 Atmospheric perturbations

The incident laser illumination and reflected light passes through the air surrounding the specimen. When the disc is running, the surrounding air is turbulent, especially at the high rotational speeds, and will have a varying optical density. The speckle intensity changes, due to the moving air and will be frozen into the speckle patterns. If the perturbations are large, distortion of the fringes may occur as a result. A similar effect is common in astronomical interferometry [Roddier and Roddier, 1987]. However, for a rotating disc, unlike astronomical interferometry, it is reasonable to assume that an equilibrium situation will develop after a sufficiently long period of time [Etemad *et al.*, 1992], in which case the effect of the moving atmosphere will become irrelevant, since the effect will be similar in both of the speckle patterns to be correlated. To establish if the windage from the surface of the specimen affects the interference fringe patterns, an obstruction was positioned in the field of view of the camera, with the purpose of disturbing the windage flow pattern (Image 153 and Image 154). Changes in the refractive index of the air, due to the heating and pressure changes caused by the disc motion, are unlikely to cause any significant fringe order error, since even substantial changes in pressure and temperature do not cause serious changes in the index.

---

[107] In each case, a 128x128 point Fourier transform was used to compute the cross-correlation function (section 4.2). The test required three entire days of computer processing, on a 33MHz 80486.

For air at a temperature t°C, pressure pN m^{-2} and wavelength $\lambda\mu$m (which is strictly the wavelength in a vacuum), the refractive index of air is given by Equation [133] [Edlén, 1953]:

$$n_{tp} = \left[\frac{0.04723}{(173.3 - \frac{1}{\lambda^2})} \cdot \frac{p(1 + p(61.3 - t)x10^{-10})}{96095.4(1 + 0.003661t)} \right] + 1 \qquad [133]$$

This equation does not consider any changes which may occur due to the *motion* of the air, which is extremely difficult to model. Nevertheless, sample calculations from this equation, Table 15, indicate that even at a pressure of 100 atmospheres, and 200°C, the change in refractive index is only 2.43%. Malmo *et al.* [1991] show that the number of fringes corresponding to a certain deformation is higher when the interferometer is operated in a more optically dense medium. In this paper, a specimen is half covered with water of refractive index of 1.331, producing 1.35 times as many fringes than obtained in the air (35% error). It can therefore be concluded that, without considering the effects of the air motion, the errors due to the refractive index fluctuations are small. The motion of the air is an important factor, which requires further investigation. For example, Shough and Kwon [1990] discuss some of the effects of eddy currents close to the aperture of an astronomical telescope, causing degradation of the detected images.

The effects of the moving air on the interferometric results described in this thesis were not fully established, due to the complex nature of the problem. However, although this error source is likely to be significant in comparison with many of the other errors described in this chapter, it is not thought to cause major deviation to the measured results.

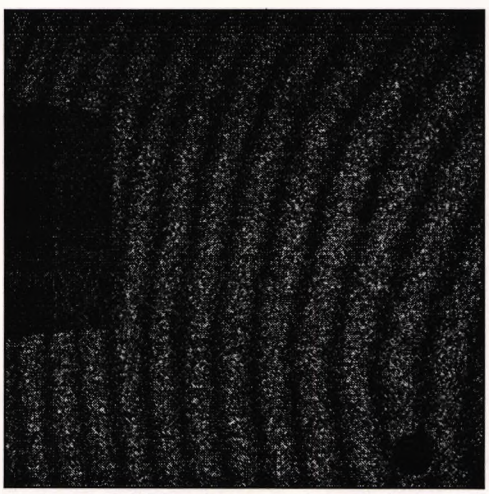


Image 153: Obstruction at 1mm

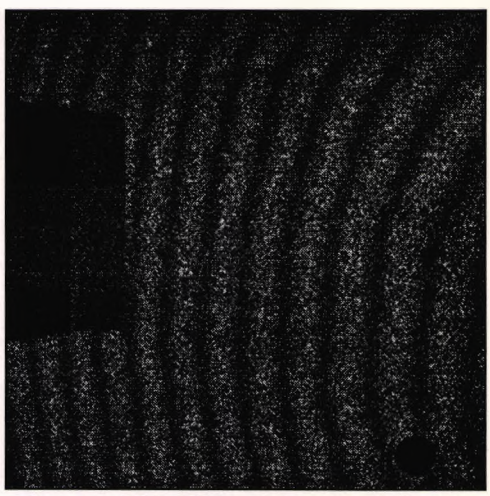


Image 154: Obstruction at 0.2mm

Temperature (°C)	Pressure (Nm^{-2})	Refractive index	Deviation from standard (%)
(standard) 27	101,325.0	1.000262	0.000
50	101,325.0	1.000243	0.002
100	101,325.0	1.000210	0.005
150	101,325.0	1.000185	0.008
200	101,325.0	1.002432	0.010
50	1,013,250.0	1.024568	0.217
200	10,132,500.0	1.014258	2.430
50	10,132.5	1.000240	0.024

Table 15: Refractive index dependency on temperature and pressure

6.4.3 Surface preparation

The specimen surface is normally spray painted with matt white automobile paint (type UN 1950 manufactured by Automobile Chemicals Ltd). The paint is used to ensure that a relatively even speckle pattern is imaged from the surface, and that maximum illumination is reflected into the camera. It was considered necessary to have complete confidence in the paint's ability to indicate accurately the state of stress of the surface. To examine this, the paint for a sector of the specimen surface was cleaned away and the surface was 'matted' with emery paper, to ensure that it was as unreflective as possible. The paint free surface caused several problems for the ESPI system, especially from glare. However, after adjusting the camera aperture, the laser power and the gain of the VS100, a few rather poor fringe



Image 155: Paint-free fringes

patterns were obtained. Image 155 shows a fringe patten from the paint free region. For this image, the specimen was accelerated from stationary to 10,250rpm in 12s. A reference speckle pattern was immediately recorded, and after 30s, a second speckle pattern was recorded (this was similar to the windage tests described in section 5.2.3). The nominal incidence angle for this test is 48° to the normal (fringe sensitivity of 0.47μm fringe^{-1}). Several similar images indicated that the fringe densities for these tests were similar to those found from the painted surface of the specimen, and it is therefore concluded that the paint does not significantly affect the measurements.

6.4.4 Timing errors

Timing errors occur when the laser illumination is delivered out of synchronism with the specimen rotation. It was explained in Chapter 3 that the Q-switch pulse for the JK 2000 laser must be accurately and repeatably produced in order to obtain speckle correlation fringes from a rotating specimen. In section 2.1.3.3, the equation for speckle decorrelation due to in-plane rotation was stated. It was also explained in section 2.1.2.1 that when using the radially sensitive in-plane speckle interferometer[108], small rotations of the specimen do not cause changes in the fringe patterns, only a reduction in the correlation of the patterns, and therefore a reduction in the signal-to-noise ratio of the fringe images. The modified shaft encoder increases the positional repeatability of the timing pulses, since in the previous shaft encoder (section 3.1.1.3), movement of the HeNe lasers due to vibration of the rig caused jitter on the timing pulses, and therefore inaccuracies in the Q-switch firing.

At a rotational speed of 20,000rpm (2,094rad s^{-1}), 100mm radius (which is typically the centre of the image), magnification of 0.02, aperture *f*32 and ruby illumination, complete decorrelation of the speckle patterns would occur if the timing error between the two images is greater than $\pm 4.77\mu$s. Preater [1987d] indicates that for good fringe patterns, the timing accuracy should be such that the images are registered to within 1 speckle, which is translated to a timing accuracy[109] of 0.5μs. It must therefore be assumed that the shaft encoder developed by Preater enabled timing accuracies of this order to be attained, even though the previous electronic control system used a relatively 'slow' chip (DS3696) to perform the voltage amplification necessary to Q-switch the laser, which would have been a limiting factor on the accuracy of the illumination delivery. This accuracy is 10 times greater than is required to prevent decorrelation at the much higher operational speeds described here. The modified electronic control unit uses an electronic 'chain' of significantly fewer TTL

[108]This analysis assumes a 'perfectly' radial sensitivity, which is not the case in this system.

[109]The magnification, aperture, rotational speed and radius are not indicated.

devices to generate the amplified Q-switch pulse. The devices used in the Q-switch fire circuits are very high speed. The modified shaft encoder, using fibre optic transmission of the timing pulses, would also generate a much steeper rising edge to the timing pulses, by virtue of the high transmission bandwidth of the optical medium. When considering these details, the modified electronic control system can be assumed to respond *at least* 100 times faster than the previous system. Therefore, the 'jitter' on the pulses will be reduced by at least 100, attaining repositional accuracies of the order of tens of nanoseconds[110].

To bring all these factors together, and taking into account the fact that the up-to-date electronic control unit, shaft encoder and image capture system generate *high contrast* speckle correlation fringes on *every image*, even at 20,000rpm, then it can be said that the timing system is not a major source of error. However, a combination of in-plane rigid body translation and timing inaccuracy does lead to an overall error which is greater than the summation of each individual effect. This is because for a simple rotation, no change occurs to any point in the radial direction, and therefore no change to the fringe pattern generated by a radially sensitive in-plane interferometer. However, for a rotation following a translation, the axis of the rotation is no longer aligned with the axis of the in-plane interferometer, and thus a component of this rotation will exist in the radial direction, causing a change to the fringe pattern. This was most probably a major source of error on the system used by Preater, which generated relatively few repeatable fringes patterns. On the current system, vibrations above approximately 14,000rpm are a major problem, due in part to the timing system.

6.5 Errors due to the specimen

6.5.1 Constriction under load

The specimen profile will alter under load, due to the Poisson's ratio effect. This is illustrated in Figure 140, which is grossly exaggerated for clarity. In terms of the interferometer, this is an out-of-plane motion, but for a constant rotational speed, the effect is the same in both images, and therefore does not affect the correlation of the speckle patterns. However, the measurement surface will be 'tilted' slightly with respect to the interferometer, and therefore the interferometer will become fractionally more sensitive to out-of-plane vibrations. It is pointed out that these effects will be very small in comparison to the likely alignment errors, since it is feasible that the surface is normally tilted with respect to the interferometer. Also, the difference in the constriction due to a rotational speed change[111] will be relatively small, and so the error in the measurement of differential strains will be small.

---

[110]This analysis assumes that the propagation delay of the gates is constant, which cannot be established easily. However, for a constant temperature, this assumption is reasonable.

[111]Most of the results in this thesis are for 'small' speed changes, typically a few thousand rpm.

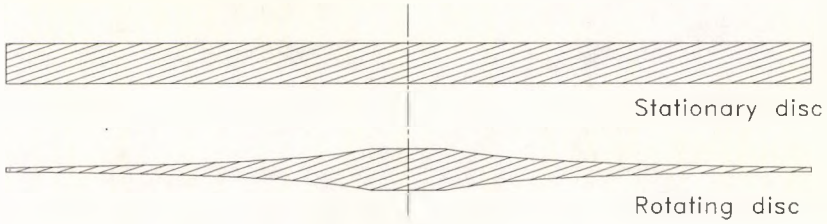


Figure 140: Constriction of the disc under load

6.5.2 In-plane vibrations

It was pointed out in the previous section that the profile of the specimen will change under load. Consequently, the 'grip' of the spigot holding the disc to the drive shaft will reduce, due to the 'thinning' of the specimen material in the grip region. In this case, the specimen may move on the shaft, causing an increased out of balance force[112], and therefore additional vibrational forces. Any out of balance force can translate to in-plane vibrations of the specimen, which could radically alter the speckle correlation fringes. This type of vibration was discussed in section 6.4.1.

6.5.3 Out-of-plane vibrations

The specimen disc is known to have a 'kink' in it, which can not be removed by skimming the surface. The maximum out of plane deviation of the high spot of the kink is approximately 80μm. At high rotational speeds, this kink will cause the disc to 'flap', as shown in Figure 141 (exaggerated), generating vibrations, air turbulence and additional surface heating. The centrifugal loading of the disc will tend to straighten the kink, but will not be sufficiently large to eliminate the effect completely, and a certain amount of flap will remain. The anticipated errors due to this type of distortion, although likely to be relatively small, were not determined. However, a static ESPI system was assembled to measure the number of fringes induced on an in-plane configuration by an out-of-plane bend of 80μm over a distance of

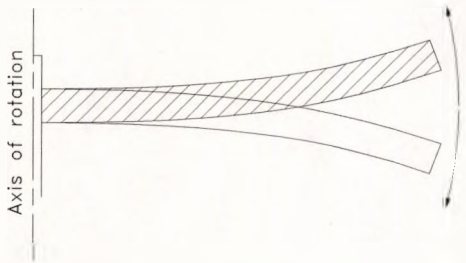


Figure 141: Out-of-plane flap of the specimen

[112]The disc is normally balanced to run on the shaft in a single position only. However, on a couple of occasions, during very high speed tests, the disc was found to have rotated around the shaft by several centimetres.

10cm (typical field of view of the rotating system)[113]. It was found that for a fringe sensitivity of 0.47μm fringe^{-1} (42° rather than 48° incidence, since a HeNe laser was used), then an 80μm bend at the periphery caused no measurable phase deviation to a carrier fringe pattern, when analysed with the Fourier transform software. Therefore, the error is less than 20^{-1} of a fringe, and since the results in this thesis typically have more than about 10 fringes, then the error can be said to be less than 0.5%. However, for many of the results, the error is likely to be much less than 0.5%.

[113]As stated, the centrifugal loading of the disc will reduce the amount of flap, so 80μm is larger than anticipated.

Discussion and Conclusion

Discussion of results

The static results presented in section 5.1.3.1 and 5.1.3.2 are included to demonstrate the effectiveness of the Fourier transform software. It was shown that when the fringe data completely occupies the array space of the VS100, and no discontinuities are present within the field, then the agreement with the measured plane strain is very good. The minor differences between the optical strain data and the strain gauge data can be attributed to several possible sources:

- Inaccuracies of the strain gauge readings.
- Imperfect loading of the specimen.
- Errors due to the analysis software.

When the fringe images contain large discontinuities, as in the tests presented in section 5.1.3.2, then the optical strain data does not agree with the analytical data. No detailed comparison of the optical strain data was performed, since a simple examination of the results provides evidence of large fluctuations in the strains. Also, the measurements are asymmetrical with respect to the horizontal axis, which is obviously not a true indication of the strain. In this case, the errors are undoubtedly due to the Fourier transform fringe analysis software, which produces inaccurate results close to regions of discontinuous data.

When the same software is applied to the rotating specimen fringe patterns, as described in section 5.2, the measured results deviate from the established theory. For example, consider Graph 9 on Page 154, which indicates the measured radial strain for a speed increase from 5,156rpm to 7,046rpm. These results give the first indication that windage heating of the surface significantly affects the measurements. When Graph 9 is examined with reference to Figure 100 (Page 150), and it is assumed that the windage heating of the surface is increasing with time[114], then it is reasonable that fringe pattern C should be closest to the theoretical results, since the load speckle pattern, C2, is recorded shortly after the acceleration period is completed. The reference speckle pattern, C1, is taken 235 seconds

[114]Until an equilibrium state is attained.

after the specimen attained the reference speed, and as can be seen from Graph 18 on Page 180 (4,991rpm plot), the disc expansion has reached an equilibrium at this time. Additional surface heating occurs during the acceleration period[115], since whatever acceleration profile is used to bring the specimen to a specific drive speed, the eventual surface temperature will be the same[116]. The temperature increase will cause the strains measured from fringe pattern C to be higher than the theory indicates. However, there will be a time lag on the strain due to the additional temperature increase, and speckle pattern C2 will only contain the effects of a portion of it. Fringe data A from Graph 9 (Page 154) is the other extreme of the measurements. As indicated in Figure 100, the reference speckle pattern, A1, was recorded very early in the test cycle, and therefore the temperature of the specimen (and the strain) will increase significantly with time (see Graph 18 on Page 180). The load speckle pattern, A2, is captured a significant period of time after the acceleration period, and so additional heating at the higher speed will occur. The strain from fringe pattern A would therefore be expected to be much higher than the other measured strains. Fringe patterns B and D are in between these two extremes.

A major reduction in the acceleration time between the tests speeds was employed to generate the fringes shown on Page 155 (fringe patterns E and F). An examination of these fringe patterns by eye shows that the density of fringes is slightly different than the previous test. The fringes have a lower density towards the left of the image[117] than those shown on Page 151 (which have a similar density across the whole image). In the high acceleration tests, the specimen was run at the reference speed for several minutes, before being accelerated very rapidly to the load speed. The radial strains would be expected to be much closer to the theory, since only a slight amount of heating will occur during the acceleration period. This is indeed the case, as shown in the graphs on Page 156.

The medium speed test described on Page 158 (Figure 109) is slightly different than the previous case, since four different reference speckle patterns (H1-K1) are correlated with the same load speckle pattern (2). The radial strains obtained from the fringe patterns, which are shown in Graph 13 (Page 161), indicate a trend which is consistent with windage heating. With reference to Figure 109, upon attaining the test speed of 10,180rpm (and during the initial acceleration), the specimen temperature will increase with time, until an equilibrium state is reached (see Graph 18 on Page 180, which presents a result at a similar speed). Therefore, speckle pattern H1 is recorded at the lowest temperature, and speckle pattern K1

---

[115]The difference between the lower plots of Graph 18, corresponding to three or four fringes.

[116]For example, refer to Graph 17 on Page 171.

[117]The left of all the images is at a higher radius (refer to Figure 98).

the highest, with I1 and J1 at intermediate temperatures between the two. Consequently, it would be expected that fringe pattern H would indicate the highest radial strain, and K the lowest (for the reason explained earlier), with all strains being higher than the theoretical measurements. However, fringe patterns J and K have similar strain results, indicating that the temperature change between 233 seconds and 323 seconds is small. A later windage test[118], the results of which are shown in Graph 18 (on Page 180), verified that this is the situation. In Graph 18, it can be seen that after about 200 seconds, the increase in the number of fringes across the image is small, indicating that the temperature of the specimen has stabilised. Figure 114 (Page 161) is the schedule of a similar test, in which three load speckle patterns (L2-M2), separated by 10 second intervals, are correlated with the same reference pattern (1). The speed change was from 9,764rpm to 12,164rpm, with a high acceleration rate. The images shown on Page 162 show an increasing numbers of fringes in relation to time. This is verified by Graph 14 (Page 163), where as expected, fringe pattern L gives the closest agreement to the theoretical prediction, and fringe pattern N is the least. The magnitude of the radial strain measured with the interferometric system is now much higher than the theory, since the first of the load speckle pattern was recorded 30 seconds after the end of the acceleration period (see Figure 114). The test schedule shown in Figure 119 on Page 165 is similar to the previous test (Figure 114), but without the 30 second delay after the acceleration period is complete. The test speeds were 15,098rpm and 16,550rpm. The radial strains shown in Graph 16 (Page 168) were generated from fringe patterns P to S, shown on Page 166. These results are similar to those shown in Graph 14, but fringe pattern P is now reasonably close to the theoretical values, since it was recorded immediately after the completion of the acceleration.

The theoretical model used to compute the expected radial strains for the rotating disc was very rudimentary, and based upon simple analytical equations. More advanced finite element models of the experiments[119], which also ignore the windage effects, agree with the analytical equations to within approximately 2% for regions without stress raising features. Therefore, the simple model was considered suitable for this application, and was used to compute the theoretical radial strains throughout this thesis. The windage effects were not considered in the model, since the computation of such effects is extremely complex[120], and far beyond the scope of this thesis. Several references to the power dissipation of a rotating disc are available, for example Etemad *et al.* [1992], but as indicated in this paper, there is a wide variation between the results of various computations and measurements.

---

[118]One of the curves of Graph 18 is for a speed of 10,080rpm, which is close enough to the reference speed.

[119]Reference: Private communication - John Brownell, Rolls-Royce PLC, Derby.

[120]Reference: Private communication - Dr Keith Pullen, Imperial College.

Also, different mathematical models of windage exist, and the agreement between them is rather poor. Therefore, as indicated, windage was not modelled.

The windage fringe pattern results, described in section 5.2.3, were generated using the test schedule shown in Figure 124. The first set of fringe patterns, for windage test 1, were taken at 4,991rpm (acceleration of 42rad s^{-2}), and are shown on Page 173. A clear expansion of the specimen with time is evident. Further fringe images in this sequence, which are not shown, were used to generate the data for the lower plot of Graph 18 on Page 180. It should be noted that each data point on Graph 18 represents a fringe pattern. The processing time required to pass each fringe pattern through the Fourier transform software is prohibitive. Therefore, to get a preliminary indication of the expansion, the number of fringes in each image was counted by eye, giving the approximate strain across the field of view[121]. The apparent 'ripples' in Graph 18 are a result of this, since fringe counting is only accurate to the nearest fringe. For more accurate work, it would be necessary to process the entire set of images, which would require more powerful computing facilities to complete the analysis in a reasonable time.

The fringes obtained from windage test 2 on Page 174 are for a rotational speed of 10,080rpm. This set of fringe patterns confirms without a doubt that the effect under observation is windage. In Image 120 for example, the fringe density appears to increase with the radius (left of the image), which is consistent with windage heating. The surface preparation was suspected as a candidate for this effect, but similar fringe densities are present in Image 155 (on Page 203), which was taken from a paint free region of the specimen. The lower two fringe patterns on Page 174 indicate that it is possible to correlate later images in the sequence with each other, to determine the heating effects over long periods of time[122]. Other windage tests, shown on Pages 175 to 179, indicate miscellaneous expansions of the specimen at various accelerations and speeds. Image 148, which was recorded at 17,394rpm, is a splendid example of the fringe density change due to radius.

Graph 18 on Page 180 is a summary of a set of windage tests, in which a clear and unmistakeable trend is evident. Graph 19 (on the same page) shows the result of varying the acceleration rate of the specimen for a windage test speed of approximately 10,000rpm. Initially, this graph appears to indicate that the overall number of fringes is dependent upon

[121]This method is very approximate, since it uses the width of the image as the gauge length.

[122]There is no logical reason why such tests could not be conducted over many hours or days.

the acceleration, which cannot be correct since the ultimate temperature of the disc is independent of the acceleration. However, with reference to Graph 17 on Page 171, which indicates the measured temperature of the disc surface, it is observed that when the disc attains the operating speed for a high acceleration rate, the initial surface temperature is lower than for the low acceleration rate, since less heating of the disc occurs during the acceleration period. Therefore, if a reference speckle pattern is captured at the instant the disc attains the operating speed, it will be recorded at a lower temperature for the higher acceleration rate[123]. The correlation of further speckle patterns with this reference pattern will produce a larger number of fringes. A similar but reverse argument can be used for low acceleration rates. Graph 20 (Page 180) is a similar test, indicating a similar result.

From an industrial point of view, perhaps the most important achievement of this project is the operable speed range increase. A documented maximum tip speed of 132m s^{-1} was obtained with the previous system [Preater, 1987b]. Fringe patterns X and Y from Page 169 were obtained at a rotational speed of 23,842rpm, which is a tip speed of 364m s^{-1}. Although no engineering data was obtained at this tip speed[124], the results indicate that speckle correlation clearly occurs, even at supersonic speeds[125]. No evidence was found to suggest that these high tip speeds were close to a fundamental speed limit. It is therefore suggested that with a more sophisticated drive assembly, higher operational speeds should be possible.

The speed range increase is significant, but has an even greater implication when coupled with the fact that highly *repeatable* images[126] are obtained at almost all tip speeds up to 245m s^{-1}. Obviously, the point about repeatability is very important for a measurement system, since potential users must have confidence in the results.

---

[123]Compare the intersects of plots A and C from Graph 17.

[124]Reliable engineering data was obtained at a maximum tip speed of 245ms^{-1}.

[125]Higher rotational speeds were not possible, due to limitations of the drive system, and safety considerations.

[126]The system developed by Preater produced very few repeatable speckle correlation fringe patterns.

Conclusion

It has been demonstrated that the technique of electronic speckle pattern interferometry can be used successfully to determine the in-plane radial strain of a rotating disc. The use of the Fourier transform technique to analyse the speckle fringe patterns facilitates the extraction of accurate phase information, which is used to determine reliably the strain at many locations. The measurement system offers several advantages over conventional strain measurement technologies. The technique is non-contacting, and therefore it neither disturbs the surface (apart from the addition of a coat of paint), nor does it suffer from the effects of direct surface contact (eg. temperature changes). It is a field array technique which permits many hundreds or even thousands of measurements to be made simultaneously, thereby providing an almost immediate visual interpretation of the specimen strains.

Under experimental conditions chosen to minimise the effects of windage, the agreement between the measured strain and theoretical predictions was good. The measured results were found to disagree with the theory under general test conditions not chosen to minimise windage, and the cause was shown to be windage heating of the disc surface. Windage and infra-red temperature tests were conducted, and confirmed the specimen expansion due to the temperature rise.

This work represents a major advancement of the technology, in terms of the operable speed range, data analysis, and implementation of the technique. It is considered that the objectives stated in the abstract of this thesis have been attained, and the technique is now suitable for industrial application. A small amount of additional work is required to fully comprehend the more complex errors discussed within, such as the effects of air flow over the specimen surface, and errors resulting from shape changes or bending of the specimen (section 6.5).

The general confidence in the measurement system has been elevated.

Further work

A significant amount of further work must be undertaken before electronic speckle pattern interferometry can be used routinely to make measurements on high speed rotating specimens. This section details some of the more interesting enhancements that could conceivably be investigated. Where a particular avenue of investigation appears prohibitively expensive, this is pointed out, since from an industrial point of view, the cost is a more important factor than the academic benefit. All costs are approximate, and valid for 1993.

Interferometer

The Electronic Speckle Pattern Interferometer described in this thesis performs well in the laboratory environment. However, the development of the technology was commissioned by Rolls-Royce, and therefore the developed system should be capable of being operated in an industrial environment, by relatively unskilled workers. The interferometer is physically quite large, and very difficult to align accurately. Consequently, a reduction in the number of optical components would be valuable, and would reduce the size of interferometer, making it easier to align. Replacing the tilt mirror with a modified method of beam tilting, fitted to the laser chassis, would allow the pulsed beam to be horizontally shifted with respect to the chassis, thereby allowing the two plane mirrors on the optical table to be removed. The use of a stepper motor to drive the tilting stage, although relatively expensive, costing over £2,000 (with driver electronics), in preference to the current DC motor, would allow more accurate and repeatable carrier fringe pattern selection. Additionally, some form of feedback from the tilt stage, which could eliminate the effects of drive backlash, would be very useful.

Mirrors of higher optical quality would increase the cost of the experimental system, but could be utilised for very accurate experimental work. However, there is a reluctance on the part of industry to invest large amounts of capital into such things, since an interferometric quality outer mirror could cost £20,000 at current prices, and could very easily be damaged (eg. by oil contamination from the spin pit). If the cost proved inhibitive, a single outer mirror could be manufactured to interferometric quality, and used to produce a set of holographic optical elements (HOE), which could furnish the desired incident wavefront. Since these elements would be considerably cheaper to manufacture than the outer mirror (possibly only about £50

each), then their destruction due to unforseen experimental circumstances would not be of major concern[127]. The incorporation of an inner mirror with a reduced radius of curvature (currently 52mm), and longer cylindrical length, would allow measurements at smaller radii to be made. This would be of value, since the radial stresses are higher near the centre, and the windage heating effects are less.

The radially sensitive in-plane electronic speckle pattern interferometer is only able to make *radial* strain measurements on a rotating specimen. In many cases, particularly in modern gas turbine components, the major stress, which is of concern to the design engineer, is the hoop stress. However, the verification of one stress will increase the confidence in the computer model. A speckle correlation technique, similar to the one described by Marom [1974], could be used to make measurements of both the radial and hoop displacements, but with a current resolution of about one thirtieth of the ESPI system. However, such a system would probably require a Nd:YAG laser or similar, since the intensity correlations would be unreliable with the ruby laser. Noh and Yamaguchi [1992][128] describe a 2D speckle correlation system for the measurement of in-plane strain, using the simple system shown in Figure 142. The system works by recording the speckle pattern from the directly illuminated surface in a reference condition. A load is then applied, and a second speckle pattern is recorded. The images are dissected into smaller regions, typically 56 sub-blocks of 64x64 pixels, and an autocorrelation is computed for each region of the reference image, by squaring the modulus of the Fourier transform, as discussed in section 4.2. Each block in the reference image is then cross-correlated with the corresponding block in the load image, again using the Fourier transform relationship, and the relative movement of the cross-correlation peak away from the autocorrelation peak is used to determine the *average* net movement of the speckles in the block. The combination of this technique, and a very high resolution CCD array[129],

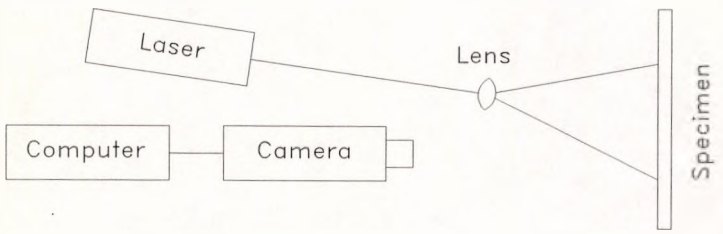


Figure 142: 2D speckle correlation for measuring in-plane strain

[127]Rolls-Royce have voiced concern about the placement of expensive optical components in a spin pit, since test specimens are sometimes destroyed during a test. In certain cases, oil spray from the drive system could also contaminate optical components.

[128]Yamaguchi and Noh [1992] contains results showing the complete stress field for a specimen.

[129]Currently, 4096x4096 pixel CCD arrays are available, but the enormous cost is restrictive.

would enable the measurement of both components of strain to be obtained, with a reasonable resolution.

Although not a direct continuation of this work, it may be possible to configure an out-of-plane electronic speckle pattern interferometer, using the same electronic control system to obtain speckle images of the specimen surface. Albeit pure speculation, since the sensitivity vector of an out-of-plane system would be perpendicular to the rotational motion, it is perceivable that no complications due to speckle blurring should occur, and speckle correlation fringes at tip speeds of up to 300m s^{-1} should be obtainable. If such a system were possible, it would resemble Figure 6 (Page 15), and could enable vibrations of the specimen to be visualised. Since the twin cylindrical mirror system would not be required for such measurements, the pulsed laser illumination could be used to illuminate the entire specimen, rather than a section of it. An out-of-plane measurement system for a rotating system based on ESPI has not been described in the literature, and would be extremely useful, since many of the problems associated with similar holographic measurements remain as yet unsolved.

Laser illumination source

The use of an improved laser source, for example Nd:YAG, which has a high repetition rate and good repeatability, would enable a significantly higher data sampling rate than is possible with the ruby laser, which requires approximately 10s to recharge. Also, modern pulsed lasers often produce considerably shorter pulse widths, at higher energy levels. Nd:YAG lasers with operating energies of 10J and pulse widths of femtoseconds are not uncommon, although the present cost is very high (well over £60,000). Such a laser would undoubtedly enable extended specimen drive speeds to be used. The *difference* in rotational speed of the specimen for which speckle correlations could be obtained would certainly increase, since the 'smearing' of the speckles during the illumination period would reduce in proportion to the pulse width.

The transient nature of the surface heating could be visualised in much greater depth with such a laser, since the repetition rate would be significantly higher than with the ruby laser. Highly repetitive pulses at frame rate (25Hz) are easily possible with Nd:YAG lasers, which could increase the sampling rate to 25Hz, rather than 0.1Hz, which is used at present.

The use of laser diodes is another possibility which could be investigated, and was looked at briefly in this research project. It was established that one of the major drawbacks with using diode lasers is that when they are switched through the device threshold, 'mode hopping' occurs, causing a significant change in the illumination coherence properties. Also, thermal

changes in the diode cavity during the switching operation cause a deviation of the device wavelength, which would cause additional fringe systems to be generated in an interferometer. More sophisticated (and expensive) laser diode drivers use active thermal correction systems to compensate for the wavelength shift due to temperature changes.

Fringe analysis

The use of the Fourier transform method of fringe analysis was found to be suitable for evaluating regions without stress raising features (eg. holes in the fringe data). When discontinuities are introduced into the data, problems with the Fourier transform methods occur, due to the global nature of the computations. The Fourier transform assumes that the data array is continuous and infinite, as explained in section 4.2.4. Therefore, the recovered phase around stress raising features is the most unreliable, since the periodic nature of the fringes is changing most rapidly in these regions. However, these zones are of greatest interest to engineers, since such stress problems are not well understood, and computer models are more inaccurate in these cases.

To generate accurate phase data in regions of elevated stress, a point method rather than global method of phase extraction would be required. With reference to Table 3 on Page 82, it can be seen that currently, the only two other methods of phase extraction feasible for this application are, 'spatial phase shifting' or 'carrier frequency phase shifting'. Intensity based methods can be ignored, since they are unreliable in the presence of noise. The spatial phase shifting method has relatively low accuracy, in comparison to the Fourier transform, carrier frequency phase shifting or temporal phase shifting methods. So, the carrier frequency phase shifting method is currently the only alternative to the Fourier transform method of fringe analysis. However, this method requires low noise fringes and an accurately determined carrier pattern. Therefore, the Fourier transform method is the most satisfactory fringe analysis scheme (even though it cannot cope with stress raising regions), but if accurate engineering data around stress raising features is required, then a new method of data extraction will have to be developed.

Data processing

The use of an Intel based computer to acquire, store and process images from an interferometric measurement system is attractive to potential users. This is mainly due to the inexpensive capital investment, relative availability of the hardware, and the huge library of professional software. Also, these computers are very adaptable to third party hardware, and many products are available to increase their performance and versatility. Nevertheless, these machines, with their complex memory architecture (see Appendix A), require proficient

programmers to perform many of the intricate tasks necessary to analyse interference fringe patterns. The incorporation of very fast processor boards (i860 or C40) would improve the situation, but the limited conventional DOS memory (640KB for real mode applications) and 'slow' data transfer rate through the motherboard expansion slots (8MHz irrespective of the processor clock speed) will always be a limiting factor. The use of extended memory (used in this research work) does increase the storage capacity of the programs, but the access to this memory is complicated and slow. The use of device drivers which switch the processor in and out of protected mode is inadequate for complex engineering computations. One other major limitation of the Intel based computers is the lack of true multitasking (although WINDOWS does provide this to a certain extent, it is currently very slow). Of course, more efficient software could be produced, using very concise programming techniques, to squeeze every ounce of power out of the computer. However, when the amount of man hours required to write such software is taken into account, it might prove disproportionately expensive. It would be substantially cheaper to purchase the extra processing power, and to make simple software modifications which would yield noticeable speed gains. As mentioned earlier, an array processor could be incorporated into the system, for a reasonably small capital cost, which would drastically decrease the execution times required for the Fourier transforms and unwrapping algorithm. Nevertheless, such a system would require a complete rewrite of the existing software, and would still only operate as a single tasking system. This could be considered as an interim solution. What is required ultimately is a fast processor (at least 60MHz), with a logical memory architecture, running a true multitasking operating system. The dramatic fall in the purchase price of very powerful Workstations[130], which operate under the reputable UNIX V operating system, will make Intel based systems obsolete for engineering problems within a few years, unless a radical change in the philosophy of these computers is effected. The incorporation of a Workstation into the electronic speckle pattern interferometer would dramatically increase the versatility of the entire system. The true multitasking nature of the operating system would allow many applications to be executed on the system simultaneously, so for example, the computer could be acquiring the speckle images with one program, and simultaneously analysing, displaying and printing the results with another. Also, some of the very sophisticated UNIX software[131] would allow enhanced visualisation of the output data, in formats unavailable on the Intel systems. Computer code written under the UNIX C compiler would be far more portable than C code written under the MS-DOS operating system, since to perform many 'low level' operations on Intel machines, it is necessary to invoke functions from MS-DOS, BIOS or device drivers.

---

[130]For example, SUN SPARC 10 or Silicon Graphics IRIS systems are currently retailing for well under £10,000.

[131]For example, the AVS program (Advanced Visualisation Software).

Since none of these function calls are included in the ANSI C standards, then the code will not be portable. Of course, C code written under MS-DOS could be produced to ANSI standards, but only through neglecting some of the more useful parts of the system, for example extended memory, the mouse, VGA graphics and the VS100 image processor. A similar argument could be used for C code written under the UNIX operating system, but in UNIX, hardware devices are configured differently to MS-DOS, and therefore the software can become more 'hardware independent'.

Another useful modification, which could be implemented fairly simply, would be to adapt the fringe analysis software to interface with a standard graphic file format, rather than directly with the VS100. For example, software which could analyse an image stored in a TIFF, GIF or similar file, would be very useful, since the widespread use of these formats would enable easy interchange of interferometric results with other research centres. Such collaboration with other institutions is both logical and efficient, especially with the modern computer links already in existence[132]. The medical profession has already realised that by using the worldwide computer networks, it is far more efficient to move the data to the expert, than it is to move the expert to the data. So for example, X-ray images are transferred by FTP to hospitals in other countries for examination by an expert, who uses electronic X-Talk to return a diagnosis. The whole process may take only minutes.

Returning to the fringe analysis application, since the graphical files contain header information about the dimensions, grey scales and compression schemes, then smaller, non-rectangular images could be analysed. This is an important point, since all the programs written for this research project expect a 512x512 image, which in some cases, can be a waste of space and processing time. Also, in the case of the programs written for this project, the separation of the image processing hardware and analysis software, which could be achieved by using standard file formats, would allow different Intel computers to analyse the fringe patterns, without the need for the VS100 to be fitted to them.

Experimentation

An obvious piece of further work would be to drive the specimen in an evacuated chamber, to eliminate the effects of windage heating of the surface. Under these conditions, the specimen would be traction free, since the atmospheric load, which acts as a resisting force to the rotation, will be zero. Rotational speed change tests could then be compared with

[132]Almost all major academic research centres, and many industrial centres, throughout the world, are linked to the IP network, and can access data in any country, in seconds. Therefore, in principle, an image could be generated by a system in London, analysed in say Australia, and the results examined back in London the same day.

established theories without having to consider the complications caused by the surrounding air flow. The laser illumination could be coupled into the chamber via special windows, with the camera, mirrors and shaft encoder all inside the chamber[133]. A successful test under these conditions would be a major advancement of the technology, since many of the parameters which are carefully controlled in the laboratory can not be controlled in an industrial spin pit facility. Also, the general organisational constraints of industry would be another test of the techniques 'real' usefulness. For example, the allotment of rigid amounts of time on an industrial pit, would test the practicality of the technology, in comparison to other established measurement techniques, which currently function under the same pressures.

Rotational speed tests with the specimen operating at an elevated temperature would be genuinely useful, since numerous rotational systems operate at high temperatures, and under these conditions, many effects, such as creep for example, are magnified. Combined with this, it would be useful to determine the maximum rotational speed, or more importantly, the maximum tip speed, for which speckle correlation fringes can be obtained. To give an example of the requirements[134], some advanced gas turbines, currently under development, may operate at temperatures of 500°C, pressures of 40 atmospheres, and tip speeds of 600m s^{-1}. It may be straightforward to obtain fringe patterns at extremely high temperatures and drive speeds, but to obtain useful engineering measurements under such conditions, a drive system and specimen which has very low amplitude vibrations is essential.

Specimens made from composite materials could be tested, since a lot of work is currently underway to understand the properties of the structures that comprise them[135]. As stated earlier, the validation of finite element computer codes would be a great achievement for an experimental system, and would ultimately lower the industrial costs of such products, since a greater degree of confidence in the computer predictions would reduce the amount of testing required[136].

Preater showed that it is possible to obtain carrier fringes on rotating specimens with various profiles (eg. Image 7 in Chapter 1 shows fringes on a rotating propeller blade). If the technology described in this thesis is to be put to real use, then it must be able to measure

---

[133]In fact, such a test is scheduled at the Defence Research Agency, Pyestock, Farnborough, later this year.

[134]Reference: Rolls-Royce personnel - private communication.

[135]See for example: Post [1990].

[136]Obviously, it is much cheaper to model a component on a computer than it is to fabricate it, and then conduct a series of tests. However, the general faith in computer models is currently not sufficient to rely on them totally.

accurately the strain on curved specimens. However, Jones and Wykes [1983] explain that the dual beam Leendertz in-plane ESPI configuration becomes sensitive to out-of-plane movements when the specimen deviates from plane. A rotating curved surface will almost certainly develop an atmospheric pressure differential between its faces, and will therefore move out-of-plane as the speed increases[137]. An investigation into the possibility of using electronic speckle pattern interferometry to test rotating curved surfaces would be very interesting, and if successful, would certainly render the technology even more useful.

Errors

A rigorous investigation of the more complex errors described in Chapter 6 would benefit considerably the appreciation of the results. As pointed out in the previous section, the evacuation of the drive chamber would go part way to determining the errors caused by air flow surrounding the specimen. However, simply comparing the results included in this thesis with any obtained from an evacuated test is insufficient, since the specimen disc will be responding in a different way with the air removed, and it will be impossible to differentiate between the measured change in the specimen, and the errors in the interferometric measurement. A purpose designed experimental programme is required to look at the air flow, rather than the surface strains of the disc. Such an experiment could be based upon the double pass Michelson interferometer described by Shough and Kwon [1990], and may give an indication of the flow patterns, rates and pressures surrounding the disc.

[137]It could of course be tested in a vacuum, but 'real world' operating tests are a great deal more informative.

References

Amada, S. (1984)
"Dynamic Stress Analysis of a Solid Rotating Disc."
Bulletin of the Japanese Society of Mechanical Engineers (27) : 230, Pages 1579-84

Amada, S. (1985)
"Dynamic shear stress analysis of discs subjected to variable rotations."
Bulletin of the Japanese Society of Mechanical Engineers (28) : 240, Pages 1029-1035

Amada, S. (1986)
"Dynamic stress analysis of a rotating solid disc subjected to cyclic rotations."
Bulletin of the Japanese Society of Mechanical Engineers (29) : 255, Pages 2771-2776

Ansair, F. and Ciurpita, G. (1987)
"Automated fringe measurement in speckle photography."
Applied Optics (26) : 9, Pages 1688-92

Archbold, E., Burch, J.M., Ennos, A.E. (1970)
"Recording of in-plane surface displacement by double-exposure speckle photography."
Optica Acta (17) : 12, Pages 883-898

Becker, F. and Yu, Y. (1985)
"Digital fringe reduction techniques applied lied to the measurement of three-dimensional transonic flow fields."
Optical Engineering (24) : 3, Pages 429-434

Beckers, J.M. (1990)
"Instrumental factors affecting the fringe contrast in optical interferometers."
Astrophysics and Space Science (171) : 1 and 2, Pages 333-339

Beeck, M.A. (1980)
"Holographic vibration analysis of rotating objects using different types of interferometers."
Proceedings of the Society of Photo-Optical and Instrumentation Engineers (210), Pages 128-134

Beeck, M.A. (1988)
"Pulsed holographic vibration analysis on high-speed rotating objects: fringe formation, recording techniques and practical applications."
Proceedings of the Society of Photo-Optical and Instrumentation Engineers (1026), Pages 186-195

Beeck, M.A. (1992)
"Pulsed holographic vibration analysis on high-speed rotating objects - fringe formation, recording techniques, and practical applications."
Optical Engineering (31) : 3, Pages 553-561

Bone, D.J., Bachor, H.A., Sandeman, R.J. (1986)
"Fringe-Pattern analysis using a 2-D Fourier Transform."
Applied Optics (25) : 10, Pages 1653-60

Bowler, I.W. and Paler, K.A. (1986)
"Gabor filter approach to fringe analysis."
Eighth international conference on pattern recognition (342), Pages 558-560

Bracewell, R.N. (1985)
"The Fourier transform and its Applications."
(McGraw-Hill International)

Brdicko, J., Olson, M.D., Hazell, C.R. (1979)
"New aspects of surface displacement and strain analysis by speckle interferometry."
Experimental Mechanics (19) : 5, Pages 160-5

Briers, J.B. and Angus, I.G. (1979)
"Speckle photography applied to the measurement of in-plane rotation."
Optica Acta (26) : 10, Pages 1229-31

Brophy, C.P. (1990)
"Effect of intensity error correlation on the computed phase of phase-shifting interferometry."
Journal of the Optical Society of America A (7) : 4, Pages 537-541

Brown, G.M. (1991)
"Practical phase unwrapping of holographic interferograms."
Proceedings of the Society of Photo-Optical and Instrumentation Engineers (1553), Pages 204-212

Bruning, J.H., Herriott, D.R., Gallagher, J.E., Rosenfeld, D.P., White, A.D., Brangaccio, D.J. (1974)
"Digital wavefront measuring interferometer for testing optics surfaces and lenses."
Applied Optics (13) : 11, Pages 2693-2703

Burch, J.M. and Forno, C. (1975)
"High sensitivity moiré grid technique for studying deformation in large objects."
Optical Engineering (14) : 2, Pages 178-185

Burch, J.M. and Forno, C. (1982)
"High resolution moiré photography."
Optical Engineering (21) : 4, Pages 602-614

Burton, D.R. and Lalor, M.J. (1989)
"Managing some of the problems of Fourier Fringe Analysis."
Proceedings of the Society of Photo-Optical and Instrumentation Engineers (1163), Pages 149-160

Butters, J.N. (1975)
"The Engineering Uses of Coherent Optics."
(Cambridge University Press)

Butters, J.N. (1977)
"Applications of ESPI to NDT."
Optics and Laser Technology (9) : 3, Pages 117-23

Butters, J.N. and Leendertz, J.A. (1971a)
"Holographic and Video Techniques applied to Engineering Measurement."
Transactions of the Institute of Measurement and Control (4) : 12, Pages 349-54

Butters, J.N. and Leendertz, J.A. (1971b)
"A double exposure technique for speckle pattern interferometry."
Journal of Physics E, (4), Pages 277-9

Butters, J.N., Jones, R., Wykes, C. (1975)
"The Engineering Uses of Coherent Optics."
(Cambridge University Press)

Butters, J.N., Jones, R., Wykes, C. (1978)
"Speckle Metrology: Chapter 6"
(Academic Press)

Button, B.L., Cutts, J., Dobbins, B.N., Moxon, C.J., Wykes, C. (1985)
"The identification of fringe positions in speckle patterns."
Optics and Laser Technology (17), Pages 189-92

Chambless, D.A. and Broadway, J.A. (1979)
"Digital filtering of speckle photography data."
Experimental Mechanics (19) : 8, Pages 286-9

Chang, M., Hu, C.P., Lam, P., Wyant, J.C. (1985)
"High precision deformation measurement by digital phase shifting holographic interferometry."
Applied Optics (24) : 22, Pages 3780-83

Chen, J., Zhu, R., Liu, L., Chen, D. (1991)
"Two dimensional Fourier transform algorithm analysing the interferogram and the fringe shift."
Proceedings of the Society of Photo-Optical and Instrumentation Engineers (1553), Pages 616-625

Chiang, F.P. (1979)
"Optical stress analysis using moiré fringes and laser speckles."
Optical Engineering (18) : 5, Pages 448-55

Chien, C.H., Turner, J.L., Swinson, W.F., Ranson, W.F. (1982)
"Extending the laser specklogram technique to strain analysis of rotating components."
Experimental Mechanics (22) : 11, Pages 434-40

Choudry, A. and Kujawińska, M. (1989)
"Fourier transform method for the analysis of fringe patterns."
Proceedings of the Society of Photo-Optical and Instrumentation Engineers (1135), Pages 122-130

Cohn, R.F. and Pryputniewicz, R.J. (1990)
"Noise and Error sources in Electro-optic Holography."
Proceedings of the Society for Experimental Mechanics, Baltimore.

Cookson, T.J., Butters, J.N., Pollard, P.C. (1978)
"Pulsed lasers in Electronic Speckle Pattern Interferometry."
Optics and Laser Technology (10) : 3, Pages 119-24

Creath, K. (1985)
"Phase-shifting speckle interferometry."
Applied Optics (24) : 18, Pages 3053-8

Creath, K. (1986)
"Comparison of phase-measurement algorithms."
Proceedings of the Society of Photo-Optical and Instrumentation Engineers (680), Pages 19-28

Creath, K. (1988)
"Phase-measurement interferometry techniques."
(Progress in Optics, Elsevier Science Publishing Company) (26), Pages 349-393

Creath, K. (1989)
"Holographic contour and deformation measurement using a 1.4 million element detector array."
Applied Optics (28) : 11, Pages 2170-5

Creath, K. (1991)
"Phase-measurement interferometry: Beware these errors."
Proceedings of the Society of Photo-Optical and Instrumentation Engineers (1553), Pages 213-220

Dändliker, R. and Thalmann, R. (1985)
"Heterodyne and Quasi-heterodyne holographic interferometry."
Optical Engineering (24) : 5, Pages 824-831

Davis, J.C. and Buckberry, C.H. (1989)
"Applications of fibre optic TV holography system to the study of large automotive structures."
Proceedings of the Society of Photo-Optical and Instrumentation Engineers (1162), Pages 279-292

Denby, D. and Leendertz, J.A. (1974)
"Plane-surface strain examination by speckle pattern interferometry using electronic processing."
Journal of Strain Analysis, (9) : 1, Pages 17-25

Deng, N. and Yamaguchi, Y. (1990)
"Automatic analysis of speckle photographs with extended range and improved accuracy."
Applied Optics (29) : 2, Pages 296-303

Dennis, A.J. and Fulton, G.B. (1989)
"Advanced structural instrumentation. Vol.II"
United Technologies Research Centre, Unclassified report R-89-2330

Deresiewicz, H. (1975)
"Acceleration Stresses in Disks of Variable Thickness."
Journal of Applied Mechanics (42), Pages 727-729

Duncan, R. (1988)
"MS-DOS Functions."
(Microsoft Press)

Duncan, R. (1989)
"MS-DOS Extensions."
(Microsoft Press)

Dyson, J. (1970)
"Interferometry as a measuring tool."
(The Machinery Publishing Company Ltd)

Edlén, B. (1953)
"The Dispersion of Standard Air."
Journal of the Optical Society of America A (43) : 5, Pages 339-344

Ennos, A.E. (1968)
"Measurement on in-plane surface strain by hologram interferometry."
Journal of Physics E (1), Pages 731-734

Ennos, A.E. (1975)
"Speckle Interferometry."
(Topics in Applied Physics (9) : Laser Speckle and Related Phenomena, Springer-Verlag)

Erbeck, R. (1985)
"Fast image processing with a microcomputer applied to speckle photography."
Applied Optics (24) : 22, Pages 3838-41

Etemad, M.R., Pullen, K., Besant., C.B., Baines, N. (1992)
"Evaluation of windage losses from high-speed disc machinery."
Proceedings of the Institution of Mechanical Engineers, A (206), Pages 149-157

Fagan, W.F., Beeck, M.A., Kreitlow, H. (1981)
"The holographic vibration analysis of rotating objects using a reflective image derotator."
Optics and Lasers in Engineering (2) : 1, Pages 22-32

Fienup, J.R. (1982)
"Phase retrieval algorithms: a comparison."
Applied Optics (21) : 15, Pages 2758-69

Forno, C. (1988)
"Deformation measurement using high resolution moiré photography."
Optics and Lasers in Engineering (8), Pages 189-212

Frankowski, G., Schillke, F., Stobbe, I., Tischer, W., Nadeborn, W. (1989)
"Comparative-studies of various carrier frequency methods on interference band evaluation in a digital interferometer"
Physical Research (10) : 29, Pages 62-66 (NOTE: In German)

Funnell, W.R.J. (1981)
"Image processing applied to the interactive analysis of interferometric fringes."
Applied Optics (20) : 18, Pages 3245-9

Gabor, J.D. (1948)
"A new microscopic principle."
Nature (161), Pages 777-778

Gabor, J.D. (1949)
"Microscopy by reconstructed wavefronts."
Proceedings of the Royal Society A (197), Pages 454-486

Gabor, J.D. (1951)
"Microscopy by reconstructed wavefronts II."
Proceedings of the Physics Society B (64), Pages 449-469

Galkin, D.S., Novikov, S.A., Pisarev, V.S. (1988)
"Semiautomatic Young-Fringe processing in strain measurement by speckle photography."
Zavodskaya Laboratoriya (54) : 9, Pages 88-91

George, N. (1985)
"About speckle"
Proceedings of the Society of Photo-Optical and Instrumentation Engineers (556), Pages 8-27

Gerchberg, R.W. and Saxton, W.O. (1972)
"A Practical algorithm for the Determination of Phase from Image and Diffraction Plane Pictures."
Optik (35) : 2, Pages 237-246

Ghiglia, G.A., Mastin, G.A., Romero, L.A. (1987)
"Cellular-Automata Method of Phase Unwrapping."
Journal of the Optical Society of America A (4) : ?, Pages 267-280

Gierloff, J.J. (1987)
"Phase Unwrapping by Regions."
Proceedings of the Society of Photo-Optical and Instrumentation Engineers (818), Pages 2-9

Gonzalez, R.C. and Wintz, P. (1987).
"Digital Image Processing. 2nd edition"
(Addison and Wesley publishing)

Goodman, J.W. (1975)
"Statistical Properties of Laser Speckle Patterns."
(Topics in Applied Physics (9) : Laser Speckle and Related Phenomena, Springer-Verlag)

Goodman, J.W. (1986)
"A random walk through the field of speckle."
Optical Engineering (25) : 5, Pages 610-612

Green, R.J. (1990)
"The use of Fourier transform methods in automatic fringe pattern analysis."
(PhD thesis, University of London: King's College)

Green, R.J., Walker, J.G., Robinson, D.W. (1988)
"Investigation of the Fourier-Transform method of Fringe Pattern Analysis."
Optics and Lasers Engineering (8), Pages 29-44

Greivenkamp, J.E. (1984)
"Generalised data reduction for heterodyne interferometry."
Optical Engineering (23) : 4, Pages 350-352

Greivenkamp, J.E. (1987)
"Sub-Nyquist Interferometry."
Applied Optics (26) : 24, Pages 5245-5258

Hariharan, P., Oreb, B.F., Brown, N. (1983)
"Real time holographic interferometry: a microcomputer system for the measurement of vector displacements."
Applied Optics (22) : 6, Pages 876-880

Horowitz, P. and Hill, W. (1980)
"The Art of Electronics."
(Cambridge University Press)

Howland, R.C.J. (1930)
"On the Stresses in the Neighbourhood of a Circular Hole in a Strip Under Tension."
Proceedings of the Royal Society A, (671), Pages 49-86

Huang, T.S. (1972)
"Two dimensional Windows."
IEEE Transactions on Audio and Electroacoustics (AU-20) : 1, Pages 88-89

Hung, Y.Y. and Hovansian, J.D. (1972)
"Full-field Surface-strain and displacement analysis of Three-dimensional Objects using Speckle Interferometry."
Experimental Mechanics (12), Pages 454-460

Hunter, J.C. and Collins, M.W. (1989)
"Typically encountered problems in the automatic analysis of infinite fringe background holographic interferograms."
(Proceedings of Fringe Analysis '89, Loughborough University : FASIG)

Huntley, J.M. (1986a)
"An image processing system for the analysis of speckle photographs."
Journal of Physics E, (19), Pages 43-9

Huntley, J.M. (1986b)
"Fast transforms of speckle photography fringe analysis."
Optics and Lasers in Engineering (7) : 3, Pages 149-61

Huntley, J.M. (1986c)
"Speckle photography fringe analysis by the Walsh Transform."
Applied Optics (25) : 3, Pages 382-6

Huntley, J.M. (1989a)
"Speckle photography fringes analysis: assessment of current algorithms."
Applied Optics (28) : 20, Pages 4316-22

Huntley, J.M. (1989b)
"Noise-immune phase unwrapping algorithm."
Applied Optics (28) : 15, Pages 3268-70

Huntley, J.M. and Benckert, L. (1992a)
"Speckle interferometry: noise reduction by correlation fringe averaging."
Applied Optics (31) : 14, Pages 2412-4

Huntley, J.M. and Benckert, L. (1992b)
"Measurement of Dynamic Crack Tip Displacement Field by Speckle Photography and Interferometry."
(Proceedings of Fringe Analysis '92, Leeds University : FASIG)

Huntley, J.M. and Field, J.E. (1989)
"High resolution moire photography: application to dynamic stress analysis."
Optical Engineering (28) : 8, Pages 926-33

Ichioka, Y. and Inuiya, M. (1972)
"Direct Phase Detecting System."
Applied Optics (11) : 7, Pages 1507-1514

Imaging Technology (1987)
"VS-100-AT User's Manual" and "ITEX 100 Programmer's Manual"
(Imaging Technology Inc. Part Nos. 47-H10027-00 and 47-S10008-05)

Isacson, S.A. and Kaufmann, G.H. (1985a)
"Two dimensional digital processing of speckle photography fringes.
1: Diffraction halo influence for the noise-free case."
Applied Optics (24) : 2, Pages 189-93

Isacson, S.A. and Kaufmann, G.H. (1985b)
"Two dimensional digital processing of speckle photography fringes.
2: Diffraction halo influence for the noisy case."
Applied Optics (24) : 10, Pages 1444-7

Itoh, K. (1982)
"Analysis of the phase unwrapping algorithm."
Applied Optics (21) : 14, Page 2470

Jain, A.K. and Christensen, C.R. (1980)
"Digital processing of images in speckle noise."
Proceedings of the Society of Photo-Optical and Instrumentation Engineers (243), Pages 46-50

Joenathan, C. (1990)
"Effect of non-linearity of the TV camera in Electronic Speckle Pattern Interferometry."
Optik (85) : 1, Pages 33-37

Johnson, G.W., Leiner, D.C., Moore, D.T. (1977)
"Phase-locked interferometry."
Proceedings of the Society of Photo-Optical and Instrumentation Engineers (126), Pages 152-160

Jones, R. (1976)
"The design and application of a speckle pattern interferometer for total plane strain field measurement."
Optics and Laser Technology, Pages 215-9

Jones, R. (1982)
"New developments in the design and application of Electronic Speckle Pattern Interferometers."
Electro-Optics/Laser Conference: Brighton, Pages 272-84

Jones, R. and Wykes, C. (1977)
"De-correlation effects in speckle pattern interferometry: 2. Displacement dependent de-correlation and applications to the observation of machine-induced strain."
Optica Acta (24) : 5, Pages 533-50

Jones, R. and Wykes, C. (1981)
"General parameters for the design and optimization of Electronic Speckle Pattern Interferometers."
Optica Acta (28) : 7, Pages 949-72

Jones, R. and Wykes, C. (1983)
"Holographic and Speckle Interferometry."
(Cambridge University Press)

Kadono, H., Takai, N., Asakura, T. (1985)
"Experimental study of the laser speckle phase in the image field."
Optica Acta (32) : 9, Pages 1223-34

Kaufmann, G.H. (1981)
"Numerical processing of speckle photography data by Fourier transform."
Applied Optics (20) : 24, Pages 4277-80

Kaufmann, G.H. (1982)
"Digital analysis of speckle photography fringes: processing of experimental data."
Applied Optics (21) : 19, Pages 3411-12

Kawase, S., Honda, T., Tsujiuchi, J. (1976)
"Measurement of Elastic Deformation of Rotating Objects by using Holographic Interferometry."
Optics Communications (16), Pages 96-98

Kerr, D. and Tyrer, J.R. (1987)
"The application of phase stepping to the analysis of ESPI fringes."
Proceedings of the Society of Photo-Optical and Instrumentation Engineers (814), Pages 379-89

Kerr, D., Mendoza Santoyo, F., Tyrer, J.R. (1989)
"A Novel approach to the extraction of phase data from ESPI fringes."
(Proceedings of Fringe Analysis '89, Loughborough University : FASIG)

Kinnestaetter, K., Lohmann, A.W., Schwider, J., Streibl, N. (1988)
"Accuracy of phase shifting interferometry."
Applied Optics (27) : 24, Pages 5082-9

Klimenko, I.S., Ryabukho, V.P., Feduleev, B.V. (1986)
"Comparison of the sensitivity and accuracy of holographic and speckle interferometry with Fourier-plane recording."
Optika Spektroskpiya (USSR) (61) : 5, Pages 699-702

Kreis, T.M. (1986)
"Digital holographic interference-phase measurement using Fourier transform techniques."
Journal of the Optical Society of America A (3) : 6, Pages 847-855

Kreis, T.M. (1987a)
"Quantitative Evaluation of Interference Patterns."
Proceedings of the Society of Photo-Optical and Instrumentation Engineers (863), Pages 68-77

Kreis, T.M. (1987b)
"Fourier transform evaluation of holographic interference patterns."
Proceedings of the Society of Photo-Optical and Instrumentation Engineers (814), Pages 365-71

Kreis, T.M. (1988)
"Automatic evaluation of interference patterns."
Proceedings of the Society of Photo-Optical and Instrumentation Engineers (1026), Pages 80-89

Kreis, T.M. (1992)
"Computer Aided Evaluation of Fringe Patterns."
(Proceedings of Fringe Analysis '92, Leeds University : FASIG)

Kreis, T.M. and Jüptner, W.P.O. (1989)
"Fourier transform evaluation of interference patterns:
The role of filtering in the spatial frequency domain."
Proceedings of the Society of Photo-Optical and Instrumentation Engineers (1162), Pages 116-125

Kujawińska, M. (1992a)
"The architecture of multipurpose fringe pattern analysis system."
(Proceedings of Fringe Analysis '92, Leeds University : FASIG)

Kujawińska, M. (1992b)
"Spatial techniques of automatic fringe pattern analysis."
(Course notes from Society of Photo-Optical and Instrumentation Engineers conf., San Diego, California)

Kujawińska, M. and Robinson, D.W. (1988)
"Multichannel phase-stepped holographic interferometry."
Applied Optics (27) : 2, Pages 312-320

Kujawińska, M. and Wójciak, J. (1991)
"High Accuracy Fourier Transform Fringe Pattern Analysis."
Optics and Lasers in Engineering (14), Pages 325-339

Kujawińska, M., Spik, A., Robinson, D.W. (1989a)
"Quantitative analysis of transient events by ESPI."
Proceedings of the Society of Photo-Optical and Instrumentation Engineers (1121), Pages 416-423

Kujawińska, M., Spik, A., Wójciak, J. (1989b)
"Fringe pattern analysis using Fourier transform techniques."
Proceedings of the Society of Photo-Optical and Instrumentation Engineers (1121), Pages 130-135

Kwon, O.Y. (1987)
"Advanced wavefront sensing at Lockheed."
Proceedings of the Society of Photo-Optical and Instrumentation Engineers (816), Pages 197-211

Kwon, O.Y. and Shough, D.M. (1985)
"Multichannel grating shift interferometers."
Proceedings of the Society of Photo-Optical and Instrumentation Engineers (599), Pages 273-279

Leendertz, J.A. (1970)
"Interferometric displacement measurement on scattering surfaces utilizing speckle effect."
Journal of Physics E, (3), Pages 214-8

Lim, J.S. and Nawab, H. (1981)
"Techniques for speckle noise removal."
Optical Engineering (20) : 3, Pages 472-80

Løkberg, O.J. (1980)
"Advances and applications of ESPI."
Proceedings of the Society of Photo-Optical and Instrumentation Engineers (215), Pages 92-5

Løkberg, O.J. (1986)
"Electronic speckle pattern interferometry."
Proceedings of the Society of Photo-Optical and Instrumentation Engineers (673), Pages 346-53

Løkberg, O.J. and Høgmoen, K. (1976)
"Use of modulated reference wave in ESPI."
Journal of Physics E (9) : 10, Pages 847-51

Løkberg, O.J. and Krakhella, K. (1981)
"ESPI using fibre optics."
Optics Communications (38) : 3, Pages 155-8

Løkberg, O.J. and Kwon, O.Y. (1984)
"Electronic Speckle Pattern Interferometry using a CO_2 laser."
Optics and Laser Technology (16) : 4, Pages 187-192

Løkberg, O.J., Malmo, J.T., Slettemoen, G.Å. (1985)
"Interferometric measurements of high temperature objects by ESPI."
Applied Optics (24) : 19, Pages 3167-72

Luxmoore, A. (1975)
"Measurement of in-plane displacements and strains by moiré and speckle methods."
(The Engineering uses of Coherent Optics : Cambridge University Press)

Lynn, P.A. (1973)
"An Introduction to the Analysis and Processing of Signals: 3rd Edition."
(Macmillan Education)

Maas, A.A.M. (1991a)
"Phase Shifting Speckle Interferometry."
(PhD thesis, Delft University of Technology, The Netherlands)

Maas, A.A.M. (1991b)
"Shape measurement using phase shifting speckle interferometry."
Proceedings of the Society of Photo-Optical and Instrumentation Engineers (1553), Pages 558-568

Macarthur, J.M. (1988)
"An investigation into the in-plane surface strain of tensile components using ESPI."
(Project report : City University, Department of Mechanical Engineering)

Macy Jr., W.W. (1983)
"Two-dimensional fringe-pattern analysis."
Applied Optics (22) : 23, Pages 3898-3901

Maeda, J. and Murata, K. (1986)
"Digital restoration of blurred images in speckle noise by a two-step procedure."
Optics Communications (60) : 1, Pages 5-8

Malcom, A.A., Burton, D.R., Lalor, M.J. (1989)
"A study of the effects of windowing on the accuracy of surface measurements obtained from the Fourier analysis of fringe patterns."
(Proceedings of Fringe Analysis '89, Loughborough University : FASIG)

Malmo, J.T., Løkberg, O.J., Ellingsrud, S. (1991)
"Interferometric measurements of objects in water by TV-holography."
Optics and Lasers in Engineering (15) : 1, Pages 25-41

Malmo, J.T., Løkberg, O.J., Slettemoen, G.Å. (1988)
"Interferometric Testing at Very High Temperatures by TV Holography (ESPI)."
Experimental Mechanics (28) : 3, Pages 315-21

Marom, E. (1974)
"Holographic Nondestructive Testing (Chapter 6, Holographic Correlation)."
(Academic Press Incorporated)

Massie, N.A. (1980)
"Real-time digital heterodyne interferometry system."
Applied Optics (19) : 1, Pages 154-160

Massie, N.A., Nelson, R.D., Holly, S. (1979)
"High performance real-time heterodyne interferometry."
Applied Optics (18) : 11, Pages 1797-1803

McBain, J.C., Honer, J.E., Stange, W.A., Ogg, J.S. (1979)
"Vibration analysis of spinning disk using image derotated holographic interferometry."
Experimental Mechanics (19) : 1, Pages 17-22

Mertz, L.N. (1979)
"Speckle Imaging, photon by photon."
Applied Optics (18) : 5, Pages 611-614

Mertz, L.N. (1981)
"Phase unwrapping in two contexts."
Proceedings of the Society of Photo-Optical and Instrumentation Engineers (373), Pages 211-14

Mertz, L.N. (1983)
"Real time fringe pattern analysis."
Applied Optics (22) : 10, Pages 1535-39

Merzkirch, W. (1990)
"Speckle Photography - Chapter 11"
(Handbook of Flow Visualization, Edited by Wen-pJei Yang)

Michelson, A.A. (1902)
"Light waves and their uses."
(University of Chicargo Press)

Moore, A.J. and Tyrer, J.R. (1990)
"Surface strain measurement with ESPI applied to fracture mechanics."
Proceedings of the Society for Experimental Mechanics, Baltimore.

Moran, S.E., Law, R.L., Craig, P.N., Goldberg, W.M. (1987)
"Optically phase locked Electronic Speckle Pattern Interferometer."
Applied Optics (26) : 3, Pages 475-91

Moran, S.E., Lugannani, R., Craig, P.N., Law, R.L. (1989)
"Optically phase-locked ESPI system performance for vibration measurement in random displacement fields."
Journal of the Optical Society of America A (6) : 2, Pages 252-69

Morimoto, Y., Seguchi, Y., Higashi, T. (1988)
"Application of moire analysis of strain using Fourier Transform."
Optical Engineering (27) : 8, Pages 650-6

Mulholland, J.D. and Calame, O. (1978)
"Lunar Crate Giordano Bruno: AD 1178 Impact Observations Consistent with Laser Ranging Results."
Science (199), Pages 875-877

Munson Jr., D.C. and Sanz, J.L.C. (1984)
"Image Reconstruction from Frequency-Offset Fourier Data."
Proceedings of the IEEE (72) : 6, Pages 661-69

Nakadate, S. and Saito, H. (1985)
"Fringe scanning speckle-pattern interferometry."
Applied Optics (24) : 14, Pages 2172-80

Nakadate, S., Yatagai, T., Saito, H. (1980)
"ESPI using digital image processing techniques."
Applied Optics (19) : 11, Pages 1879-3

Nguyen, D. (1986)
"Development of ESPI applied to examination of surface in-plane strain of rotating components."
(Project report : City University, Department of Mechanical Engineering)

Noh, S. and Yamaguchi, I. (1992)
"Two-dimensional Measurement of Strain Distribution by Speckle Correlation."
Japan Journal of Applied Physics (31) : 2, Pages 505-510

Nuttall, A.H. (1981)
"Some windows with very good sidelobe behaviour."
IEEE Transactions on Acoustics, Speech and Signal Processing (29) : 1, Pages 84-91

O'Donovan, P.C., Atkinson, J.T., Burton, D.R., Lalor, M.J. (1992)
"Practical assessment of fringe quality (through Fourier analysis)."
(Proceedings of Fringe Analysis '92, Leeds University : FASIG)

Osten, W. and Höfling, R. (1990)
"The inverse modulo process in automatic fringe analysis - problems and approaches."
Proceedings of the Society for Experimental Mechanics, Baltimore.

Paler, K. and Bowler, I.W. (1986)
"Gabor filters applied to ESPI images."
Proceedings of the Second Conference on Image Processing and Applications, Pages 258-62

Parker, R.J. (1990)
"A Quarter Century of Thermoplastic Holography."
Proceedings of the Society for Experimental Mechanics, Baltimore.

Parker, R.J. and Jones, D.G. (1986)
"Industrial holography - The Rolls-Royce experience."
Proceedings of the Society of Photo-Optical and Instrumentation Engineers (699), Pages 111-126

Philips, J.W. and Schrock, M. (1971)
"Note on the Shear Stresses in Accelerating Disks of Variable Thickness."
International Journal of Mechanical Sciences (13), Pages 445-449

Pickering, C.J.D. and Halliwell, N.A. (1986)
"Automatic Analysis of Young's Fringes in Speckle Photography and Particle Image Velocimetry."
(Proceedings of Fringe Analysis '86, Loughborough University : FASIG)

Pirodda, L. (1982)
"Shadow and projection moiré techniques for absolute and relative mapping of surface shapes."
Optical Engineering (21), Pages 640-649

Pirodda, L. (1989)
"Conjugate wave holographic interferometry for the measurement of in-plane deformations."
Applied Optics (28) : 10, Pages 1842-44

Powell, R.L. and Stetson, K.A. (1965)
"Interferometric vibration analysis by wavefront reconstruction."
Journal of the Optical Society of America A (55) : ?, Pages 1593-8

Post, D. (1990)
"Moiré interferometry: Advances and Applications."
Proceedings of the Society for Experimental Mechanics, Baltimore.

Preater, R.W.T. (1980a)
"In-plane strain measurement on large rotating structures."
Proceedings of Electro-Optics/Laser International (UK), Pages 133-138

Preater, R.W.T. (1980b)
"Non-contact method of in-plane strain measurement on rotating structures."
Proceedings of the Society of Photo-Optical and Instrumentation Engineers (236), Pages 58-61

Preater, R.W.T. (1982)
"Further developments of in-plane strain measurement of rotating structures."
Proceedings of the Society of Photo-Optical and Instrumentation Engineers (369), Pages 591-594

Preater, R.W.T. (1983)
"Electronic Speckle Pattern Interferometry for rotating structures using a pulsed laser."
Proceedings of the Society of Photo-Optical and Instrumentation Engineers (398), Pages 225-228

Preater, R.W.T. (1984a)
"Analysis of rotating component strains using electronic speckle pattern interferometry."
Proceedings of the Society of Photo-Optical and Instrumentation Engineers (473), Pages 40-43

Preater, R.W.T. (1984b)
"In-plane strain measurement on rotating structures using pulsed laser Electronic Speckle Pattern Interferometry."
Proceedings of the International Commission for Optics (ICO-13), Pages 674-675

Preater, R.W.T. (1985)
"Pulsed laser ESPI applied to particular rotating component problems."
Proceedings of the Society of Photo-Optical and Instrumentation Engineers (599), Pages 174-177

Preater, R.W.T. (1985)
"Pulsed laser ESPI applied to particular rotating component problems."
Proceedings of the Society of Photo-Optical and Instrumentation Engineers (599), Pages 174-177

Preater, R.W.T. (1986a)
"A novel optical system for the analysis of in-plane strain on high speed rotating components."
Proceedings of Electro-Optics/Laser International (UK)

Preater, R.W.T. (1986b)
"Pulsed laser electronic speckle pattern interferometry for the analysis of high performance brake discs and other rotating components."
Proceedings of VDI Verlag (617), Pages 295-299

Preater, R.W.T. (1986c)
"Measuring rotating component strain using ESPI."
Proceedings of the Society of Photo-Optical and Instrumentation Engineers (673), Pages 373-376

Preater, R.W.T. (1986d)
"Optical strain measurement of rotating components."
Proceedings of the Society of Photo-Optical and Instrumentation Engineers (699), Pages 145-151

Preater, R.W.T. (1987a)
"Video holographic interferometry."
Proceedings of the Society of Photo-Optical and Instrumentation Engineers (746), Pages 58-60

Preater, R.W.T. (1987b)
"Pulsed electronic speckle pattern interferometry in experimental stress analysis."
Proceedings of the Society of Photo-Optical and Instrumentation Engineers (863), Pages 208-212

Preater, R.W.T. (1987c)
"Analysis of rotating components strains using pulsed ESPI."
Proceedings of the International Commission for Optics (ICO-14), Pages 69-70

Preater, R.W.T. (1987d)
"In-plane strain measurement on rotating structures."
(External report : City University, Department of Mechanical Engineering)

Preater, R.W.T. (1988)
"Measuring rotating component in-plane strain using conventional pulsed ESPI and optical fibres."
Proceedings of the Society of Photo-Optical and Instrumentation Engineers (952), Pages 245-250

Preater, R.W.T. (1989)
"Pulsed and Fibre Optic ESPI for the analysis of in-plane strain on rotating components."
Proceedings of the Society of Photo-Optical and Instrumentation Engineers (1136), Pages 359-363

Preater, R.W.T. (1990a)
"In-plane displacement measurement on rotating components using pulsed laser ESPI."
Proceedings of the Society of Photo-Optical and Instrumentation Engineers (1399), Pages 164-171

Preater, R.W.T. (1990b)
"3-D Photoelasticity and TV-holography for the analysis of rotating components."
(Applied Stress Analysis: Elsevier Applied Science)

Press, W.H., Flannery, B.P., Teukolsky, S.A., Vetterling, W.T. (1988)
"Numerical recipes in C: The Art of Scientific Computing."
(Cambridge University Press)

Proakis, J.G. and Manolakis, D.H. (1988)
"Introduction to digital signal processing."
(Maxwell MacMillan International)

Pryputniewicz, R.J. (1985)
"Speckle metrology techniques and their applications."
Proceedings of the Society of Photo-Optical and Instrumentation Engineers (556), Pages 90-8

Pryputniewicz, R.J. and Bowley, W.W. (1978)
"Techniques of holographic displacement measurement: an experimental comparison."
Applied Optics (17) : 11, Pages 1748-56

Pryputniewicz, R.J. and Stetson, K.A. (1980)
"Determination of the sensitivity vectors in hologram interferometry from two known rotations of the object."
Applied Optics (19) : 13, Pages 2201-2205

Reddy, T.Y., Lakshminarayana, H.V., Srinath, H. (1974)
"Elastic Stresses in an Accelerating Circular Disk."
Journal of Applied Mechanics (41), Pages 817-819

Reid, G.T. (1986)
"Automatic fringe pattern analysis: A Review"
Optics and Lasers in Engineering (7) : 1, Pages 37-68

Robinson, D.W. (1983)
"Automatic fringe analysis with a computer image-processing system."
Applied Optics (22) : 14, Pages 2169-83

Robinson, D.W. (1987)
"Holographic and Speckle Interferometry in the UK: A review of recent developments."
Proceedings of the Society of Photo-Optical and Instrumentation Engineers (814), Pages 330-337

Robinson, D.W. and Williams, D.C. (1986)
"Digital phase stepping speckle interferometry."
Optics Communications (57) : 1, Pages 26-30

Roddier, C. and Roddier, F. (1987)
"Interferogram analysis using Fourier transform techniques."
Applied Optics (26) : 9, Pages 1668-1673

Rossi, J.P. and Maystre, D. (1985)
"Speckle: An electromagnetic theory for shallow rough surfaces."
Optica Acta (32) : 11, Pages 1427-1444

Ru, Q., Honda, T., Tsujiuchi, J., Ohyama, N. (1988)
"Fringe analysis by using 2-D Fresnel transform."
Optics Communications (66) : 1, Pages 21-24

Ru, Q., Ohyama, N., Honda, T., Tsujiuchi, J. (1989)
"Constant radial shearing interferometry with circular gratings."
Applied Optics (28) : 15, Pages 3350-3353

Saleh, B.E.A. and Rabbani, M. (1980)
"Linear filtering of speckled images."
Optics Communications (35) : 3, Pages 327-31

Santoyo, F.M., Kerr, D., Tyrer, J.R. (1988)
"Interferometric fringe analysis using a single phase step technique."
Applied Optics (27) : 21, Pages 4362-4

Santoyo, F.M., Shellabear, M.C., Tyrer, J.R. (1991)
"Whole field in-plane vibration analysis using pulsed phase-stepping ESPI"
Applied Optics (30) : 7, Pages 717-721

Schwider, J. (1990)
"Advanced evaluation techniques in interferometry."
(Progress in Optics, Elsevier Science Publishing Company) (28), Pages 273-359

Sciammarella, C.A. (1982)
"The moiré method - a review."
Experimental Mechanics (22) : 11, Pages 418-433

Sciammarella, C.A., Amadshahi, M.A., Subbaraman, B. (1987)
"A computer based moiré technique to measure very small displacements."
Proceedings of the Society of Photo-Optical and Instrumentation Engineers (814), Pages 262-68

Sharp, B. (1989)
"Electronic Speckle Pattern Interferometry (ESPI)"
Optics and Lasers in Engineering (11), Pages 241-255

Shaw, R.H. (1992)
"A preview of Microsoft C/C++ 7 and the Microsoft Foundation Classes for Windows."
Micorsoft Systems Journal (UK) (1) : 2, Pages 29-50

Shekher, C. and Vaish, J.N. (1983)
"Study of the effect of speckle movement on the fringe contrast in holographic interferometry."
Journal of Optics (India) (112) : 4, Pages 104-4

Shough, D.M., Kwon, O.Y., Leary, D.F. (1990)
"High-speed interferometric measurement of aerodynamic phenomena."
Proceedings of the Society of Photo-Optical and Instrumentation Engineers (1221), Pages 394-403

Sikora, J.P. and Mendenhall, F.T. (1974)
"Holographic vibration study of a rotating propeller blade."
Experimental Mechanics (14) : 6, Pages 230-232

Sirkis, J.S., Chen, Y.M., Singh, H., Cheng, A.Y. (1992)
"Computerized optical fringe pattern analysis in photomechanics: a review"
Optical Engineering (31) : 2, Pages 304-314

Slettemoen, G.Å. (1977)
"Optimal signal processing in ESPI."
Optics Communications (23) : 2, Pages 213-16

Slettemoen, G.Å. (1979)
"General analysis of fringe contrast in Electronic Speckle Pattern Interferometry."
Optica Acta (26) : 3, Pages 313-27

Slettemoen, G.Å. (1980)
"ESPI system based on speckle reference beam."
Applied Optics (19) : 4, Pages 616-23

Slud, E.V. (1988)
"Subpixel Translation-Registration of Random Fields."
IEEE Transactions on Geoscience and Remote Sensing (26) : 4, Pages 487-490

Smith, F.G. and Thompson, J.H. (1988)
"Optics: 2nd edition"
(John Wiley and Sons)

Smythe, R. and Moore, R. (1984)
"Instantaneous phase measuring interferometers."
Optical Engineering (23) : 4, Pages 361-364

Spetzler, H. (1986)
"Interesting examples of Holographic Interferometry."
The Physics Teacher (24) : 2, Pages 80-85

Spik, A. (1987)
"Two-dimensional phase decoding from bounded fringe patterns by using the Fourier-transform method."
Optica Applicata (17) : 4, Pages 349-354

Steel, W.H. (1967)
"Interferometry."
(Cambridge University Press)

Stern, M. (1965)
"Rotationally Symmetric Plane Stress Distributions."
Zeitschrift für angewandte Mathematik und Mechanik (45), Pages 446-447

Stetson, K.A. (1975)
"Optical system for the dynamic analysis of rotating structures, Phase 1 - Design study."
United Technologies Research Centre Report R76-992054-100
UTRC, East Hartford, CT, USA.

Stetson, K.A. (1976a)
"Optical system for the dynamic analysis of rotating structures, Phase 2 - Hardware Development."
United Technologies Research Centre Report R76-992054-200
UTRC, East Hartford, CT, USA.

Stetson, K.A. (1976b)
"Optical system for the dynamic analysis of rotating structures, Phase 3 - System Applications."
United Technologies Research Centre Report R76-992054-300
UTRC, East Hartford, CT, USA.

Stetson, K.A. (1978)
"The use of an Image Derotator in Hologram Interferometry and Speckle Photography of Rotating Objects."
Experimental Mechanics (18) : 2, Pages 67-73

Stetson, K.A. (1990)
"Use of sensitivity vector variations to determine absolute displacements in double exposure hologram interferometry."
Applied Optics (29) : 4, Pages 502-4

Storey, P.A. (1984)
"Holographic vibration analysis of a rotating fluttering fan."
Journal of the American Institute of Aeronautics and Astronautics (22) : 2, Pages 234-241

Storey, P.A. (1986)
"Holographic Interferometry of Rotating Components: decorrelation limitations of the double pulsed technique."
Proceedings of the Society of Photo-Optical and Instrumentation Engineers (599), Pages 66-73

Takasaki, H. (1970)
"Moiré topography."
Applied Optics (9) : 6, Pages 1467-1472

Takeda, M. (1985)
"Subfringe interferometry fundamentals."
Japanese Journal of Optics (24), Pages 2604-2611

Takeda, M. (1990)
"Spatial-carrier fringe-pattern analysis and its applications to precision interferometry and profilometry: An overview."
Industrial Metrology (1), Pages 79-99

Takeda, M., Ina, H.,Kobayashi, S. (1982)
"Fourier-transform method of fringe-pattern analysis for computer based topography and interferometry."
Journal of the Optical Society of America A (72) : 1, Pages 156-160

Tang, S. (1970)
"Note on shear stresses in an accelerating disk."
International Journal of Mechanical Sciences (12), Pages 205-207

Tatam, R.P., Davis, J.C., Buckberry, C.H., Jones, J.D.C. (1990)
"Holographic surface contouring using wavelength modulation of laser diodes."
Optics and Laser Technology (22) : 5, Pages 317-321

Theocaris, P.S. (1969)
"Moiré Fringes in Strain Analysis."
(Pergamon Press)

Tian, Q. and Huhns, M.N. (1986)
"Algorithms for Subpixel Registration."
Computer Vision, Graphics, and Image Processing (35), Pages 220-233

Tischer, M. (1989)
"PC System Programming: An in-depth reference for the DOS programmer."
(Abacus)

Tobias, S.A. and Arnold, R.N. (1959)
"The influence of Dynamical Imperfections on the Vibration of Rotating Disks."
Proceedings of the Institute of Mechanical Engineers (171), Pages 669-690

Towers, D.P., Judge, T.R., Bryanston-Cross, P.J. (1989)
"A Quasi Heterodyne holographic technique and automatic algorithms for phase unwrapping."
Proceedings of the Society of Photo-Optical and Instrumentation Engineers (1163), Pages 95-119

Tribolet, J.M. (1977)
"A New Phase Unwrapping Algorithm."
IEEE Transactions on Acoustics, Speech and Signal Processing (25) : 2, Pages 170-177

Tsuruta, T. and Itoh, Y. (1970)
"Holographic Interferometry for Rotating Subject."
Applied Physics Letters (17), Pages 85-87

Tur, H., Chin, K.C., Goodman, J.W. (1982)
"When is speckle noise multiplicative?"
Applied Optics (21) : 7, Pages 1157-9

Tyrer, J.R. (1986)
"Critical review of recent developments in ESPI."
Proceedings of the Society of Photo-Optical and Instrumentation Engineers (604), Pages 95-103

Tyrer, J.R. (1988)
"The use of TV holography (ESPI) for Loudspeaker Chassis and Cabinet Modal Analysis."
Journal of the Audio Engineering Society (36) : 5, Pages 342-349

Varman, P. and Wykes, C. (1982)
"Smoothing of speckle and moiré fringes by computer processing."
Optics and Lasers in Engineering (3) : 2, Pages 87-100

Vest, C.M. (1979)
"Holographic Interferometry."
(John Wiley and Son)

Vikhagen, E. (1990)
"Nondestructive testing by use of TV holography and deformation phase gradient calculation."
Applied Optics (29) : 1, Pages 137-144

Vogt, E., Geldmacher, J., Dirr, B., Kreitlow, H. (1985)
"Hybrid vibration mode analysis of rotating turbine-blade models."
Experimental Mechanics (25), Pages 161-170

Vrooman, H.A. and Maas, A.A.M. (1989)
"Image processing in digital speckle interferometry."
(Proceedings of Fringe Analysis '89, Loughborough University : FASIG)

Wang, C.T. (1953)
"Applied Elasticity."
(McGraw-Hill, New York)

Whitworth, M.B., Huntley, J.M., Field, J.E. (1991)
"Measurement of the dynamic crack tip displacement field using high resolution moire photography."
Proceedings of the Society of Photo-Optical and Instrumentation Engineers (1554), Pages 282-288

Wiener, N. and Paley, R.E.A.C. (1934)
"Fourier transforms in the complex domain."
(American Mathematical Society)

Winther, S. (1988)
"3D Strain Measurements using ESPI."
Optics and Lasers in Engineering (8), Pages 45-57

Winther, S. and Slettemoen, G.Å. (1984)
"An ESPI contouring technique in strain analysis."
Proceedings of the Society of Photo-Optical and Instrumentation Engineers (473), Pages 44-47

Wolfram, S. (1983)
"Cellular automata."
Los Alamos Science (9), Los Alamos National Laboratory, Pages 2-21

Womack, K.H. (1984)
"Interferometric phase measurement using spatial synchronous detection."
Optical Engineering (23) :4, Pages 391-5

Wykes, C. (1977)
"De-correlation effects in speckle pattern interferometry: 1. Wavelength change dependent de-correlation with application to contouring and surface roughness measurement."
Optica Acta (24) : 5, Pages 517-532

Wykes, C. (1982)
"The use of ESPI in the measurements of static and dynamic surface displacements."
Optical Engineering (21) : 3, Pages 400-6

Wykes, C. (1987)
"A theoretical approach to the optimisation of ESPI fringes with limited laser power."
Journal of Modern Optics (34) : 4, Pages 539-54

Wykes, C. and Flanagan, M. (1987)
"The use of a diode laser in an ESPI system."
Optics and Laser Technology (19) : 1, Pages 37-9

Wykes, C., Butters, J.N., Jones, R. (1981)
"Fringe contrast in ESPI."
Applied Optics (23) : 5, Pages 720-721

Yamaguchi, I. and Noh, S. (1992)
"Deformation measurement by 2-D Speckle Correlation."
Proceedings of the Society of Photo-Optical and Instrumentation Engineers (1756), Pages 106-118

Yonemura, M. and Hagihara, S. (1987)
"Fringes visibility in Electronic speckle pattern interferometry."
Proceedings of the Society of Photo-Optical and Instrumentation Engineers (814), Pages 352-6

Zweig, D.A. and Hufnagel, R.E. (1990)
"A Hilbert Transform Algorithm for Fringe-Pattern Analysis."
Proceedings of the Society of Photo-Optical and Instrumentation Engineers (1333), Pages 295-302

A APPENDIX

Appendix A: PC Fundamentals

This appendix deals with some of the fundamentals of the computer hardware and software described in this thesis. The hardware used was an 80486 computer fitted with 16,000KB of memory, a 180MB hard disk and super VGA graphics adaptor. Additional hardware includes the Imaging Technology VS100 frame store, Amplicon Liveline PC36AT card, Adaptec 1522 SCSI, SyQuest SQ555 removable hard disk drive, and a Seikio CP-250 250MB tape drive.

A.1 Intel 80x86 processor family

The Intel 80286, 80386 and 80486 form an upwardly compatible family of central processing units (CPUs) fitted to AT type computers. The more advanced 386 and 486 CPU's currently operate at clock speeds in the range 40-66MHz, and offer an impressive range of machine code intructions and internal chip registers. They have two modes of operation, called *real* and *protected*. Normal MS-DOS applications run in real mode, and are limited to 640KB of memory (called base or conventional memory). Unfortunately, this mode is the least efficient of the two, and is almost unqiuely supported by applications software. The advent of the WINDOWS operating system allows the computer to be operated in protected mode, but this system is incompatible with a vast array of existing software[138].

When operating the computer under the MS-DOS, simply adding more memory chips to the computer does not overcome the memory limitation, because the extra memory can only be accessed with the processor switched into protected mode. To solve this problem, manufactures came up with two additional types of memory, called *expanded* and *extended*. Expanded memory is not used in any of the software applications described in this thesis, and will not be discussed further. Extended memory is described in a little more detail in section A.3, since it is used extensively in this thesis to store the huge amounts of data generated by the two-dimensional Fourier transform software.

[138]Including the ITEX link library for the VS100 image processor.

A.2 MS-DOS operating system (Version 5.0)

The Microsoft disk operating system (MS-DOS) gets the computer up and running, and controls the operation of the computer's activities. It is a manager for the flow, entry and display of software and data, to and from each part of the computer system [Duncan, 1988; Tisher, 1989]. In order to run a program, you must first run the operating system.

Version 5.0 of MS-DOS was used as the development environment for all software written for this research project. MS-DOS version 5.0 was chosen because, unlike earlier versions of MS-DOS, this version allows very large hard disk partitions, which is useful when large amounts of data (images) are to be stored. Also, the extended DOS functions (device drivers) and the DOS program itself can be made to execute from the high memory area (HMA), thus leaving more base memory for applications programs.

A.3 Extended Memory Specification

The simplified memory structure of the AT class of computers is shown in Figure 143. Extended memory is the region of the memory map above 1024KB. This memory is not normally accessible to the applications programmer, but the use of device drivers provides a means of access. The extended memory specification (XMS) defines a software interface that allows real-mode application programs to use the extended memory in a cooperative and hardware independent manner. The XMS allows applications to allocate, resize and release blocks of three basic types:

- The "high memory area" (HMA) at addresses between 1024KB and 1088KB.
- Extended memory blocks (EMBs) from addresses above 1088KB.
- Upper memory blocks (UMBs) at addresses between 640KB and 1024KB.

Installation of the device driver provided by Microsoft (called HIMEM.SYS) is accomplished by adding the statement 'DEVICE=HIMEM.SYS' to the CONFIG.SYS file (in the root directory of the boot drive). Once the driver has been sucessfully installed, applications programs can access its functions by finding what the entry point address is. To do this, it is necessary to execute interrupt 0x2F with the AX register set to 0x4310, which will return the entry point in registers ES:BX. The entry point must be saved as a variable. Once the entry point is known, programs simply issue

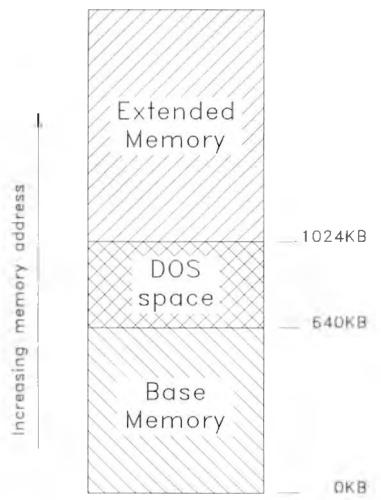


Figure 143: PC memory

an indirect far call to the entry point with the function request stored in AH. Interrupt 0x2F is no longer required. For a complete list of the available extended memory functions, see Duncan [1989].

At the time of writing, access to the extended memory of the computer was not a straightforward task (as can be seen). However, the advent of more powerful compilers for the PC will make the task simpler. The C/C++ (version 7.0) compiler offered by Microsoft appears to support both extended memory and protected mode programming of the 80x86 processors [Shaw, 1992], but closer investigation indicates that it is basically the same method as offered by the device driver, but with simplified function calls. Therefore, no decrease in data access time would be gained by using the C++ functions.

A.4 Minimum hardware requirements

The following (minimum) computer hardware configuration is required for operation:

80286 (16MHz) based AT compatible computer (with 80287 math coprocessor).
VGA colour graphics.
MS-DOS version 3.3.
6MB memory (extended); expanded memory is not supported.
40MB hard disk (with at least 30MB free).
Microsoft compatible mouse and device driver.

However, the following configuration is strongly recommended:

80486 (33 MHz or higher) compatible computer.
VGA colour graphics.
MS-DOS version 5.0.
16MB memory (extended).
180MB hard disk.
Microsoft compatible mouse and device driver.

The VS100 should be configured to a memory base address of 0xD0000 and a register base address of 0x300. The software has been sucessfully tested on the latter of the two configurations. It should be stressed that some form of mass storage device is essential for interferometric work (see section 3.2.1.5)

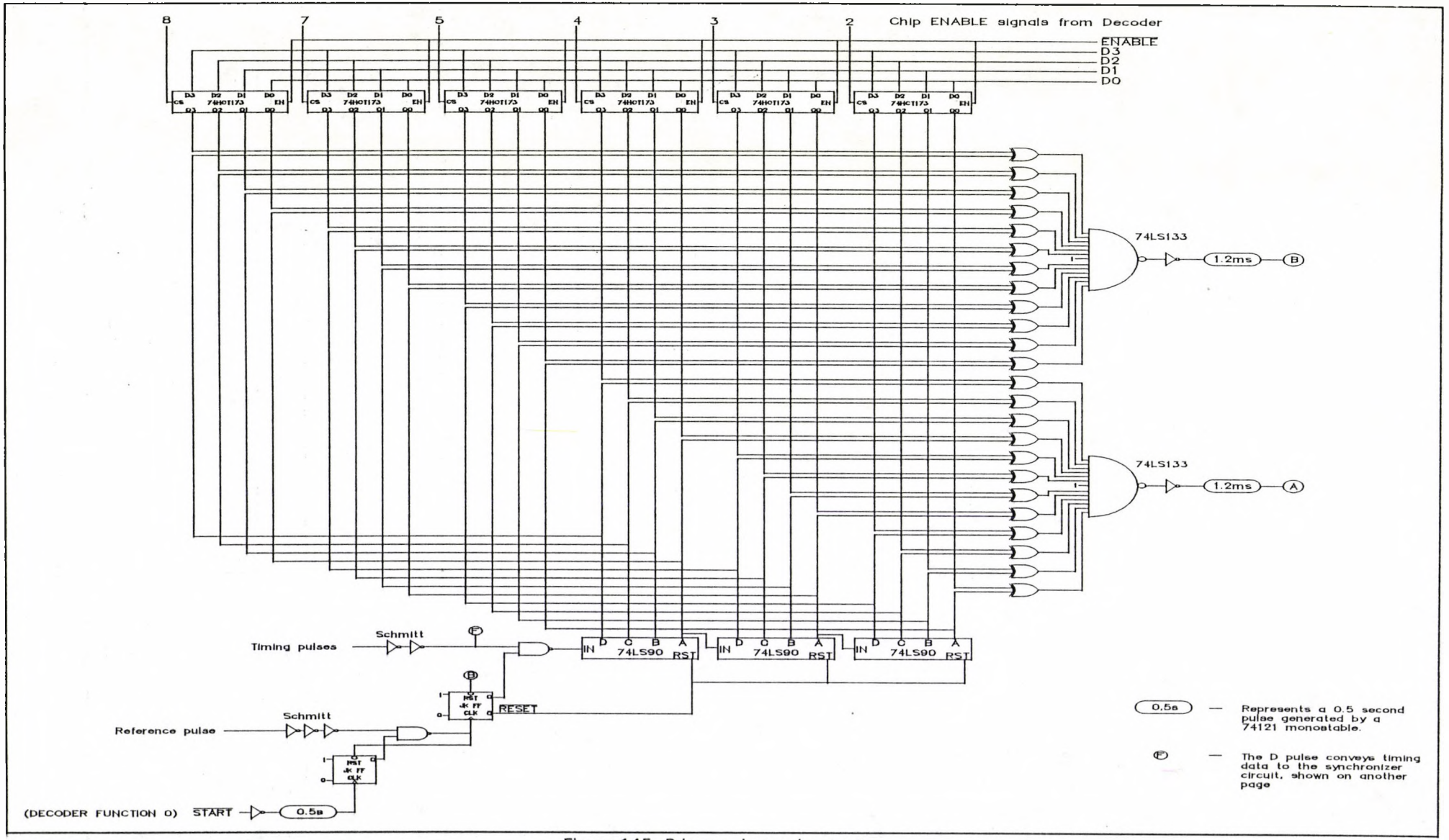


Figure 145: Primary electronic counter

B APPENDIX

Appendix B: Software fragments

B.1 One dimensional FFT algorithm

This routine computes the Fourier transform of an array of 512 data points using the fast Fourier transform algorithm. The routine is written in standard C and should be portable between compilers. It has been sucessfully used on the Microsoft C compiler (version 6.0). The real and imaginary parts of the data to be transformed should be stored in arrays xr and xi, which should be defined as double precision. The W table is a precalculated array of sines and cosines necessary for the transform. See section B.2 for an example of a calling program.

Upon exit, xr and xi contain the transformed real and imaginary data.

```
/* preprocessor commands */
#include <math.h>

#define SR512 22.627417

/*
 *      This routine is used to perform an FFT on a set of 512 data points.
 *
 *      It calculates the real and imaginary parts of the data to an
 *      accuracy of 17 decimal places - standard double on Microsoft C.
 *
 *      Written By Robin Swain, City University, London
 *      First coding : 31 July 1990.
 *
 *      UPDATE NOTES:
 *
 *      This version was edited on 24 September 1990 to use double precision
 *      in the calculations.
 *
 *      The W table must be precalculated and passed to the routine
 *      through the wr and wi parameters.
 *      NOTE: wr and wi must be in double precision....
 *
 */

/* Function prototypes */
static rever(unsigned int *rtn,unsigned int cnt,int lp);  /* Reverse order */


int fftrcs (double *xr, double *xi, double *wr, double *wi)       /* Function start */
{
        register int i, j, k;
        unsigned int ii, rvs;
        int sft = 10, pwr = 9, length = 512;
        /* values for a 512 value transform */

        int    n2, ptr, numw;
        int    gstep, wstep;
        double tmpr, tmpi, tmp;
```

```
        n2 = length >> 1;

        /*
         * Rearrange the terms to compensate for final
         * butterfly order.
         * This could be done after butterflying just as
         * easily.
         */

                for (ii=0; ii < length; ii++) {
                rever(&rvs, ii, pwr);

                        if (rvs > ii) {
                                tmp = xr[ii];
                                xr[ii] = xr[rvs];
                                xr[rvs] = tmp;
                                tmp = xi[ii];
                                xi[ii] = xi[rvs];
                                xi[rvs] = tmp;
                        }  /* If then statement */
        }  /* II loop */

        /*
         * now do the butterfly stages.
         */

        for (numw=1; numw <= n2; numw = gstep) {
                gstep = numw << 1;
                ptr = 0;
                wstep = n2 / numw;
                for (i=0; i<numw; i++, ptr += wstep) {
                        for (j=i; j<length; j += gstep) {
                                k = j + numw;
                                tmpr = (wr[ptr] * xr[k]) - (wi[ptr] * xi[k]);
                                tmpi = (wr[ptr] * xi[k]) + (wi[ptr] * xr[k]);
                                xr[k] = xr[j] - tmpr;
                                xi[k] = xi[j] - tmpi;
                                xr[j] += tmpr;
                                xi[j] += tmpi;
                        } /* J loop */
                }  /* I loop */
        } /* numw loop */

        for (i=0;i<512;i++) {
            xr[i] = xr[i]/SR512;
            xi[i] = xi[i]/SR512;
            }
             /* Complete definition
              * FFT is scaled by 1/SQRT(N) so that reverse transform
              * may use the same routine.
              */

        return (0);

} /* End of fft routine */


static rever(unsigned int *rtn,unsigned int cnt,int lp)

{
        register int i;
        register int loop;
        loop = lp - 1;

        *rtn = 0;
        for (i=0; i<lp; i++) {
                if (cnt & (1<<i))
                        *rtn |= (1<<(loop-i));
        } /* I loop */
} /* reverse function */
```

B.2 Fourier transform calling program

This section explains how to call the routine presented in section B.1. First, the W table must be computed (only computed once at the beginning of the calling program). Then the data to be transformed is placed into arrays xr and xi. Reordering the sequence is discussed in section 4.2.1.3. If the data is purely real, all values of array xi are zeroed (this is the case for a forward image transform). The value of PI is defined in the preprocessor section of the program.

```
/* Definitions */
double  wr[256],wi[256];                /* W table real/imaginary arrays */
double  xr[512],xi[512];                /* data real/imaginary arrays */
double  alpha,theta;                    /* Misc variables */
int     i;

        .... intermediate program statements ....

/* Compute W table */
alpha = -(PI/(double)256);
for (i=0; i<256; i++) {
        theta = alpha * (double)i;
        wr[i] = cos(theta);
        wi[i] = sin(theta); }

....    intermediate program:
        data to be transformed
        placed in xr and xi ....

/* Reorder Fourier transform sequence */
for (i=1;i<512;i+=2) {   *(xr+i) = - *(xr+i);
                         *(xi+i) = - *(xi+i); }

/* call Fourier transform routine */
fftrcs(xr,xi,wr,wi);

/* FFT data is stored in xr and xi, overwriting the input data */
```

B.3 Modified snap instruction of VS100

The conventional snap instruction of the VS100 (included with the ITEX link library) is a snap on field rather than a snap on frame. A modified version was coded to perform snap on even frame. This section of code will only be of use to those familiar with ITEX, and the programming of the VS100. For more information see Imaging Technology [1987].

The registers ZOOM and STATUS_CONTROL are defined in the ITEX header file "ITEX100.H". The register CONTROL is defined in the header of the program, and points to one of the output registers of the PC36AT card. In this piece of code, bit 1 of the CONTROL register is used to control the scanning beam of the camera (bit set = beam on).

```
/* Make sure the VS100 is operating in the correct mode */
andreg(ZOOM,0xCFFF);                    /* zero regmux1/2 */
orreg(ZOOM,0x2000);                     /* Status & Control */
andreg(STATUS_CONTROL,0x0FFF);          /* Freeze acquire operations */
```

```
        ... Issue start instruction to ECU and check for interrupt ...


/* Initiate a snap on even frame command */
andreg(STATUS_CONTROL,0x0FFF);                  /* Clear acquire mode bits */
orreg(STATUS_CONTROL,0x2000);                   /* Snap on frame */
outp(CONTROL,0x02);                             /* blank camera */

/* wait for completion of operation  - tight loop */
do {} while (testreg(STATUS_CONTROL,0x7000));   /* has ACQMD1 changed to 0 */

andreg(STATUS_CONTROL,0x0FFF);                  /* clear acquire mode bits */
orreg(STATUS_CONTROL,0x2000);                   /* Snap on frame */
outp(CONTROL,0x03);                             /* unblank */

/* hold process here until field pulse */
waitvb();                                       /* This waits for vertical blanking
                                                 * MUST be next field pulse */

/* Modify the gain of the VS100 and enable interrupts */
setgain(NEWGAIN);
_asm  STI                                       /* Set interrupt flag */
```

C APPENDIX

Appendix C: Numerical results

This appendix contains the numerical results obtained from the various fringe patterns presented in section 5.2.2. The tables refer to the 'optical strain gauges' shown in Figure 144. The average (AVG) and standard deviation (STD) are calculated for each radius.



Figure 144: Optical gauge locations

	Optical strain gauge reading (μstrain) [radius in mm]									
	A 118.7	B 113.7	C 108.7	D 103.7	E 98.7	F 93.7	G 88.7	H 83.7	I 78.7	J 73.7
1	101.8	101.1	99.4	104.4	106.4	107.2	111.4	112.1	105.9	103.4
2	97.3	99.7	105.6	102.2	96.8	104.9	114.5	111.8	105.4	109.5
3	95.7	103.8	102.0	100.8	101.7	103.0	104.3	104.9	104.4	102.5
4	96.0	99.5	99.7	95.6	95.8	100.9	104.2	103.8	102.8	100.1
5	88.0	97.6	102.6	97.7	98.3	105.1	102.3	102.6	104.9	100.6
6	88.7	96.4	98.3	100.7	100.3	96.8	97.9	100.8	101.1	102.5
7	93.3	98.1	93.7	94.7	101.8	98.8	99.9	103.1	97.4	102.4
8	88.2	88.0	94.2	100.2	100.4	98.4	104.5	105.3	97.1	94.8
9	87.6	89.1	94.2	103.5	96.8	96.3	116.8	95.0	97.6	97.8
Avg	93.0	97.0	98.9	100.0	99.8	101.3	106.2	104.4	101.8	101.5
Std	4.8	5.0	4.0	3.2	3.1	3.7	6.2	5.0	3.4	3.8

Table 16: Optical strain gauge readings for fringe pattern A (3mm gauge length)

	Optical strain gauge reading (μstrain) [radius in mm]									
	A 118.7	B 113.7	C 108.7	D 103.7	E 98.7	F 93.7	G 88.7	H 83.7	I 78.7	J 73.7
1	54.3	57.5	62.9	65.4	62.7	63.3	73.8	61.9	54.2	63.5
2	52.8	56.4	56.9	57.6	60.9	64.5	63.2	67.4	64.4	58.1
3	42.1	49.4	56.0	59.9	55.8	56.0	64.0	65.9	64.4	64.2
4	46.3	47.6	54.2	59.8	62.2	62.0	63.5	65.0	62.7	61.1
5	45.5	49.6	54.9	60.0	59.3	61.1	62.0	65.6	66.3	58.2
6	48.1	49.5	52.1	53.7	54.3	57.9	62.6	59.6	62.0	64.9
7	46.7	52.2	53.3	53.7	57.1	61.0	61.0	64.8	63.9	58.3
8	42.8	48.8	53.1	56.3	56.6	61.3	63.9	58.3	60.4	60.6
9	45.2	48.6	51.1	52.8	53.9	57.2	64.5	51.1	59.4	51.3
Avg	47.1	51.1	54.9	57.7	58.1	60.5	64.3	62.2	62.0	60.0
Std	3.9	3.4	3.3	3.8	3.1	2.7	3.5	4.9	3.4	4.0

Table 17: Optical strain gauge readings for fringe pattern B (3mm gauge length)

	Optical strain gauge reading (μstrain) [radius in mm]									
	A 118.7	B 113.7	C 108.7	D 103.7	E 98.7	F 93.7	G 88.7	H 83.7	I 78.7	J 73.7
1	56.3	48.1	54.0	56.1	48.6	54.1	52.6	54.4	63.3	64.0
2	42.7	53.4	40.5	45.3	47.9	42.3	50.5	59.2	58.5	50.1
3	42.8	47.9	40.4	44.6	52.3	44.3	53.4	53.3	48.9	54.6
4	40.8	47.9	42.6	39.5	43.2	43.4	49.1	48.0	43.9	54.9
5	33.1	40.1	54.3	42.0	39.9	42.1	43.4	44.6	43.9	48.3
6	26.6	39.7	46.1	40.2	43.9	44.9	43.4	51.7	43.4	43.5
7	33.6	42.8	39.6	37.2	39.1	50.5	46.3	45.8	47.1	56.2
8	33.7	36.4	35.6	39.6	42.9	48.0	50.7	44.1	51.7	44.3
9	29.3	37.9	42.5	43.5	47.4	48.4	48.6	42.2	40.4	45.7
Avg	37.7	43.8	44.0	43.1	45.0	46.4	48.7	49.3	49.0	51.3
Std	8.5	5.4	6.1	5.2	4.1	3.9	3.4	5.4	7.2	6.3

Table 18: Optical strain gauge readings for fringe pattern C (3mm gauge length)

	Optical strain gauge reading (μstrain) [radius in mm]									
	A 118.7	B 113.7	C 108.7	D 103.7	E 98.7	F 93.7	G 88.7	H 83.7	I 78.7	J 73.7
1	72.3	79.8	77.6	76.3	83.9	77.8	77.9	101.9	84.5	83.3
2	68.3	72.6	78.0	76.6	76.7	84.5	83.0	83.4	83.9	81.8
3	68.9	71.4	72.1	72.3	77.6	80.8	85.1	83.1	78.5	88.3
4	66.1	69.7	71.3	71.9	75.9	73.1	77.1	85.1	77.0	92.8
5	66.2	77.1	75.7	71.0	76.2	73.9	76.0	82.1	74.9	82.1
6	68.4	71.9	69.6	71.2	75.0	75.9	80.0	72.0	76.2	79.7
7	66.6	73.3	72.2	70.1	72.5	78.6	76.8	78.0	87.0	79.6
8	66.2	70.7	68.1	69.4	78.3	80.8	79.7	87.6	80.5	77.5
9	62.9	69.9	70.9	70.3	76.3	99.2	86.8	77.9	73.6	73.5
Avg	67.3	72.9	72.8	72.1	76.9	80.5	80.3	83.5	79.6	82.1
Std	2.4	3.2	3.3	2.5	2.9	2.4	3.6	7.8	4.4	5.4

Table 19: Optical strain gauge readings for fringe pattern D (3mm gauge length)

	Optical strain gauge reading (μstrain) [radius in mm]									
	A 118.7	B 113.7	C 108.7	D 103.7	E 98.7	F 93.7	G 88.7	H 83.7	I 78.7	J 73.7
1	18.5	30.7	26.8	24.4	32.1	37.3	40.7	43.6	46.5	48.9
2	20.4	27.3	26.5	25.9	37.3	41.1	39.2	46.3	45.3	40.8
3	18.3	26.1	31.0	24.4	30.3	36.9	39.4	42.3	43.1	44.4
4	25.3	21.8	25.1	28.2	25.3	36.1	39.9	39.6	40.3	41.3
5	26.6	19.4	28.8	27.9	24.8	31.5	37.8	42.9	42.3	41.6
6	25.0	20.7	27.2	27.9	26.7	30.5	39.7	41.9	42.6	38.1
7	22.8	18.7	28.2	27.5	28.6	31.1	38.7	44.7	38.5	34.7
8	13.9	23.7	25.8	24.5	31.1	36.1	38.3	39.0	37.8	37.0
9	14.8	22.4	21.4	21.8	29.4	36.3	37.4	35.0	39.3	40.7
Avg	20.6	23.4	26.8	25.8	29.5	35.2	39.0	41.7	41.7	40.8
Std	4.4	3.7	2.5	2.1	3.6	3.3	1.0	3.2	2.8	3.9

Table 20: Optical strain gauge readings for fringe pattern E (3mm gauge length)

	Optical strain gauge reading (μstrain) [radius in mm]									
	A 118.7	B 113.7	C 108.7	D 103.7	E 98.7	F 93.7	G 88.7	H 83.7	I 78.7	J 73.7
1	18.6	24.5	44.2	48.5	41.1	65.5	67.1	59.4	55.0	80.6
2	5.7	37.9	34.1	43.5	38.8	62.4	62.6	66.0	69.3	92.5
3	38.4	48.1	23.9	39.1	43.3	55.5	59.1	67.8	69.5	75.8
4	47.1	25.1	38.6	43.7	47.5	49.0	57.8	65.9	65.9	73.4
5	8.2	23.6	38.8	43.7	39.5	66.2	54.0	60.9	71.1	82.8
6	47.2	32.7	36.2	32.8	42.0	64.0	57.5	52.9	71.1	92.6
7	24.3	27.3	27.8	38.9	39.7	50.5	52.7	60.8	75.5	69.9
8	14.1	25.1	26.7	41.0	42.8	59.5	70.3	58.7	70.9	65.0
9	14.5	20.4	26.7	46.1	49.5	49.6	44.4	61.8	65.9	70.6
Avg	24.2	39.4	33.0	42.5	42.7	58.0	28.4	61.6	68.2	78.1
Std	15.2	8.3	6.6	3.4	3.5	6.6	7.3	4.3	5.4	9.2

Table 21: Optical strain gauge readings for fringe pattern F (3mm gauge length)

	Optical strain gauge reading (μstrain) [radius in mm]									
	A 118.7	B 113.7	C 108.7	D 103.7	E 98.7	F 93.7	G 88.7	H 83.7	I 78.7	J 73.7
1	57.3	68.8	93.2	83.5	92.6	82.1	102.3	89.4	97.3	95.2
2	66.1	70.1	90.2	89.0	82.9	102.2	93.2	80.1	96.8	97.8
3	57.1	79.6	59.1	68.8	87.0	94.5	75.4	94.3	88.5	93.3
4	64.5	59.3	80.2	83.9	78.9	99.2	95.5	101.6	87.5	106.6
5	80.9	49.5	74.8	74.8	76.1	82.3	80.0	84.7	96.8	92.5
6	54.7	60.1	45.3	65.7	91.6	70.5	88.5	93.9	86.5	92.6
7	67.6	51.3	59.6	70.1	86.1	79.5	82.0	81.2	80.3	92.3
8	64.5	56.4	51.9	66.8	87.1	88.4	82.4	80.1	79.2	83.4
9	59.6	63.3	64.9	69.5	77.5	82.1	74.6	77.6	71.6	86.9
Avg	63.6	62.0	68.8	74.7	84.4	86.8	86.0	87.0	87.2	93.4
Std	7.5	9.0	15.8	8.1	5.6	9.6	9.0	7.8	8.5	6.2

Table 22: Optical strain gauge readings for fringe pattern G (3mm gauge length)

	Optical strain gauge reading (μstrain) [radius in mm]									
	A 118.7	B 113.7	C 108.7	D 103.7	E 98.7	F 93.7	G 88.7	H 83.7	I 78.7	J 73.7
1	111.7	92.5	115.6	102.5	114.8	139.7	119.4	128.0	129.5	148.7
2	106.4	102.4	110.3	106.1	113.6	119.2	127.0	135.7	128.1	134.8
3	87.3	102.6	111.4	110.0	98.0	126.9	120.7	130.9	123.8	140.8
4	85.6	100.7	98.7	109.4	117.7	113.7	121.4	126.7	128.9	126.8
5	97.9	90.8	117.8	105.2	112.3	118.9	123.2	129.4	128.6	128.3
6	104.8	101.9	108.5	102.4	106.7	122.1	122.1	133.6	130.1	130.6
7	92.3	107.7	99.6	109.9	113.0	116.4	130.7	124.1	129.9	125.5
8	97.6	106.0	104.0	108.4	109.9	135.7	128.9	132.4	132.2	124.7
9	95.3	94.9	107.1	104.9	115.0	121.6	122.9	123.9	119.9	107.1
Avg	97.7	99.9	108.1	106.5	111.2	123.8	124.0	129.4	127.9	129.7
Std	8.2	5.6	6.2	2.8	5.5	8.3	3.7	3.9	3.5	10.9

Table 23: Optical strain gauge readings for fringe pattern H (3mm gauge length)

	Optical strain gauge reading (μstrain) [radius in mm]									
	A 118.7	B 113.7	C 108.7	D 103.7	E 98.7	F 93.7	G 88.7	H 83.7	I 78.7	J 73.7
1	74.7	98.7	68.1	118.9	91.7	106.3	115.7	120.0	117.3	99.9
2	75.7	98.6	94.7	98.8	92.6	103.1	102.1	119.8	104.5	119.8
3	78.1	97.3	82.9	98.7	90.3	100.4	109.9	111.5	102.3	119.9
4	75.7	81.1	94.4	87.9	110.3	92.5	105.8	105.3	105.8	107.8
5	80.3	93.0	86.7	103.1	97.2	108.8	95.2	112.2	92.7	119.2
6	70.6	85.4	80.9	91.7	101.2	104.5	99.6	112.3	115.8	106.4
7	68.7	86.4	88.7	87.1	100.2	107.4	104.5	97.6	109.4	112.4
8	78.5	82.6	97.5	87.0	105.7	104.5	114.8	114.4	110.1	107.5
9	70.1	93.5	83.4	84.4	98.4	104.3	95.3	107.4	96.1	104.4
Avg	74.7	90.7	86.4	95.3	98.6	103.5	104.8	111.2	106.0	110.8
Std	3.8	6.6	8.5	10.4	6.2	4.5	7.2	6.7	7.8	7.0

Table 24: Optical strain gauge readings for fringe pattern I (3mm gauge length)

	Optical strain gauge reading (μstrain) [radius in mm]									
	A 118.7	B 113.7	C 108.7	D 103.7	E 98.7	F 93.7	G 88.7	H 83.7	I 78.7	J 73.7
1	76.1	80.0	77.5	96.9	93.1	91.5	101.2	104.9	108.1	89.4
2	81.8	68.2	86.1	92.0	87.9	87.6	96.6	100.7	103.1	102.4
3	75.8	77.2	83.2	87.5	91.9	92.4	91.4	100.9	96.4	99.5
4	68.8	76.9	80.6	84.8	93.3	91.7	91.8	95.9	99.2	101.9
5	71.6	79.6	80.1	83.9	92.7	90.9	90.6	97.0	100.9	105.2
6	83.2	63.8	76.3	77.6	91.1	92.9	90.8	105.6	100.6	99.6
7	67.4	77.4	67.8	83.4	89.9	91.7	97.9	92.6	94.4	110.0
8	66.1	80.6	79.1	74.2	90.7	101.3	102.9	98.7	94.3	97.1
9	72.8	62.7	77.5	74.5	95.1	85.3	99.1	89.8	86.7	101.4
Avg	73.7	74.0	78.7	83.9	91.7	91.7	95.8	98.5	98.2	100.7
Std	5.7	6.7	4.8	7.2	2.0	4.1	4.5	5.0	5.8	5.3

Table 25: Optical strain gauge readings for fringe pattern J (3mm gauge length)

	Optical strain gauge reading (μstrain) [radius in mm]									
	A 118.7	B 113.7	C 108.7	D 103.7	E 98.7	F 93.7	G 88.7	H 83.7	I 78.7	J 73.7
1	78.9	83.4	84.6	92.1	89.6	90.3	109.0	96.1	105.3	102.4
2	74.6	76.4	83.1	76.5	87.5	93.9	95.6	98.3	97.4	97.9
3	68.9	65.7	87.7	84.0	83.8	87.3	98.5	96.4	96.1	95.5
4	68.6	74.9	79.8	70.6	83.3	96.9	90.3	97.3	92.4	90.1
5	68.7	71.5	86.6	74.7	76.4	91.3	90.8	103.1	97.5	95.2
6	72.8	50.7	77.7	75.5	75.4	102.2	85.1	93.9	99.9	90.6
7	67.6	64.2	75.4	78.5	79.9	88.7	99.6	88.8	93.4	87.6
8	67.2	63.7	74.8	78.4	80.5	102.1	90.5	95.5	91.8	87.2
9	60.2	65.0	69.1	77.5	90.9	89.3	113.9	85.5	99.2	74.9
Avg	69.7	68.4	79.9	78.6	83.9	93.6	97.0	95.0	97.0	91.3
Std	5.0	8.9	5.8	5.8	5.2	5.3	8.9	4.9	4.0	7.5

Table 26: Optical strain gauge readings for fringe pattern K (3mm gauge length)

	Optical strain gauge reading (μstrain) [radius in mm]									
	A 118.7	B 113.7	C 108.7	D 103.7	E 98.7	F 93.7	G 88.7	H 83.7	I 78.7	J 73.7
1	114.7	115.1	132.0	129.5	129.4	136.8	141.3	139.9	147.4	126.8
2	108.0	123.6	120.8	122.1	127.2	138.2	139.4	130.1	136.9	148.2
3	111.3	115.2	116.0	134.8	118.8	146.8	121.7	135.2	131.7	135.6
4	92.4	116.0	112.4	124.2	124.4	129.1	131.1	133.6	135.0	142.6
5	91.1	118.8	110.4	125.1	127.4	130.7	131.7	132.7	140.8	133.2
6	100.9	112.4	124.3	110.6	125.2	130.7	129.5	136.1	130.4	142.7
7	108.5	101.9	123.1	118.8	124.8	129.0	138.3	131.0	131.9	129.6
8	97.4	115.0	115.7	114.9	122.8	140.9	133.4	139.9	130.5	132.6
9	103.8	104.1	125.0	107.2	127.4	125.6	137.6	137.8	145.8	124.7
Avg	103.1	113.6	120.0	120.8	125.3	134.2	133.8	135.1	136.7	135.1
Std	7.8	6.4	6.5	8.4	3.0	6.5	5.8	3.4	6.2	7.5

Table 27: Optical strain gauge readings for fringe pattern L (3mm gauge length)

	Optical strain gauge reading (μstrain) [radius in mm]									
	A 118.7	B 113.7	C 108.7	D 103.7	E 98.7	F 93.7	G 88.7	H 83.7	I 78.7	J 73.7
1	128.4	136.7	131.2	131.4	139.0	142.9	146.1	142.1	137.9	155.5
2	126.3	142.2	144.6	131.8	146.1	158.6	154.6	155.6	150.7	163.4
3	130.4	124.8	139.3	135.8	137.4	130.6	146.1	156.6	158.4	149.1
4	136.8	130.3	140.7	134.6	134.6	152.7	146.7	151.2	151.4	152.5
5	126.4	128.3	136.1	136.7	137.2	160.8	144.4	148.6	151.0	148.4
6	122.4	126.9	132.8	145.5	140.6	151.4	144.2	154.8	145.2	147.3
7	120.7	126.0	127.4	138.8	145.6	148.7	152.1	151.6	143.4	149.3
8	122.2	130.4	128.2	140.0	142.9	155.7	156.4	152.7	150.3	143.1
9	128.3	127.4	131.5	136.7	163.8	122.7	143.4	147.8	137.8	135.4
Std	126.9	130.3	134.6	136.8	143.0	147.1	148.2	151.2	147.3	149.3
Avg	4.7	5.3	5.6	4.1	8.2	12.2	4.6	4.3	6.4	7.3

Table 28: Optical strain gauge readings for fringe pattern M (3mm gauge length)

	Optical strain gauge reading (μstrain) [radius in mm]									
	A 118.7	B 113.7	C 108.7	D 103.7	E 98.7	F 93.7	G 88.7	H 83.7	I 78.7	J 73.7
1	122.5	154.5	140.2	152.0	155.2	156.3	164.4	165.5	154.3	153.2
2	155.6	155.5	151.6	160.1	152.4	155.2	165.3	165.8	168.9	167.4
3	149.3	143.7	144.1	136.5	156.2	157.2	167.4	164.9	161.2	147.2
4	115.9	139.5	130.4	142.6	157.6	158.2	145.2	172.8	167.0	169.8
5	144.5	126.8	138.6	147.3	160.3	147.5	156.9	160.1	180.7	161.1
6	136.9	127.1	150.4	155.6	144.7	166.5	168.4	158.2	159.8	159.2
7	137.4	139.8	158.3	150.6	155.8	156.8	170.6	152.2	170.2	152.7
8	129.7	158.2	144.2	142.7	149.9	159.6	156.1	172.1	161.1	150.2
9	129.5	146.3	164.6	140.5	165.1	165.2	160.3	176.1	147.8	148.6
Avg	135.7	143.5	146.9	147.5	155.2	158.1	161.6	165.3	163.4	156.6
Std	12.0	10.9	9.9	7.2	5.6	5.3	7.5	7.2	9.1	7.7

Table 29: Optical strain gauge readings for fringe pattern N (3mm gauge length)

	Optical strain gauge reading (μstrain) [radius in mm]									
	A 118.7	B 113.7	C 108.7	D 103.7	E 98.7	F 93.7	G 88.7	H 83.7	I 78.7	J 73.7
1	47.8	51.6	58.4	83.2	71.1	65.9	75.9	110.5	71.0	66.5
2	46.3	51.4	59.5	68.9	65.9	72.8	81.4	76.3	99.6	82.1
3	26.1	58.0	51.0	70.4	66.3	68.6	84.5	78.5	92.8	80.8
4	46.3	48.6	53.1	66.1	75.6	65.8	78.8	78.6	94.7	77.1
5	49.3	47.9	56.7	59.5	68.8	71.2	76.8	84.4	79.9	82.3
6	37.5	53.0	54.4	60.9	69.9	69.2	72.5	85.6	82.0	82.3
7	36.7	49.8	54.2	57.9	64.2	70.3	76.8	85.5	79.7	86.1
8	45.2	38.9	59.0	56.6	78.9	80.2	75.6	80.0	73.9	85.6
9	41.8	65.4	54.0	73.1	70.1	75.5	74.0	67.9	71.2	87.9
Avg	41.9	51.6	55.6	66.3	70.1	71.1	77.4	83.0	82.8	81.2
Std	7.0	6.8	2.8	8.1	4.4	4.4	3.5	11.0	10.0	6.0

Table 30: Optical strain gauge readings for fringe pattern O (3mm gauge length)

	Optical strain gauge reading (μstrain) [radius in mm]									
	A 118.7	B 113.7	C 108.7	D 103.7	E 98.7	F 93.7	G 88.7	H 83.7	I 78.7	J 73.7
1	41.3	61.9	81.8	88.3	76.3	87.1	85.0	77.9	86.9	94.6
2	57.5	63.0	69.8	75.8	91.6	80.0	80.2	94.8	87.7	112.9
3	53.2	58.2	62.0	71.4	80.1	81.1	96.4	91.2	110.0	96.4
4	53.9	63.3	59.8	70.1	78.4	84.6	85.9	93.7	90.1	97.9
5	48.9	63.4	57.1	78.5	69.3	93.2	89.5	90.4	90.9	97.4
6	53.9	58.8	63.6	79.2	72.4	74.3	86.9	91.7	108.4	80.9
7	57.7	66.8	61.5	66.2	91.0	76.6	81.6	82.6	96.7	87.9
8	46.1	68.7	70.6	66.5	75.0	69.6	89.0	88.9	97.4	86.5
9	65.2	60.9	52.9	73.6	71.9	71.2	89.4	77.6	88.2	107.5
Avg	53.1	62.8	64.3	74.4	78.4	79.7	87.1	87.6	95.1	95.8
Std	6.6	3.2	8.1	6.6	7.5	7.3	4.5	6.2	8.3	9.5

Table 31: Optical strain gauge readings for fringe pattern P (3mm gauge length)

	Optical strain gauge reading (μstrain) [radius in mm]									
	A 118.7	B 113.7	C 108.7	D 103.7	E 98.7	F 93.7	G 88.7	H 83.7	I 78.7	J 73.7
1	102.4	94.3	112.8	105.6	112.9	120.1	110.6	107.7	107.4	101.4
2	88.2	98.5	105.8	107.5	115.9	116.8	117.2	114.9	113.7	122.6
3	93.5	86.0	100.9	99.7	108.5	123.2	111.6	120.5	113.9	115.0
4	85.6	97.3	104.9	100.0	109.0	113.1	117.3	108.6	112.3	119.1
5	95.7	88.1	105.3	105.7	96.1	102.6	120.5	112.7	116.4	124.3
6	92.8	86.1	99.3	101.9	103.1	105.9	103.0	113.4	116.7	121.9
7	88.3	94.4	103.7	97.4	104.3	111.0	108.0	111.6	111.2	112.9
8	92.3	97.8	99.3	102.7	106.5	109.7	113.6	106.5	118.7	113.2
9	91.2	105.3	97.6	107.5	113.7	100.7	110.2	117.4	107.5	120.4
Avg	92.2	94.2	103.3	103.1	107.8	111.5	112.4	112.6	113.1	116.8
Std	4.6	6.1	4.4	3.4	5.8	7.2	5.1	4.3	3.7	6.7

Table 32: Optical strain gauge readings for fringe pattern Q (3mm gauge length)

	Optical strain gauge reading (μstrain) [radius in mm]									
	A 118.7	B 113.7	C 108.7	D 103.7	E 98.7	F 93.7	G 88.7	H 83.7	I 78.7	J 73.7
1	109.3	123.3	126.1	162.0	121.9	130.6	133.2	129.5	129.5	113.6
2	110.1	116.7	125.8	123.4	133.1	130.7	133.4	132.9	123.2	142.4
3	87.2	116.0	116.1	123.7	127.0	138.7	133.7	136.9	125.9	132.1
4	104.9	108.6	114.1	126.7	117.6	128.0	134.2	125.7	121.6	147.6
5	112.3	108.6	115.6	115.8	117.2	127.9	132.2	129.6	129.9	134.7
6	103.7	110.3	114.1	119.7	115.0	117.1	127.0	127.7	126.7	131.1
7	107.4	114.7	114.3	115.2	123.7	133.6	125.6	123.0	120.5	126.2
8	108.5	113.6	127.3	122.4	116.7	132.0	127.7	130.4	127.7	132.4
9	108.5	123.7	121.9	124.2	130.4	123.0	127.3	133.0	126.8	144.6
Avg	105.8	115.1	119.5	125.9	122.5	129.1	130.5	129.9	125.8	133.9
Std	7.0	5.3	5.4	13.3	6.1	5.9	5.3	3.9	3.1	9.8

Table 33: Optical strain gauge readings for fringe pattern R (3mm gauge length)

	Optical strain gauge reading (μstrain) [radius in mm]									
	A 118.7	B 113.7	C 108.7	D 103.7	E 98.7	F 93.7	G 88.7	H 83.7	I 78.7	J 73.7
1	135.4	149.0	130.5	125.7	133.7	157.1	143.4	151.9	150.4	135.6
2	124.0	121.9	124.8	137.4	146.1	144.0	151.2	142.5	139.6	144.7
3	133.2	108.3	126.8	129.9	139.8	153.5	141.3	141.0	154.5	144.5
4	118.8	139.5	112.2	137.5	141.6	137.8	150.2	143.3	131.2	159.7
5	122.9	126.9	134.8	137.1	135.9	144.3	144.2	148.9	145.3	142.9
6	121.8	124.3	136.8	131.7	133.8	139.5	135.9	143.4	149.2	147.3
7	130.4	131.2	128.1	133.4	132.3	142.6	137.0	137.6	144.0	142.4
8	102.3	139.2	126.2	132.3	130.3	149.9	150.3	143.2	147.6	151.0
9	136.2	131.3	124.9	133.0	138.2	145.6	149.2	147.8	152.3	160.3
Avg	125.0	130.2	127.2	133.1	136.9	146.0	144.7	144.4	146.0	147.6
Std	10.0	11.1	6.7	3.7	4.7	6.0	5.5	4.1	6.7	7.7

Table 34: Optical strain gauge readings for fringe pattern S (3mm gauge length)

D APPENDIX

This appendix contains diagrams of the main parts of the modified electronic control unit. These diagrams are not strictly circuit diagrams, but indicate the main design of the control system.

Figure 145 is the 3 digit BCD counter (counter 1) shown in Figure 34. Figure 146 is counter 2 from Figure 34. The other parts of the control system are not presented in this appendix.

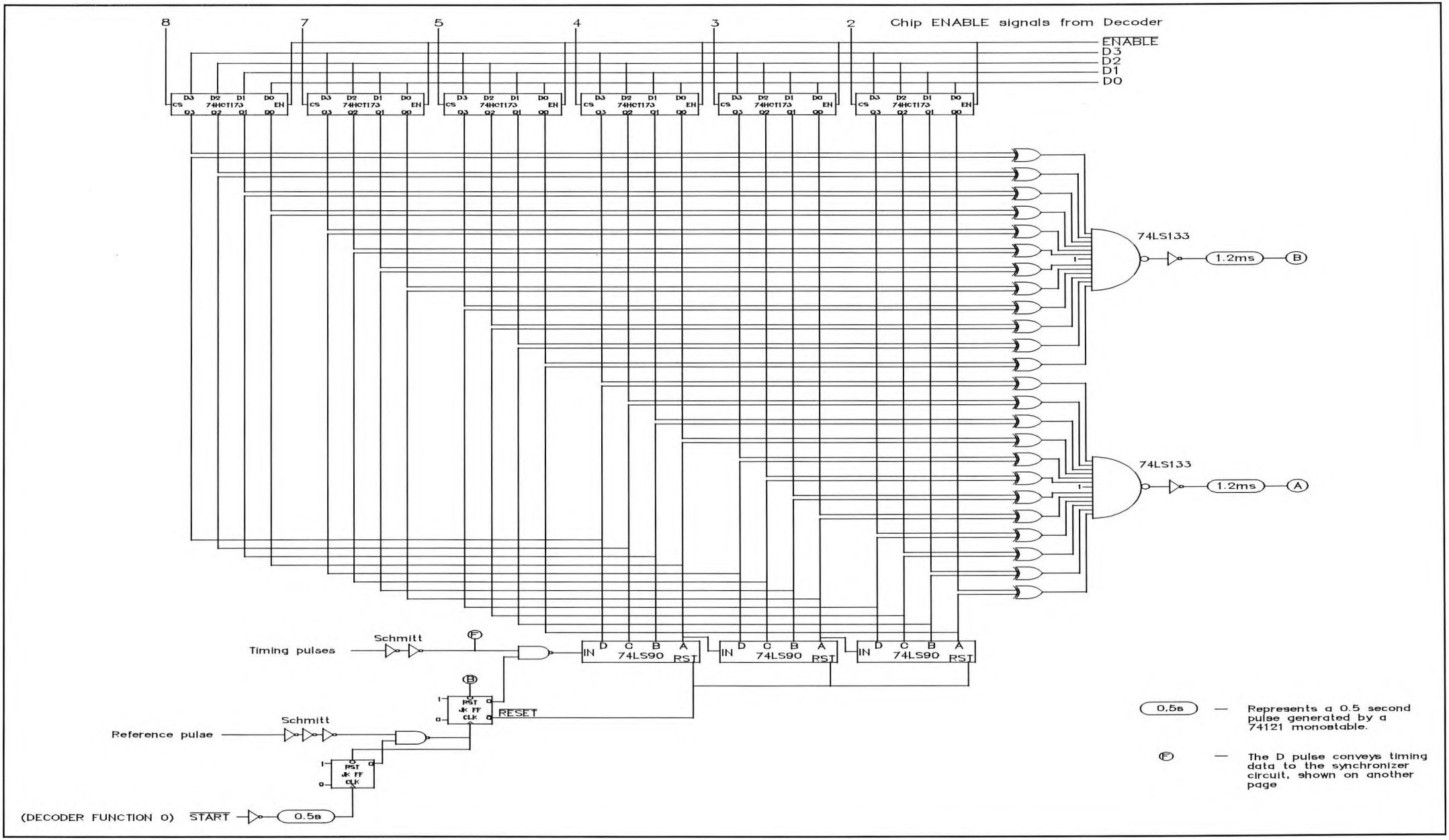


Figure 145: Primary electronic counter

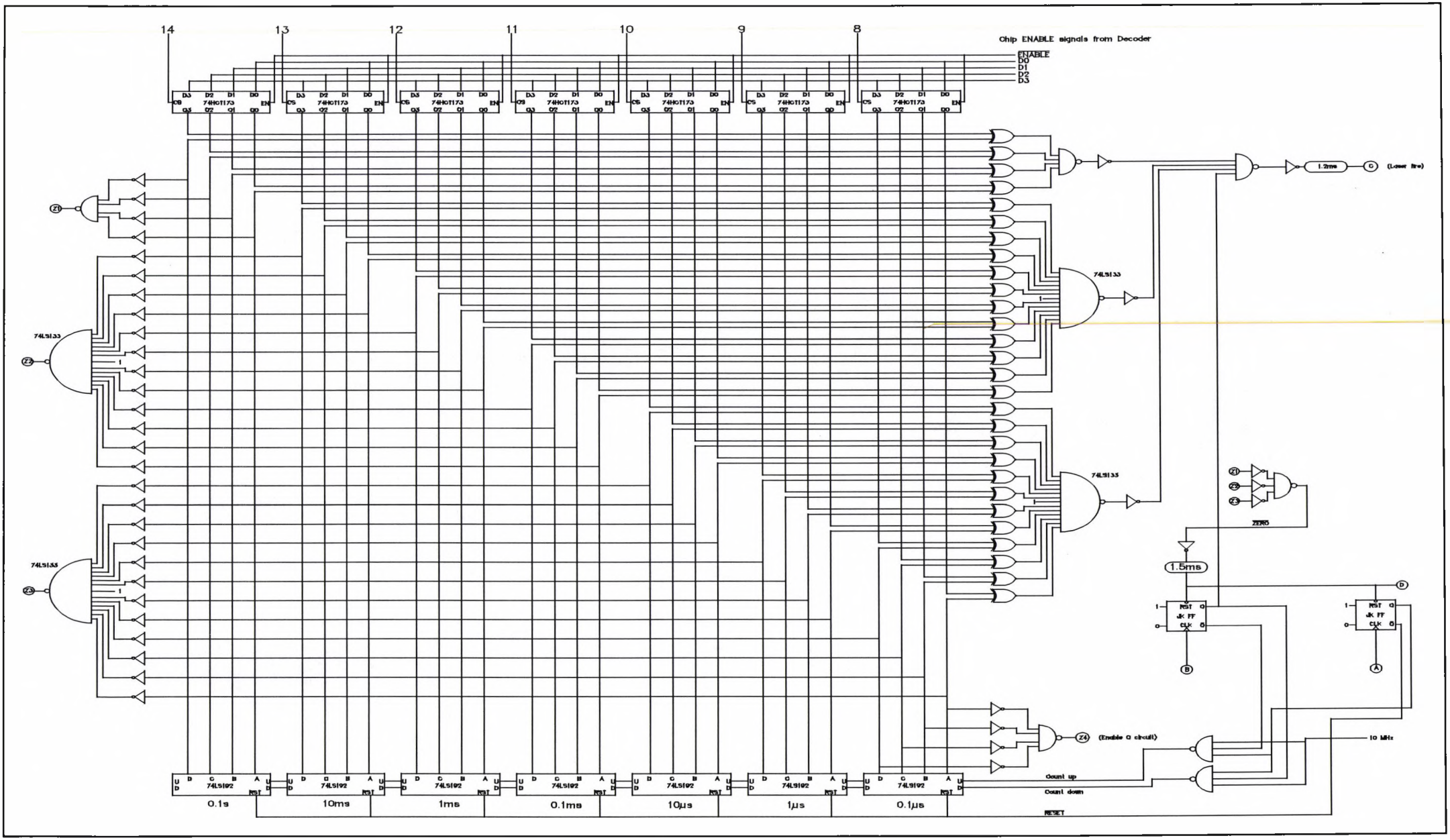


Figure 146: Secondary electronic counter